Université du Québec

Institut national de la recherche scientifique

Centre Eau Terre Environnement

TAKING ACTIVE AND PASSIVE BCI OUTSIDE: ON THE IMPORTANCE OF PRE-PROCESSING AND AMPLITUDE MODULATION FEATURES

Par

Olivier Rosanne

Thèse présentée pour l'obtention du grade de
Doctorate of Sciences, Ph.D
en Centre Énergie Matériaux Télécommunications

Jury d'évaluation

Président du jury et examinateur interne	Prof. Zakaria Abou El Houda INRS
Examinateur externe 1	Prof. Sarah Power Faculty of engineering and applied science Memorial University
Examinateur externe 2	Prof. Arash Mohammadi Concordia Institute of Information Systems Engineering Concordia University
Directeur de recherche	Prof. Tiago H. Falk
Codirecteur de recherche	Prof. Alcyr Alves de Oliveira Jr UFCSPA

© Droits réservés de Olivier Rosanne, July 2024

Tout ce que je sais, c'est que je ne sais rien.

Socrate

REMERCIEMENTS

Ces années de thèse ont été une expérience formidable qui m'a beaucoup appris et de laquelle je ressors grandi.

Je tiens à exprimer ma plus profonde gratitude à mon directeur de thèse, Pr. Tiago Falk, pour m'avoir donné l'opportunité de poursuivre mes études sur un sujet qui me passione. Sa confiance, sa bienveillance et sa sagesse m'ont accompagné tout au long de ce parcours de doctorat. Ce fut un immense plaisir de travailler avec lui.

Je souhaite également remercier chaleureusement tous mes amis et collègues du laboratoire MuSAE. Je garde en mémoire de très bons moments passés en leur compagnie et j'espère en vivre d'autres. Leurs conseils et leur soutien ont grandement enrichi mes compétences et mon sens critique nécessaire à tout scientifique.

Je suis profondément reconnaissant envers ma famille, dont l'amour et le soutien m'ont permis de ne jamais me sentir seul dans les moments les plus difficiles. À ma mère, pour sa confiance infaillible et ses efforts considérables qui m'ont permis de surpasser mes limites et de m'épanouir. À ma compagne, Marilia, qui a changé ma vie et m'apporte joie et bonheur chaque jour.

Enfin, un grand merci à toutes les personnes qui, de près ou de loin, ont contribué à la réalisation de cette thèse. Votre aide, vos encouragements et vos conseils ont été précieux.

RÉSUMÉ

Les Interfaces Cerveau-Ordinateur (ICOs) sont des systèmes qui mesurent et interprètent l'activité cérébrale pour fournir un retour d'information ou effectuer des actions, permettant un contrôle direct ou une interaction avec d'autres systèmes par la pensée. Parmi les différents capteurs capables de mesurer l'activité cérébrale, les EEG sont les plus souvent employés, car ils constituent une solution peu coûteuse, non-invasive, et offrent une excellente résolution temporelle. Bien que leur efficacité soit inférieure à celle des méthodes invasives comme l'ECoG, les EEG ont l'avantage de ne pas nécessiter une intervention chirurgicale, permettant ainsi leur utilisation par la grande majorité des individus. À l'origine, les ICOs ont été principalement développées pour des applications médicales, offrant des alternatives non-pharmacologiques pour traiter et assister quotidiennement les patients souffrant de troubles neurologiques. Elles permettent notamment d'améliorer l'autonomie des patients pendant la rééducation et de réduire la charge de travail pour le personnel soignant.

Sur le plan économique, une croissance considérable est attendue dans le marché des ICOs, avec des bénéfices allant de 2 milliards USD en 2023 atteignant entre 5,4 et 10,65 milliards USD d'ici 2030. Cet intérêt relativement récent pour les ICOs est lié à la miniaturisation des composants électroniques, à l'amélioration des performances des batteries et au perfectionnement des capteurs EEG dits 'secs'. Ces innovations ont permis une réduction des coûts, faisant passer les ICOs des expériences contrôlées en laboratoire à une utilisation accessible au grand public. L'avènement de la réalité virtuelle (RV) et des technologies d'apprentissage profond a également ouvert de nouvelles perspectives pour les ICOs, en améliorant l'immersion et en personnalisant les contenus en fonction des réactions et des besoins spécifiques de chaque utilisateur.

Cependant, les performances des ICOs restent insuffisantes et varient fortement au cours du temps et d'un utilisateur à un autre. Les facteurs environnementaux impactent la qualité du signal, qui est fortement dégradé par de multiples sources d'interférences. De plus, des facteurs liés à l'utilisateur comme la fatigue, la frustration, et le niveau d'attention, ainsi que les variations structurelles d'un individu à un autre, affectent également les performances des ICOs. Ces défis créent une boucle de rétroaction négative où la diminution de la précision réduit la fiabilité du système et la satisfaction de l'utilisateur.

Pour relever ces défis, cette thèse doctorale propose des solutions pour améliorer les performances, la portabilité et l'interprétabilité des systèmes ICO. Trois innovations principales ont été développées. Premièrement, nous proposons d'incorporer la modulation d'amplitude (MA) comme nouvelle représentation des signaux EEG pour améliorer la robustesse des ICOs actives. Ces caractéristiques ont montré une robustesse aux artefacts dans les applications ICOs passives, suggérant des avantages potentiels pour les ICOs actives. Deuxièmement, nous présentons un filtre adaptatif conçu pour éliminer les artefacts de mouvement spécifiques aux données EEG mobiles. Ce filtre a été testé à l'aide d'une base de données collectée auprès de participants réalisant la batterie de tâches Multi-Attribute Task Battery-II dans diverses conditions. Troisièmement, nous explorons l'impact de différents niveaux de suppression d'artefacts sur la caractérisation de la cybercinétose, en proposant l'utilisation de la modulation d'amplitude EEG pour la détection et l'interprétation de l'activité corticale relative à la cybercinétose.

À travers cette thèse, nous espérons améliorer la fiabilité des ICOs et contribuer à leur transition vers des applications pratiques pour le grand public.

Mots-clés Électroencéphalographie, interface cerveau-ordinateur, modulation d'amplitude, élimination des artefacts, filtrage adaptatif, état mental, évaluation de la charge mentale, activité physique, électroencéphalographie ambulatoire, cybercinétose, réalité virtuelle.

ABSTRACT

Brain Computer Interface (BCI) system measure and interpret brain activity to provide feedback or perform actions, allowing for direct control or interaction with other systems directly with the mind. Among the various sensors capable of measuring brain activity, Electroencephalogram (EEG) is the most commonly used because it is an inexpensive and non-invasive solution that offers excellent temporal resolution. Although its effectiveness is inferior to that of invasive methods such as ECoG, EEG has the advantage of not requiring surgical intervention, making it accessible to the vast majority of individuals. Initially, BCIs were primarily developed for medical applications, offering non-pharmacological alternatives to treat and assist individuals with neurological conditions. They allow patients, for instance, to enhance their autonomy during rehabilitation and reduce the workload of the healthcare staff.

From an economic perspective, significant growth is expected in the BCI market, with profits ranging from 2 billion USD in 2023 to between 5.4 and 10.65 billion USD by 2030. This relatively recent interest in BCIs can be attributed to technological innovations such as the miniaturization of electronic components, improved battery performance, and refinement of dry EEG sensors. These advancements have resulted in cost reductions, allowing BCIs to transition from controlled laboratory experiments to more accessible and publicly available applications. The emergence of Virtual Reality (VR) and deep-learning technologies has also created new opportunities for BCIs to improve immersion and customize content based on the unique reactions and needs of each user.

However, the performance of BCIs remains insufficient, and varies significantly over time and among users. Environmental factors affect the quality of the signals, which are heavily degraded by multiple sources of interference. Additionally, user-related factors, such as fatigue, frustration, attention level, and individual structural variations, also affect the performance of BCIs. These challenges create a negative feedback loop in which a decrease in precision reduces the reliability of the system and user satisfaction.

In this doctoral thesis, we present solutions to improve BCI performance, portability, and interpretability. Three main innovations have been developed. First, we propose the use of Amplitude Modulation (AM) as a new representation of EEG signals to improve the robustness of the active BCIs. These features have shown robustness to artifacts in passive BCI applications, suggesting the potential advantages for active BCIs. We employed them across 21 binary classification tests from combinations of seven mental tasks and we found that the average kappa score for these classifications increased from 0.57 to 0.62 when combined with conventional PSD features. An examination of the top-selected features showed the predominance of the AM-based measures, comprising over 77% of the top-ranked features.

Second, we present an adaptive filter designed to eliminate specific movement artifacts in EEG mobile data. This filter was tested using a dataset collected from participants performing Multi-Attribute Task Battery-II under various conditions. Accuracy as high as 95% could be achieved with a random forest based mental workload classifier with ambulant users.

Third, we explored the impact of different artifact removal levels on cybersickness characterization, proposing the use of EEG amplitude modulation to detect and interpret cortical activity related to cybersickness. Experimental results show that minimal pre-processing retains artifacts that may be useful for cybersickness detection (e.g., head and eye movements), while more advanced

methods enable the extraction of more interpretable neural patterns that may help the research community gain additional insights on the neural underpinnings of cybersickness. Our experiments show that the proposed amplitude modulation features comprise roughly 60% of the top-selected features for EEG-based cybersickness detection.

With these innovations, we aim to improve the reliability of BCIs and contribute to their transition towards practical applications for the general public.

Keywords electroencephalography, brain-computer interface, amplitude modulation, artifact removal, adaptive filtering, mental state, mental workload assessment, physical activity, ambulatory EEG, cybersickness, virtual reality

CONTENTS

LISTE DES FIGURES

LIST OF TABLES

GLOSSARY

AAR Automatic artifact Removal. 63, 74, 75, 82–86, 95, 103

aBCI Active Brain-Computer Interface. 4–6, 10, 12, 103

ADJUST Automatic EEG artifact Detection based on the Joint Use of Spatial and Temporal features. 24, 36, 63, 68

AF Adaptive filter. xvii, 63, 68, 70

AM Amplitude Modulation. vii, 10, 11, 13, 25–28, 33, 36, 37, 49, 55, 64, 68, 74, 78, 86, 91, 98–100, 102, 104, 105

AM-BCPL Amplitude Modulation inter-band coupling. xv, xviii, 26, 78, 84, 88

AM-CCPL Amplitude Modulation inter-channel coupling. xv, xviii, 26, 78, 84, 87, 98

AMP Amplitude Modulation Power. xvi, xviii, xix, 26, 28, 36, 37, 40, 41, 43–47, 49–54, 84, 86, 87, 96

ASR Artifact Subspace Reconstruction. xviii, xix, xxx, 24, 63, 68, 76, 82–85, 88–90, 92–95

BCI Brain Computer Interface. vii, viii, xv, 1–10, 12, 15, 17, 20, 21, 25, 28–34, 36, 42, 43, 48, 55, 103–105

BCPL Inter-band coupling. xviii, xix, 77, 84, 88, 91, 92, 99

BFT Band-filtered time-series. 77

CCOR Phase circular correlation of narrow-band filtered time series. 25, 28

CCORAM Phase circular correlation of amplitude modulation time series. xvi, 37, 40, 41, 43

CCPL Inter-channel coupling. xviii, 77, 84, 87, 90, 92, 98

EEG Electroencephalogram. vii, 2, 17

EOG Electrooculography. xvii, 23, 35, 36, 75–77, 82, 83, 101

ERP Event-related potential. 4, 20

FB Filter bank. 26, 27

FIR Finite impulse response. 26, 77

FLD Fisher linear discriminant. 37, 40, 43

FMS Fast Motion Sickness Scale. xvii–xix, xxi, 32, 73, 75, 78–80, 84, 86–88, 90–98, 100, 101

fNIRS Functional near-infrared spectroscopy. 7, 10, 17, 31, 34, 35

HAPPE The Harvard Automated Processing Pipeline for Electroencephalography. xvii, 24, 25, 63, 68, 70, 71

ICA Independent component analysis. 23, 24, 60, 75, 76, 95

ITR Information Transfer Rate. 6, 30

mRMR Minimum redundancy maximum relevance. xxxv, xxxvi, 37, 65, 68, 101

MW Mental workload. xvi, 8, 10, 32, 57–61, 103

PA Physical activity. xxi, 10, 57, 66, 68–71, 103

pBCI Passive Brain-Computer Interface. 5, 6, 10

PCA Principal component analysis. 23

PMSC Phase and Magnitude Spectral Coherence. 25, 28, 64, 68

PSD Power Spectral Density. vii, xvi, xviii, xix, 11, 25, 33, 36, 37, 40, 41, 43, 44, 47–54, 64, 68, 74, 77, 82, 84, 86, 87, 91, 96, 99, 102, 103

RF Random forest. xvii, xxi, 65–68, 70

RFE Recursive feature elimination. 37

RMSE Root-mean-square error. xxi, 80, 81, 93, 97

SNR Signal-to-Noise Ratio. xvii, 81, 82

SSVEP Steady-State Visual Evoked Potentials. 4, 20, 105

SVM Support Vector Machine. xvii, xxi, 29, 30, 38, 39, 65–68

SVR Support Vector Regressor. xvii, 79, 80, 101

VR Virtual Reality. vii, 1, 2, 9, 31, 32, 73, 74, 87, 97, 99–101, 105

wICA Wavelet-enhanced independent component analysis. 24, 63, 68

CARACTÉRISTIQUES DE MODULATION D'AMPLITUDE EEG POUR UNE PERFORMANCE AMÉLIORÉE DES ICO

Synopsis

0.1 Introduction

0.1.1 Interfaces Cerveau-Ordinateur

Les interfaces cerveau-ordinateur (ICO) sont des systèmes qui utilisent l'activité cérébrale de l'utilisateur comme entrée pour fournir un retour d'information ou effectuer une action, permettant ainsi le contrôle ou l'interaction avec un autre système directement par la pensée (Marcos-Martínez et al., 2023; Khalaf et al., 2019). Différents types de capteurs ont été utilisés pour enregistrer l'activité cérébrale, les capteurs EEG (électroencéphalographie) étant les plus populaires en raison de leur faible coût, leur caractère non-effractif et leur excellente résolution temporelle. Les modalités effractives comme l'ECoG, bien que plus efficaces, nécessitent une intervention chirurgicale pour implanter des électrodes dans le tissu cérébral.

Les ICO ont principalement été développées pour des applications médicales, offrant une alternative non pharmacologique pour le traitement et le soutien des patients souffrant de troubles neurologiques (Marcos-Martínez et al., 2023; Wood et al., 2014). Par exemple, les ICO permettent aux patients de gagner en autonomie pendant la réhabilitation, réduisant ainsi la charge de travail du personnel soignant. En 2023, la taille du marché des ICO était estimée à 2 milliards USD et devrait atteindre entre 5,4 et 10,65 milliards USD en 2030 (Market.us, 2024; IMARC Group, 2023). Cette croissance rapide est due à la baisse des prix des casques EEG, désormais disponibles à moins de 1000 USD, les rendant accessibles à un public plus large (He et al., 2023).

L'émergence de nouveaux matériaux, comme les matériaux mémoristiques, promet de révolutionner l'avenir de l'électronique et de contribuer à la miniaturisation et à la réduction des coûts des équipements ICO (Tzouvadaki et al., 2023). Les innovations dans les capteurs EEG secs, plus puissants et flexibles, ont également contribué au développement des EEG sans fil, marquant le début de la transition des enregistrements EEG en laboratoire vers des applications pour le grand public dans des environnements écologiques tels que le salon.

Récemment, l'émergence de nouveaux dispositifs de réalité virtuelle (RV), comme le Hololens de Microsoft et l'Oculus Rift de Meta, combinée à l'introduction de capteurs EEG à bas prix sur le marché, a ouvert des perspectives prometteuses pour la réhabilitation et la formation professionnelle (Lupu et al., 2018). Bien que les études combinant ICO et RV soient encore limitées (Palumbo, 2022), l'intégration de ces technologies permet une surveillance continue et objective de l'état physiologique de l'utilisateur en temps réel pendant les simulations (Lopes et al., 2024). Le système ICO fournit ainsi un canal de communication supplémentaire qui peut améliorer l'immersion et permettre la personnalisation du contenu en fonction des préférences ou des besoins spécifiques de l'utilisateur.

La fusion des deux technologies a conduit à la commercialisation de casques avec EEG intégré, tels que Kaptics, Galea (Bernal et al., 2022), OpenICO et Emotiv, parmi d'autres. Ainsi qu'au développement de logiciels tels que MindMaze, une plateforme de réhabilitation neurologique combinant réalité virtuelle et ICO. Cette technologie est utilisée cliniquement pour la réhabilitation des patients ayant subi des AVC et des lésions cérébrales.

0.1.1.1 Definition

Les interfaces homme-machine (HCI) sont des systèmes de communication qui forment généralement une boucle entre les parties "Utilisateur" et "Ordinateur". La partie "Ordinateur" reçoit des informations de la partie "Utilisateur" et les analyse pour fournir la réponse la plus appropriée à la tâche en cours. Les ICO appartiennent à la catégorie des interactions homme-machine (HCI) avec la particularité de collecter des informations sur l'utilisateur directement à partir de son activité cérébrale, transcendant ainsi les modalités intermédiaires conventionnelles telles que les compétences motrices fines ou la voix. La figure 1.1 illustre, à l'aide d'un diagramme, la boucle de communication formée entre l'utilisateur et la machine, ainsi que les principales étapes d'un pipeline typique de ICO.

0.1.1.2 ICO Basées sur l'EEG

L'EEG mesure l'activité électrique générée par la synchronisation et la dépolarisation de grandes populations de neurones. Ce type de capteur présente de nombreux avantages. Tout d'abord, ils sont portables et non-effractifs, permettant de les intégrer dans des casques ou des bandeaux prêts à l'emploi. Les capteurs secs et flexibles sont simplement en contact avec le cuir chevelu et ne laissent aucune marque (Marcos-Martínez et al., 2023). De plus, le coût de l'équipement EEG est faible comparé à d'autres modalités (Khalaf et al., 2019).

En outre, les signaux enregistrés ont une excellente résolution temporelle, avec une fréquence d'acquisition généralement comprise entre 128 Hz et 1000 Hz. Néanmoins, l'ensemble des tissus, le crâne et le volume crânien se comportent comme un filtre passe-bas, en consequence, l'activité cérébrale la plus importante enregistrée par l'EEG n'est disponible qu'en dessous de 100 Hz (Fiałek et al., 2016).

L'EEG est particulièrement sensible au bruit, contrairement aux modalités basées sur l'activité métabolique, comme la spectroscopie proche infrarouge (SPIR), qui offrent une meilleure robustesse (Shin et al., 2018). En effet, de nombreuses sources externes peuvent produire des signaux électromagnétiques d'amplitude supérieure à ceux du cortex cérébral, rendant ces systèmes plus susceptibles aux interférences.

0.1.1.3 Types de ICO

Les ICO peuvent être classées en deux grandes catégories: actives/réactives et passives. Récemment, le terme ICO hybride a été attribué à une ICO qui dépend simultanément de plusieurs modalités ou paradigmes.

ICO Actives et Réactives Les ICO actives (ICOa) détectent l'activité corticale spécifique et volontaire de l'utilisateur pour un contrôle direct des dispositifs, améliorant ainsi l'autonomie des personnes souffrant de déficits moteurs (Zander et al., 2009; Kumar et al., 2015). Les ICO réactives, une sous-catégorie des ICOa, identifient l'attention de l'utilisateur envers des stimuli sensoriels spécifiques, basés sur des réactions neuronales bien différenciées (Lotte et al., 2019; Won et al., 2022).

ICO Passives Les ICO passives (ICOp) sont utilisées pour analyser l'état émotionnel et cognitif de l'utilisateur en se basant sur l'activité corticale résultant de l'interaction avec un système tiers (Zander et al., 2009; Lotte et al., 2019). Elles permettent une analyse objective des états mentaux

comme la charge mentale, la relaxation et la fatigue, et sont particulièrement utiles dans des applications d'automatisation adaptative, de surveillance de l'engagement, et de prévention des accidents (Aricò et al., 2016; Sciaraffa et al., 2022).

0.1.2 Défis des ICO basées sur l'EEG

Malgré le potentiel des ICO, plusieurs défis majeurs subsistent, notamment l'état psychologique de l'utilisateur et sa familiarité avec la technologie ICO. La fatigue mentale, la frustration et le niveau d'attention peuvent affecter significativement les performances des ICO (Myrden et al., 2015; Hwang et al., 2009). De plus, la variabilité inter- et intra-sujets, ainsi que la qualité variable des signaux, sont les principaux obstacles pour améliorer la robustesse des systèmes ICO.

0.1.3 Contributions de la Thèse

Cette thèse doctorale a pour objectif d'améliorer la performance, la portabilité et l'interprétabilité des systèmes ICO, en proposant des innovations dans le prétraitement des signaux et l'extraction des caractéristiques. L'analyse de la modulation d'amplitude (MA) est proposée comme une nouvelle caractéristique de signaux EEG, offrant une représentation plus fidèle de certains mécanismes neurologiques fondamentaux.

0.1.4 Organisation de la Thèse

Le chapitre 2 présente les fondations théoriques des ICO basées sur les signaux EEG. Le chapitre 3 explore l'amélioration des ICO actives par l'utilisation des caractéristiques de modulation d'amplitude. Le chapitre 4 propose une méthode de prétraitement des données EEG pour améliorer la détection de la charge mentale pour des sujets ambulants. Le chapitre 5 aborde la détection de la cybercinétose avec des algorithmes de prétraitement et des caractéristiques MA. Enfin, le chapitre 6 résume les contributions de chaque étude de cette thèse et propose des perspectives futures pour les ICO.

0.2 Chapitre: 2: Cadre théorique

0.2.1 Le cerveau humain

0.2.1.1 Structure

L'encéphale humain contient approximativement 86,1 milliards de neurones (Azevedo et al., 2009), organisés en structures locales et interconnectés par un réseau complexe comprenant 60 trillions de synapses. Ce système complexe et dynamique fonctionne grâce à des mécanismes opérant à différents niveaux hiérarchiques, allant de l'échange d'ions dans les synapses (Südhof, 2021; Ferguson et al., 2020) à l'activité des circuits neuronaux locaux et interrégionaux (Peron et al., 2020; Simpson et al., 2013).

L'encéphale est divisé en trois parties principales: le cerveau (ou cérébrum), le tronc cérébral et le cervelet. Le cérébrum comprend le néocortex, une couche externe qui est subdivisée en lobes ayant des rôles fonctionnels spécifiques, liés à divers aspects du traitement cognitif et sensoriel (Lotte et al., 2015; Shepherd, 2003):

Lobe occipital Situé dans la partie postérieur du cerveau, il traite les informations visuelles et permet la reconnaissance d'objets et de mots.

Lobe pariétal Étend les capacités du cortex visuel pour la représentation spatiale, l'attention spatiale et la navigation.

Cortex moteur Localisé dans le lobe frontal postérieur, il planifie et exécute les mouvements, et montre une activité caractéristique lors de l'imagerie motrice.

Lobe frontal Impliqué dans des fonctions d'ordre supérieur telles que la prise de décision, l'attention et le raisonnement logique.

Lobe temporal Spécialisé dans l'analyse des événements futurs, la mémoire, la contextualisation des informations et le langage.

0.2.1.2 Neurones

Les neurones se composent de trois parties principales: les dendrites, le soma et l'axone. Les dendrites reçoivent des signaux via des synapses, le soma contient le noyau et les organites cellulaires, et l'axone transmet des signaux électriques à d'autres neurones (Shepherd, 2003). Les neurones transmettent l'information par des changements de polarité membranaire, libérant des neurotransmetteurs aux synapses. Les connexions locales qui réalisent les opérations élémentaires au sein du cortex se coordonnent pour intégrer des fonctions d'ordre supérieur, telles que l'encodage sensoriel, la mémoire, l'attention et la prise de décision.

0.2.2 Étude de l'activité cérébrale

Les études sur l'activité cérébrale ont pour objectif d'associer un état mesuré du cerveau à un comportement spécifique. Pour cela, un cadre de référence est défini, souvent l'activité au repos, caractérisée par un spectre de bruit brownien '1/f' connu sous le nom de 'mode par défaut'. Cette activité de référence varie selon les individus et dans le temps, nécessitant des mesures généralisables (Bell et al., 2012). Pendant l'exécution d'une tâche mentale, la distribution spectrale et spatiale de l'activité change, les neurones se synchronisent pour amplifier les signaux pertinents et des réseaux de communication inter-corticale se forment. Mesurer cette activité permet de caractériser précisément le comportement étudié.

0.2.2.1 Modalités

L'activité neurologique peut être évaluée par son empreinte électromagnétique via l'EEG ou par son activité métabolique comme la spectroscopie proche infrarouge fonctionnelle (SPIR). L'EEG mesure l'activité électrique des neurones corticaux tandis que le SPIR détecte les variations métaboliques liées à l'oxygénation du sang, offrant une résolution spatiale supérieure, mais une détection plus lente des réponses aux événements (Huster et al., 2014; Shin et al., 2018).

0.2.2.2 Ondes cérébrales

Les cellules du système nerveux central répondent à certains stimuli par des oscillations à différentes fréquences. Les principales bandes de fréquences observées sont:

Ondes Delta (0.5 - 4 Hz) Associées au sommeil profond et aux états de haute synchronisation (Steriade et al., 1993; Eggermont, 2021).

Ondes Thêta (4-8 Hz) Liées à l'encodage de la mémoire et à la navigation (Pignatelli et al., 2012).

Ondes Alpha (8-12 Hz) Observées lors de l'éveil au repos, elles sont impliquées dans la vigilance et l'attention (Da Silva, 2023; Liu et al., 2012).

Ondes Bêta (13-30 Hz) Associées à la mémoire, à l'attente d'un événement ou d'un stimuli sensoriel (Griffiths et al., 2021a,b; Betti et al., 2021; Abbasi et al., 2020; Basha et al., 2023).

Ondes Gamma (30-100 Hz) Liées aux fonctions cognitives de haut niveau telles que la perception, l'attention et la mémoire de travail (Brooks et al., 2020; Han et al., 2022a; Guan et al., 2022; Liu et al., 2022; Getachew et al., 2021; Lewis et al., 2021).

0.2.2.3 Paradigmes EEG

L'activité cognitive se manifeste par des variations d'amplitude suite à un stimulus (potentiels évoqués) ou par des oscillations dans certaines bandes de fréquences et régions corticales. Ces activités typiques sont utilisées par les ICO passives et actives (Yu et al., 2022a; Khademi et al., 2022; Zhou et al., 2022; Zhao et al., 2016).

0.2.3 Structure générale d'un pipeline d'ICO

Le pipeline typique d'une ICO comprend plusieurs étapes (Ruiz et al., 2014):

Acquisition des Données Les signaux EEG sont collectés selon le système international 10-20, garantissant une cohérence entre l'électrode et la région corticale mesurée malgré les différences morphologiques entre individus.

Prétraitement Cette étape vise à réduire les artefacts environnementaux et physiologiques qui peuvent masquer les informations neuronales utiles.

Extraction des Caractéristiques Les caractéristiques EEG sont calculées pour capturer les informations essentielles. Les caractéristiques standard incluent la densité spectrale de puissance (DSP), la cohérence de phase et de magnitude spectrale, et les nouvelles caractéristiques basées sur la modulation d'amplitude (MA).

Inférence L'activité est ensuite classifiée ou quantifiée à partir des caractéristiques extraites, généralement en utilisant des modèles d'apprentissage automatique.

Retour d'Information Les résultats de l'inférence sont traduits en une réponse adaptée à l'objectif de l'ICO.

0.2.3.1 Acquisition des données

Les études EEG s'appuient conventionnellement sur le système international 10-20 pour définir l'agencement des électrodes sur le cuir chevelu du participant, garantissant une association cohérente entre l'électrode et la région corticale mesurée malgré les différences morphologiques entre les individus. Chaque position d'électrode est identifiée par des lettres (région corticale) et des chiffres (hémisphère gauche ou droit) (Oostenveld et al., 2001; Padfield et al., 2019). La Figure 2.3 illustre cet agencement. Le nombre et la distribution des électrodes varient selon les besoins de l'étude pour améliorer la portabilité ou se concentrer sur une région d'intérêt spécifique.

0.2.3.2 Prétraitement

Les artefacts des signaux EEG Les artefacts peuvent être environnementaux ou physiologiques (Huster et al., 2014). Les artefacts environnementaux proviennent de l'environnement d'enregistrement, tels que le bruit des lignes électriques. Les artefacts physiologiques incluent des activités capturées par l'EEG non générées directement par l'activité corticale, comme les contractions musculaires et les clignements des yeux (Lotte et al., 2015). Les clignements des yeux apparaissent comme des pics d'amplitude, affectant particulièrement les électrodes frontales (Kumar et al., 2015).

Suppression des artefacts Traditionnellement, les artefacts sont éliminés par inspection visuelle des segments affectés, mais ce processus est lent et coûteux. Des algorithmes automatiques tels que l'ICA (*Independent Component Analysis*) et le PCA (*Principal Component Analysis*) ont été développés pour distinguer et éliminer les artefacts (Huster et al., 2014; Kumar et al., 2015). Des techniques d'apprentissage automatique, comme MARA (Winkler et al., 2011) et ICLabel (Pion-Tonachini et al., 2019), permettent d'automatiser le prétraitement en identifiant et supprimant les composants associés aux artefacts après une analyse ICA (Lotte et al., 2019).

En plus des techniques de réduction du bruit, des filtres spatiaux et spectraux sont utilisés pour améliorer les signaux EEG, comme les filtres spatiaux communs (CSP) qui amplifient les composants utiles et les filtres spectraux qui éliminent les fréquences basses (< 1 Hz) et hautes (> 50 Hz) affectées par le bruit.

Algorithmes de suppression automatique des artefacts Divers algorithmes automatiques de suppression des artefacts sont couramment utilisés :

ASR Artifact Subspace Reconstruction (ASR) Rejette les composants de grande variance grâce à une analyse en composantes principales avant reconstruction (Chang et al., 2019).

ADJUST Identifie et élimine les artefacts stéréotypés (mouvements oculaires, clignements, battements cardiaques) (Mognon et al., 2011).

Wavelet-ICA Combine la décomposition en ondelettes et l'ICA pour mieux préserver les propriétés spectrales et de cohérence de phase (Castellanos et al., 2006).

HAPPE Convient aux EEG à faible densité et aux échantillons limités, utilisant wICA et MARA pour détecter et rejeter les composants artefactuels (Gabard-Durnam et al., 2018).

Segmentation des données L'activité cérébrale capturée par les signaux EEG est non stationnaire. Il est donc courant de segmenter le signal en fenêtres temporelles quasi-stationnaires, appelées "epoch", pour effectuer des analyses statistiques (Huster et al., 2014). La durée des "epoch" varie selon les études, allant de quelques secondes à plusieurs minutes.

0.2.3.3 Extraction de caractéristiques EEG standard

Densité spectrale de puissance (DSP) Mesure la puissance de chaque composant fréquentiel pour évaluer l'activité mentale.

Coherence spectrale en phase et en magnitude (CSPM) Mesure la connectivité entre les régions corticales (Aoki et al., 1999).

Corrélation circulaire de phase (CCOR) Quantifie la connectivité entre les sites corticaux de manière plus robuste aux synchronies de phase aléatoire (Burgess, 2013).

0.2.3.4 Caractéristiques proposées de modulation d'amplitude de puissance

Les caractéristiques MA quantifient le taux de changement de sous-bandes fréquentielles spécifiques, révélant les interactions entre différents processus cérébraux et la communication à longue distance (Tort et al., 2010; Seeber et al., 2014; Voytek et al., 2010; Zanto et al., 2011; Clayton et al., 2015). Le processus de traitement des signaux EEG pour extraire les caractéristiques MA inclut:

- Décomposition en cinq bandes spectrales conventionnelles (delta, theta, alpha, beta, gamma) à l'aide d'un filtre à réponse impulsionnelle finie (RIF).
- Extraction de l'enveloppe des signaux filtrés par la transformée de Hilbert.
- Filtrage de l'enveloppe pour obtenir des séries temporelles MA.

Seules 14 des 25 séries temporelles MA possibles sont valides selon le théorème de Bedrosian (Trajin et al., 2008). La Figure 2.4 montre le processus d'extraction des caractéristiques MA. Les caractéristiques MA sont notées selon la convention '<bande modulée>-m<modulant>'.

0.2.3.5 Caractéristiques de couplage dérivées de la modulation d'amplitude

CSPM-MA Étend la capacité des caractéristiques CSPM aux modulations d'amplitude, utile pour la surveillance des états affectifs (Clerico et al., 2015, 2018).

CCORAM Examine les relations entre les dynamiques temporelles des oscillations et les interactions entre différentes régions du cortex.

0.2.3.6 Sélection des caractéristiques

La sélection des caractéristiques est cruciale pour réduire la dimensionnalité des entrées du classificateur, améliorant ainsi la performance de l'ICO (Remeseiro et al., 2019). Les algorithmes de sélection se divisent en trois catégories: basés sur des filtres, intégrés et enveloppants. Les algorithmes basés sur des filtres utilisent des tests statistiques pour évaluer l'importance des caractéristiques, tandis que les méthodes intégrées et enveloppantes intègrent la sélection des caractéristiques dans le processus d'entraînement du modèle ou évaluent plusieurs sous-ensembles de caractéristiques.

0.2.3.7 Apprentissage automatique

Deux types de modèles sont utilisés: les modèles classiques d'apprentissage automatique et les modèles d'apprentissage profond. Les modèles classiques incluent les modèles linéaires (LDA, régression linéaire), les modèles à base de noyau (SVM), les arbres de décision (Random Forest) et les modèles non paramétriques (K-plus proches voisins) (Aggarwal et al., 2019). Les modèles d'apprentissage profond, comme les réseaux de neurones récurrents (RNN) et les réseaux de neurones convolutifs (CNN), nécessitent une grande quantité de données mais offrent des performances supérieures (Schmidt, 2019; Wu, 2017).

0.2.3.8 Configuration des tests et indicateurs de performance

L'évaluation d'un modèle de classification repose sur des métriques telles que l'exactitude et le score Kappa, calculés à partir des valeurs de vrai positif (VP), faux positif (FP), vrai négatif (VN) et

faux négatif (FN). La validation croisée et les tests de permutation sont des méthodes couramment utilisées pour obtenir des évaluations robustes et fiables des modèles d'apprentissage automatique (Shin et al., 2018).

0.2.4 Datasets

Trois ensembles de données ont été utilisés dans cette thèse: le WAUC et le « VR-Induced Cybersickness Detection Dataset », tous deux employés pour des applications ICO passive, et le « Hybrid NIRS-EEG Brain-Computer Interface Dataset » pour une application ICO actives.

0.2.5 Conclusion

Ce chapitre a décrit l'origine de l'activité corticale capture par les EEGs, les avantages de l'EEG et les composants clés d'un pipeline ICO typique. Sur cette base théorique, les chapitres suivants présentent des contributions pour l'amélioration des ICOs.

0.3 Chapitre 3: Amélioration de la précision des interfaces cerveau-ordinateur actives

0.3.1 Préambule

Ce chapitre est compilé à partir de matériel extrait du manuscrit publié dans la revue MDPI Sensors (Rosanne et al., 2023).

0.3.2 Introduction

Les interfaces cerveau-ordinateur (ICO) actifs sont reconnues pour leur potentiel significatif dans la rééducation neurologique après un AVC. Ces systèmes offrent un suivi en temps réel de l'activité de l'utilisateur permettant de guider le patient de manière plus efficace et autonome durant le traitement. Ils constituent par ailleurs des systèmes de communication utile pour les patients souffrant de paralysie. Malgré leur potentiel, l'application clinique reste limitée en raison de leur fiabilité encore insuffisante.

L'un des défis majeurs de la technologie ICO est le taux d'erreur important lors de l'identification d'activités neurologiques exclusivement associe à une commande mentale exécuter par l'utilisateur. Leur faible précision s'explique d'une part par la variabilité d'un individu à un autre des schémas de l'activité neurologique mesure. D'autre part, certains facteurs physiologiques propres à un même individu tel que la fatigue ou la frustration influence négativement la détection de ces mêmes schémas.

Les approches traditionnelles pour améliorer la robustesse des ICOs incluent les systèmes multimodaux i.e. base sur l'emploi de différents types de capteurs ainsi que l'emploi de modèle d'apprentissage profond, qui par leur complexité montre une plus grande robustesse dans leur analyse des signaux EEG. Néanmoins, ces solutions ne parviennent pas à généraliser le même niveau de performances de détection à une plus large population.

Dans ce chapitre, nous proposons une représentation des signaux EEG basée sur la modulation d'amplitude (MA). Cette approche est pertinente, car la MA est une caractéristique du signal EEG associe à des mécanismes fondamentaux dans la coordination entre multiples populations de neurones. L'extraction de cette caractéristique aboutit alors à une identification plus fiable de

l'activité mentale par le système ICO, augmentant ainsi leur fiabilité pour les applications cliniques. Pour valider cette méthode, nous avons utilisé un ensemble de données d'ICO actif comprenant sept tâches mentales. Cette étude nous a permis d'explorer l'efficacité des caractéristiques MA dans la classification binaire de 21 paires de taches.

0.3.3 Protocole Expérimental

Notre étude emploie une base de données EEG open-source décrite dans (Banville et al., 2017), contenant des enregistrements EEG et SPIR durant l'exécution de sept types de tache mentale: Rotation mentale, complétion de mot, imagerie musicale, visualisation mentale de visage, imagerie moteur, navigation mentale et soustraction. Les données ont été collectées auprès de 12 participants sur une période de 3 à 5 semaines, chaque session comprenant des répétitions aléatoires des tâches mentales.

0.3.4 Pré-traitement du Jeu de Données

Les signaux EEG bruts ont été prétraités en utilisant la boîte à outils EEGLAB disponible sur MATLAB. Les étapes de pré-traitement incluent un filtrage encoche, un filtrage passe-bande, des algorithmes de réjection automatique de bruit, i.e., fastICA+ADJUST, l'interpolation des signaux supprimés et un référencement.

0.3.5 Extraction des Caractéristiques

Les caractéristiques de densité spectrale de puissance (DSP) ont été extraites comme base de comparaison, avec des segments de signaux EEG divisés en fenêtres de 1 seconde. Les caractéristiques de MA ont été calculées avec des fenêtres de 4 secondes glissantes toutes les 3 secondes, et les caractéristiques de corrélation circulaire de phase des signaux MA (CCPMA) ont été extraites pour quantifier la connectivité entre différentes régions corticales.

0.3.6 Sélection des Caractéristiques, Classification, et Figures de Mérite

Nous avons utilisé le discriminant linéaire de Fisher pour ordonner les caractéristiques de signaux EEG en fonction de leur pouvoir de discrimination entre les taches mentale. Un sous-ensemble des meilleures caractéristiques a par la suite été utilisé pour la classification. Nous avons employé une validation croisée à division stratifiée avec un classificateur SVM à noyau RBF. Enfin, la mesure de kappa a servi à évaluer les performances du classifieur.

0.3.7 Résultats

Les résultats montrent que la combinaison des caractéristiques de MA avec les caractéristiques DSP a amélioré la performance de classification dans la majorité des paires de tâches mentales testées. En particulier, l'ajout des caractéristiques MA a significativement augmenté les scores kappa pour 17 des 21 paires de tâches mentales. Pour les quatre autres paires, aucun changement significatif n'a pas été observé avec une augmentation dans trois cas et une diminution pour le dernier. L'analyse des scores kappa moyens a révélé que les caractéristiques combinées de MA, DSP et de CCPMA montre de meilleures performances de classification. La tâche de rotation

mentale a obtenu les meilleurs scores de discrimination, tandis que les tâches d'imagerie faciale et de musicale ont obtenu les scores les plus faibles.

0.3.8 Discussion

Les caractéristiques de MA se sont révélées prometteuses pour améliorer la précision des ICOs actives, car elles capturent des informations complémentaires aux caractéristiques DSP traditionnelles. Les résultats ont montré que les caractéristiques MA sont particulièrement efficaces pour représenter les dynamiques de traitement neuronal locales, notamment dans les tâches nécessitant des processus cognitifs complexes tels que la rotation mentale et la navigation mentale. Par exemple, les caractéristiques MA ont permis de mieux distinguer les tâches de rotation mentale en capturant des motifs spécifiques dans les bandes de fréquences beta et thêta, souvent associées aux fonctions de mémoire et d'attention visuo-spatiale.

En outre, les caractéristiques MA se sont avérées plus robustes aux artefacts, ce qui est crucial pour les ICOs actifs utilisés en environnements réels. Les analyses topographiques ont révélé des distributions distinctes des caractéristiques MA à travers les régions du cortex, indiquant une meilleure capture des activités neuronales spécifiques à chaque tâche mentale. Par exemple, les tâches de rotation mentale et de navigation ont montré une activité prononcée dans les régions pariétales et frontales, correspondant à l'engagement des réseaux neuronaux impliqués dans le traitement de l'espace et de la mémoire.

Les résultats suggèrent que les caractéristiques MA pourraient enrichir notre compréhension des processus neuronaux sous-jacents aux différentes tâches mentales et offrir des améliorations pour les systèmes ICOs actifs. Ces caractéristiques pourraient être particulièrement utiles pour suivre et compenser les variations inter-sujets et intersessions, améliorant ainsi la précision et la fiabilité des ICOs actives dans des applications pratiques.

0.4 Chapitre 4: Évaluation de la charge mentale chez les utilisateurs hautement mobile

0.4.1 Préambule

Ce chapitre est basé sur des travaux publiés dans le journal Frontiers in Neuroscience (Rosanne et al., 2021).

0.4.2 Introduction

De nombreuses professions, telles que les premiers intervenants (pompiers, policiers, ambulanciers) et les pilotes, sont souvent confrontées à des défis cognitifs incluant la surcharge d'informations, le multitâche, les interruptions et la fatigue. Dans de nombreux cas, ces individus sont également exposés à une combinaison de facteurs physiques et mentaux qui contribuent à une charge mentale (CM) élevée, augmentant ainsi les risques d'erreurs pouvant être fatales. Par conséquent, la surveillance de la CM a gagné en popularité ces dernières années. Il est difficile pour les méthodes d'évaluation subjective et comportementale de fournir des mesures en temps réel de la CM, ce qui restreint leur utilisation dans les systèmes automatisés conçus pour améliorer les performances des tâches en temps réel. C'est pourquoi des mesures neuronales et physiologiques discrètes, telles que l'électroencéphalographie (EEG), sont considérées comme une alternative viable. Des recherches antérieures ont démontré l'efficacité de l'évaluation de la CM basée sur

l'EEG dans des environnements contrôlés, tels que chez les pilotes et les conducteurs, où les participants sont principalement immobiles. Malgré les progrès de la technologie EEG portable, la présence d'artefacts de mouvement exacerbée par la sensibilité des électrodes sèches reste un défi important. De plus, les algorithmes d'amélioration de l'EEG existants, conçus principalement pour éliminer les artefacts oculaires et musculaires, sont insuffisants dans des scénarios impliquant des utilisateurs fortement mobiles. Pour répondre à cette problématique, nous proposons dans ce chapitre l'utilisation d'un filtre adaptatif pour éliminer les artefacts de mouvement spécifiques au déplacement à partir de données EEG mobiles. Les signaux extrait d'un accéléromètre place sur le torse des participants sont utilisés comme signaux de référence pour le filtre adaptatif. L'algorithme a été testé sur une base de données collectée en interne auprès de 48 participants alors qu'ils effectuaient la batterie de tâches multi-attributs - II (Santiago-Espada et al., 2011) dans deux conditions de charge de travail (basse et élevée) et deux types d'activité physique (vélo stationnaire et tapis roulant), chacun à trois niveaux d'intensité (aucun, moyen et élevé).

0.4.3 Matériels et Méthodes

0.4.3.1 Collecte de données

Les données ont été recueillies auprès de 48 participants (23 femmes, âge moyen 27,4 ± 6,6 ans), dont 22 ont utilisé un tapis roulant et 26 un vélo d'intérieur. Les participants utilisant le tapis roulant portaient un harnais de sécurité pour éviter les chutes. Le protocole expérimental comportait deux niveaux de charge mentale (faible/élevée) induits par le logiciel MATB-II, et trois niveaux d'activité physique (aucun, moyen, élevé). Chaque session expérimentale, correspondant à une combinaison spécifique de charge mentale et d'activité physique, durait 10 minutes, suivie d'une pause de 5 minutes. Artefacts de mouvement Les effets des mouvements, en particulier pendant la marche/course, sont illustrés par les représentations spectrales moyennes des canaux EEG et des signaux d'accéléromètre. Les artefacts de mouvement, couvrant les bandes de fréquences de 0,11 à 20 Hz, perturbent la qualité de l'EEG, justifiant l'utilisation d'un filtre adaptatif pour les atténuer.

0.4.3.2 Filtrage Adaptatif et algorithmes de réduction des artefacts

Un schéma de filtrage adaptatif est proposé pour éliminer les artefacts de mouvement des signaux EEG en utilisant des signaux d'accéléromètre comme référence. Le filtre est ajusté par la méthode des moindres carrés normalisées pour estimer et supprimer les artefacts de mouvement, améliorant ainsi la qualité des signaux EEG. Quatre algorithmes de réduction automatique des artefacts sont utilisés comme références : ASR, ADJUST, Wavelet-ICA et HAPPE. Ils sont testés individuellement ou en combinaison : ASR+wICA et ASR+ADJUST. Le filtre adaptatif proposé est également testé en combinaison avec ces algorithmes.

0.4.3.3 Extraction de caractéristiques

Des caractéristiques spectrales de densité de puissance (DSP), de modulation d'amplitude (MA), de cohérence spectrale de phase et de magnitude (CSPM), et de cohérence spectrale de modulation d'amplitude (CSPM-MA) sont extraites des signaux EEG bruts et prétraiter par diverse combinaison d'algorithme de rejection automatique de bruit. Le classement et la sélection des caractéristiques sont effectués à l'aide de la méthode mRMR.

0.4.4 Résultats et Discussion

0.4.4.1 Performance de classification

La comparaison des performances de classification entre deux niveaux d'intensité de la charge mentale montre une amélioration significative avec l'emploi du filtrage adaptatif. Les performances les plus élevées sont observés avec l'emploi des caractéristiques de modulation d'amplitude et les conditions d'activité physique élevée. Le meilleur résultat de classification est obtenu avec une combinaison du filtrage adaptatif et de l'algorithme HAPPE, atteignant une précision de 97,90%.

0.4.4.2 Importance des caractéristiques

Une analyse des caractéristiques sélectionnées par mRMR montre que les caractéristiques MA sont les plus pertinentes pour l'évaluation de la charge mentale, suivies par les mesures de cohérence spectrale. Les caractéristiques extraites des régions pariétales et frontales sont particulièrement importantes, reflétant les aspects liés à l'intégration sensorimotrice et à l'attention.

0.4.5 Conclusion

Ce chapitre propose un prétraitement des signaux EEG base sur l'emploi d'un filtre adaptatif pour améliorer l'évaluation de la charge mentale en conditions hautement mobile. Les résultats expérimentaux démontrent l'efficacité de cette approche, en particulier lorsqu'elle est combinée avec l'algorithme HAPPE, pour obtenir des mesures précises de la charge mentale malgré les artefacts de mouvement.

0.5 Chapitre 5: Évaluation de la cybersickness : prétraitement de l'EEG et importance de la modulation d'amplitude

0.5.1 Préambule

Ce chapitre présente une analyse approfondie de l'impact du pré-traitement des signaux EEG sur la caractérisation du cybersickness. Le contenu est basé sur des travaux publiés dans le journal Frontiers in Virtual Reality (Rosanne et al., 2024).

0.5.2 Introduction

Avec l'essor de la Réalité Virtuelle (RV) dû aux avancées technologiques, des environnements très réalistes et polyvalents sont devenus accessibles au grand public et sont utilisés dans des domaines variés tels que la médecine, la thérapie et la formation professionnelle. Cependant, le développement de la RV est entravé par la cybercinétose: un phénomène similaire au mal des transports, comprenant vertiges, nausées, maux de tête et désorientation. Bien que son origine ne soit pas entièrement connue, l'hypothèse la plus accepte serait la conséquence d'un conflit sensoriel. Le niveau et la dynamique temporelle de la cybercinétose sont communément évalués à partir de questionnaires. Cependant cette méthode est subjective et impacte négativement l'expérience utilisateur. La recherche de mesures objectives basée sur les bio-signaux constitue donc une meilleure alternative, même si la présence d'artefacts dans ces derniers influence la qualité des mesures. Ce chapitre présente nos contributions dans deux axes principaux: (1) l'impact

de différents niveaux de suppression d'artefacts sur la caractérisation du cybercinétose, en partant d'un prétraitement minimal jusqu'à l'emploi d'algorithme plus agressifs ne laissant que les signatures d'origine neuronales; et (2) l'analyse des caractéristiques de modulation d'amplitude (MA) de l'EEG aboutissant à une meilleure compréhension de l'activité cérébrale liée à la cybercinétose.

0.5.3 Matériels et Méthodes

0.5.3.1 Jeu de données EEG

Nous avons utilisé un jeu de données libre d'accès décrit dans (Li et al., 2021a), comprenant des données de 20 participants soumis à deux scénarios RV conçus pour induire progressivement une cybercinétose: la traversée d'un tunnel et une simulation de montagne russe. L'intensité de la cybercinétose a été mesurée chaque minute à l'aide du questionnaire « Fast Motion Sickness ».

0.5.3.2 Pré-traitement

Trois niveaux de pré-traitement des signaux EEG ont été explorés:

1. Minimal: Filtrage passe-haut pour éliminer les dérives de basse fréquence, préservant la majorité des artefacts potentiels.
2. ASR + ICLabel: Combinaison de l'algorithme de reconstruction de sous-espace d'artefacts (ASR) et d'une étape de rejet des composants indépendants (ICA) à partir du modèle « ICLabel ».
3. RegICA + Filtre Adaptatif: Utilisation de RegICA un traitement pipeline contenant un filtre adaptatif auquel a été fourni les signaux de l'accéléromètre place sur la tête et le signal électrooculogramme (EOG).

0.5.3.3 Extraction des Caractéristiques

Les caractéristiques traditionnelles de densité spectrale de puissance (DSP) et de couplage, ainsi que les caractéristiques de modulation d'amplitude (MA) ont été calculées. Les caractéristiques DSP et MA ont été évaluées sur des fenêtres de 2, 5, 8, 20 et 30 secondes.

0.5.3.4 Organisation des tests

Pour maximiser les données disponibles pour l'entraînement, nous avons utilisé une méthode de d'autoamorçage sur les segments EEG d'une minute, en appliquant une validation croisée en K sous-ensemble stratifiés.

0.5.4 Résultats Expérimentaux

0.5.4.1 Étude d'Ablation I : Impact des Artefacts

L'analyse de l'information mutuelle entre les signaux EEG et les mouvements oculaires/de tête a révélé que le pré-traitement minimal conservait le plus d'artefacts, tandis que l'ASR + ICLabel en retirait le plus.

0.5.4.2 Étude d'Ablation II : Combinaison de Pré-traitement, Taille de fenêtre temporelle et Type de Caractéristiques

Les caractéristiques DSP et MA se sont avérées les plus corrélées avec les scores du questionnaire FMS. De plus les pré-traitements minimal et ASR + ICLabel, les fenêtres de 8 et de 20 secondes présentent les corrélations les plus fortes.

0.5.4.3 Étude d'Ablation III : Sélection de Caractéristiques

L'analyse des meilleures caractéristiques a montré une prédominance des caractéristiques de modulation d'amplitude, soulignant leur rôle crucial dans la caractérisation de la cybercinétose.

0.5.5 Discussion

L'étude montre que la MA fournit des informations essentielles sur les processus neuronaux sous-jacents au cybercinétose, tels que la coordination de l'information sensorielle et la régulation de l'attention. En particulier, les interactions observées entre les bandes de fréquence bêta et alpha reflètent des mécanismes complexes de traitement cognitif et de réponse au conflit sensoriel. La conservation des artefacts peut améliorer la précision de la prédiction en fournissant des informations multimodales, incluant des indices sur les mouvements de la tête et des yeux qui sont pertinents pour la détection du cybercinétose. Les résultats suggèrent que, bien que les méthodes de pré-traitement avancées permettent une meilleure compréhension des motifs neuronaux, un pré-traitement minimal peut être plus efficace pour la détection du cybercinétose, en capturant à la fois les signaux neuronaux et les artefacts physiologiques utiles.

0.5.6 Conclusion

Ce chapitre démontre l'importance des caractéristiques EEG de modulation d'amplitude et de la sélection stratégique du niveau de pré-traitement pour la caractérisation de la cybercinétose. Ces résultats offrent de nouvelles perspectives pour l'amélioration des systèmes de détection et de compréhension du cybercinétose dans les environnements RV.

0.6 Conclusion

0.6.1 Résumé des contributions

Les contributions de cette thèse peuvent être résumées en deux majeurs parties.

0.6.1.1 Modulation d'amplitude pour une meilleure représentation de l'activité corticale

Dans le chapitre 3, nous avons proposé un nouveau jeu de caractéristiques pour les ICO actives (ICOa), basé sur les dynamiques de modulation d'amplitude des différentes sous-bandes de l'EEG. Par des expériences approfondies, nous avons démontré les avantages des caractéristiques proposées ainsi que leur complémentarité avec les caractéristiques spectrales classiques. Une discussion détaillée a été fournie pour explorer les mécanismes cognitifs complexes mesurés par

ces nouvelles caractéristiques et conjecturer leur rôle dans l'amélioration de la précision des ICO pour différentes tâches mentales.

Les résultats présentés dans les chapitres 4 et 5 montrent l'importance des mesures proposées pour les applications passives des ICO, utilisées dans la prédiction de la charge mentale et de la Cybercinétose. Nos résultats démontrent l'avantage de combiner la modulation d'amplitude, le couplage et la densité spectrale de puissance (DSP), chacune de ces caractéristiques capturant des attributs spécifiques de l'activité cérébrale.

0.6.1.2 Impact des algorithmes automatisés de suppression des artefacts dans des contextes pratiques

Les chapitres 4 et 5 présentent une comparaison de différents algorithmes de suppression des artefacts dans deux contextes pratiques pour les ICO : les utilisateurs très mobiles et les simulations de réalité virtuelle. Dans le chapitre 4, les résultats expérimentaux ont montré qu'en combinant un schéma de filtrage adaptatif avec d'autres méthodes d'amélioration traditionnelles, nous avons réussi à éliminer efficacement les artefacts de mouvement dans des conditions d'enregistrement extrêmes. Cette stratégie de prétraitement optimale a permis d'atteindre la meilleure précision de prédiction de la charge mentale et de trouver des informations pertinentes sur l'activité cognitive sous-jacente de la charge mentale (CM) et son interaction avec l'activité physique (AP). Dans le chapitre 5, nous avons traité un ensemble de données EEG publiquement disponible sur le mal des transports avec trois méthodes de prétraitement, allant de méthodes minimales à plus complexes pour supprimer les mouvements de la tête et des yeux. Nos résultats mettent en évidence l'importance des stratégies de prétraitement contextuelles pour à la fois l'interprétabilité de l'activité cérébrale et l'amélioration de la précision des ICO.

0.6.2 Recherche future

0.6.2.1 Apprentissage profond

Malgré les inconvénients majeurs des techniques d'apprentissage profond, le domaine s'améliore constamment, et des innovations récentes ont progressivement relevé de nombreux défis mis en évidence ici. Par exemple, les modèles basés sur l'attention (Cisotto et al., 2020; Toa et al., 2021) possèdent des capacités contextuelles qui améliorent le rapport signal-bruit et la précision. De plus, la couche d'attention fournit des informations claires sur les aspects importants des données d'entrée qui justifient les décisions du modèle. La recherche récente s'est également concentrée sur l'explicabilité de l'IA plutôt que sur la performance, avec le développement de techniques d'intellignece artificielle explicable (XAI) (Islam et al., 2022a; Morabito et al., 2023). Ces techniques peuvent fournir des insights importants pour une meilleure utilisation et interprétabilité des ICO.

0.6.2.2 ICO adaptative

Comme discuté dans le chapitre 1, l'état psychologique de l'utilisateur influence de manière significative la performance de la détection de motifs dans les ICO actives basées sur l'EEG. Les ICO passives étant généralement employées pour surveiller l'état mental de l'utilisateur à l'aide de biomarqueurs, leur combinaison avec les ICO actives pourrait potentiellement améliorer l'explicabilité et l'adaptabilité des ICO. Les ICO contextuelles peuvent s'appuyer sur les biomarqueurs des ICO

passives fonctionnant simultanément avec les ICO actives pour déterminer les meilleurs paradigmes ou changer de stratégies afin de maximiser la précision en fonction de la situation.

0.6.2.3 Localisation des sources

Les capteurs EEG ont une excellente résolution temporelle; cependant, en raison des propriétés physiques des tissus et du crâne, ils n'ont un bon ratio signal sur bruit que pour les activités spectrales en dessous de 100 Hz. Bien que l'activité spectrotemporelle soit importante, les sources spatiales d'activité et la communication entre circuits locaux distants véhiculent également des informations cruciales (Shepherd, 2003). Une solution consiste à augmenter la résolution spatiale de l'EEG en utilisant de multiples électrodes EEG. L'utilisation d'algorithmes de localisation des sources combinés avec une description spectrotemporelle puissante, telle que les caractéristiques de modulation d'amplitude (MA), pourrait améliorer encore la précision et réduire le délai des systèmes modernes de ICO. Le développement de tels outils devrait être exploré dans les futurs travaux.

0.6.2.4 Sélection et calibration des bandes optimales spécifiques à chaque sujet

Cette étude utilise des caractéristiques de modulation d'amplitude basées sur les bandes de fréquences conventionnelles (delta, thêta, alpha, bêta et gamma). Toutefois, il est intéressant de personnaliser ces bandes pour chaque utilisateur afin de réduire les variations inter- et intra-sujets (Huster et al., 2014; Sciaraffa et al., 2022). Par exemple, la fréquence alpha individuelle (IAF) et la décomposition en modes empiriques (EMD) permettent d'adapter l'analyse aux spécificités de chaque individu (Guger et al., 2000). Il serait également pertinent d'évaluer l'impact de ces bandes spécifiques dans de futurs projets, comme cela a été utile pour le diagnostic de la maladie d'Alzheimer (Lopes et al., 2021). De plus, utiliser des caractéristiques spécifiques à un paradigme bien connu pendant la calibration peut aider à évaluer la performance potentielle de l'ICO pour chaque utilisateur.

0.6.3 Conclusion

Les interfaces cerveau-ordinateur ont récemment connu une transition, passant d'une technologie conçue pour des études en laboratoire et des cas de traitement médical spécifique à un outil accessible au grand public et reconnu pour son utilité dans de nombreux secteurs industriels. Les innovations en apprentissage profond, en équipements de réalité virtuelle et en composants électroniques ont significativement influencé ce développement. Cependant, les technologies ICO font encore face à plusieurs obstacles, tels que la robustesse réduite, la variabilité de performance d'un utilisateur à l'autre et le manque d'interprétabilité de l'activité cérébrale mesurée. Dans cette thèse, nous espérons avoir contribué à l'avancement du domaine en proposant deux innovations : une meilleure représentation des signaux EEG par l'utilisation des caractéristiques de MA et leur effet combiné avec des méthodes de prétraitement optimisées pour permettre des résultats fiables, généralisables et interprétables, applicables à des situations et scénarios réels.

1 INTRODUCTION

1.1 Brain Computer Interface

Brain Computer Interface (BCI) are systems based upon the user's brain activity as input to deliver feedback or perform an action, enabling control or interaction with another system directly with the mind (Marcos-Martínez et al., 2023; Khalaf et al., 2019). Different types of sensors have been used to record brain activity. Among these, EEG sensors are the most popular owing to their low cost, low invasiveness, and excellent temporal resolution. Whereas invasive modalities such as ECoG, despite their greater efficacy, require surgical intervention to implant electrodes directly into the cerebral tissue Oosugi et al. (2017); Haufe et al. (2018); John et al. (2018).

Since the beginning, BCI have mainly been developed for medical applications, offering a non-pharmacological alternative for the treatment and support of patients with mental deficiencies (Marcos-Martínez et al., 2023; Wood et al., 2014). For example, the use of BCI allows the patient to gain more autonomy during rehabilitation, thus reducing the workload of healthcare providers. Still to this day, the healthcare sector remains the largest segment in the BCI market. While in 2023 the size of the BCI market was estimated to USD $2 billion, it has been predicted to reach between USD 5.4 and 10.65 Billion in 2030 (Market.us, 2024; IMARC Group, 2023).

One of the driving forces behind this rapid growth is the cut in EEG headsets price, now available under $1000 USD, which make them affordable for a broader part of the public (He et al., 2023). The development of noninvasive BCI has opened up opportunities for the development of hardware and software applications integrating BCI as an additional interface.

Recently, a patient case involving a neuronal chip has gained significant attention, raising critical ethical concerns (Liv et al., 2023; Bonaci et al., 2014; WANG et al., 2023; Waisberg et al., 2024). This invasive BCI was manufactured by Neuralink, a company that seeks to establish direct communication between the brain and electronic devices. Neuralink's BCI enables individuals with tetraplegia to control applications using specific and voluntary mental activity.

The emergence of new technologies such as memristive materials promises to revolutionize the future of electronics and further contribute to miniaturization and reduction of the cost of BCI equipments (Tzouvadaki et al., 2023). Innovations in dry EEG sensors, which are more powerful and flexible, have also contributed to the development of wireless EEGs, marking the beginning of the transition from EEG recording in controlled settings such as laboratory to applications for the general public in ecological settings such as living room.

Recently, the emergence of new Virtual Reality (VR) devices, such as Microsoft's Hololens and Meta's Oculus Rift (Lupu et al., 2018) and the introduction of low-cost EEG sensors in the market

have opened up promising prospects for rehabilitation and professional training. Although studies combining BCI and VR are still limited (Palumbo, 2022), the integration of these two technologies allows for continuous and objective monitoring of the user's physiological state in real time during simulations (Lopes et al., 2024). BCI system thus provides an additional communication channel that can enhance immersion and enable the customization of content tailored to user's preferences or specific needs.

The fusion of the two technologies has led to the marketing of Head-mounted displays with integrated EEG, such as Kaptics, Galea (Bernal et al., 2022), OpenBCI, and Emotiv, among others. As well as the development of software such as MindMaze, a neurological rehabilitation platform combining virtual reality and BCI. This technology is used clinically for the rehabilitation of patients with stroke and brain injuries.

In addition to medical applications, the use of BCI in multimedia and video games is expanding rapidly (Hughes et al., 2021; Market.us, 2024). Educational (Bhise et al., 2023) and security applications (McDonnell et al., 2024) are also growing areas in which BCI could play a significant role. However, these recent advances are still in early stages, and further advancements are required before BCI can be widely adopted by the general public (Ahn et al., 2014; Zhu et al., 2024).

1.1.1 Definition

Human-computer interfaces (HCI) are communication systems that generally form a loop between the 'User' and 'Computer' parts. The 'Computer' part receives information from the 'User' part and analyzes it to provide the most appropriate response to the current task. Brain Computer Interface (BCI) belong to the category of Human-Computer Interaction (HCI) with the particularity of collecting user information directly from their brain activity, thus transcending conventional intermediate modalities such as fine motor skills or voice. Figure 1.1 illustrates with a diagram the communication loop formed between the user and the machine, as well as the main stages of a typical BCI pipeline.

1.1.2 EEG based BCI

The Electroencephalogram (EEG) measures the electrical activity generated by the synchronization and depolarization of large populations of neurons. This type of sensor possesses numerous advantages. First and foremost, they are portable and non-invasive, allowing them to be integrated into ready-to-use helmets or headbands. The dry and flexible sensors are simply in contact with the scalp and leave no mark (Marcos-Martínez et al., 2023). Furthermore, the cost of EEG equipment is low compared to other modalities (Khalaf et al., 2019).

Moreover, the recorded signals have excellent temporal resolution, with the acquisition frequency generally ranging between 128 Hz and 1000 Hz. Nevertheless, the ensemble of tissues, the skull,

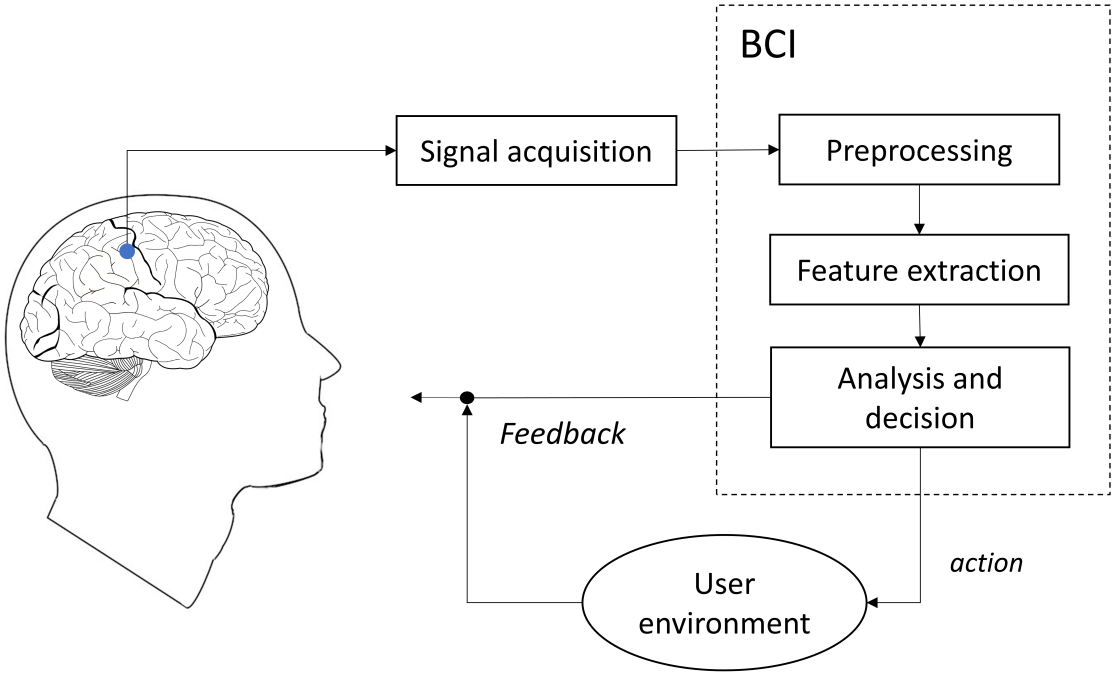

Figure 1.1 : Non-invasive BCI systems are, by nature, a feedback loop with two unidirectional interfaces: sensors record information about the brain activity of the user which is then interpreted by the system to provide feedback (conditioned or not) either with a direct output presented to the user or indirectly by altering its environment. The recorded information typically involves signals processed through a step-by-step pipeline to provide a task-related, meaningful response.

and the cranial volume behave as a low-pass filter resulting in the most important brain activity recorded by EEG available below 100 Hz (Fiałek et al., 2016).

EEG is particularly sensitive to noise, unlike modalities based on metabolic activity, such as near-infrared spectroscopy (NIRS), which offer better robustness (Shin et al., 2018). This is because many external sources can produce electromagnetic signals of greater amplitude than those of the cerebral cortex, making these systems more susceptible to interference.

1.1.3 Types of BCIs

Various types of BCI exist depending on their usage and characteristics. Generally, BCI are classified into two main categories: passive and active/reactive. Recently, the term hybrid BCI has been attributed to a BCI that depends simultaneously on multiple modalities or paradigms.

1.1.3.1 Active and Reactive BCI

Active Brain-Computer Interface (aBCI) is specialized in detecting the specific and voluntary cortical activity of the user for direct device control (Zander et al., 2009). They constitute particularly important solutions for improving the autonomy of individuals suffering from motor deficits, because they provide an alternative channel of communication (Kumar et al., 2015) and allow interaction with everyday objects (Zhang et al., 2015). However, only a limited number of mental commands present sufficiently distinct cortical activities to be detectable by EEG signals, which requires rigorous selection of the most suitable mental tasks to optimize the performance of the BCI system (Fiałek et al., 2016).

Reactive BCI, a subcategory of aBCI, specializes in identifying the focus of a user's attention towards a set of sensory stimuli. They operate based on voluntary actions by the user, but attention is deduced from the specific neural reaction to each stimulus (Zander et al., 2009). Reactive BCI are used in the detection and classification of events in cortical activity, either of endogenous or exogenous source, through sensory stimulation or 'stimulus' (Huster et al., 2014; Kumar et al., 2015). EEG paradigms, such as Steady-State Visual Evoked Potentials (SSVEP) and Event-related potential (ERP), are employed in these cases because the neural responses they induce are well-known and differentiable (Lotte et al., 2019). An example of reactive BCI is the P300 speller (Won et al., 2022). The applications of aBCI in individuals with cognitive deficits can be categorized into two main areas: rehabilitation and assistance.

The goal of BCI-based rehabilitation is to restore partial or full cognitive and motor capabilities lost after an accident or injury (Khalaf et al., 2019; Aggarwal et al., 2019). This approach is based on the plasticity of the brain, which refers to its ability to reorganize by forming new connections between neurons. Thus, when a part of the brain is damaged, the associated cognitive function is lost; however, it can be redistributed to another part of the brain through learning to compensate for the deficit (Vourvopoulos et al., 2019).

If rehabilitation is not complete, aBCI can also be used to improve the quality of life of patients (Kumar et al., 2015). They allow for the control of prostheses by interpreting cortical or muscle activity, as well as communication systems (Huster et al., 2014; Zhang et al., 2014b). The primary beneficiaries of this solution are patients with severe neurological disorders, such as stroke (Xu et al., 2014), amyotrophic lateral sclerosis (ALS) (Hwang et al., 2009; Shindo et al., 2011), and Parkinson's disease (Khalaf et al., 2019).

Over time, the application of BCI for healthy individuals has become more popular (Zander et al., 2009), and BCI can be used to improve cognitive abilities (Aggarwal et al., 2019), control connected objects (Edlinger et al., 2011), and video games (Plass-Oude Bos et al., 2010; Fiałek et al., 2016) (Fiałek et al., 2016).

In terms of applications, BCI can be used synchronously or asynchronously. A synchronous BCI interprets a signal at predefined and known times that the user and system are aware of (Lotte et al., 2015). In an asynchronous BCI application, the user can initiate a command at any time and the system must be capable of distinguishing between periods of inactivity and the time when a command is initiated (Zhou et al., 2020).

1.1.3.2 Passive BCI

Passive Brain-Computer Interface (pBCI) are used in applications where the user interacts with a third-party system. Unlike aBCI, where a voluntary change in the user's brain activity is used to perform an action, it is the cortical activity resulting from the interaction between the user and the third-party system that is used by pBCIs (Zander et al., 2009). Additionally, although aBCI is intended for online use, pBCIs are used both online and offline (Lotte et al., 2019). The advantage of pBCIs is that they allow for an objective analysis of the user's emotional and cognitive state, where traditional methods based on questionnaires can be biased and and increase cognitive load.

pBCIs are used to monitor the user's intrinsic mental activity, such as their emotional state, mental workload, level of attention, relaxation, and fatigue (Aggarwal et al., 2019; Zander et al., 2017; Park et al., 2020; Sciaraffa et al., 2022). Owing to the limitations of non-invasive modalities, such as EEG, pBCIs are considered more applicable than aBCI, which requires a higher transfer rate of information and greater accuracy (Shishkin, 2022).

One of the major applications of pBCI is Adaptive Automation, which allows for modulation of the functioning of a third-party system (Aricò et al., 2016; George et al., 2010). For instance, it can adapt to the level of difficulty of a task (Prinsen et al., 2022) and optimize user performance. Several factors can impair user performance: the time taken during a task, the difficulty of the task (Lotte et al., 2019), environmental distractions, or the user's physiological and emotional state (Bagheri et al., 2022).

However, workload reduces short-term memory performance and increases stress (Lotte et al., 2019). In fact, a task that is too simple (underload) can reduce the user's level of attention, whereas a task that is too complex (overload) can increase stress levels (Sciaraffa et al., 2022). Both situations present a high risk of error, slower reaction times, and reduced performance (Zander et al., 2017). Therefore, adapting the workload to its optimal level is an important issue in many domains. To address this problem, pBCI was used to measure workload indicators (Aricò et al., 2016; Sciaraffa et al., 2022).

pBCI can also be used to enhance the user experience (Plass-Oude Bos et al., 2010). For example, they can be used to adapt the narrative structure of video games, allowing for automatic content customization (Aggarwal et al., 2019; George et al., 2010) and improved immersion (Plass-

Oude Bos et al., 2010). It is also possible to detect errors perceived by the user or loss of control over the system (Zander et al., 2009).

pBCIs can also be used as a monitoring system, evaluating the user's level of engagement in learning tasks (Prinsen et al., 2022) and for preventing accidents during high-risk operations (e.g., for surgeons, air traffic controllers, pilots, etc.) (Sciaraffa et al., 2022). In the medical field, they are used to detect and prevent epileptic seizures (Huster et al., 2014) and to confirm a diagnosis by following the patient's progress in a coma (Galiotta et al., 2022).

A pBCI can also provide an additional communication channel between the user and a system. For instance, by automating certain aspects of the automobile driving experience using the user's cortical activity as a supplementary sensor for the vehicle (Aggarwal et al., 2019; Zander et al., 2017).

1.2 Challenges of EEG-BCIs

Despite the great potential of both active and passive BCI, there are still several major challenges that need to be overcome. From the user's perspective, psychological state and familiarity with BCI technology influence the efficacy of rehabilitation.

Studies have shown that mental states such as fatigue, frustration, and attention level can significantly affect BCI performance (Myrden et al., 2015; Hwang et al., 2009). Because learning to use a BCI system demands considerable mental effort, user fatigue is a significant psychological factor that underscores the importance of user motivation in the successful adoption of BCI systems (Nijboer et al., 2010). Furthermore, other factors such as individual attention span and spatial ability also contribute to the variable reliability of BCI in practical scenarios (Kleih et al., 2015; Jeunet et al., 2016). This creates a negative feedback loop, where reduced accuracy diminishes the system's reliability, leading to user frustration, which further degrades the system's performance and acceptance (Plass-Oude Bos et al., 2010).

One of the main performance criteria for BCI is its accuracy, which is a measure that counts the number of successes out of the total number of detections. For aBCI, whose response time is just as important, we generally use the notion of Information Transfer Rate (ITR) (Plass-Oude Bos et al., 2010), which measures the number of mental commands correctly decoded by the system per unit time (Xu et al., 2020). Current BCI technology has a very low information transfer rate compared to traditional modes of communication, such as speech or manual input, which limits its application to healthy individuals (Zander et al., 2011). The state-of-the-art ITR has reached 3000 bits/min (Shi et al., 2024).

Overall, several major challenges related to the robustness of BCI still exist, such as inter- and intra-subject variability (Xu et al., 2021; Zhou et al., 2022), as well as varying signal quality

(e.g., signals obtained from gel-based versus dry electrodes) and artifacts, which can bury specific task-related brain activity within noise (Lee et al., 2020; Naser et al., 2023).

An effective BCI system must also be easy to use. However, it is rare for BCI systems based on noninvasive modalities that are directly usable by a new user (Zander et al., 2017). BCI performance is highly dependent on the settings that the system has been trained for; thus, any out-of-domain test settings can drastically reduce accuracy.

Calibration sessions are therefore necessary to achieve a nominal level of performance on a new individual (Shindo et al., 2011). This is partly due to the lack of large EEG datasets of consistent quality and structure (Prinsen et al., 2022), although progress has been made in this regard (Obeid et al., 2016; Markiewicz et al., 2021; Shishkin, 2022).

Furthermore, not all brains are equal, and current EEG analysis methods fail to detect specific activities. Cortical activity captured by EEG electrodes changes over time (Müller et al., 2008). Typically, the brain executes tasks passing through a succession of different states that exhibit distinct EEG patterns in the signals. For example, it is estimated that approximately one-third of BCI users fail to use a system (Lotte et al., 2015). Thus, detection quality varies from one individual to another (Müller et al., 2008; Zhou et al., 2022; Xu et al., 2021).

Several approaches have been proposed to improve the robustness of BCI. Multimodal systems, or so-called hybrid BCI (Liu et al., 2021; Li et al., 2019), take advantage of different neurophysiological modalities (e.g., eye and facial movements or hemodynamics via Functional near-infrared spectroscopy (fNIRS)) to improve BCI accuracy.

Other approaches include the development of new signal processing and feature extraction tools to help distinguish important brain patterns from noise. For example, in the last few decades, developments in features such as fractal dimension and entropy measures (Varshney et al., 2021; Angsuwatanakul et al., 2020), as well as the use of amplitude envelope-based features (Agarwal et al., 2023; Dzianok et al., 2021) to complement traditional spectral power (Ko et al., 2021; Bascil et al., 2016; Tiwari et al., 2022), spectral coherence (Cattai et al., 2021; Tao et al., 2021), and time-domain statistics (Nisar et al., 2022) features.

Recently, deep learning models have emerged as data-driven methods that can help advance BCI technologies (Chakladar et al., 2020; Wang et al., 2020; He et al., 2021; Mai et al., 2021). Although such data-driven methods have shown improved accuracy on specific datasets, they are known to be poorly generalized across datasets (He et al., 2021; Roy et al., 2019) and may introduce new vulnerabilities (e.g., susceptibility to adversarial attacks (Meng et al., 2023; Zhang et al., 2021)).

Although deep learning models offer a better generalization capacity (Müller et al., 2008; Jiang et al., 2019), especially for complex datasets such as EEGs, they require very large volumes of data for training, thus limiting their applicability in studies where such datasets are scarce. The excellent results obtained with these models were then contested because they may be related to

overfitting (Tsimenidis, 2020; Yildirim, 2020; Roy et al., 2019, 2022). Moreover, despite efforts to make models interpretable, their “black box" nature poses a significant challenge that limits their clinical use (Bouazizi et al., 2024; Torres et al., 2023; Joucla et al., 2022). This opaque nature also makes them vulnerable to adversarial attacks (Jiang et al., 2019), and the features learned on training datasets are not always interpretable (Jeong et al., 2019; Fan et al., 2021) or are necessarily associated with known neurological processes (Torres et al., 2023; Lopes et al., 2023).

Some decades ago, BCI was restricted to studies in laboratories and controlled environments, which reduced the number of artifacts to a smaller, better-known group (Huster et al., 2014), where participants were systematically seated, as illustrated in Figure 1.2. Instructions were provided to limit head movements and blinks in order to minimize the number of artifacts in the collected EEG signals.

Moreover, contact between the electrodes and scalp was ensured using a conductive gel or saline solution. This type of setup is still commonly used today, although it increases the installation time (Sciaraffa et al., 2022) and is inconvenient for participants who must wash their hair to remove the gel (Li et al., 2021b). Even though saline-based electrodes leave less residue on the hair (Sciaraffa et al., 2022), the evaporation of the solution gradually degrades the quality of EEG signals (Lotte et al., 2015). Recent technological advancements (Li et al., 2021b) have allowed dry electrodes to achieve a performance comparable to that of gels (Zander et al., 2017). The latter facilitates the preparation of the montage that is directly in contact with the scalp. However, dry electrodes are known to be more susceptible to artifacts. Given their ease of integration, they are now widely integrated into headsets and headbands.

Passive BCIs have also emerged as potential candidates for automated instrumental Mental workload (MW) assessment (Mullen et al., 2015; Lean et al., 2012). Successful applications have been shown in aircraft pilots and car drivers (Borghini et al., 2014), and air traffic controllers (Aricò et al., 2016), to name a few. Numerous different features have been explored and shown to be useful, including power spectral, magnitude, and phase coherence features (Aghajani et al., 2016; Dimitrakopoulos et al., 2017; So et al., 2017). For example, increases in theta and decreases in alpha band power have been shown in the prefrontal and parietal brain regions when task difficulty increases (Borghini et al., 2014). Temporal complexity measures have also shown some robustness against ocular and muscular artifacts (Tiwari et al., 2019), and spectrotemporal measures have been shown to provide complementary information to conventional power spectral ones (Albuquerque et al., 2019b). However, most available studies have relied on stationary users, such as sitting pilots and drivers (Johnson et al., 2015; Borghini et al., 2014), or have controlled for body movements (Hogervorst et al., 2014). It is not clear what performance can be achieved once users become mobile.

Direct enhancement of EEG signals, however, may remove some important details from the EEG signal, affecting classification accuracy (Delorme, 2023). For example, automated enhancement of EEG signals has been shown to affect different diagnostic tasks, such as Alzheimer’s disease

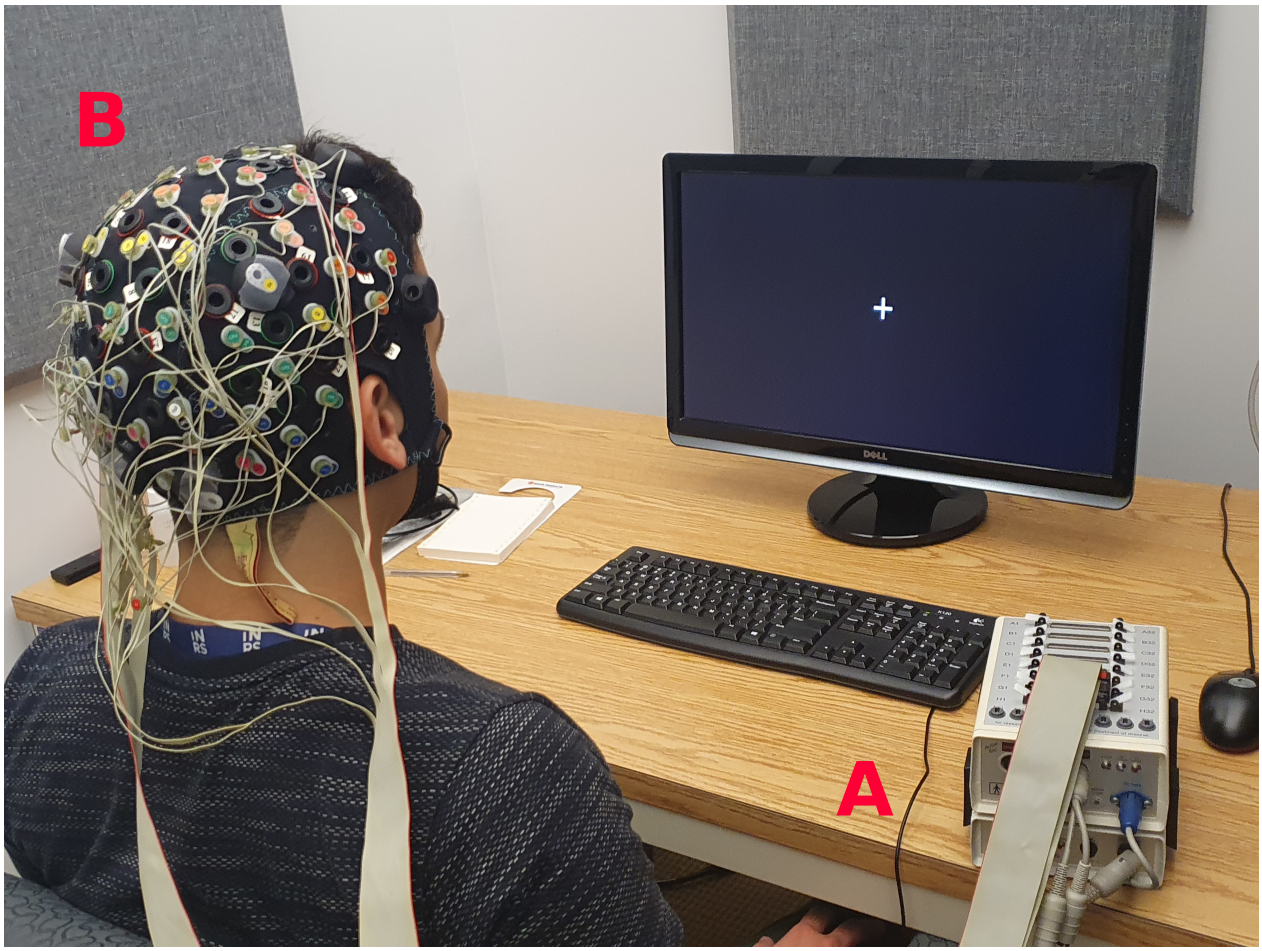

Figure 1.2 : Typical EEG experimental setup. The participant is seated in a closed room, with an electrode cap placed on the head (A). The equipment amplifies and converts analog EEG measurements to digital signals (B).

diagnosis (Cassani et al., 2014). One area in which this may also be true is in the use of passive BCIs for cybersickness detection in VR. While EEG signals can be very sensitive to artifacts, especially physiological (Zhang et al., 2015) such as head movement, eye blinks, eye movements and heart rate (Lee et al., 2020; Naser et al., 2023), these measures may actually be useful for cybersickness prediction. Thus, while automated enhancement algorithms exist (e.g., (Yildirim, 2020; Delorme, 2023)), their use may not always be warranted (Huster et al., 2014).

1.3 Thesis Contributions

The objective of this thesis is to enhance the performance, portability, and interpretability of active and passive BCI systems to facilitate their transition to practical applications. To achieve this goal, we aimed to improve two critical components of BCI systems: signal pre-processing and feature extraction. In particular, we are interested in exploring amplitude modulation as a more useful representation of cortical activity measured using electroencephalography (EEG).

In Chapter 3, in response to the need for better signal representation, we propose to improve aBCI robustness by incorporating a new signal representation that allows for the measurement of Amplitude Modulation (AM) dynamics and cross-frequency coupling using electroencephalography (EEG) signals. Amplitude modulation is a fundamental mechanism of cognitive processes (Bondar' et al., 2000; Hidalgo et al., 2022; Hilla et al., 2020). As stated in (Bondar' et al., 2000), "The presence of the amplitude modulation in bioelectrical processes is of a fundamental nature since it is a direct reflection of the control, synchronization, regulation, and intersystem interaction in the nervous and other body systems."

Amplitude Modulation (AM) features have been shown to be useful for mental and cognitive state characterization (Albuquerque et al., 2020; Clerico et al., 2015, 2018) as well as for health diagnostics (Fraga et al., 2013; Trambaiolli et al., 2011). First, it addresses the inherent non-stationary nature of EEG signals, which traditionally complicates the detection of neural activity patterns. Second, AM features have been shown to be more robust to artifacts in pBCI applications (e.g., (Cassani et al., 2018)). Thus, they may be able to assist with artifact robustness in aBCI. Third, cortical hemodynamics measured using fNIRS have been shown to be correlated with amplitude modulations measured from EEG signals (Trambaiolli et al., 2020), thus suggesting that amplitude modulation may be a good indicator of local neural processing. Because multimodal EEG–fNIRS systems have been shown to outperform EEG systems alone (Banville et al., 2017), the proposed features may be able to capture multiple signal modalities using a single electrode, thus also improving user experience while making BCI more robust. Finally, cross-frequency amplitude and phase coherence features have been linked to different cognitive processes; thus, they may further assist with inter- and intra-subject variability (Herrmann et al., 2004; Thatcher, 2012; French et al., 1984; Aydore et al., 2013).

In Chapter 4, we show that classical EEG enhancement algorithms, conventionally developed to remove ocular and muscle artifacts, are not optimal in settings where participant movement (e.g., walking or running) is expected. As such, we present the use of an adaptive filter to remove movement-specific motion artifacts from the mobile EEG data. Accelerometer signals measured from the participants' torsos were used as reference signals for the adaptive filter. The algorithm was tested on a database collected in-house from 48 participants while they performed the Multi-Attribute Task Battery-II (Santiago-Espada et al., 2011) under two Mental workload (MW) conditions (low and high) and two Physical activity (PA) types (stationary bike and treadmill), each at three activity levels (none, medium, and high).

In Chapter 5, we first explore the impact of different levels of artifact removal – from very basic techniques where head/body artifacts are kept, to more advanced pipelines leaving only neural signatures for evaluation – on cybersickness characterization. While the former effectively transforms EEG into an embedded multimodal system, thus potentially improving detection accuracy, the latter can uncover the specific neurological patterns associated with cybersickness, thus leading to potential interventions to mitigate symptoms. We then extend our analysis beyond conventional

EEG Power Spectral Density (PSD) features and propose the use of EEG Amplitude Modulation (AM) and connectivity features for the detection of cybersickness symptoms.

1.4 Publications derived from the thesis

Publications included in the thesis

Articles published in refereed journals

“EEG Amplitude Modulation Analysis across Mental Tasks: Towards Improved Active BCIs,” **Rosanne, O.**, Alves de Oliveira, A., and Falk, T. H., Sensors, vol. 23, no. 23, p. 9352, 2023. (Rosanne et al., 2023) [Chapter 3]

“Adaptive filtering for improved EEG-based mental workload assessment of ambulant users,” Rosanne, O., Albuquerque, I., Cassani, R., Gagnon, J.-F., Tremblay, S., and Falk, T. H., Frontiers in Neuroscience, vol. 15, p. 611962, 2021. (Rosanne et al., 2021) [Chapter 4]

Under review

"Cybersickness assessment: To Pre-Process or Not to Pre-Process? On the Role of EEG Enhancement for Cybersickness Characterization and the Importance of Amplitude Modulation Features, " Rosanne, O., Benesch, D., Kratzig, G., Paré, S., Bolt, N., Falk, T. H., submitted to Virtual Reality [Chapter 5]

Conference proceedings and abstracts

“Performance comparison of automated EEG enhancement algorithms for mental workload assessment of ambulant users,” Rosanne, O., Albuquerque, I., Gagnon, J.-F., Tremblay, S., and Falk, T. H., 2019 9th International IEEE/EMBS Conference on Neural Engineering (NER), pp. 61-64, 2019. (Rosanne et al., 2019a)

Other publications

“Estimating distribution shifts for predicting cross-subject generalization in electroencephalography-based mental workload assessment,” Albuquerque, I., Monteiro, J., **Rosanne, O.**, and Falk, T. H., Frontiers in Artificial Intelligence, vol. 5, p. 992732, 2022. (Albuquerque et al., 2022)

"Neural interface instrumented virtual reality headsets: Toward next-generation immersive applications," Cassani, R., Moinnereau, M.-A., Ivanescu, L., Rosanne, O., and Falk, T. H., IEEE Systems, Man, and Cybernetics Magazine, vol. 6, no. 3, pp. 20-28, 2020. (Cassani et al., 2020a)

"Quantifying multisensory immersive experiences using wearables: is (stimulating) more (senses) always merrier?," De Jesus Jr, B., Lopes, M., Moinnereau, M.-A., Gougeh, R. A., Rosanne, O. M., Schubert, W., Oliveira, A. A., and Falk, T. H., Proceedings of the 2nd Workshop on Multisensory Experiences-SensoryX'22, 2022. (De Jesus Jr et al., 2022)

"Nat (UR) e: Quantifying the relaxation potential of ultra-reality multisensory nature walk experiences," Lopes, M. K. S., de Jesus, B. J., Moinnereau, M.-A., Gougeh, R. A., Rosanne, O. M., Schubert, W., de Oliveira, A. A., and Falk, T. H., 2022 IEEE International Conference on Metrology for Extended Reality, Artificial Intelligence and Neural Engineering (MetroXRAINE), pp. 459-464, 2022. (Lopes et al., 2022)

"Cross-subject statistical shift estimation for generalized electroencephalography-based mental workload assessment," Albuquerque, I., Monteiro, J., Rosanne, O., Tiwari, A., Gagnon, J.-F., and Falk, T. H., 2019 IEEE International Conference on Systems, Man and Cybernetics (SMC), pp. 3647-3653, 2019. (Albuquerque et al., 2019a)

"Fusion of spectral and spectro-temporal EEG features for mental workload assessment under different levels of physical activity," Albuquerque, I., Rosanne, O., Gagnon, J.-F., Tremblay, S., and Falk, T. H., 2019 9th International IEEE/EMBS Conference on Neural Engineering (NER), pp. 311-314, 2019. (Albuquerque et al., 2019b)

1.5 Thesis organization

In this introductory chapter, we discuss the current innovations and obstacles faced by BCI technology as well as our contribution in this field. The remainder of this thesis is organized as follows.

Chapter 2 presents the theoretical foundations of BCI, based on EEG signals. From the origin of the neuronal activity captured by sensors to the extraction of information associated with cortical processes. The different stages of a typical BCI pipeline are also detailed, and will serve as the basis for the experiments presented in the following chapters.

Chapter 3 tests the use of amplitude modulation features to improve aBCI by comparing the performance of classifications between different types of mental activities obtained using traditionally employed features. This chapter explores this new representation of EEG signals as a solution for the better identification of neural processes, thus ensuring greater accuracy and generalization of BCI.

In Chapter 4, we present an adaptive filter, a data-driven pre-processing method to improve the detection of the mental workload of a user performing intense physical activity.

Chapter 5 focuses on the detection of cybersickness using a virtual reality headset. Different pre-processing algorithms are tested to assess their effects on the accuracy and interpretability of the cortical activity when combined with AM features. We suggest that the choice of the most suitable pre-processing algorithm varies greatly depending on the application and that in the case of cybersickness detection, this choice involves a trade-off between interpretability and detection efficiency. In addition, this chapter explores the benefits of AM features in interpreting the cognitive processes accompanying cybersickness.

Finally, Chapter 6 summarizes the contributions of this thesis and present some remaining challenges to be addressed as future work to develop more portable, reliable, and high-performance applications of this technology.

2 THEORETICAL BACKGROUND, MATERIALS, AND METHODS

2.1 The human brain

2.1.1 Structure

The human brain contains approximately 86.1 billion neurons (Azevedo et al., 2009) that are organized into local regions and process information through the exchange of signals along a complex network consisting of 60 trillion synapses. This system is highly complex and dynamic, and its functioning depends on mechanisms operating at different hierarchical levels (Shepherd, 2003), such as ion exchange within synapses (Südhof, 2021; Ferguson et al., 2020), the electrical activity of neurons (Yu et al., 2017), and the activity of local (Peron et al., 2020) and inter-regional cortical circuits (Simpson et al., 2013).

The brain is divided into three major parts: the cerebrum, brainstem, and cerebellum. The study of neurological activity for BCI focuses on the cerebellum, which comprises an outermost layer, the neocortex. This region contains three main components: the main neurons, the intrinsic neurons, and the input fibers (Shepherd, 2003). Although anatomical variation exists between individuals, the neocortex can be subdivided into lobes with specific high-level functional roles (Lotte et al., 2015), namely:

Occipital lobe The occipital lobe is located in the posterior region of the brain and is specialized in processing visual information. The neurons in this area and their networks specialize in extracting features such as visual patterns, colors, and spatial orientation. The information extracted characterizes the observed environment and allows the recognition of objects and words, among other things. Activity in this region of the brain can be observed during the recall of a familiar place or face or the mental rotation of a 3D object (see Chapter 3).

Parietal lobe The parietal lobe extends the visual cortex's capabilities for processing visual information. However, it is specialized for higher-order functions such as the construction of a mental representation of space, spatial attention that filters important information, and planning and navigation. The parietal lobe is also the center of processing sensory information other than vision. They are responsible for integrating various sensory stimuli into a coherent representation of the environment. In addition, they play an important role in language and social skills.

Motor cortex The motor cortex is located in the posterior part of the frontal lobe. It is responsible for the planning and execution of movements. EEG studies on motor imagery show that this part of the cortex presents characteristic activity when imagining movements with or without

actually performing them. The results presented in Chapter 3 show the activity in this region during a motor imagery task. However, the motor cortex also plays a role in other elementary functions including language and memory.

Frontal lobe The frontal lobe is located in the anterior part of the cortex and possesses numerous roles that are generally related to higher functions such as decision-making, attention, logical reasoning, and emotional state. It is in direct interaction with other areas of the cortex, particularly the parietal region, thus allowing for cognitive attention management and integration of relevant information into the situation. It is involved in most mental tasks and its importance is particularly evident in arithmetic tasks (see Chapter 3).

Temporal lobe The temporal lobe is specialized in analyzing future events, short- and long-term memory, contextualizing information, and language. It serves as a significant connecting hub between various brain regions, particularly deeper structures such as the limbic system.

2.1.2 Neurons

Neurons are composed of three main components: dendrites, somas, and axons. Dendrites are successive branches that receive signals from other neurons via synapses. Synapses are entrances that can either excite or inhibit the cell, thereby changing the membrane potential of the neuron. The soma is a cell body that contains the nucleus and major cellular organelles. Finally, an axon is a long fiber that propagates an electrical charge to neurons located at varying distances from the cell (Shepherd, 2003).

Neurons transmit information through a change in the polarity of their membrane, which results in the release of chemical messengers called neurotransmitters at the synapse level. Synapses are connections between neurons that can serve multiple functions at different timescales. The nature and complexity of connections between neurons constitute a fundamental part of the elementary operations of the cortex: binary and analog logical operations, routing and addressing of information, amplification, and temporal and spatial contrasts. These elementary operations are combined across local circuits to implement higher-level functions such as encoding and processing of sensory information, memory, attention, and decision-making.

2.2 Study of brain activity

The general purpose of studies on cerebral activity is to associate a measured state of the brain with its associated behavior. However, the measurements generally correspond to a combination of activities unique to the studied behavior and activity with no relationship.

To achieve this, it is essential to first define the reference framework. Most studies consider the activity of an individual at rest, without reflection or a specific action, as a reference state. This

state is characterized by EEG signals in a spectrum with a general '1/f' shape corresponding to Brownian noise. This is defined in the literature as the 'default mode.' Although conscious activity is considered suspended, unconscious activity persists and is unique to each individual. Consequently, the reference measurement framework varies over time and across individuals, which implies that the reference-measured activity must be as generalizable as possible.

The spectral and spatial distribution of activity changes when an individual performs a mental task. Neurons become synchronized to amplify relevant signals and form inter-cortical communication networks. Measuring this activity contrasts with the reference activity to precisely characterize the studied behavior (Bell et al., 2012).

2.2.1 Modalities

Neurological activity can be assessed through its electromagnetic signature using electroencephalography (EEG), or by its metabolic activity, such as Functional near-infrared spectroscopy (fNIRS). fNIRS measures metabolic activity by utilizing the differential absorption of oxygenated and deoxygenated hemoglobin in blood cells through infrared reflections, which provides superior spatial resolution compared to electromagnetic-based modalities (Huster et al., 2014). However, detecting a relative change in response to an event using fNIRS requires a delay of approximately 10 s (Shin et al., 2018). Unlike EEG, fNIRS do not differentiate between inhibitory and excitatory activities. Nonetheless, owing to their complementary nature, both modalities have been used in a hybrid BCI to enhance performance (Zander et al., 2011).

Electroencephalogram (EEG) records the electrical activity of a limited number of neurons. Only neurons with axial symmetry can form dipoles that generate an electric potential field. These neurons must be oriented perpendicular to the scalp and located on the surface of the cortex to allow their electric field to be captured. Finally, they must be organized into dense networks to facilitate the summation of individual electric fields. Pyramidal neurons meet all these criteria; they are typically organized in a palisade formation, which results in the synchronization of their discharge, inducing a sufficiently strong electric field for measurement. In contrast, interneurons have a radial structure and their electrical activity is much weaker. Figure 2.1 illustrates the electric field generated by a pyramidal neuron during an action potential.

2.2.2 Brain waves

Central nervous system cells respond to certain inputs by generating oscillations at various frequencies. Two fundamental mechanisms are at the origin of the oscillations measured by EEGs: intrinsic membrane properties allow some types of neurons to generate rhythmic firing (Shepherd, 2003) and interactions between output neurons and inhibitory neurons in local circuit interactions

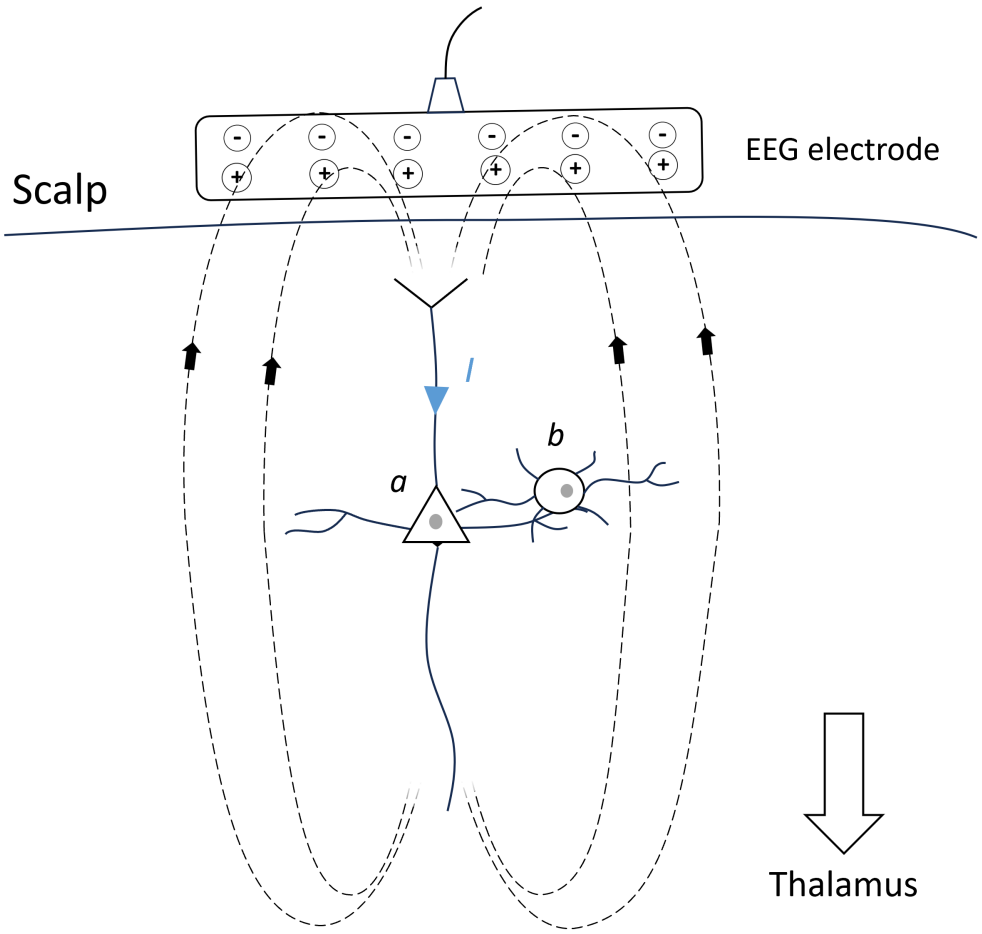

Figure 2.1 : Original simplified illustration of EEG measurement principle. The EEG electrode placed on the scalp captured the change in the electric field generated by a pyramidal neuron (a) during the action potential. The blue arrow represents the current flow from the dendrites to the axon terminal. The generated electric field is represented by dotted curves and black arrows. Interneurons (b) connect with multiple pyramidal cells via inhibitory synapses and can be involved in the generation of brain waves observed in EEG signals.

(Llinás et al., 2006; Cohen, 2017). The role of these oscillations is hypothesized to be to select and amplify a relevant signal across a local population of neurons (Fries, 2015). This local activity is reflected on a larger scale through functional communication between different cortical areas (Marcos-Martínez et al., 2023), which can be observed through inter-regional and cross-spectral coupling measurements.

Decomposition of frequency bands has been employed since the beginning of EEG studies. Repetitive patterns and oscillations at different paces and amplitudes are visible in the temporal representation of the signals. The first band to be defined was the alpha band, characterized by slow and strong amplitude oscillation observed when the eyes are closed and the subject is at rest. This discovery was later followed by beta, which is characterized by a fast but weaker amplitude. Currently, the EEG spectrum is decomposed into five main conventional frequency bands.

Delta Waves (0.5-4 Hz) These are the slowest and are prominent during deep sleep and in brain states requiring high synchronization (Steriade et al., 1993). The generation of delta waves has been linked to the intrinsic properties of thalamocortical neurons and their involvement in cognitive processes, such as anticipation, predictive coding, and modulating reaction times (Eggermont, 2021). As discussed in Chapter 5, this function may be linked to the top-down control of brain decision centers on local cortical activity through modulation of the amplitude of the alpha and beta frequency bands (Bourdillon et al., 2020).

Theta Waves (4-8 Hz) Commonly associated with memory encoding and navigation, theta rhythms are prominently seen in the hippocampus and cortical areas. These waves are primarily driven by the interaction between the hippocampus and entorhinal cortex (Pignatelli et al., 2012). Inhibitory neurons, particularly those using gamma-aminobutyric acid (GABA), play a key role in rhythmically inhibiting pyramidal cells to produce a characteristic oscillatory pattern (Llinás et al., 2006). In Chapters 3 and 5, we suggested that the theta band is associated with the processes of encoding, temporal integration, and sensory information storage in memory.

Alpha Waves (8-12 Hz) Alpha waves are typically observed in the posterior regions of the brain during relaxed wakefulness, especially with closed eyes. They involve a feedback loop between the cortex and thalamus, where inhibitory neurons in the thalamus synchronize the activity of cortical neurons, thereby creating a rhythmic pattern (Da Silva, 2023). The exact role of the alpha band is still unknown, but it has been linked to arousal, attention, and vigilance (Liu et al., 2012) and as a regulatory pattern of local neuronal circuits (Li et al., 2020; Roux et al., 2013). In Chapters 3 and 5, activity in the alpha band suggests its role in coordinating information processing processes. Specifically, oscillations in this frequency band reflect the mechanism of inhibition that is necessary to regulate coherent information processing.

Beta Waves (13-30 Hz) These waves are associated with memory (Griffiths et al., 2021a,b), expectation (Betti et al., 2021), and somatosensory feedback (Abbasi et al., 2020). They are primarily generated in the motor cortex but are present in various brain regions. The generation of beta waves involves reciprocal interaction between cortical layers, where the rhythmic inhibition of pyramidal neurons by GABAergic interneurons creates oscillatory patterns. Cortico-cortical and thalamocortical circuits also play crucial roles (Basha et al., 2023). According to the results presented in Chapters 4 and 5, the beta band is strongly involved in the visuomotor and motor imagery processes. Moreover, it appears to play an important role in memory and anticipation, reflecting the state of alertness, as discussed in Chapter 3.

Gamma Waves (30-100 Hz) Associated with high-level cognitive functioning (Brooks et al., 2020), including perception (Han et al., 2022a), attention, and working memory, gamma waves are generated by the interaction between excitatory and inhibitory neurons. The critical mechanism here involves the pyramidal interneuron network gamma (“PING”) model, in which excitatory neurons stimulate inhibitory interneurons, which in turn provide rhythmic inhibition back to excitatory neurons (Guan et al., 2022; Liu et al., 2022; Getachew et al., 2021). This

interplay results in fast and synchronous firing patterns that are characteristic of gamma waves (Lewis et al., 2021). In Chapter 4, we suggested that the gamma band may be linked to the sensory-motor integration observed during physical activity. In general, the gamma band reflects a wide variety of fundamental neural functions observed during the execution of various mental tasks, as mentioned in Chapter 3. Finally, in Chapter 5, we discuss the strong interaction of the gamma band with lower-frequency bands such as the alpha band, suggesting the complex and hierarchical coordination of cognitive processes.

Figure 2.2 illustrates the decomposition of a typical EEG signal into five conventional band components. These five conventional bands can be further divided into sub-bands, such as low and high beta and gamma or mu; however, they are less commonly studied because the exact boundaries vary from subject to subject. For example, age is an important factor in the shift in the alpha frequency towards the theta frequency (Tröndle et al., 2023; McSweeney et al., 2023). In fact, recent studies have suggested the importance of customized bands for participants (Iwama et al., 2024; Wriessnegger et al., 2020; Kamiński et al., 2012).

2.2.3 EEG paradigms

Cognitive brain activity can take various forms, each of which reflects different aspects of a cognitive process. For instance, temporary variations in amplitude are observed after the presentation of a stimulus known as an ERP. In addition, oscillations occur in certain frequency bands and specific regions of the cortex, such as the mu and beta bands in the sensorimotor region (Yu et al., 2022a; Khademi et al., 2022) during motor imagery, such as sensory motor rhythm (Zhou et al., 2022; Zhao et al., 2016). In occipito-parietal regions, SSVEP are observed during sensory stimulation. Finally, when the mental task is complex, different regions of the cortex communicate with each other through inter-regional circuits. The dynamically formed networks can be observed through measures of coupling and connectivity (Marcos-Martínez et al., 2023).

These typical activities visible in EEG signals have led to the formation of commonly employed paradigms used in passive and active BCI research, according to their applications.

2.3 BCI pipeline overview

The typical structure of a BCI pipeline comprises of several stages. Initially, the EEG signals are collected from the user. Subsequently, the pre-processing phase reduces noise and enhances the signal. Feature extraction, tailored to the paradigm used, includes sub-steps, such as segmentation, feature calculation, scaling, and pruning. Depending on the application, the inference stage involves classifying an activity or quantifying it (through regression) based on these features. Models are generally pretrained offline before being used online, although continuous online training is also

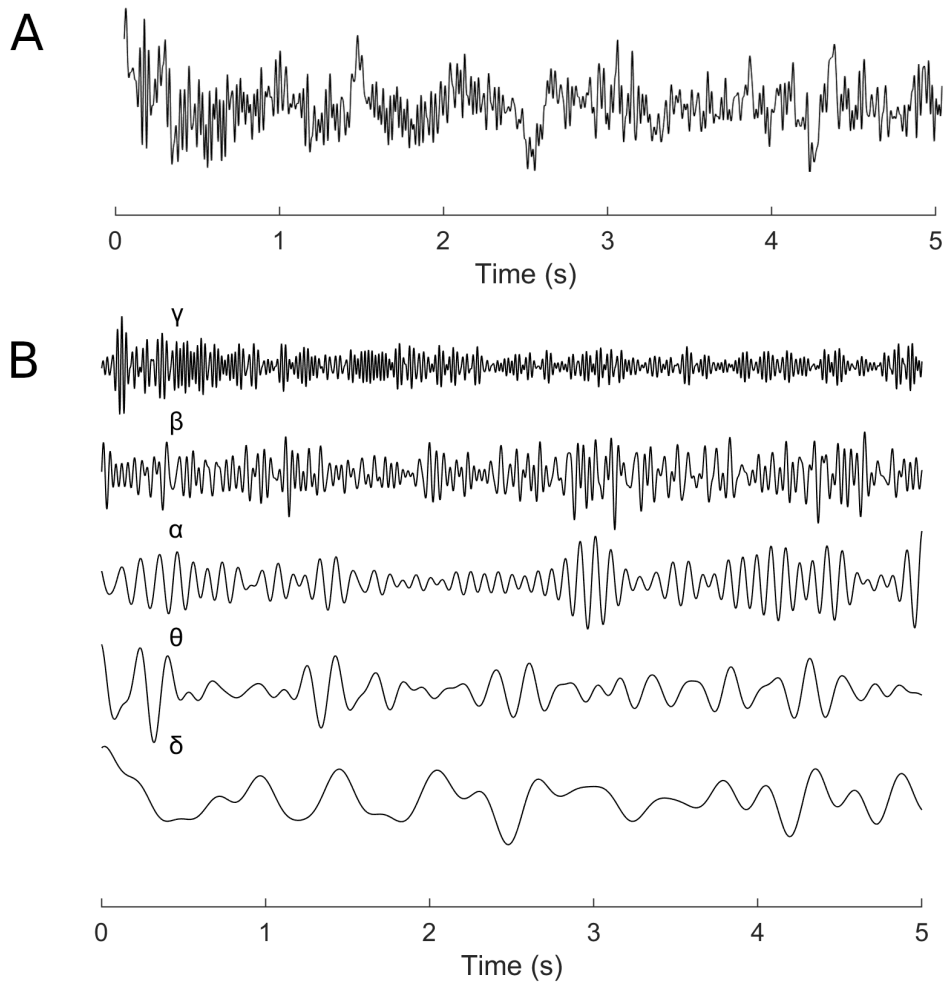

Figure 2.2 : A. Raw EEG signal time representation over a 5-second duration, capturing typical neural activity. B. Decomposition of the raw EEG signal from panel A into five conventional frequency bands (top to bottom): gamma, beta, alpha, theta, and delta, each band delineating distinct ranges of neural oscillations.

possible. Finally, feedback translates the inference result into an adapted response aligned with the objective of BCI (Ruiz et al., 2014).

2.3.1 Data acquisition

Conventionally, EEG studies rely on the international 10-20 system to define the arrangement of electrodes on a participant's scalp. This system ensures a coherent association between the electrode and the region of the cortex to be measured despite the morphological differences between individuals. Each electrode position is identified using a combination of letters and numbers. The letters represent the region of the cortex where the electrode is located, while the numbers indicate whether the electrode is located in the left hemisphere (odd numbers) or the right hemisphere (even numbers) (Oostenveld et al., 2001; Padfield et al., 2019).

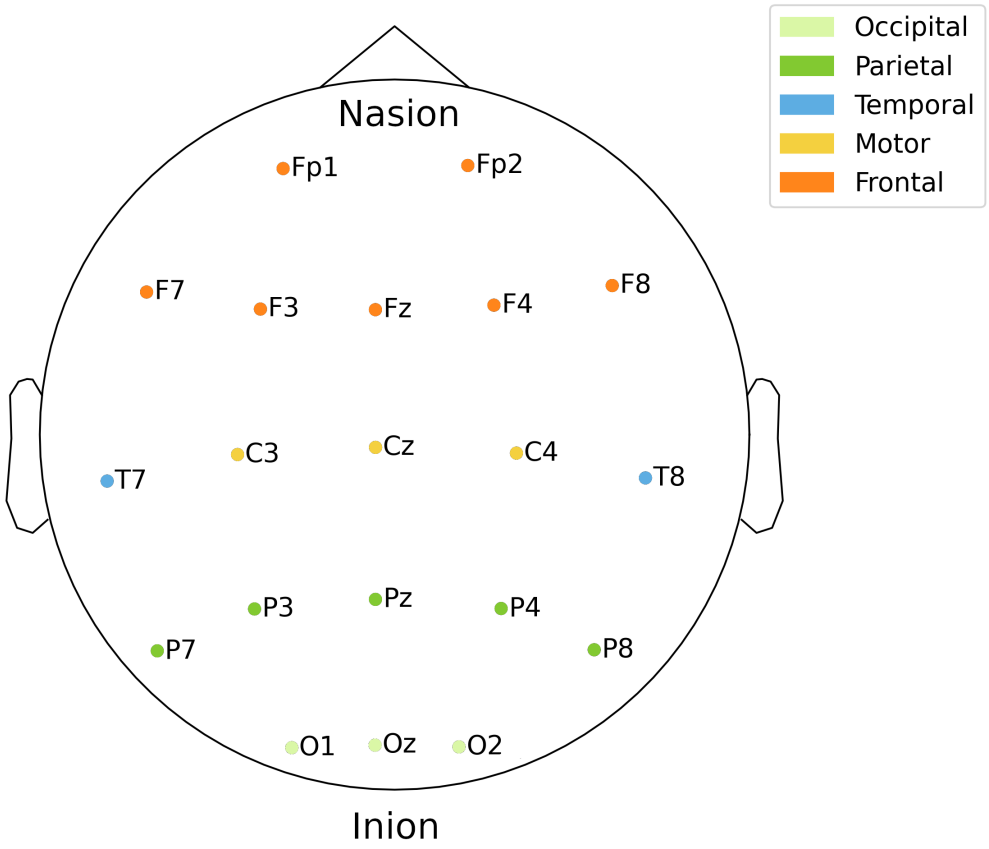

Figure 2.3 : EEG Montage of the 10-20 System: Electrode positions are color-coded for clarity, with light green markers for occipital electrodes, green for parietal, blue for temporal, yellow for motor, and orange for frontal regions.

Figure 2.3 illustrates the arrangement of the EEG electrodes on the scalp according to the international 10-20 system. The number and distribution of electrodes may vary depending on the needs of the study to allow for better portability or to concentrate on the analysis of brain activity in a region of interest.

2.3.2 Pre-processing

2.3.2.1 Artifacts in EEG

Two types of artifacts may hide useful neural information recorded in EEG signals: environmental and physiological artifacts (Huster et al., 2014). Environmental artifacts are those that come from an environment in which EEG signals are recorded, and a typical example of noise is produced by electrical lines. The magnetic field of the alternating current can be captured by the EEG, resulting in the addition of a sinusoidal component of 50 or 60 Hz, depending on the country, to the signals.

Another source of non-physiological noise comes from the electrodes. For example, poor contact with the skin owing to thick hair or improper placement results in rapid amplitude changes and poor capture of neurological activity. The impedance of the electrode changes over time (drying gel or normal sweating of the skin), which is reflected in the slow variation in the offset (drift) (Huster et al., 2014; Kumar et al., 2015). This type of artifact can be reduced, depending on the type of electrode used.

Physiological artifacts in EEG recordings, in turn, correspond to all activities captured by the EEG that are not directly generated by cortical activity but are of physiological nature. This includes muscle contractions in the neck and head whose electrical activity spreads to the scalp (Lotte et al., 2015). This type of noise affects the high frequencies in the EEG spectrum (Huster et al., 2014). Eye-blinking is the most frequently encountered noise source in EEG studies. The blinking of the eyes appears in EEG signals as amplitude peaks, particularly affecting frontal electrodes (Kumar et al., 2015). Additionally, the movement of the eyes can be compared to a rotating dipole electrical field captured by the electrodes (Lotte et al., 2015). As mobile applications emerge, and as we will show in Chapter 4, movement and participant gait may also generate specific artifacts in the EEG signal that need to be suppressed.

2.3.2.2 Artifact removal

Traditionally, artifacts are removed from EEG signals by visually inspecting the signals and rejecting the affected segments by experts. However, this process is slow, expensive, and requires expertise. The automation of this process is challenging because the properties of both signals and artifacts are variable (Huster et al., 2014; Kumar et al., 2015). Over the past two decades, several automatic processing algorithms have been proposed. These algorithms are based on transformations that highlight the unique properties of each type of artifact in order to distinguish and remove them from the signal. The most popular methods are based on reversible decomposition such as Independent component analysis (ICA) or Principal component analysis (PCA). Notably, ICA allows for linear recombination of EEG signals into components whose statistical independence is maximized (Huster et al., 2014). However, the use of this type of tool is only valid under certain conditions (Kumar et al., 2015).

Techniques based on machine learning have been proposed to automate pre-processing. When the activity of artifacts is known, for example, when eyeblink signals EOG are used to capture ocular activity, regression models can be used to subtract this activity from EEG signals (Lotte et al., 2019). However, when no information about artifacts is available, it is possible to use models trained on datasets corrected by experts. This is the case, for example, for MARA (Winkler et al., 2011) or ICLabel (Pion-Tonachini et al., 2019), which after ICA, can identify independent components associated with artifact sources and remove them when a certain level of confidence is reached.

In addition to noise-reduction techniques, it is common in EEG studies to utilize algorithms that improve signals. Spatial filters such as common spatial patterns (CSP) are employed to amplify useful components that are not directly accessible in the original representation space (Marcos-Martínez et al., 2023; Müller et al., 2008). The same occurs for spectral filters that remove low (< 1 Hz) and high frequencies (> 50 Hz), which are often affected by noise or when the studied activity operates in a predefined frequency range. For instance, studies on motor imagery have focused on the mu (8-12 Hz) and beta (12-30 Hz) bands, which contain the most significant activity.

2.3.2.3 Automatic artifact removal algorithms

As previously mentioned, numerous EEG enhancement algorithms have been developed over the years. Most have been developed to remove eye and muscular artifacts. Some are completely autonomous, while others rely on expert supervision. Here, four algorithms widely used for automatic (i.e., not relying on human intervention) EEG enhancement are used as benchmarks.

ASR Artifact Subspace Reconstruction (ASR) is a method developed to remove transient and large-amplitude artifacts from noisy EEG. It relies on principal component analysis to reject large variance components before reconstruction. This method relies on automatically identifying clean portions of the EEG signal and using these segments to determine thresholds for rejecting components. As stated in (Chang et al., 2019), ASR has become the standard benchmark for EEG enhancement. Interested readers are referred to (Mullen et al., 2015) for more details on the ASR method.

ADJUST Automatic EEG artifact Detection based on the Joint Use of Spatial and Temporal features (ADJUST) is an automatic artifact removal method that relies on “templates” of the effects of stereotyped artifacts (e.g., due to eye movements, blinks, and heartbeats) on independent components. Components related to stereotyped artifacts are then removed and the signal is reconstructed. It has been reported that non-stereotyped artifacts, such as those due to movement, are not accurately removed with ADJUST, and multiple methods are required. More details on ADJUST can be found in (Mognon et al., 2011).

Wavelet-ICA Wavelet-enhanced independent component analysis (wICA) relies on wavelet coefficient thresholding of independent components to reject artifactual components. This method has been shown to outperform conventional ICA and to better preserve EEG spectral and phase coherence properties (Castellanos et al., 2006), especially for low-density EEG configurations (Cassani et al., 2014).

HAPPE The Harvard Automated Processing Pipeline for Electroencephalography (HAPPE) is a pipeline suitable for low-density EEG channels and limited data samples. It relies on wICA and the multiple artifact rejection algorithm (MARA) to detect the artifactual components for rejection.

The interested reader is referred to (Gabard-Durnam et al., 2018) for complete details of the HAPPE method.

2.3.2.4 Data segmentation

Cerebral activity, particularly that captured by EEG signals, is non-stationary. Thus, the properties of the signal, such as its entropy or spectral power distribution, can be considered stable over a short period. Therefore, it is common practice to segment a signal through a series of temporal windows that can optionally overlap to conduct statistical analyses on portions of the signal considered quasi-stationary (Huster et al., 2014). These portions are commonly referred to as "epochs". The duration of the epochs vary depending on the study. It can be as short as one second for active BCI studies, or as long as several minutes for sleeping studies.

2.3.3 Standard EEG features

Power Spectral Density Features The brain's activity is inherently oscillatory, and this is a fundamental characteristic of its functioning. Spectral analysis, therefore, is an extremely useful tool for characterizing neuronal activity. For a given signal, PSD measures the power of each frequency component, thereby allowing the evaluation of mental activity. PSD features are employed in each chapter either as a reference feature or by combining them with AM features.

Phase and Magnitude Spectral Coherence Phase and Magnitude Spectral Coherence (PMSC) features are useful for measuring the connectivity between cortical regions, as these techniques measure the covariance of the phase and magnitude between two signals. Interested readers can refer to (Aoki et al., 1999) for more details on the PMSC computation. These features were used in Chapter 4.

Phase Circular Correlation Although metrics such as phase-locked value and magnitude-squared coherence have traditionally been used to quantify the connectivity between cortical sites, they have been criticized for their vulnerability to coincidental phase synchrony, which can result in misinterpretation of the results (Burgess, 2013). To address this, we use the Phase circular correlation of narrow-band filtered time series (CCOR) method (Burgess, 2013) to examine the connections between different electrode pairs, which is motivated by the increased robustness of the method, as well as its ability to account for phase covariance within electrode pairs. These features are presented in Chapter 3.

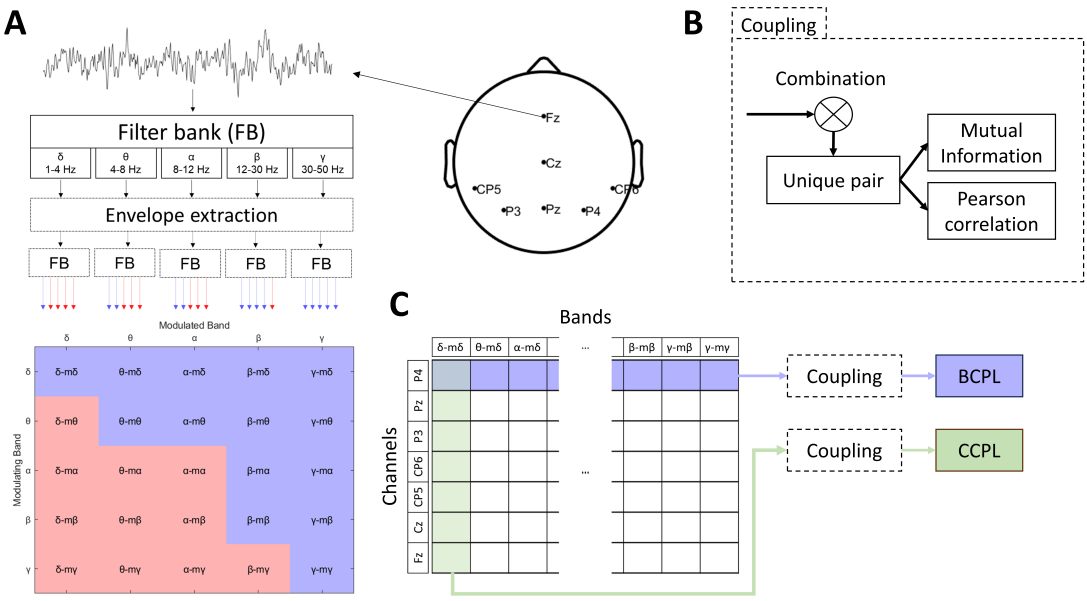

Figure 2.4 : A. Flow chart illustrating the procedure for amplitude modulation time-series extraction from EEG signals. In the top-left corner, the straight line denotes the original and band-filtered EEG signal. Dashed lines and adjoining blocks represent envelope extraction and processing stages, respectively. Based on Bedrosian's theorem, the bottom left matrix differentiates between valid (blue) and invalid (red) amplitude modulation time series. B. Abstract data flow showing the general extraction process of coupling measurements from a set of time series. C. Schematic representing how time series are selected for the computation of either Amplitude Modulation inter-channel coupling (AM-CCPL) or Amplitude Modulation inter-band coupling (AM-BCPL).

2.3.4 Proposed Amplitude Modulation Power features

Amplitude Modulation (AM) features quantify the rate-of-change of specific frequency sub-bands and provides insight into cross-frequency magnitude-magnitude coupling/interactions and reveals interactions between different brain processes (Tort et al., 2010; Seeber et al., 2014; Voytek et al., 2010), as well as long-range communication (Zanto et al., 2011; Clayton et al., 2015).

The signal processing steps involved in the extraction of Amplitude Modulation Power (AMP) features is shown in Figure 2.4A. The process involves the decomposition of EEG signals into five spectral bands using a Filter bank (FB). The bands selected for this study included the conventional delta (1–4Hz), theta (4–8 Hz), alpha (8–12 Hz), beta (12–30 Hz), and gamma (30–50 Hz) bands, given their established roles in representing neuronal dynamics (Newson et al., 2019). We use a zero-phase FIR filter to execute signal filtering, which consists of two successive filtering steps in opposing directions on a mirror-padded version of the input signal. The outcome is a series of signals representing power dynamics across each frequency band over time.

Subsequently, we obtain the envelope using the absolute value of the Hilbert transform.

The Hilbert transform $\mathcal{H}\{x_{bf}(t)\}$ of a signal $x_{bf}(t)$ in the time domain is defined as follows:

$$\mathcal{H}\{x_{bf}(t)\} = \frac{1}{\pi}\,\text{p.v.}\int_{-\infty}^{\infty}\frac{x_{bf}(\tau)}{t-\tau}\,d\tau,$$

where p.v. denotes the Cauchy principal value.

In the spectral domain, the Hilbert transform translates into multiplication by $-j\,\mathrm{sgn}(f)$, where $\mathrm{sgn}(f)$ is the sign function defined as

$$\mathrm{sgn}(f) = \begin{cases} 1 & \text{if } f > 0 \\ 0 & \text{if } f = 0 \\ -1 & \text{if } f < 0 \end{cases}$$

The Fourier transform of signal $x_{bf}(t)$ is denoted $X_{bf}(f)$. Thus, the Fourier transform of the analytical signal $X_a(f)$ is given by

$$X_a(f) = \mathcal{F}\{x_a(t)\} = \begin{cases} 2X_{bf}(f) & \text{if } f > 0 \\ X_{bf}(f) & \text{if } f = 0 \\ 0 & \text{if } f < 0 \end{cases}$$

Combining these expressions, we obtain the following time-domain relationship for the analytical signal.

$$x_a(t) = \mathcal{F}^{-1}\{X_a(f)\} = \mathcal{F}^{-1}\left\{2U(f)X_{bf}(f)\right\},$$

where $U(f)$ denotes the Heaviside step function.

$$U(f) = \begin{cases} 1 & \text{if } f \geq 0 \\ 0 & \text{if } f < 0 \end{cases}$$

The signal envelope corresponding to the instantaneous amplitude is given by the absolute value of the analytical signal $|x_a(t)|$.

This envelope is then filtered using the same FB based decomposition, culminating in a set of 5-by-5 AM time-series (shown in the bottom part of the figure) that represent the spectral decomposition of the power dynamics within each specific EEG frequency band, that is, the measure of the amplitude–amplitude coupling of two EEG frequency bands.

For notation, we refer to these 25 signals as '<modulated band>-m<modulant>', where 'modulated band' refers to one of the five bands from the first filtering step and 'modulant' pertains to the band applied during the second filtering step. A visual representation of the entire set of AM time series according to this convention is shown in the bottom matrix of Figure 2.4A. However,

according to Bedrosian's theorem (Trajin et al., 2008), not all of these 25 signals are possible; in fact, only 14 of them are possible, as low-frequency bands modulated by high-frequency bands are invalid. A more in-depth description of amplitude modulation-based features can be found in (Fraga et al., 2013; Cassani et al., 2018).

The extraction of AMP features involves calculating the average power of epoched AM time-series. The epoch duration varies across different experiments, and the specific settings were outlined for each chapter individually.

2.3.5 Coupling features derived from Amplitude Modulation

PMSC-AM Phase and Magnitude Spectral Coherence of Amplitude Modulation Features (PMSC-AM) extends the capacity of PMSC features to amplitude modulations. These features were recently proposed for affective state monitoring and are useful for arousal and valence prediction (Clerico et al., 2015, 2018). These features are based on the modulated signals of each band, which make up a total of 14 signals per channel (see (Clerico et al., 2018) for more details).

CCORAM CCOR is also computed from amplitude modulation timeseries to study the relationship between the temporal dynamics of oscillations and the interaction between different regions of the cortex.

2.3.6 Feature selection

Features are used to characterize properties of the EEG signals. They commonly capture statistical, spatial (Mousavi et al., 2019), spectral, and/or temporal information. The relevance of these features depends on the type of application. For instance, for motor imagery, features measuring activity in the mu and beta bands of the motor cortex will be most useful, whereas for a passive BCI aimed at monitoring the user's affective state, features measuring frontal asymmetry in the alpha band could be most useful.

Therefore, it is common practice in EEG studies to use a feature selection or reduction process to retain only the necessary information (Remeseiro et al., 2019). The selection criteria are typically based on the available data and aim to improve the performance of the BCI (Huster et al., 2014). For example, for an active BCI, measures of coupling such as correlation or mutual information (Khalaf et al., 2019) between each feature and label can be used. The goal is to minimize intra-class variance while maximizing inter-class variance (Lotte et al., 2015).

The three primary categories of selection algorithms are filter-based, embedded, and wrapper-based. Filter-based methods utilize statistical tests to evaluate the importance of a feature in predicting labels, whereas embedded methods integrate feature selection directly into the model-

training process. Finally, wrapper methods evaluate multiple subsets of features based on their performance on a given model, which is generally more computationally expensive but optimizes the performance.

The process of feature extraction and selection is critical in BCI systems because it reduces the dimensionality of the features input to the classifier. Simple algorithms, such as filter-based selection, generally provide a better interpretation of the data, while more complex algorithms, such as wrapper and embedded methods, are more difficult to interpret but offer better performance (Huster et al., 2014). For example, embedded algorithms such as decision trees and random forests incorporate feature selection into model construction, whereas wrapper methods use approaches such as genetic algorithm search to evaluate different subsets of features.

2.3.7 Machine learning

There are two main types of models: the so-called “classical” machine-learning models and, more recently, deep-learning models. Among the classical models, there are subcategories, with the main ones being linear models, such as Linear Discriminant Analysis (LDA) (Aggarwal et al., 2019), linear regression (LR), kernel-based models, such as SVM (Aggarwal et al., 2019), decision tree models, such as Random Forest (Sciaraffa et al., 2022), and non-parametric models, such as K-nearest neighbors. Classical models have the advantage of being relatively simple and are particularly effective for small datasets (Aggarwal et al., 2019).

Deep learning, which has revolutionized the field of machine learning, comprises complex architectures based on artificial neural networks. These networks mimic certain aspects of the functioning of biological neurons through successive linear combination operations, thereby transforming the input data into a more meaningful feature space. The most popular types of networks include Recurrent Neural Networks (RNN) (Schmidt, 2019), adapted to sequential data, and Convolutional Neural Networks (CNN) (Wu, 2017), designed for spatially structured data, such as images.

Depending on the nature of the problem, models can be trained using labeled data (supervised learning) or unlabeled data (unsupervised learning). Unsupervised learning aims to identify recurring patterns in unlabeled data by employing algorithms, such as k-means, to group samples based on their similarity. This is particularly useful for certain passive BCI applications, despite their generally inferior performance compared to supervised models. On the other hand, supervised learning methods train models to predict dependent variables from independent variables. These dependent variables can be qualitative (discrete, categorical), referred to as classification tasks, or quantitative (continuous), for regression problems (Lotte et al., 2015). Supervised learning is typically employed by active BCIs to translate EEG data into commands (Shindo et al., 2011).

The best classification performance is usually achieved with a binary classification task with train/test data coming from the same subject. Increasing the number of classes for prediction

reduces the performance of most models (Lotte et al., 2015). In the case of active BCIs, it is essential that the mental tasks to be classified be associated with distinct cortical patterns (Shin et al., 2018). The probability that two mental tasks activate similar regions of the cortex increases with the number of tasks to be classified. Furthermore, some models, such as SVM, only support binary classification, thus One-versus-One or One-versus-All strategies are generally used in this case (Shin et al., 2018). Multiclass systems with good accuracy constitute a significant advantage for BCIs because it involves a higher ITR (Shin et al., 2018). Moreover, combining data from multiple users to enrich a dataset allows for better generalization of models and, consequently, better performance with new user data.

Deep-learning models require a significantly larger amount of data than classical models. EEG studies most often rely on small datasets with an average of 20 participants (Zhou et al., 2022). Despite the development of open-access EEG dataset platforms, access to high-quality EEG signals has remained insufficient. Additionally, each dataset has its own technical and structural specificities, which makes concatenation of different datasets difficult (Hinss et al., 2021). This is a major limitation that has hampered the wide usage of deep learning methods that are generalizable and interpretable in the BCI field.

2.3.8 Testing setup and figures-of-merit

The quality of a model is assessed using different metrics, depending on the type of problem. In the classification problem, the metrics used are typically based on four values: True Positive (TP), False Positive (FP), True Negative (TN), and False Negative (FN). Based on these values, two figures-of-merit are used in this thesis, namely:

- **Accuracy** :
  - Accuracy is the ratio of correct predictions (positive and negative) to all predictions.
  - $$\text{Accuracy} = \frac{TP + TN}{TP + FP + TN + FN}$$
- **Kappa Score** :
  - The kappa score evaluates the agreement between two raters, taking into account the probability of agreement due to chance. The two classes are defined as follows:
  - $$\kappa = \frac{P_o - P_e}{1 - P_e}$$
  - where P_o (proportion of agreement observed) and P_e (proportion of agreement expected by chance) are given by:

–

$$P_o = \frac{TP + TN}{TP + FP + TN + FN}$$

–

$$P_e = \left(\frac{(TP + FP) \cdot (TP + FN)}{(TP + FP + TN + FN)^2}\right) + \left(\frac{(TN + FP) \cdot (TN + FN)}{(TP + FP + TN + FN)^2}\right)$$

Evaluating a model is a crucial step that includes testing the accuracy of its predictions on a dataset that has not been used during training, i.e., on unseen data. However, this type of evaluation is not statistically robust, because only one portion of the data is used for testing. Cross-validation is a more reliable method for evaluating the performance of a machine learning model as it uses multiple subsets of data to test the model, thus reduces the variance of the results, and provides a more stable estimate of performance. Cross-validation is a critical procedure for obtaining a robust and reliable evaluation of machine learning models, maximizing the use of available data, while minimizing issues with overfitting.

Alternatively, a permutation test may be used to evaluate the significance of the observed results. It is a non-parametric statistical technique that evaluates whether the performance of a model is significantly better than that expected by random chance (Shin et al., 2018). In Chapter 5, we conduct a permutation test to corroborate the efficacy of the regressor in forecasting cybersickness.

2.4 Datasets

This section presents the datasets used in this thesis. Chapters 4 and 5 used datasets employed for physiological reaction monitoring: mental workload and cybersickness induced during the VR experience. Their use is therefore oriented towards passive BCI applications. Chapter 3, in turn, uses a dataset for mental task classification that corresponds to an active BCI application. The WAUC and VR-Induced Cybersickness Detection datasets are publicly available, while the mental task dataset was collected in-house and describe in (Banville et al., 2017).

2.4.1 Hybrid NIRS-EEG Brain-Computer Interface Dataset

The objective of this dataset (Banville et al., 2017) is to test the classification of seven mental tasks for an active multimodal BCI using EEG and fNIRS. EEG signals from 12 participants were collected using a 62-electrode EEG system with a sampling frequency of 512 Hz. The fNIRS data were collected by using a 16-source system with 24 detectors. The task battery consisted of 3 s of baseline, followed by 15 s of execution of one of the randomly selected mental tasks. The dataset also includes subjective evaluations of task load and preference, making it a comprehensive resource for active BCI research on cognitive task recognition and hybrid modality performance. More details about the dataset are provided in Chapter 3.

2.4.2 WAUC

The WAUC (Workload Assessment Under physical aCtivity) dataset (Albuquerque et al., 2020) was created to develop biomarkers to measure mental workload based on physiological signals. It contains data from 48 subjects who performed tasks under six different combinations of two levels of mental load and three levels of physical load while walking/jogging on a treadmill or riding a stationary bike. Mental workload (MW) was induced using the computerized MATB-II task, which simulates piloting tasks and requires moderate-to-high levels of mental load. Different levels of physical activity intensity were included in the experiment to simulate situations encountered in the field by high-risk professionals such as airline pilots, police officers, and firefighters. The development of MW biomarkers will ultimately help prevent accidents due to fatigue or excessive workloads. More details about the dataset are provided in Chapter 4.

2.4.3 VR-Induced Cybersickness Detection

The VR-Induced Cybersickness Detection Dataset (Li et al., 2021a) is a collection of neurological and physiological signals recorded from 40 participants while viewing VR content designed to induce cybersickness (tunnel and roller coaster). The experiment involved measuring symptom intensity using a Fast Motion Sickness Scale (FMS) scale questionnaire. The aim of this study was to explore the role of the human vestibular network (HVN) during CS and develop effective detection and mitigation strategies. EEG recordings were collected using an eight-channel EEG device (NE StarStim 8™) at seven locations, with a sampling rate of 500 Hz. Autonomic signals included heart rate (HR), heart rate variability (HRV), and fingertip and forehead temperatures, as well as head movement information captured via an accelerometer. In this thesis, only the EEG and head movement information are used. More details about the dataset are provided in Chapter 5.

2.5 Conclusion

In this chapter, we have provided some theoretical background describing the origin of the cortical activity detected by EEGs to motivate the newly proposed amplitude modulation features. We then highlight the key components of the typical BCI pipeline, from signal pre-processing to feature extraction and the classification stage, thus providing a high-level view of the material and methods used throughout the thesis, including a brief description of the three different datasets used in our experiments.

3 IMPROVING ACTIVE BCI ACCURACY WITH AM FEATURES

Preamble

This chapter is compiled from material extracted from (Rosanne et al., 2023).

3.1 Introduction

Brain Computer Interface (BCI) technology has emerged as an influential communication tool with extensive applications in numerous fields, including entertainment, marketing, and mental state monitoring. Medical applications, particularly in neurorehabilitation (Said et al., 2022; Värbu et al., 2022), remain the predominant use of active BCI, as they can improve the quality of life of patients suffering from amputations or paralysis due to neuronal damage, such as stroke (Milani et al., 2022; Vatinno et al., 2022).

Despite the great potential of both active and passive BCI, several major challenges must be overcome. For example, psychological factors such as user fatigue, frustration, and attention levels impede successful adoption of BCI systems. Moreover, inter-subject and inter-session variability and low signal quality contribute to the limited reliability of BCI in practical scenarios.

Traditional approaches to improving BCI robustness include multimodal systems, hybrid BCI, and the development of new signal processing and feature extraction tools. Recently, deep learning models have emerged as data-driven methods that can help advance BCI technologies (Chakladar et al., 2020; Wang et al., 2020; He et al., 2021; Mai et al., 2021). Although such data-driven methods have shown improved accuracy on specific datasets, they are known to be poorly generalized across datasets (He et al., 2021; Roy et al., 2019) and may introduce new vulnerabilities (e.g., susceptibility to adversarial attacks (Meng et al., 2023; Zhang et al., 2021)).

In this chapter, we propose to improve the robustness of active BCI by incorporating a new signal representation that allows for the measurement of Amplitude Modulation (AM) dynamics and cross-frequency coupling using electroencephalography (EEG) signals. While such a representation has been used in the past for Alzheimer's disease biomarker development (Cassani et al., 2019; Jesus Jr et al., 2021) and passive BCI monitoring (Clerico et al., 2018), it is explored here as a new feature of active BCI.

The proposed method has several advantages over conventional PSD features (Grass et al., 1938; Buzsáki et al., 2012; Barlow, 1985), which motivated this study. First, it addresses the inherent non-stationary nature of EEG signals, which traditionally complicates the detection of neural activity patterns. Second, AM dynamic features have been shown to be more robust to artifacts in passive

BCI applications (e.g., (Cassani et al., 2018)). Thus, they may be able to assist with artifact robustness in the active BCI. Third, cortical hemodynamics measured using Functional near-infrared spectroscopy (fNIRS) have been found to correlate with amplitude modulations measured using EEG signals (Trambaiolli et al., 2020), suggesting that amplitude modulation is a good indicator of local neural processing. Since multimodal EEG–fNIRS systems have been shown to outperform EEG systems alone (Banville et al., 2017), the proposed features may be able to capture multiple signal modalities using a single electrode, thus also improving user experience while making BCI more robust. Lastly, cross-frequency amplitude and phase coherence features have been linked to different cognitive processes; thus, they may further assist with inter- and intra-subject variability (Herrmann et al., 2004; Thatcher, 2012; French et al., 1984; Aydore et al., 2013).

To validate the proposed method, we used an active BCI dataset comprising of seven mental tasks, as will be detailed below. The dataset allowed us to explore the effectiveness of the proposed features in 21 binary-classification tests.

3.2 Materials and Methods

In this section, we describe the dataset, extracted features, and feature ranking and classification algorithms used.

3.2.1 Experimental Protocol

The present study used the open-source BCI database described in (Banville et al., 2017). This dataset investigates the discrimination of distinct neural response patterns associated with seven different mental tasks using features extracted from both EEG and fNIRS modalities. The seven mental tasks include mental rotation (ROT), word generation (WORD), mental subtraction (SUB), mental singing (SING), mental navigation (NAV), motor imagery (MI), and face imagery (FACE). Mental rotation, word generation, and mental subtraction are classified as brainteasers, while mental singing, mental navigation, and motor imagery are classified as dynamic imagery tasks and face imagery is classified as a static imagery task. Table 3.1 describes each mental task.

Multimodal data were collected from 12 participants who were fluent in English and/or French, had no history of neurological disorders, and had no previous experience with BCI. The participants consented to participating in the study and monetary compensation was provided after each completed session. All participants agreed with the terms and conditions of the study, which was approved by the INRS Research Ethics Committee.

The data were collected over three recording sessions of 2 to 3 hours each, during a period of 3 to 5 weeks. Each session consisted of four sub-sessions, in which each mental task was randomly repeated four times. Each sub-session began and ended with a 30 s baseline period, during which

Tableau 3.1 : Short description of each mental task.

Mental Task	Task Description
Mental Rotation (ROT)	Participants had to imagine the 3D rotation of two objects and determine whether the objects were identical
Word Generation (WORD)	A letter was presented randomly and the participants needed to find as many words as possible beginning with this letter
Subtraction (SUB)	Participants had to execute the mental subtraction of 1 to 2 digit numbers from a 3 digit number
Singing (SING)	Participants had to choose a song and then mentally sing it while paying attention to the emotions that they felt
Navigation (NAV)	Participants had to imagine walking from one room to another in their past or current residence
Motor Imagery (MI)	Participants had to imagine moving their fingers
Face Imagery (FACE)	Participants had to remember the face of a friend

the participants were asked to remain in a neutral mental state and fixate on the cross at the center of their screen. Before each trial, a 3 s countdown screen identified the task to be performed. Once the countdown was over, the participants had to execute the required mental task for a period of 15 s and were instructed to carry out the task as many times as possible during that period. Each trial was followed by a rest period of random duration, sampled from a uniform distribution of between 10 and 15 s, in which participants were asked to continue minimizing movements but were allowed to blink, swallow, etc. The participants were also required to complete a subjective evaluation questionnaire between the second and third sub-session of each session. The stimuli and questionnaire were implemented using Presentation software (Neural Behavioral Systems, USA). More details about the experimental protocol can be found in (Banville et al., 2017).

EEG data were recorded using a BioSemi ActiveTwo system with 62 electrodes and 4 EOG electrodes. The experiment used a standard 10-10 system for electrode placement, but without AF7 and AF8, where holders were used for fNIRS probes instead. Only data from nine participants were analyzed as data from Participants 2 and 8 were rejected due to excessive artifacts and higher overall drowsiness levels observed during the recordings. Data from Participant 12 were rejected because the three required sessions were not completed. These participant exclusions matched those suggested in (Banville et al., 2017) and were replicated here to facilitate comparisons. Moreover, while 60 fNIRS optodes were also included in the dataset, they were not analyzed in this study.

3.2.2 Dataset Pre-Processing

Utilizing the publicly available EEGLAB MATLAB toolbox (Delorme et al., 2004), we first pre-processed the raw EEG signals. Initially, the EEG dataset was re-referenced to the Cz channel, which was later

removed. To eliminate electrical grid noise, we applied a notch filter of between 59 and 61 Hz. To tackle high-frequency noise and signal drift arising from electrode impedance variation, a band-pass finite impulse response (FIR) filter, ranging from 0.1 Hz to 50 Hz, was employed.

To facilitate comparisons to the results in (Banville et al., 2017), channels P8 and O1 were also discarded. Moreover, the first 2 and 14 markers from subject 3 (session 1) and subject 5 (session 1) showed discrepancies with the experimental protocol and were also discarded. We then used the fastICA algorithm (Hyvarinen, 1999) to extract independent components. These components were further evaluated using the ADJUST algorithm (Mognon et al., 2011), allowing us to identify and automatically remove components associated with artifacts. To mitigate the potential impact of lost data, all channels removed in the earlier stages of pre-processing were restored using spherical interpolation. Following this, the EOG channels were removed and the dataset was re-referenced to the average. For detailed examination and replication purposes, the pre-processing script is available at the following GitHub repository: `https://github.com/OlivierRS/EEG-Preprocessing-with-ADJUST`.

3.2.3 Feature Extraction

3.2.3.1 Power Spectral Density (Baseline) Features

As a means of comparison to the proposed amplitude modulation features, we utilized PSD features as the baseline. Initially, the pre-processed EEG signals were segmented into epochs, starting 1 s before the beginning of each mental task and continuing for 15 s thereafter, generating a total epoch duration of 16 s. Subsequently, these epochs were subdivided into non-overlapping 1 s time windows. The PSD was calculated from each of these windows using Welch's method, employing the MNE toolbox (Gramfort et al., 2013), where the power of each frequency was normalized by the sum of the entire power spectrum. PSD features were extracted from several conventional frequency bands, including theta (4–8 Hz), alpha1 (8–10 Hz), alpha2 (10–12 Hz), beta1 (12–21 Hz), beta2 (21–30 Hz), theta to beta (8–30 Hz), and delta to gamma (0–50 Hz), for each EEG electrode. In addition to the PSD features, we also extracted power ratios, notably alpha (8–12 Hz) to beta (12–30 Hz) and theta to beta ratios, for each electrode. Subsequent to the extraction process, all features underwent log-scaling.

3.2.3.2 Proposed Amplitude Modulation Power Features

Amplitude Modulation features were computed from EEG signals using the implementation described in Section 2.3.4 of Chapter 2. As mentioned previously, while AMP features have been explored for use as biomarkers for neurodegenerative diseases or passive BCI, they were explored here for active BCI control. One important aspect of active BCI is being as close to real-time as possible in

order to maximize the information transfer rate. However, AMP features have an inherent latency in that envelopes greater than 1 s (i.e., the window sizes typically used for PSD features) are needed. In the past, 8 seconds windows have been shown to be optimal for biomarker development (Fraga et al., 2013). Here, we proposed to reduce this to 4 seconds but with a sliding window of 3 seconds, suggesting that decisions can be made every second after the initial 'buffer' period. This approach yielded 11 distinct feature time 'frames' per trial for each frequency band, covering the total trial duration from -1 to 15 s. The features were normalized by the total spectral power at the corresponding time frame.

3.2.3.3 Phase Circular Correlation of Amplitude Modulated Signals

In addition to analyzing power time dynamics using AMP features, we also extracted features to quantify the connectivity between cortical sites. Although metrics such as phase locked value and magnitude squared coherence have traditionally been used for this purpose, they have been criticized for their vulnerability to coincidental phase synchrony, which can result in the misinterpretation of the results (Burgess, 2013). To address this, we used the CCORAM method (Burgess, 2013) to examine the connections between different electrode pairs, a choice motivated by the increased robustness of the method, as well as its ability to account for phase co-variance within electrode pairs. To reduce computational demands and avoid excessive dimensionality, we only used a subset of electrodes, specifically F7, F8, T7, T8, C3, C4, P7, P8, O1, and O2. This selection was based on a strategy to maximize the spatial span using a 19-channel montage and minimize the effects of source propagation by excluding neighboring channels (Mizuhara et al., 2004; Murias et al., 2007). With this approach, we calculated the CCORAM for each possible pair within the selected 14 AM bands.

3.2.4 Feature Selection, Classification, and Figures of Merit

Feature selection methods are essential in removing redundant features and avoiding the curse of dimensionality. Methods such as Minimum redundancy maximum relevance (mRMR) (Ding et al., 2005) and Recursive feature elimination (RFE) (Guyon et al., 2002) account for interactions among features in their selection process, aiming to minimize redundancy within the selected feature set. Despite their effectiveness, these techniques pose computational challenges, especially in scenarios involving datasets with extensive numbers of features. In contrast, the Fisher linear discriminant (FLD) (Fu et al., 2020), a filter-based selection method, offers a more practical solution as it evaluates individual features iteratively with significantly lower computational complexity.

For classification, we employed a stratified shuffle split cross-validation approach. In this approach, the aggregated data from all participants were divided, maintaining a 90-10 split for training and testing, respectively, ensuring the proportional representation of both classes in each

subset. This procedure was reiterated 100 times, using a different random split each time, to foster a robust estimation of the model's performance. The hyperparameters of the SVM, with radial basis function kernels, C, and gamma, were optimized in the training set, leveraging a cross-validated grid search. For the figure-of-merit, we used the average kappa score metric on the predicted labels from the test set for each of the 100 bootstrap trials.

3.2.5 Eigendecomposition-Based Ranking of Binary Classifications

In this study, we examined the interactions between mental tasks via a series of 21 binary classification tasks, aiming to critically assess the influence of amplitude modulation-based features. However, this approach poses a challenge as the insights derived from individual binary classification could only offer a partial understanding of the mental task patterns. To address this, we employed a methodology utilizing eigendecomposition to derive a ranking score, hereafter referred to as the 'prestige score' based on terminology from the established literature (Sikarwar et al., 2021). The detailed process of extracting the prestige score is depicted in Figure 3.1.

This approach provides insights into the relative importance of mental tasks by considering the entire set of classification performances. The prestige score not only reflects the immediate kappa scores of mental tasks in discriminating against other tasks but also synthesizes the entire set of classification performances represented by kappa scores for task pairs. In particular, when a task is inherently difficult to identify and consequently yields a low discriminative score, having one or two binary classifications with high kappa scores can lead to the overestimation of its true discriminative capacity. With this methodology, we could analytically discern the genuine discriminative scores of the tasks that secured high kappa scores, revealing the relative ease of achieving such scores and thereby justifying the adjustment of these scores to accurately reflect the task's true discriminative nature.

Figure 3.1 depicts an illustration of the process of extracting the prestige scores. On the right side of the figure, the step-by-step procedure for applying eigendecomposition to a 7×7 interaction matrix is demonstrated. This matrix is constructed by incorporating the 21 kappa or Fisher score measurements in its upper triangle, each element of which represented a measurement from a pair of tasks. The analytical process yields the prestige score, associated with the eigenvector with the highest eigenvalue. Utilizing the Perron–Frobenius theorem, these prestige scores are identified as normalized positive vectors that reveal the latent influences that each class held as dictated by the chosen metric (Keener, 1993). To maintain the relative magnitudes of the interactions captured in the different dataset folds during data amalgamation, each prestige score is scaled by its corresponding eigenvalue. This approach avoids the empirical analysis that is traditionally conducted on 7×7 interaction matrices, allowing for a more robust and succinct interpretation of the influences of mental tasks through 7-element vectors. Consequently, plotting the feature distribution of individual mental tasks becomes a more streamlined alternative to the conventional

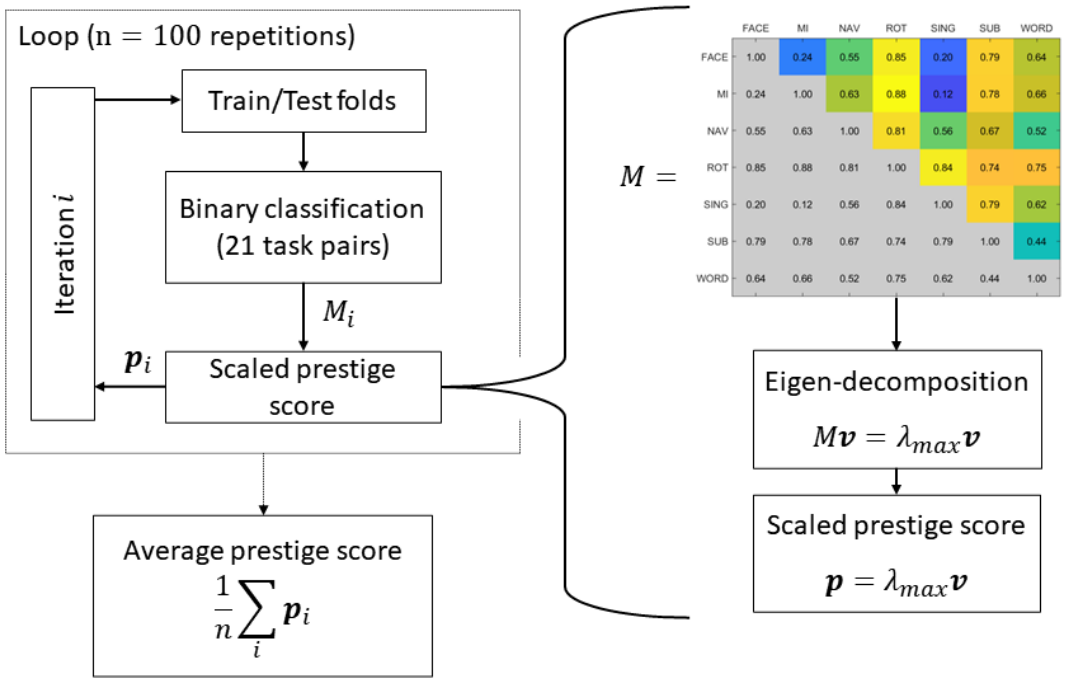

Figure 3.1 : Flow chart illustrating the computation of the scaled prestige scores, depicting how the 21 kappa score measurements were generated in each iteration and arranged in the 7 $\times$ 7 interaction matrix 'M', followed by the eigendecomposition and final averaging of the prestige scores. Kappa scores are used as an illustrative example.

method of illustrating all 21 pairs of mental task combinations. Subsequently, the left side of Figure 3.1 clarifies the iterative procedure employed to amalgamate the prestige scores.

3.3 Experimental Results

In this section, we describe the experimental results in terms of the impact of the proposed features, the ranking of the mental tasks, and a discussion on the top-selected features.

3.3.1 Estimation of Optimal Feature Set Size

To estimate the most suitable balance between reducing overfitting risk and ensuring high classifier accuracy, we proceeded to identify the optimal number of features by systematically testing various feature set sizes. Figure 3.2 depicts the relationship between the quantity of the top-selected features, ranked using the Fisher linear discriminant scores, and the performance of a vanilla SVM classifier. The x-axis represents the number of selected features and the y-axis represents

the grand average kappa score derived from all 21 task pair classifications. In total, three combinations of feature types were tested and the model performance using PSD, AMP+PSD, and AMP+CCORAM+PSD are shown in yellow, orange, and blue, respectively. We used the kappa scores to analyze the curve and determine the exact number of features for when the accuracy started to plateau. As can be seen, this occurred after 2000 features for all feature type combinations. Above this threshold, the performance gain was negligible and potential overfitting issues could appear. Henceforth, only experiments with classifiers trained using this number of top features will be reported.

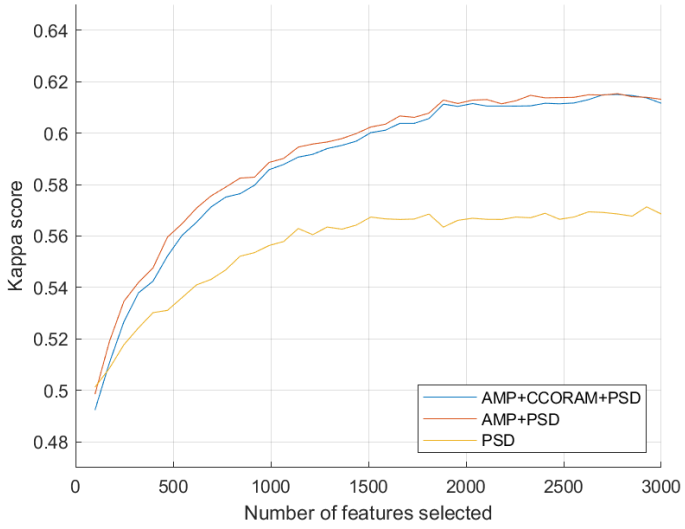

Figure 3.2 : Grand average of task pair kappa scores versus the number of features. The top 2000 features were chosen for subsequent experiments.

Following feature selection, we conducted an in-depth analysis of the distribution of all selected features, categorizing them by type and analyzing them within each top feature subset based on both appearance frequency and FLD score. The AMP features were predominant, representing 74.14% of the selected pool with a cumulative score of 70.02%. PSD features followed, accounting for 22.72% with a cumulative score of 27.11%. The CCORAM features were the least represented at 3.14%, contributing 2.86% to the cumulative score.

3.3.2 Impact of Proposed Features on Classification Performance

Figure 3.3 shows the kappa scores obtained for each of the 21 possible task pairs for PSD features alone (orange), PSD features combined with the proposed AMP features (red), and all three feature sets together (blue). As can be seen, the incorporation of AMP features significantly enhanced performance across 17 of the 21 task pairs. For the remaining four task pairs, the accuracy still increased in three, just not significantly (i.e., ROT-WORD, NAV-WORD, and FACE-SING),

while the accuracy actually dropped relative to using PSD features alone in one (ROT-SUB). Task pairs associated with mental activities, such as SUB, WORD, FACE, and SING, generally showed negligible enhancements. Notably, the MI-SING and FACE-SING pairs registered the lowest kappa values. These tasks, which are intricately linked to cognitive functions, such as working memory, long-term affective retrieval, and both auditory and visual memory processing, could inherently possess greater inter-subject variability due to their abstract nature, while factors such as individual cognitive approach, mental state, and problem-solving strategy could influence the outcome, leading to subjective disparities.

Overall, the average kappa scores across all 21 task pairs were 0.6221, 0.6237, and 0.5761 for the AMP+CCORAM+PSD, AMP+PSD, and PSD models, respectively. These findings suggest that in the majority of cases, AMP features capture exclusive information that is not obtained through PSD alone.

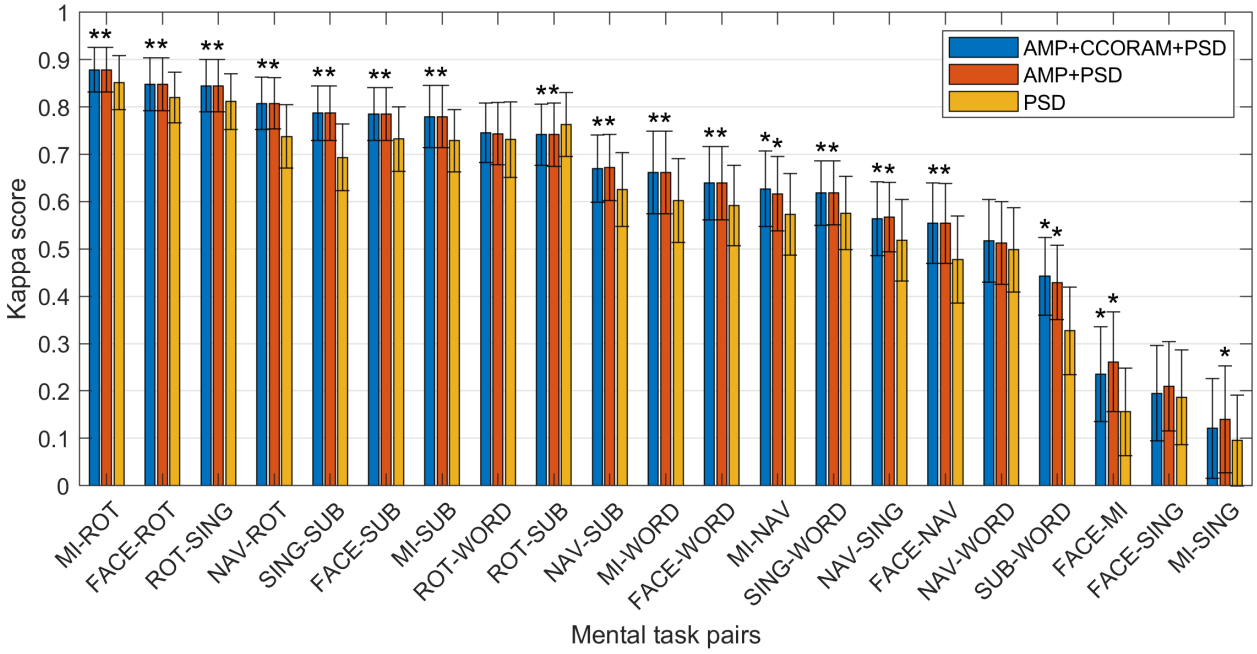

Figure 3.3 : Comparison of the kappa scores of the AMP+CCORAM+PSD (blue), AMP+PSD (red), and PSD (orange) models, derived from the selection of the 2000 optimal features. Columns AMP+CCORAM+PSD and/or AMP+PSD with a symbol * indicate a significant difference relative to PSD results, with a significance level alpha of 0.05.

3.3.3 Ranking of Mental Task Kappa Scores

By employing the eigendecomposition ranking technique, we estimated the discriminative power of the individual mental tasks. Figure 3.4 illustrates the estimated individual kappa scores for each of the seven mental tasks, which were derived from the averaged prestige score vectors across the 100 dataset folds. These vectors were procured through the ranking method outlined previously, employing the kappa score interaction matrix. In essence, each iteration of the classification pipeline

produced a single interaction matrix, from which a prestige score was extracted. This procedure was repeated across all folds to ultimately average the prestige scores, thereby providing an estimate of the ”true” kappa score for each mental task. As a result, mental tasks with higher relative scores were suggestive of a consistently superior discriminating pattern quality, revealing exclusive patterns that distinctly characterized such tasks. The outcomes of this analysis are shown in Figure 3.4, where the discriminatory power of each task is displayed in decreasing order of prestige score.

As can be seen, the rotation (ROT) task achieved the highest score. Interestingly, in (Banville et al., 2017), this task was shown to be preferred amongst the participants, despite its demanding nature. This capacity for differentiation could be attributed to its primarily visual nature, which reduces the subjectivity typically present in tasks involving complex processing, such as memory or emotion, thereby exhibiting more discernable neuronal patterns. Conversely, our findings showed that the FACE and SING tasks were the least accurately identified, a result that was in alignment with feedback given by subjects in (Banville et al., 2017), suggesting that these were their least favorite tasks.

The navigation (NAV) and subtraction (SUB) tasks placed second and third in this analysis, both of which were liked by subjects in (Banville et al., 2017). Interestingly, while the motor imagery (MI) task demonstrated a similar kappa score to the FACE and WORD tasks in our study, its use is widespread within the active BCI community. It has been hypothesized that MI-induced patterns may be overshadowed when paired with brain teaser tasks. This could be observed in task pairs such as FACE–MI and SING–MI. The intricate dynamics of MI, involving both promising classifications in certain configurations and limitations in others, underscores a complex landscape that necessitates a careful and balanced consideration when selecting tasks for BCI applications.

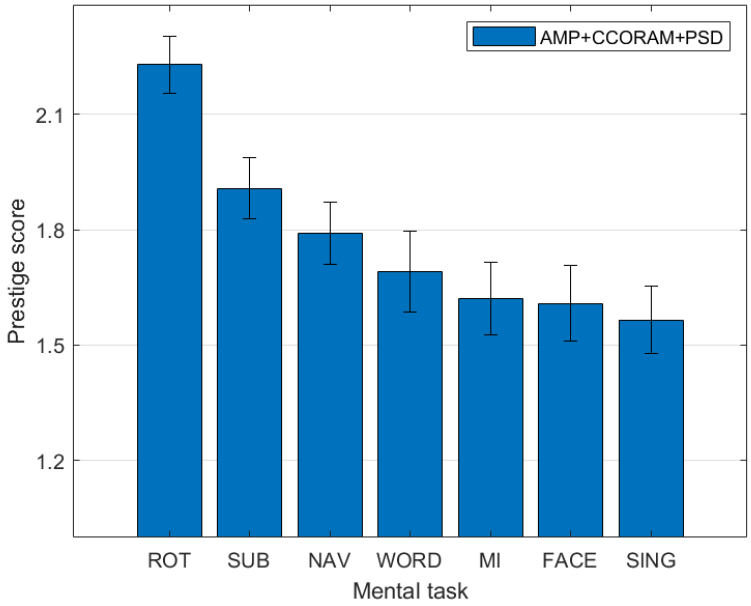

Figure 3.4 : Ranking of individual mental tasks using PSD+AMP+CCORAM features, derived from pairwise classification kappa scores. A higher rank indicates a more distinct pattern, facilitating the model's ability to discriminate one mental task from others.

3.3.4 Mental Task Feature Analysis

In a similar vein to the analysis performed in the previous section and depicted by Figure 3.1, we re-conducted this analysis with the goal of understanding which feature patterns most efficiently captured neural patterns for different tasks. We started by constructing a 7×7 matrix for each feature. Each cell in these matrices corresponded to the FLD score for a pair of mental tasks when differentiated using that particular feature. Consequently, each matrix provided a snapshot of the discriminative power of a single feature across different task pairs. From these matrices, prestige scores were derived for each feature, reflecting its distributed discriminative power across the mental tasks.

This analysis was repeated for all features and then aggregated per feature type group, i.e., AMP, CCORAM, or PSD. Figure 3.5 summarizes our findings. As can be seen, the AMP features were the most efficient in capturing discerning patterns for each individual mental task, followed by the traditional PSD features. Particularly in the ROT task, AMP demonstrated a marked effectiveness over PSD, whereas for the SUB task, both AMP and PSD showed similar discriminative power. Meanwhile, the contribution of the CCORAM feature type was notably lower, showing no clear leaning towards any specific task, indicating its limited utility in this context. It is hoped that these findings will provide insights for researchers developing active BCI regarding what features to use depending on the mental task in question.

3.3.5 Multidimensional Analysis of Relevant Features

For each individual feature, which were associated with unique combinations of channels, bands, and feature types, we computed a distinct prestige score, representing their ranking across mental tasks. Utilizing these scores, we constructed topoplots to visually represent the distribution of feature rankings across the EEG scalp. For the AMP feature type, the corresponding topoplots for each band are illustrated in Figures 3.6– 3.10. Similarly, for the PSD feature type, Figures 3.11–3.13 display the topoplots of the prestige score distributions for each band.

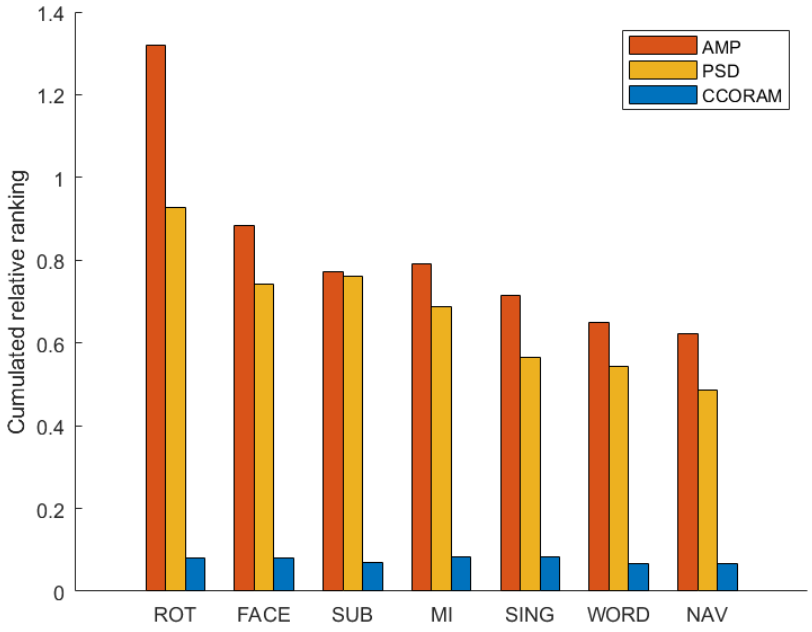

Figure 3.5 : Average Fisher-based prestige scores of mental tasks per feature type (AMP, PSD, and CCORAM).

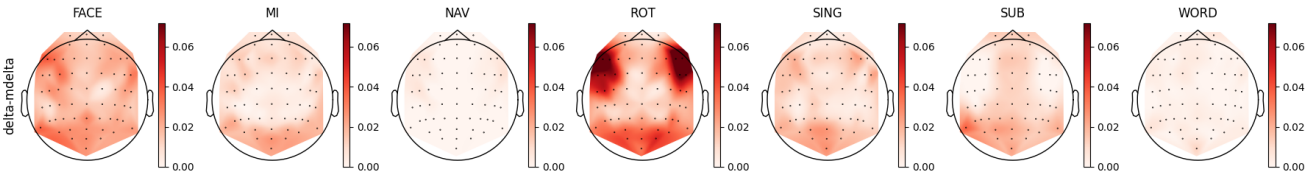

Figure 3.6 : Ranking distribution of AMP features related to the delta band.

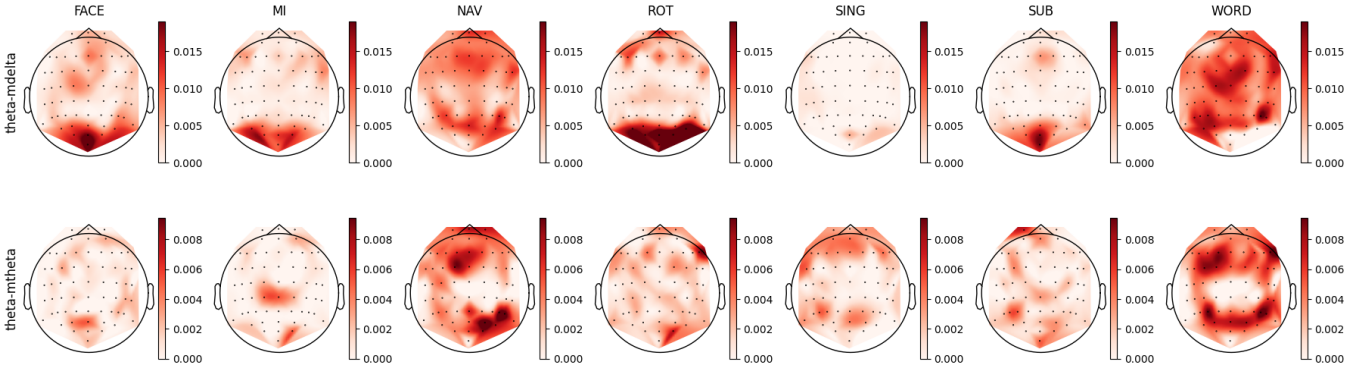

Figure 3.7 : Ranking distribution of AMP features related to the theta band.

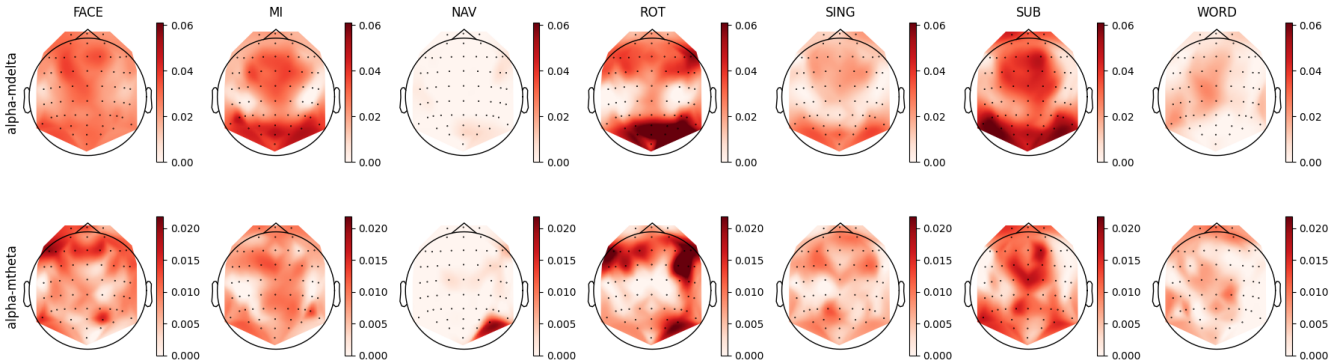

Figure 3.8 : Ranking distribution of AMP features related to the alpha band.

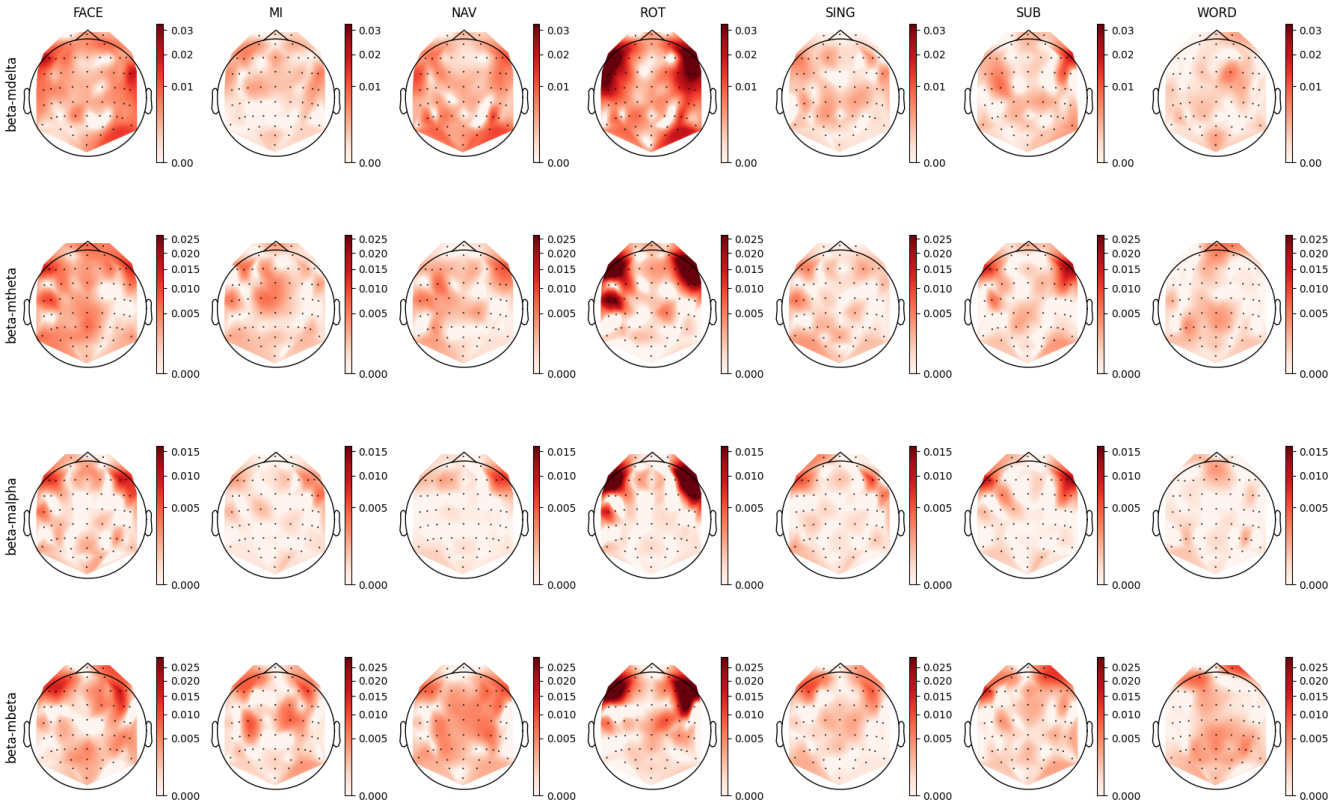

Figure 3.9 : Ranking distribution of AMP features related to the beta band.

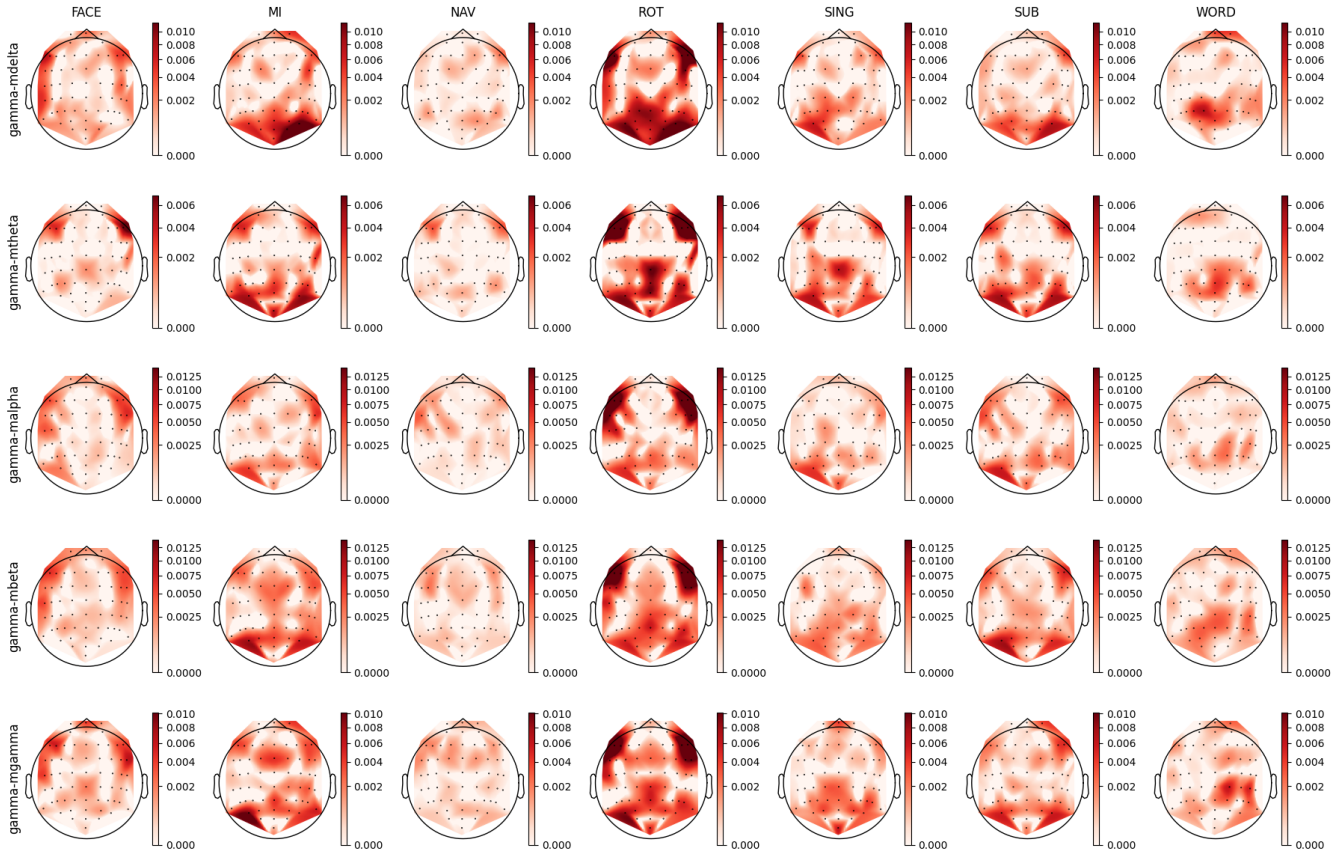

Figure 3.10 : Ranking distribution of AMP features related to the gamma band.

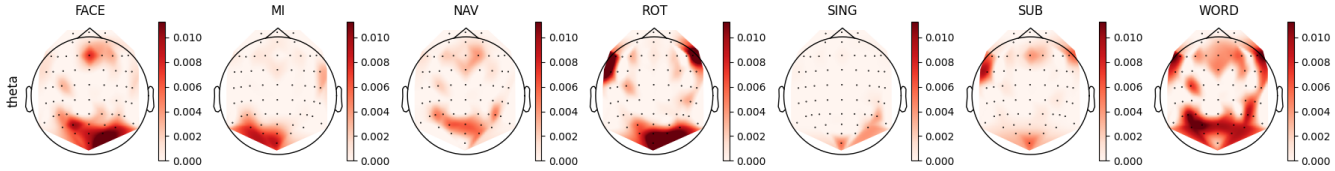

Figure 3.11 : Ranking distribution of PSD features for the theta band.

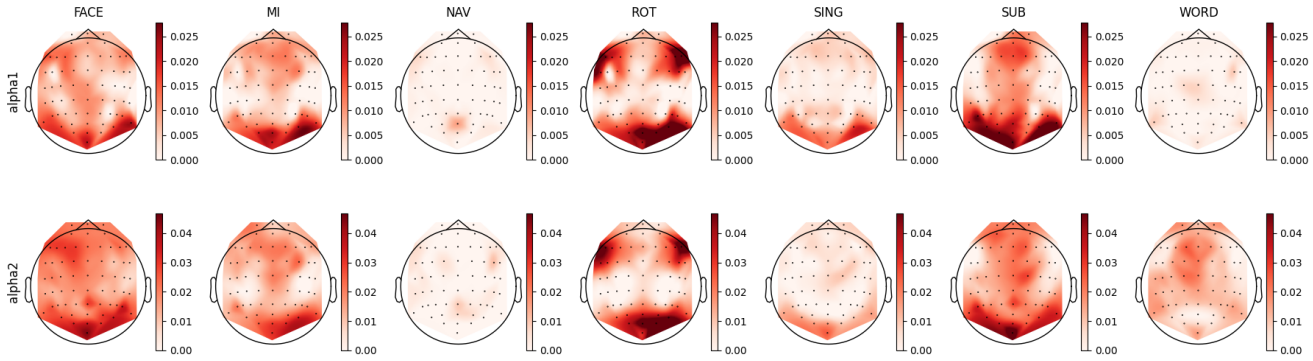

Figure 3.12 : Ranking distribution of PSD features for the alpha band.

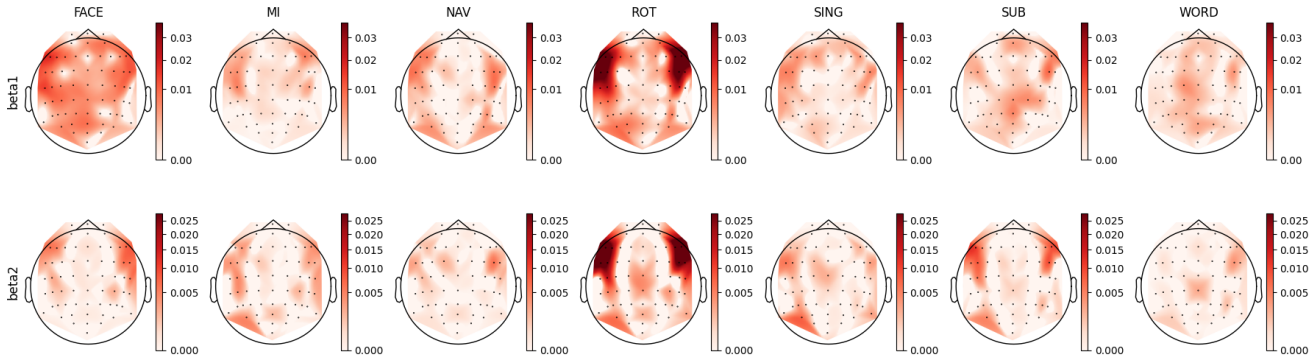

Figure 3.13 : Ranking distribution of PSD features for the beta band.

3.4 Discussion

The proposed amplitude modulation features are postulated to mirror core biological mechanisms within the brain that are potentially engaged in processing stimuli and directing behavioral responses (Trambaiolli et al., 2018; Autthasan et al., 2019; Hilla et al., 2020; Clerico et al., 2018). Numerous studies have suggested that amplitude modulation patterns in EEG signals could be indicative of mechanisms for controlled inhibition (Jensen et al., 2010; Prada et al., 2014; Zarjam et al., 2012; Hilla et al., 2020) and cognitive process integration (Weiss et al., 2012; Palva et al., 2018; Daume et al., 2017), and correlate with energy consumption in cortical tissues (Herweg et al., 2016). Based on our experiments, such features offer a supplemental layer of information that could enrich traditional PSD features in classifying mental states and tasks, thus improving the robustness of active BCI systems. In the following subsections, we postulate the underpinnings of these new features and their complementary roles to PSDs.

3.4.1 Beta Band Analysis

The beta frequency sub-band, which serves numerous roles depending on its location and context in the brain (Weiss et al., 2012; Freeman et al., 2016), is dominantly involved in long-term memory and stimuli processes (Klimesch, 1999; Harmony et al., 1996). It facilitates the binding of temporally separated information into meaningful entities and aids in maintaining task-specific cognitive processes over extended periods (Weiss et al., 2012). Figure 3.13 illustrates topoplots that depict the spatial distribution of the prestige scores for relevant PSD features associated with the beta band. A comparative examination of the topoplots for the FACE and ROT tasks revealed analogous patterns, with both demonstrating bilateral frontotemporal patterns in the beta band.

A similar bilateral frontal pattern is seen in the beta–mbeta band in the AMP topoplots in Figure 3.9. Additionally, the AMP topoplots unveiled noteworthy patterns in the parieto-occipital-temporal region for the beta–mdelta and beta–mtheta bands. Beta activity modulated by the lower delta and theta bands was disseminated across the scalp, while the distribution of faster beta dynamics, specifically beta–malpha and beta–mbeta, was inclined towards the frontal area. The observation of slow temporal beta activity dynamics in the occipital-parietal area could suggest top-down control via the slow wave dynamics of specialized visual processing brain structures (Silberstein, 2006b; Weiss et al., 2012; Mizuhara et al., 2005; Plank et al., 2010). This activity is congruent with the visual nature of the FACE task. Conversely, fast beta activity dynamics were localized in the frontal area, implying the potential association with long-term memory and recall processes. It is well established that slow waves play a pivotal role in facilitating long-distance communication between distinct brain structures, with the interactions between the beta and theta bands contributing to the binding of neuronal information across both time and space (Mizuhara et al., 2007; Weiss et al., 2012).

In both the motor imagery (MI) and navigation (NAV) tasks, there was a notable presence of activity in the motor cortex, emphasizing their shared reliance on motor functions. For the MI task, the literature has typically reported amplitude changes in the mu band (7.5 Hz to 12.5 Hz) and beta band oscillations in the motor cortex (Han et al., 2022b; Xu et al., 2019), although this is not evidenced in the PSD topoplots presented in Figure 3.13. Nevertheless, this typical MI beta activity can be observed in the AMP topoplots in Figure 3.9. Here, beta activity in the MI task could be delineated into beta–mtheta and beta–mbeta AM bands, suggesting a role for beta in maintaining long-term motor action.

For the NAV task, a slight similarity was discerned between the distributions of the beta1 PSD and corresponding AMP topoplots. This resemblance unveiled insights into the multifarious nature of beta band activity, hinting at processes such as the recall of familiar memories and the long-term binding of information. In particular, the beta–mdelta and beta–mbeta bands in the AMP topoplot exhibited relevant bilateral frontotemporal and occipital patterns. We hypothesized that beta–mdelta activity in frontotemporal areas was indicative of processes related to recalling familiar

memories, possibly due to the involvement of the limbic system (Mizuhara et al., 2005; Alahmari, 2021; Mizuhara et al., 2004, 2007; Weiss et al., 2012). This system is a well-known generator of delta band oscillations, with delta band activity from the medial temporal cortex being notably associated with assessing the familiarity of sensory stimuli (Norman et al., 2003; Herweg et al., 2016; Collins et al., 2018).

Further, beta–mbeta activity may be associated with the long-term temporal binding of information, a crucial aspect considering that the NAV task involved navigating through familiar terrain over extended durations. This band, depicting the fast temporal dynamics of beta oscillations in the prefrontal area, could reflect communication from the limbic system to the cortex, a mechanism that is integral to working and long-term memory processes (Weiss et al., 2012; Plank et al., 2010; Mizuhara et al., 2007). In addition, beta–mtheta activity revealed an exclusive pattern in the left cortical hemisphere, potentially related to memory restitution.

In both the ROT and SING tasks, a general agreement between AMP and PSD was observed, with the presence of beta–mbeta activity in the motor cortex aligning with the necessity for advanced visuomotor functions in ROT and the long-term maintenance of specific processes in SING (Mizuhara et al., 2005; Weiss et al., 2012). These observations collectively highlighted the consistent binding role of beta–mbeta activity across varied tasks.

In the PSD topoplots in Figure 3.13, relevant activity in the beta1 band was observed in the parietal and motor cortices during the WORD task. This pattern can be similarly observed in the AMP topoplots in Figure 3.9, within the beta–mdelta, beta–mtheta, and beta–mbeta bands. Notably, there was a diminished contribution from the anterior frontal region in the case of the beta–malpha band.

Following these observations, the AMP topoplots illustrated in Figure 3.9 underscored the significance of the motor cortex during the WORD task. This suggests the pivotal roles of motor functions in linguistic tasks (Weiss et al., 2012; Soltanlou et al., 2017). The presence of the beta–mbeta and beta–mtheta bands further accentuated the potential of fast beta band dynamics in binding large neuronal assemblies (Weiss et al., 2012; Anwar et al., 2016; Silberstein, 2006b).

3.4.2 Theta Band Analysis

As shown in Figure 3.11, the FACE task presented a relevant feature distribution in the occipital-parietal region and a partial presence in the frontal cortex. This pattern could be divided into two complementary patterns observed in the theta–mdelta and theta–mtheta bands in Figure 3.7. While the theta–mdelta band clearly represented most of the relevant activity located in the prefrontal, motor, and occipital cortices, the theta–mtheta band exhibited precise relevant activity in the occipital-parietal area. The theta band is known to be involved in memory retrieval (Plank et al., 2010; Mizuhara et al., 2004; Freeman et al., 2016; Herweg et al., 2016; Alahmari, 2021; Cebolla

et al., 2017; Klimesch, 1999) and the process of visual information encoding. This activity aligned with the requirements of the FACE task, which was a visual task necessitating memory retrieval.

For the MI task, the slow temporal dynamics of the theta band, represented by theta–mdelta, suggested modulated attention across time by the PFC. In contrast, faster theta power changes, represented by the theta–mtheta band, seemed mainly to contribute to the decoding of recalling visual information. In the MI task, the patterns observed across PSD and AMP, particularly in theta–mtheta band, supported the hypothesis of sensory feedback processing, providing a nuanced understanding of the reactivation of specialized sensory brain structures.

In the NAV task, both the PSD and AMP topoplots in Figures 3.7 and 3.11, respectively, showcase parietal and prefrontal activity, hinting at the activation of visual processing regions and working memory involvement, with theta oscillations likely reflecting a decoding mechanism for previously learned information (Silberstein, 2006b; Daume et al., 2017). Similarly, the ROT task presented theta patterns in the occipital-parietal regions that are associated with visual stimuli encoding, while frontal patterns in theta–mdelta band could be interpreted as reflecting problem-solving processes.

Despite the absence of prominent patterns in PSD for the SING task, the theta–mtheta activity in AMP revealed the involvement of the frontal and parietal regions, potentially indicating memorized information retrieval, maintaining the consistent hypothetical role of theta's involvement in information encoding (Herweg et al., 2016; Klimesch, 1999; Mukundan et al., 2017).

Regarding the WORD task, the AMP topoplots in Figure 3.7 provide nuanced insights into the theta band's temporal dynamics and reveal a left prefrontal cortex lateralization, aligning with the literature on hemisphere association with linguistic functions. Further, the importance of the motor cortex, as highlighted in the AMP topoplots, aligned with the literature regarding its involvement in linguistic tasks (Vukovic et al., 2017).

3.4.3 Alpha Band Analysis

By examining the FACE task in Figure 3.12, it can be seen that both the alpha1 and alpha2 bands exhibited relevant occipital-parietal spatial distributions, as well as left frontal distribution. In the AMP topoplots presented in Figure 3.8, such patterns are also identifiable; however, the alpha–mdelta band showed diffused relevant activity across the entire scalp, while the alpha–mtheta band distribution was focused in the frontal and left occipital areas. These findings suggest two levels of speed in the alpha power temporal dynamics: slow variation in alpha activity seemed to be related to global scope function, while faster temporal dynamics seemed to be related to specific functions, such as executive and visual processing. Alpha oscillations, known for their relation with inhibition (Sauseng et al., 2005; Mizuhara et al., 2005; Jensen et al., 2010), show modulation by slow waves in the delta band, indicating the possible involvement of the limbic system as a modulated attention process. We could hypothesize that remembering a familiar face requires the sustained inhibition

of new stimuli processing, as well as coordination between visually specialized brain structures (occipital) and specialized executive/emotion-related brain structures (frontal) (Sauseng et al., 2005).

Regarding the MI task, the mu band (7.5 to 12.5 Hz) is typically considered to be a relevant oscillation frequency within the motor cortex during motor imagery (Yu et al., 2022a; Molla et al., 2020). This pattern was also discernible in our feature analysis of the PSD topoplots in Figure 3.12, where we noted relevant activity for both the alpha1 (8 to 10 Hz) and alpha2 (10 to 12 Hz) bands in the motor cortex, coupled with observations of parietal-occipital activity for both bands. Upon contrasting this observed activity with that in the AMP topoplots, similar distributions of the relevant features were evident in the alpha–mdelta and alpha–mtheta bands. Specifically, the topoplot of alpha–mdelta band in Figure 3.8 illustrates pronounced and widespread activity in the motor cortex, suggesting that mu activity becomes more discernible when considering the slow temporal dynamics of alpha oscillations. We further hypothesized that the MI task necessitated the partial inactivity of the motor region as the movement was imagined and not executed, explaining the presence of slow modulated inhibition in the motor area. Furthermore, the alpha–mdelta band exhibited highly relevant activity in the parietal-occipital regions, potentially indicating the inhibition of visual stimuli (Freeman et al., 2016), analogous to observations made in the FACE task. The alpha–mtheta band displayed a subdued pattern in the parietal-occipital cortex, with the distribution being more centralized in the somatosensory cortex. This activity was noteworthy as it suggested the presence of some form of virtual sensory feedback accompanying the imagined motor activity.

For the ROT task, the PSD topoplots depicted in Figure 3.12 exhibit consistent patterns for the alpha1 and alpha2 bands, showcasing activity in the bilateral frontal and right occipital regions. Delving deeper into the AMP topoplots, as seen in Figure 3.8, a clear distinction arises between two brain areas: the alpha–mdelta band was concentrated in the right occipital area, while alpha–mtheta band was prominently active in the bilateral frontal regions. This differentiation implied that the alpha–mdelta band was notably associated with controlled attention in the visual cortex, a nuanced insight provided by the comprehensive temporal analysis inherent to AMP features. This discerned alpha activity in both frontal and occipital areas potentially reflected a dynamic shift in attention and modulated inhibition across time. This interpretation aligned coherently with the demands of the ROT task, which necessitated the processing of visual stimuli coupled with logical evaluation.

For the SING task, the alpha–mtheta band was notably relevant in the prefrontal cortex and left parietal cortex, as evidenced more clearly by AMP than PSD. The alpha–mdelta band presented a comparable, albeit more diffuse, cortical-frontal activity. Unlike the other tasks, SING did not primarily involve visual processing, explaining the absence of any significant occipital activity. However, the task could necessitate imagined visual constructs or advanced sensorial representation, implicating the somatosensory, motor, and prefrontal cortices. The pronounced presence of alpha–mdelta activity in the prefrontal cortex could signify the greater influence of sympathetic structures during song recollection.

Intriguingly, the SUB task exhibited distribution patterns analogous to those of the SING task. This similarity was characterized by pronounced prefrontal activity in both the alpha–mdelta and alpha–mtheta bands, along with a bilateral occipital-parietal pattern. This pattern is observable in the alpha1 and alpha2 bands in the PSD topoplots represented in Figure 3.12 and the alpha–mdelta and alpha–mtheta bands in the AMP topoplots depicted in Figure 3.8. These observed distributions suggested the potential reliance on working memory and visual cues in the SUB task (Herweg et al., 2016; Spüler et al., 2016; Soltanlou et al., 2017). Lastly, the AMP topoplots for the WORD task revealed a left asymmetry in the cortical distribution of relevant features, a characteristic only present in the alpha2 band in the PSD topoplots. This asymmetry aligned with reports in the existing scientific literature (Riès et al., 2016).

3.4.4 Delta Band Analysis

As shown in Figure 3.6, the delta band exhibited a uniform distribution of relevant features across the scalp in all tasks, illustrating its role in modulating various cognitive processes throughout the brain. Notably, in the FACE and ROT tasks, the increased relevance of delta activity in the bilateral frontotemporal and parietal-occipital regions was observed, emphasizing its pivotal role in modulating attention (Zarjam et al., 2012; Prada et al., 2014) and facilitating the integration and coordination of sensory information (Harmony et al., 1996). This temporal synchronization is especially crucial in tasks requiring coherent communication among different brain regions for structured cognitive task execution. In the MI, SING, and SUB tasks, a subtle yet noticeable relevance in the parietal-occipital regions underscored the delta band's versatility in contributing to functions like motor imagery, sensory processing, and working memory. The insights derived from analyzing the delta band AMP topoplots across tasks (Figure 3.6) underscored the delta band's fundamental role in attention modulation, the temporal binding of neurological activity, and sustaining cognitive processing.

3.4.5 Gamma Band Analysis

As can be seen in Figure 3.10, for the FACE task, the relevant gamma band activity in the somatosensory area and bilateral frontotemporal regions emphasized its role in the processing of sensory information associated with recalling previously learned stimuli. The rapid oscillations of the gamma band were indicative of localized neuronal activity (Silberstein, 2006b; Weiss et al., 2012; Jensen et al., 2010), making neurons more receptive to specific stimuli and thereby aiding in the retrieval of specific visual information (Norman et al., 2003; Mukundan et al., 2017; Freeman et al., 2016; Herweg et al., 2016). In the MI task, the prominence of the gamma band in the motor and premotor cortices was consistent with the localized activation of neuronal structures associated with imagined motor activity. This suggests that the gamma band is closely linked with tasks that

involve motor planning without actual movement. In the ROT task, all modulated gamma bands depicted in Figure 3.10 exhibited consistent distributions of relevant activity across a variety of cortical areas. The observed patterns of activity aligned with the multifaceted demands of the ROT task, which necessitated the concurrent engagement of abstract visual representation, advanced sensory processing, working memory, and executive functions. In both the SING and SUB tasks, the primary patterns in the somatosensory and parietal cortices marked the gamma band's significance in sensory processing, which is required in tasks in which sensorial patterns are reactivated, such as mental singing. Lastly, the WORD task displayed lateral patterns in the gamma–mdelta and gamma–mbeta bands in the left parietal cortex, with a shift towards the right parietal area in the gamma–mtheta, gamma–malpha, and gamma–mgamma bands. Such hemispheric specialization echoed with the previously observed patterns in the theta and alpha bands and further aligned with the well-established concept of hemisphere dominance in language processing (Riès et al., 2016).

3.4.6 Performance Interpretation

In light of the distinctive patterns observed across the different bands and mental tasks, we propose additional interpretations for some of the performance results. For the ROT task, unique distribution patterns were apparent in both the alpha and beta bands, depending on the temporal dynamics, alongside noticeable activity in the right motor cortex in the beta–mbeta band. These patterns, revealed by the AMP topoplots, offered additional insights beyond what PSDs could provide, thereby potentially explaining the clear differences in the accumulated prestige scores observed in Figure 3.5.

When comparing the MI task to the SING task, several similarities emerged, including the involvement of the alpha band in the motor cortex and parietal-occipital regions and the presence of beta band activity in the motor and sensorimotor cortices, as well as frontotemporal areas. These similarities could account for the low kappa score observed for the MI-SING mental task pair in Figure 3.3. Lastly, the SUB task demonstrated clear similarities in both the PSD and AMP topoplots for the alpha and beta bands and comparable occipital activity in the theta band. These similarities in the distributions of both feature types could account for the small differences in prestige scores observed in Figure 3.5.

In conclusion, distinguishing between the band amplitude dynamics in slow and fast components significantly enhanced our understanding of the roles of such bands. This was particularly crucial as slow oscillations are typically associated with long-distance communication between distinct brain regions, while fast oscillations correspond to intensive neurological activity. While our analysis provided an initial step towards understanding the neural oscillations and regional distributions underlying different tasks, a complete picture of brain dynamics is yet to emerge. Further investigations into functional connectivity and synchronization between different brain areas during tasks will provide more insights into the complex brain networks involved in mental processes.

Overall, our findings highlight the potential of AM features as promising tools for uncovering task-related changes across different frequencies and brain regions. By reflecting fundamental neurological mechanisms, such as inter-areal communication and top-down control, AM features could potentially enrich our understanding of the complexities of brain activity. These findings underscore the need to incorporate and investigate AM features in future BCI research.

3.5 Conclusion

In this chapter, we proposed a new feature set for active BCI based on the amplitude modulation dynamics of different EEG sub-bands. Via extensive experimentation, we showed the benefits of the proposed features, as well as their complementarity to conventional power spectral features. An in-depth discussion was provided to explore the complex cognitive mechanisms being measured by the new features and conjecture their roles in improving BCI accuracy for different mental tasks. As for future work, we wish to explore the use of the proposed features for adaptive BCI, where the mental states of users can be tracked in real time (e.g., fatigue, frustration) to adjust active BCI classification. Such cognitive states are known to affect active BCI accuracy and may be a major limiting factor in BCI use in neurorehabilitation applications (Myrden et al., 2015; Hougaard et al., 2021; Évain et al., 2016).

4 ADAPTIVE FILTERING AND AMPLITUDE MODULATION FEATURES FOR MENTAL WORKLOAD ASSESSMENT FOR AMBULATORY USERS

Preamble

This chapter is compiled from material extracted from (Rosanne et al., 2021).

4.1 Introduction

Many professions, such as first responders (firemen, policemen, paramedics) and pilots, are often faced with cognitive challenges, including information overload, multitasking, interruptions, and fatigue. In many cases, these individuals are also exposed to a combination of physical and mental factors that further contribute to a high Mental workload (MW), thus resulting in increased chances of errors, which could be life-threatening. Therefore, MW monitoring has gained popularity in recent years.

It is difficult for subjective and behavioral assessment methods to provide real-time measures of MW; thus, they have limited application in closed-loop systems to improve task performance. Therefore, unobtrusive neuronal and physiological measures such as EEGs are considered viable alternatives. Previous research has demonstrated the effectiveness of EEG-based MW assessments in controlled environments, such as pilots and drivers, where participants are largely stationary.

Despite progress in wearable EEG technology, the presence of motion artifacts further exacerbated by the sensitivity of dry electrodes remains a significant challenge. Moreover, existing EEG enhancement algorithms, designed mainly to remove ocular and muscle artifacts, fall short in scenarios involving highly ambulatory users. To overcome this limitation, in this Chapter, we propose the use of an adaptive filter to remove movement-specific motion artifacts from mobile EEG data. Accelerometry signals measured from the participants' torsos were used as reference signals for the adaptive filter. The algorithm was tested on a database collected in-house from 48 participants while they performed the Multi-Attribute Task Battery - II (Santiago-Espada et al., 2011) under two workload conditions (low and high) and two Physical activity (PA) types (stationary bike and treadmill), each at three activity levels (none, medium, and high).

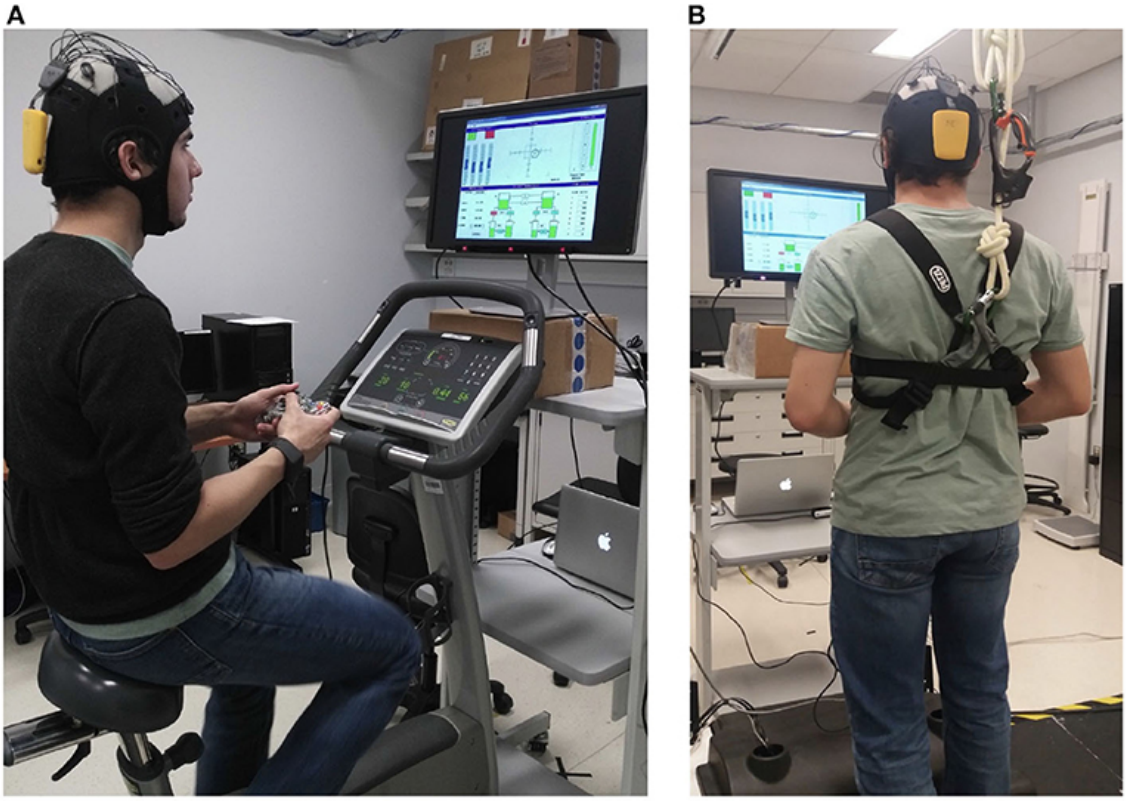

Figure 4.1 : Participant using a stationary bike (A) or a treadmill with safety harness (B) during the experiment. The harness ensures participant safety while allowing free movement.

4.2 Materials and Methods

4.2.1 Data collection

Data was collected from 48 participants (23 females, 27.4 $\pm$ 6.6 year old), of which 26 a stationary bike as illustrated in Figure 4.1A and 22 utilized a treadmill during the experiment. Participants using the treadmill were asked to wear a safety harness around their chest in order to avoid falls as shown in Figure 4.1B. The experimental protocol was approved by the Ethics Boards at INRS and Université Laval, participants provided written consent, and were monetarily compensated for their time.

The experimental protocol comprised two MW levels (low/high) elicited through the MATB-II software, which has participants executing three simultaneous tasks: system monitoring, tracking, and resource management, as presented in Figure 4.2. Low and high MW settings were implemented based on changing the difficulty levels for each of the three tasks. As an example, a low MW task was composed by “easy” versions of the three tasks. Participants used an Xbox 360 joystick to interact with the MATB-II interface.

While executing MATB-II, subjects were asked to either bike or walk/jog on a treadmill at three levels of physical activity (PA): no movement, medium (treadmill: 3 km/h, bike: 50 rpm), and high

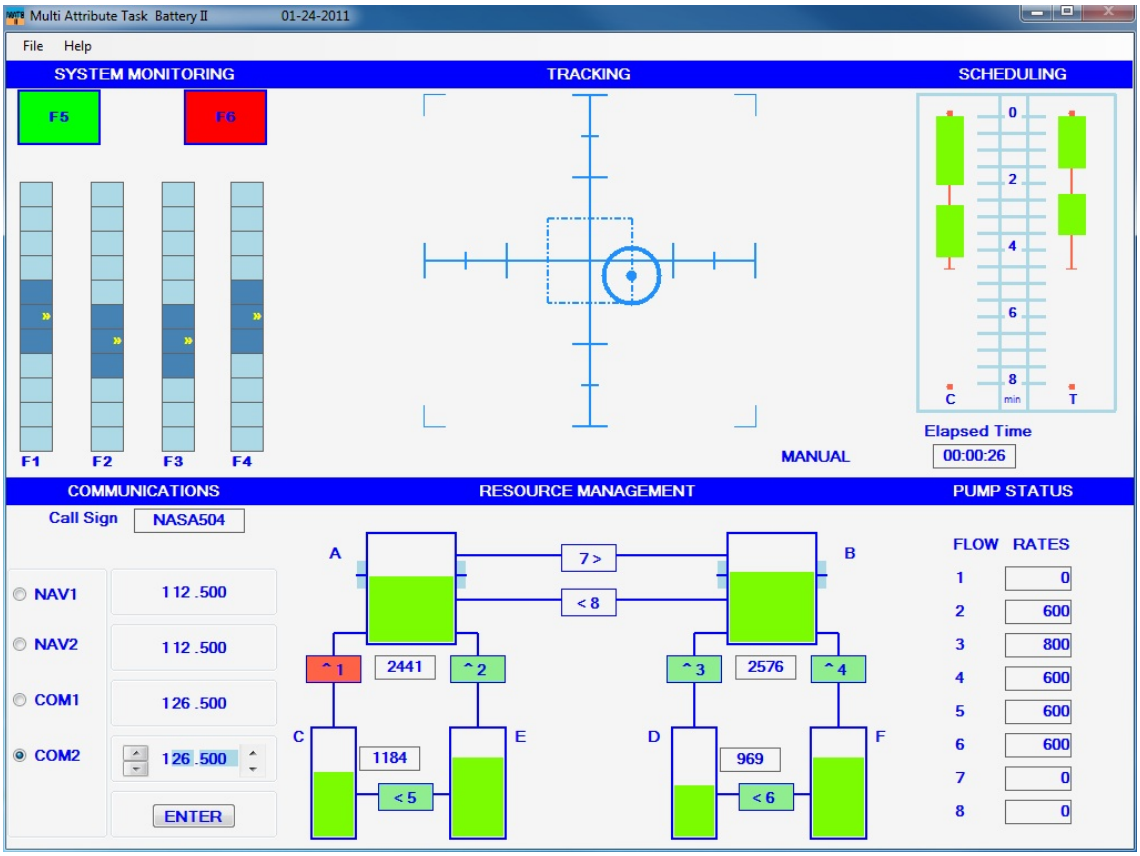

Figure 4.2 : Graphical interface of the MATB-II software used to modulate high and low MW levels

(treadmill: 5 km/h, bike: 70 rpm). In total, six combinations of MW and physical activity were tested. The experiment was then split into six sessions, each one corresponding to one of the six combinations described above, counterbalanced to avoid ordering effects. Each session took 10 minutes to run and was systematically followed by a 5-minute break. Before every session, two baseline periods were recorded. The first corresponded to one minute without task nor physical activity. The second corresponded to one minute with only physical activity at the same level to be executed in the upcoming session. At the end of the experiment, each subject was asked to fill the NASA-TLX questionnaire (Hart et al., 1988) to subjectively evaluate their perceived workload levels, as well as the reported their fatigue levels using the Borg scale (Borg, 1998).

EEG data was acquired from the participants using the Neurolectrics Enobio 8-channel portable headset with the following channel locations according to the international 10-20 system: Fp1, Fp2, AF7, AF8, T9, T10, P3, P4 (see Fig. 4.3). Signals were collected at a sampling rate 500 Hz and were later downsampled to 250 Hz. Two virtual inter-hemispheric bipolar signals were also computed, namely Fp1-Fp2 and P3-P4. Movement activity was also recorded with a sampling rate of 50 Hz using the embedded accelerometer available in the Zephir Bioharness wearable device, which was placed on the chest of each subject. Accelerometry data was upsampled to 250 Hz to coincide with the EEG data. The interested reader is referred to (Albuquerque et al., 2020) for more details about the database.

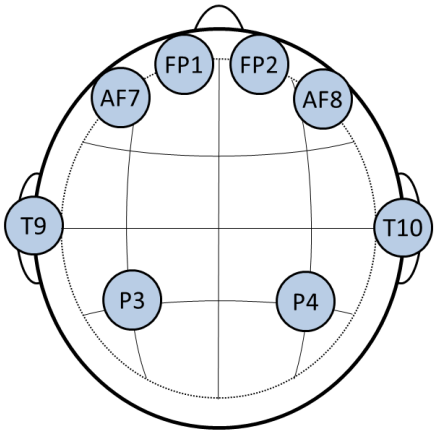

Figure 4.3 : Electrode placement using the international 10-20 system.

4.2.2 Movement artifacts

To illustrate the effects of movement, particularly in the walking/jogging conditions, Fig. 4.4 depicts the average spectral representation of each of the eight EEG channels, as well as that of the accelerometer signals (bottom plot) during ten seconds of the high physical activity condition. Here, the accelerometer signal corresponds to a L2-normalization of the accelerometer x, y, and z axes. As can be seen, particularly for the frequency range below 10 Hz, there is a significant effect from gait/movement on the EEG spectra, something previously reported in the literature (Nathan et al., 2016; Zhang et al., 2014c). As movement artifacts are known to be detrimental to EEG quality (Gao et al., 2010; McMenamin et al., 2011), this has motivated the proposal of an adaptive filter using the accelerometer signal as a reference signal.

Movement artifacts observed in EEG signals can be caused either by a relative movement between the skin and the electrode (Burbank et al., 1978) or by a change in electrical potential when the skin stretches and contracts during movement (de Talhouet et al., 1996; Kearney et al., 2007). Movement artifacts have been reported to span spectral content between 0.11-20 Hz (Bouten et al., 1997), thus overlap with frequency bands relevant for mental workload monitoring (Mak et al., 2013). Conventional EEG enhancement algorithms, traditionally developed for ocular and muscle artifacts (Urigüen et al., 2015; Zou et al., 2019; Mucarquer et al., 2019), have been shown to help with ambulatory users. For example, in (Gwin et al., 2010), ICA and component-based template regression was used to remove gait movement artifacts from EEG event related potentials. ICA-based decomposition was also used to remove head movements in (Onikura et al., 2015).

Notwithstanding, these conventional solutions have been shown to interfere with MW assessment (Rosanne et al., 2019b). Moreover, ICA-based enhancement methods typically rely on human intervention to remove artifactual components, thus have limited use in real-time applications. Adaptive filtering, in turn, has been used to reduce head movement artifacts (Mihajlović et al., 2014) and simulated random noise in EEGs (Raya et al., 2002). To the best of our knowledge, however,

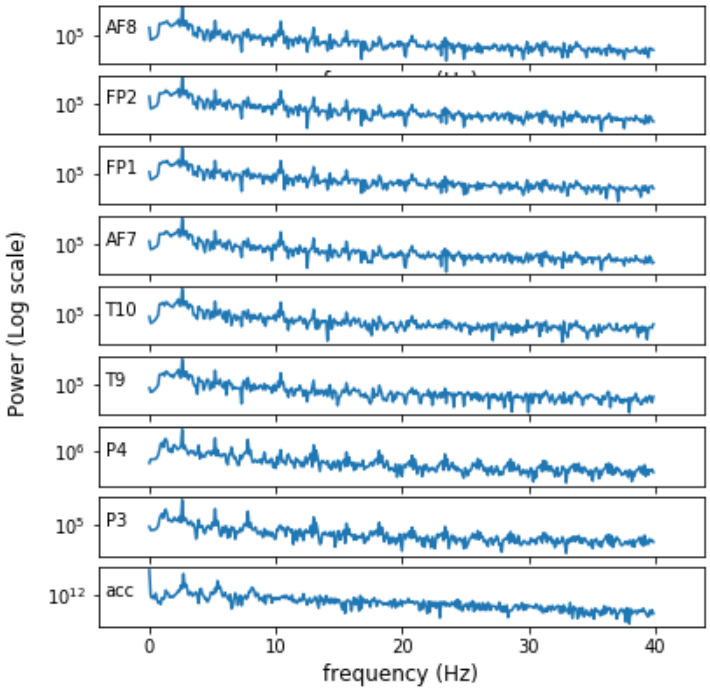

Figure 4.4 : Average spectral representation of the eight EEG signals and the accelerometer signal over 10 seconds of recording for the low MW and high PA condition.

the use of adaptive filtering, with or without combined "blind" filtering approaches (i.e., that do not rely on human intervention), has yet to be quantified for EEG-based mental workload monitoring of ambulant users. We aim to fill this gap.

4.2.3 Adaptive Filtering

Figure 4.5 depicts a block diagram of the adaptive filtering scheme explored herein. Signal $x(n)$ corresponds to the accelerometer signal, whereas $s(n)$ corresponds to the neuronal activity signal. From the accelerometer signal, movement artifacts are modeled and represent $y(n)$. When added to the neuronal activity signal $s(n)$, the output represents the noisy EEG signal $d(n) = s(n) + y(n)$ recorded during physical activity. The goal of the adaptive filter is to find the optimal distortion weights $\hat{W}(n)$ from the accelerometer signal $x(n)$ to best estimate the movement artifacts via $\hat{y}(n)$ and remove their effects from the noisy EEG signal via $e(n) = d(n) - \hat{y}(n)$.

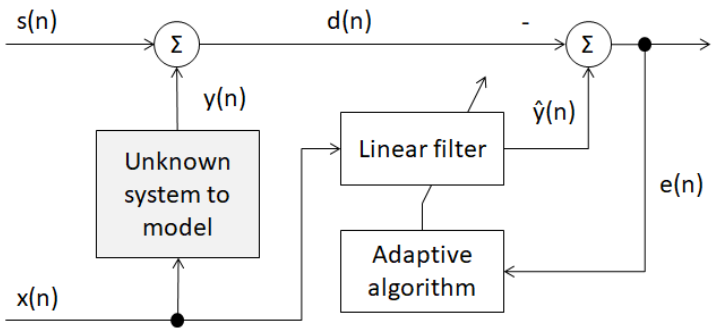

Figure 4.5 : Block diagram of proposed adaptive filter.

More specifically:

$$\hat{y}(n) = \hat{W}(n) * x(n), \tag{4.1}$$

and 4.2.

$$\begin{aligned} e(n) &= d(n) - \hat{y}(n), \\ e(n) &= y(n) + s(n) - \hat{y}(n). \end{aligned} \tag{4.2}$$

The filter weights are found using the normalized least mean squares (NLMS) procedure (Diniz et al., 1997) for loss function $C(n)$ using the steepest descent algorithm, i.e.:

$$\begin{aligned} \nabla_{\hat{w}^H} C(n) &= \nabla_{\hat{w}^H} \mathbb{E}\left[e(n)^2\right] \\ &= \mathbb{E}\left[2e(n)\nabla_{\hat{w}^H} e(n)\right] \\ &= -2\mathbb{E}\left[x(n)e(n)\right], \end{aligned} \tag{4.3}$$

where ∇ is the gradient operator and $\mathbb{E}[\cdot]$ the expected value. This leads to the following update rule:

$$\hat{w}(n+1) = \hat{w}(n) + \mu\mathbb{E}[x(n)e(n)], \tag{4.4}$$

where $\mu/2$ is the step size.

We approximate the last term using the single-sample unbiased estimator $\mathbb{E}[x(n)e(n)] = \frac{x(n)e(n)}{|x(n)|^2}$, thus simplifying (4.4) to:

$$\hat{w}(n+1) = \hat{w}(n) + \frac{\mu x(n)e(n)}{|x(n)|^2}. \tag{4.5}$$

Here, a filter length of 500 samples was used, corresponding to a signal duration of two seconds. Figure 4.6 depicts the noisy and enhanced EEG signals, as well as the accelerometry signal, to visually showcase the movement effects on the EEG signal and the effectiveness of the adaptive filter.

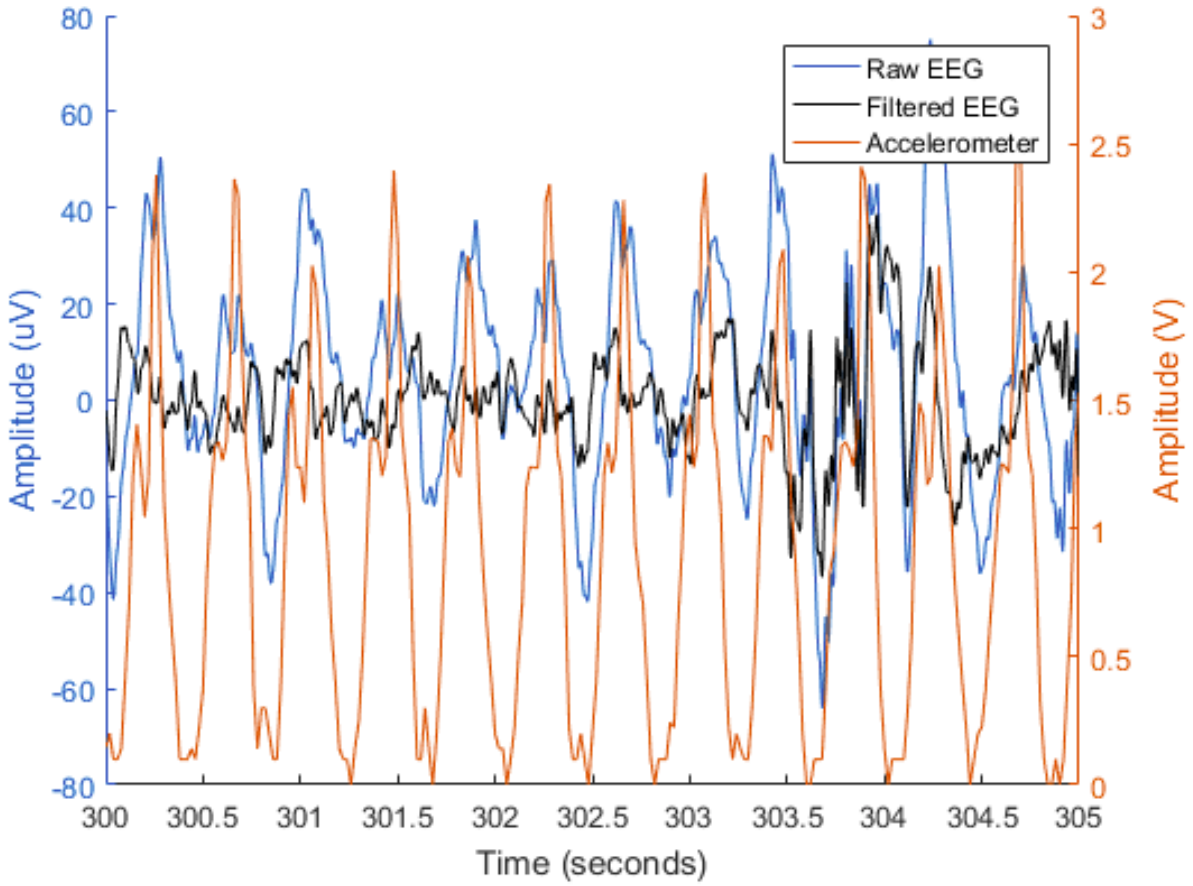

Figure 4.6 : Time representation of a 5-second EEG segment from electrode AF8 before (blue) and after (black) adaptive filtering. The L2-normalization of the x, y and z accelerometry axes is represented in orange.

4.2.4 Benchmark automated artifact removal algorithms

Here, four AAR algorithms described in section 2.3.2.2 in Chapter 2 are used as benchmarks: ASR, ADJUST, wICA and HAPPE. They are tested either alone or in combination with each other: ASR+wICA and ASR+ADJUST. Moreover, the proposed adaptive filter was also used in combination with the benchmark algorithms to explore their combined effectiveness. Henceforth, results represented as 'Raw' assume no enhancement, 'Adaptive filter (AF)' when only the adaptive filter has been applied, and methods combined with AF will be preceded by the prefix 'AF_'. These algorithms are applied to the entire signals prior to epoching.

4.2.5 Feature extraction

Prior to feature extraction, EEG signals were first filtered with a FIR band-pass filter in the range 1-45 Hz. The following feature sets were extracted from the raw and enhanced signals:

4.2.5.1 Power Spectral Density

PSD features were computed from nine frequency bands, namely: delta (1-4 Hz), theta (4-8 Hz), alpha (8-12 Hz), beta (12-30 Hz), low gamma (30-45 Hz), delta to beta (1-30 Hz), theta to beta (4-30 Hz), low alpha (8-10 Hz) and high alpha (10-12 Hz). The relative power of each of these bands was calculated by normalizing per-band values by the full-band power. A total of 90 PSD features were extracted. Numerous studies have reported the usefulness of such features for mental workload assessment (Craik et al., 2019; Liu et al., 2017; Zhang et al., 2019).

4.2.5.2 Amplitude Modulation

AM feature have been extracted using the implementation presented in Chapter 2 in section 2.3.4. A total of 140 features were extracted that provide robustness against movement artifacts, as described in (Albuquerque et al., 2018).

4.2.5.3 Phase and Magnitude Spectral Coherence

Phase and Magnitude Spectral Coherence (PMSC) features are useful for measuring connectivity between cortical regions as these techniques measure co-variance of the phase and magnitude between two signals. The interested reader is referred to (Aoki et al., 1999) for more details on PMSC computation. PMSC is computed for two pairs of electrodes, namely FP1-FP2 and P3-P4 for each 5 sub-bands (delta, theta, alpha, beta, gamma). A total of 20 PMSC features were extracted. These features are motivated from (Zhang et al., 2014a; Zarjam et al., 2015) that have shown their usefulness in mental workload assessment.

4.2.5.4 Phase and Magnitude Spectral Coherence of Amplitude Modulation Features (PMSC-AM)

PMSC-AM extends the capacity of PMSC features to amplitude modulations. These features were recently proposed for affective state monitoring and showed useful for arousal and valence prediction (Clerico et al., 2015, 2018). They are explored here for the first time as correlates of mental workload. These features are based on the modulated signals of each band which make a total of fourteen signals per channels (see (Clerico et al., 2018) for more details). After splitting the signals into epochs, the magnitude spectral coherence and phase coherence is then computed for the FP1-FP2 and P3-P4 channel pairs only. A total of 56 features were extracted.

4.2.6 Feature selection and ranking

Feature selection is a common step in classification tasks to remove redundant (Ding et al., 2005) or irrelevant features (Blum et al., 1997) and for dimensionality reduction (Fan et al., 2008) to improve classification performance. In this study, we rely on the so-called Minimum redundancy maximum relevance (mRMR) filter method (Peng et al., 2005) which not only finds the most relevant features for the task at hand, but removes features with high mutual information, thus minimizing redundancy. The algorithm has been shown to be extremely useful for EEG-based affective state assessment (e.g., (Clerico et al., 2018; Cassani et al., 2014)). In addition to feature selection, we further rank the importance of the top-features using a wrapper-based method. It is important to emphasize that feature selection/ranking is not crucial here, given the number of features explored. Nonetheless, we use it to obtain insights into the neuronal patterns related to mental workload during activity and how such patterns may be affected by movement artifacts.

4.2.7 Classification and hyperparameter tuning

We are interested in exploring the effects of movement artifacts and, consequently, EEG enhancement on mental workload assessment. Here, we assume the binary problem of classifying low versus high mental workload levels. Two conventional classifiers are explored, namely Random forest (RF) (Qi, 2012) and SVM. A repeated (10 times) 10-fold cross validation testing setup is used.

For hyperparameter tuning, the cross-validation grid search available in the scikit-learn library (Pedregosa et al., 2011a) was explored. This approach, however, yielded a high number of trees (around 500) for the RF classifier, as compared to the amount of available data (Oshiro et al., 2012). As an alternative, we empirically fixed tree depth to 8 and stopped adding trees once the evolution of the area under the curve - receiver operating characteristics (AUC-ROC) became constant across out-of-bag conditions. Next, a similar strategy was used to optimize tree depth and we fixed the number of trees to the value found in the previous analysis. In both cases, a stratified 5-fold cross-validation procedure was used with all subjects to ensure reliable generalization performance.

Figure 4.7 shows the evolution of AUC-ROC scores for the training and out-of-bag (oob) sets as a function of number of trees. When building each random tree in the forest, not all features and samples of the dataset are used. Instead, a small randomly-selected set called the bootstrap bag is used to build a single tree; this bag is different for each tree. The oob set, thus, corresponds to the remaining unused samples. The accuracy with the oob set is shown to stabilize at around 100 trees. Moreover, Figure 4.8 depicts accuracy as a function of tree depth. As can be seen, for the out-of-bag set the accuracy plateaus at around a depth of 10. Henceforth, these values are used in our experiments.

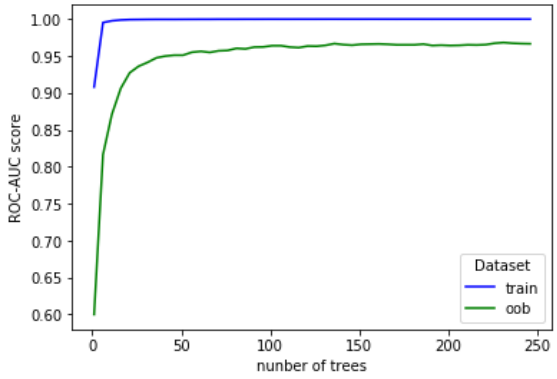

Figure 4.7 : Evolution of AUC-ROC for training and out-of-bag (oob) sets as a function of number of trees.

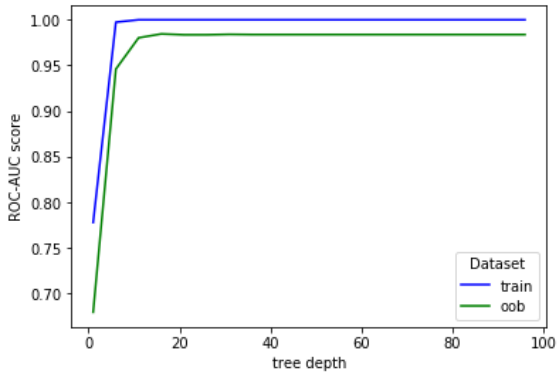

Figure 4.8 : Evolution of AUC-ROC for training and out-of-bag (oob) sets as a function of tree depth.

Figure 4.9 presents accuracy values obtained during a grid search to find the optimal C and gamma values of the support vector classifier. It can be seen that the best accuracy is reached with $C = 310$ and $\gamma = 0.001$ with a Radial Basis Function kernel; these values are used henceforth.

4.3 Result and discussion

4.3.1 Classification performance

4.3.1.1 Ablation study

In order to estimate the impact of the adaptive filter on EEG enhancement, mental workload classification accuracy is reported with and without its use. Tables 4.1 and 4.2 present classification accuracy values for the RF and SVM classifiers, respectively. While each column corresponds to a tested benchmark enhancement algorithm, with or without (termed “Base”) adaptive filtering, each row corresponds to a specific feature set used for classification in the low and high Physical activity (PA) conditions. Row labelled “All” indicates fusion of all features. Results reported are the average of a 10-fold cross-validation test setup repeated ten times by shuffling the partitions

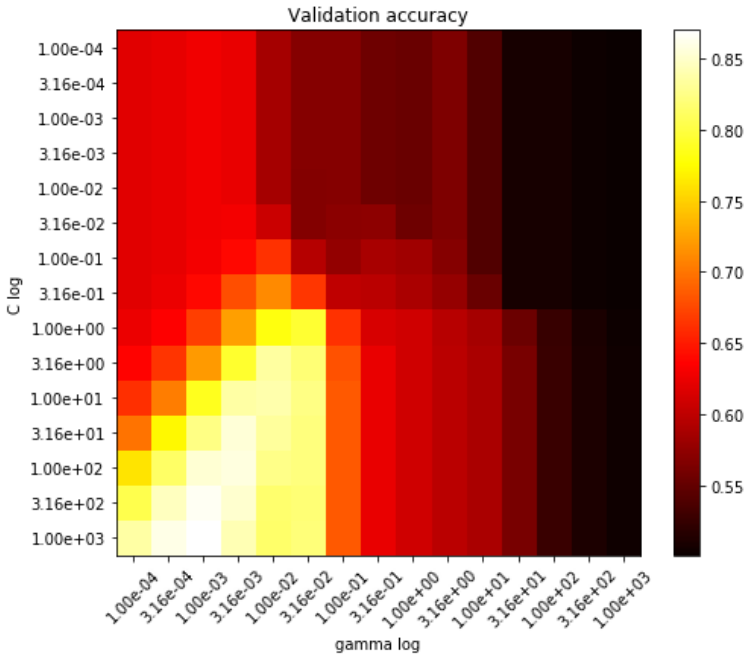

Figure 4.9 : Accuracy hyperparameter grid search for the SVM classifier.

Tableau 4.1 : RF mental workload classification accuracy for different feature and enhancement algorithm configurations.

Random Forest		Raw		ASR		ADJUST		HAPPE		ASR+ADJUST		ASR+wICA		wICA	
		Base	AF	Base	AF	Base	AF	Base	AF	Base	AF	Base	AF	Base	AF
PSD	low PA	86.27	85.59‡	88.60	89.71‡	89.23	88.89	86.25	92.96‡	93.68	90.37‡	92.34	92.73	88.66	90.87‡
	high PA	87.15	85.05‡	89.55	89.89	89.92	89.76	89.57	90.91‡	89.14	91.80‡	94.13	94.61‡	89.14	91.69‡
AM	low PA	83.91	84.28†	84.78	86.48‡	88.12	88.26	83.90	91.93‡	91.94	87.28‡	87.26	89.47‡	84.83	87.88‡
	high PA	83.83	84.77‡	86.84	89.21‡	88.27	89.08‡	87.33	89.36‡	87.62	89.13‡	90.91	92.60‡	85.59	89.27‡
PMSC	low PA	84.23	85.76‡	82.67	82.66	90.05	92.26‡	87.85	95.15‡	89.38	87.08‡	84.33	82.44‡	84.66	86.03‡
	high PA	82.07	82.78‡	80.74	79.95‡	86.79	88.08‡	89.80	90.51‡	89.90	84.84‡	82.44	80.46‡	81.31	83.81‡
PMSC-AM	low PA	65.79	70.81‡	67.89	68.32	66.62	71.92‡	73.84	78.34‡	67.77	64.99‡	70.18	67.48‡	65.56	70.19‡
	high PA	67.90	74.10‡	67.57	67.66	69.59	70.56‡	71.46	75.71†	68.46	64.78‡	67.75	67.05†	68.59	72.09‡
All	low PA	89.17	95.03‡	90.23	94.32‡	92.55	95.65‡	93.24	97.90‡	96.21	93.56‡	93.61	95.86‡	90.49	96.22‡
	high PA	88.89	91.20‡	90.77	93.39‡	94.22	95.36‡	94.54	97.89‡	93.36	93.54	94.95	95.19	90.20	93.97‡

Tableau 4.2 : SVM mental workload classification accuracy for different feature and enhancement algorithm configurations.

SVM		Raw		ASR		ADJUST		HAPPE		ASR+ADJUST		ASR+wICA		wICA	
		Base	AF	Base	AF	Base	AF	Base	AF	Base	AF	Base	AF	Base	AF
PSD	low PA	59.31	59.35	61.72	60.16‡	64.08	67.16‡	67.98	73.57‡	70.72	71.37	66.66	63.13‡	59.99	59.82
	high PA	64.22	66.56‡	65.78	67.81‡	68.40	70.00‡	67.56	73.58‡	67.61	71.91‡	69.29	70.96‡	64.79	70.07‡
AM	low PA	56.75	59.03‡	58.37	61.05‡	61.63	69.18‡	62.69	73.39‡	69.48	68.65†	60.74	62.74‡	56.15	59.63‡
	high PA	62.49	65.35‡	66.67	64.64‡	68.88	69.66‡	66.16	70.94‡	68.45	70.36‡	68.80	66.77‡	63.27	67.22‡
PMSC	low PA	60.25	72.25‡	60.70	69.61‡	61.59	68.45‡	63.94	75.11‡	70.45	68.22‡	61.06	69.71‡	61.07	73.27‡
	high PA	60.43	71.86‡	65.79	68.48‡	67.97	69.62‡	70.80	72.98‡	72.09	67.64‡	66.35	69.04‡	60.05	71.34‡
PMSC-AM	low PA	56.05	62.53‡	56.57	58.89‡	56.03	62.04‡	59.83	65.23‡	59.37	58.68†	56.60	58.04‡	55.36	59.79‡
	high PA	59.35	65.37‡	59.63	60.29	61.36	61.69	59.11	63.43‡	58.49	58.61	59.96	62.62‡	60.10	64.21‡
All	low PA	64.94	78.34‡	66.59	73.54‡	73.28	80.25‡	78.88	87.49‡	76.60	79.58‡	68.22	75.37‡	66.87	77.39‡
	high PA	71.37	81.09‡	73.31	76.26‡	78.33	81.03‡	79.38	86.93‡	78.94	77.88‡	74.42	77.72‡	71.22	81.86‡

each time. Whenever the achieved results with the adaptive filter were significantly different (based on a paired t-test) than without, results are indicated with superscripts "†" and "‡" for $p \leq 0.05$ and $p \leq 0.01$, respectively.

As can be seen from the Tables 4.1 and 4.2, the adaptive filter significantly improved accuracy for most tested configurations, particularly for features derived from the amplitude modulation analysis, as well as for the high physical activity conditions in which movement artifacts are most pronounced. Overall, the RF classifier consistently outperformed the SVM.

For PSD based features, the best results were achieved with a combination of ASR and ADJUST methods (93.68%), followed closely by HAPPE and AF (92.96%) for low physical activity conditions and the ASR-wICA-AF combination for high PA conditions. Similar accuracy values were achieved for the AM and PMSC feature sets. The PMSC-AM features, on the other hand, resulted in the lowest values, thus suggesting that they may not be useful for mental workload assessment when used alone. Overall, fusion of the different feature sets showed to result in the highest accuracy for both RF and SVM classifiers, thus suggesting their complementarity. The highest accuracy achieved was of 97.90% with the HAPPE-AF combination for both the high and low PA conditions. Such findings show that by combining all feature sets with the proposed adaptive filtering and HAPPE enhancement methods, the same mental workload measurement accuracy can be achieved despite physical activity levels.

4.3.1.2 Effect of number of features

The results reported in Tables 4.1 and 4.2 relied on all extracted features. In order to investigate the impact of feature dimensionality on overall accuracy, Figure 4.10 depicts the achieved accuracy as a function of number of features used, in decreasing importance, as ranked by mRMR. Here, the AF-HAPPE enhancement combination is used with the RF classifier and the average accuracy over a single 10-fold cross-validation setup is used. For this comparison, default classifier parameters are used in order to gauge the effectiveness of the features per se, and not the classifier. As can be seen, sharp increases in accuracy are achieved with the first 60 features and then slight increases occur after 100 and then 200 features are considered. A small gap is seen for both low and high physical activity conditions once all 306 features are used. If feature dimensionality is of concern, the achieved results and the small gap between low and high PA conditions suggest that 236 features can be a good compromise (94% and 90%, low and high PA, respectively), followed by 111 features (91% and 87%, low and high PA, respectively). For comparison, with the top-60 features, accuracy of 84% and 88% are achieved, respectively.

4.3.2 Top-ranking features

To obtain insights from top-selected features, we performed an in-depth analysis of the top-60 features selected from the combined “All” feature set in the low and high physical activity conditions using both the raw data and the top-performing AF+HAPPE enhanced data; Table 4.3 lists these features.

Tableau 4.3 : Top-60 features for different Physical activity (PA) and signal processing conditions. Feature names are self explanatory and follow the feature-electrode notation; 'tab' corresponds to 4-30 Hz spectral subband power; 'dtab' to 1-30 Hz; 'phc' to phase coherence; and 'msc' to magnitude square coherence.

Raw		AF+HAPPE	
Low PA	High PA	Low PA	High PA
beta-malpha-P4	msc-beta-mtheta-FP1-FP2	gamma-mgamma-FP1-FP2	phc-beta-mdelta-FP1-FP2
alpha-mdelta-AF8	msc-delta-P3-P4	delta-P3-P4	gamma-mdelta-P4
tab-FP1	gamma-mdelta-T10	gamma-mbeta-P4	beta-mdelta-T9
alpha-AF8	alpha-mtheta-T10	alpha1-T9	gamma-mtheta-AF8
theta-mtheta-FP1	alpha-mdelta-FP1	beta-malpha-AF7	beta-mtheta-AF8
gamma-mdelta-P4	gamma-mtheta-FP2	theta-mtheta-T9	beta-mtheta-P4
gamma-mtheta-T10	beta-mdelta-AF7	gamma-mdelta-P4	gamma-mdelta-AF8
theta-mtheta-T9	beta-mtheta-P4	dtab-T10	theta-mtheta-P3-P4
theta-mtheta-FP1-FP2	beta-mdelta-FP1-FP2	beta-mtheta-AF7	tab-FP2
theta-mtheta-T10	beta-mdelta-T10	theta-P3-P4	gamma-malpha-FP1-FP2
alpha1-FP1-FP2	alpha-mtheta-AF8	delta-mdelta-FP1	alpha-T9
alpha-mtheta-P3	alpha-mdelta-P3	gamma-mtheta-FP2	gamma-mdelta-FP2
gamma-mtheta-FP2	msc-alpha-mdelta-FP1-FP2	gamma-mdelta-P3	beta-T9
gamma-mbeta-FP2	alpha-FP2	tab-T9	msc-gamma-mdelta-FP1-FP2
theta-mdelta-FP1-FP2	beta-malpha-P4	beta-mdelta-P3	beta-mdelta-FP2
alpha-mtheta-P3-P4	alpha-AF8	gamma-mdelta-FP2	alpha2-P4
gamma-malpha-P3	theta-mdelta-FP1-FP2	dtab-T9	dtab-P3
dtab-T9	alpha2-T10	theta-mtheta-FP1-FP2	gamma-mtheta-T10
beta-mbeta-P3-P4	theta-FP2	gamma-mbeta-AF8	beta-mtheta-FP2
tab-T9	tab-FP2	gamma-mdelta-FP1	gamma-P3
delta-mdelta-AF7	alpha2-T9	beta-P3	beta-mtheta-T9
phc-delta-mdelta-P3-P4	beta-mtheta-P3	gamma-mgamma-FP2	gamma-mtheta-FP2
gamma-mbeta-P4	gamma-malpha-P3-P4	theta-mdelta-FP1	gamma-mbeta-P3
beta-mbeta-T9	gamma-malpha-FP2	phc-beta-mtheta-P3-P4	gamma-FP1
beta-mbeta-P3	theta-T10	gamma-mgamma-P3	delta-AF8
dtab-AF7	beta-mdelta-P3-P4	theta-mtheta-P3	beta-malpha-FP1-FP2
gamma-malpha-FP2	dtab-T9	gamma-mgamma-FP1	gamma-mtheta-FP1-FP2
theta-T10	beta-T10	beta-mtheta-FP1	gamma-mtheta-P4
gamma-malpha-T9	tab-T10	gamma-mgamma-P3-P4	delta-mdelta-FP1
theta-mtheta-AF8	gamma-T9	gamma-mbeta-FP1-FP2	beta-malpha-AF7
gamma-mtheta-P3	theta-mtheta-P3	beta-malpha-P3	theta-mdelta-P4
gamma-T10	dtab-FP1	gamma-mtheta-FP1	msc-beta-mtheta-FP1-FP2
delta-AF7	beta-P3	alpha2-T9	delta-mdelta-AF8
delta-mdelta-P3-P4	msc-gamma-FP1-FP2	beta-mdelta-P4	tab-FP1-FP2
alpha-mtheta-T10	msc-alpha-mtheta-FP1-FP2	delta-mdelta-P4	beta-AF8
beta-mdelta-P3-P4	alpha-mtheta-FP2	delta-P4	beta-mtheta-P3
gamma-mtheta-P3-P4	alpha1-P3-P4	phc-theta-P3-P4	beta-P3-P4
beta-mdelta-P3	gamma-mdelta-P3-P4	gamma-mbeta-FP1	gamma-mdelta-T9
alpha-T10	delta-mdelta-P4	gamma-malpha-FP1-FP2	alpha1-T10
alpha2-P3-P4	gamma-P3	theta-mdelta-P3	delta-mdelta-FP2
theta-mdelta-P4	alpha1-T9	beta-malpha-P4	msc-beta-mbeta-FP1-FP2
beta-mtheta-P3-P4	beta-mtheta-P3-P4	beta-mtheta-P3-P4	beta-mdelta-P4
theta-mdelta-T10	alpha-mdelta-FP2	beta-mbeta-P4	alpha-T10
msc-beta-mdelta-P3-P4	gamma-T10	gamma-mtheta-FP1-FP2	gamma-mgamma-T9
phc-beta-P3-P4	beta-P3-P4	beta-mbeta-FP2	msc-delta-P3-P4
alpha-mdelta-P4	msc-beta-mdelta-FP1-FP2	gamma-malpha-FP1	msc-beta-malpha-FP1-FP2
gamma-FP1-FP2	delta-FP1-FP2	delta-mdelta-P3-P4	msc-gamma-mtheta-FP1-FP2
theta-P3-P4	msc-gamma-mtheta-FP1-FP2	gamma-mbeta-FP2	gamma-malpha-P3-P4
phc-delta-P3-P4	beta-P4	delta-FP1-FP2	gamma-malpha-T9
alpha1-P3-P4	tab-P4	gamma-mbeta-P3-P4	delta-mdelta-P4
beta-mdelta-T9	delta-T9	beta-mbeta-FP1-FP2	msc-delta-FP1-FP2
alpha1-T9	dtab-T10	gamma-T10	beta-mdelta-AF7
gamma-mdelta-P3-P4	alpha-mdelta-T10	gamma-mgamma-T10	beta-mbeta-P3-P4
theta-P4	msc-beta-FP1-FP2	gamma-mbeta-T10	gamma-mtheta-AF7
alpha2-P4	msc-theta-FP1-FP2	gamma-malpha-P3-P4	gamma-mtheta-P3-P4
dtab-P3	dtab-P4	beta-mdelta-P3-P4	gamma-mbeta-P3-P4
theta-FP2	delta-P3-P4	theta-mdelta-P3-P4	msc-theta-FP1-FP2
beta-FP2	tab-T9	alpha-mdelta-T9	beta-mtheta-AF7
alpha2-T9	msc-delta-FP1-FP2	dtab-FP1	msc-alpha-FP1-FP2
alpha-P3	beta-FP2	gamma-malpha-T10	phc-gamma-FP1-FP2

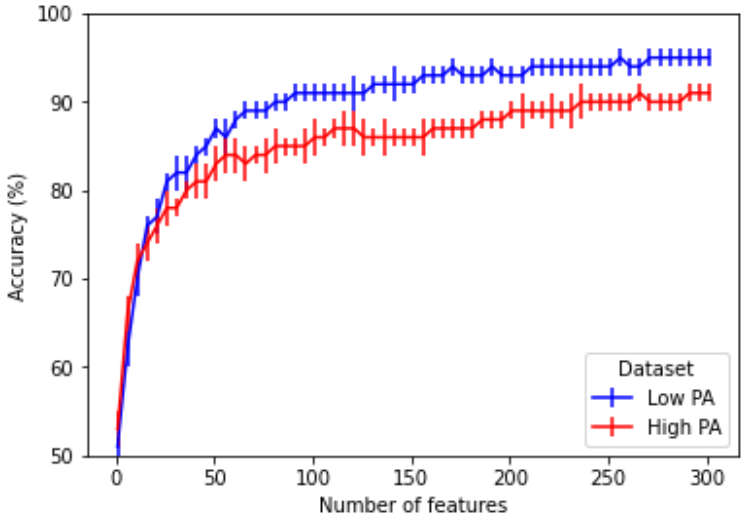

Figure 4.10 : Accuracy versus number of features for a RF classifier and a combined AF-HAPPE enhancement pipeline.

As can be seen, for all conditions tested, modulation spectral features resulted in the majority of the top 60 features. For example, for the high PA conditions without and with AF_HAPPE processing, they corresponded to 50% and 70% of the top features, respectively. This corroborates findings from (Albuquerque et al., 2018, 2019b; Clerico et al., 2018) that show the importance of such features for mental workload and affective state assessment, as well as their robustness to movement artifacts.

Coherence based measures, in turn, were the second top-performing features and appeared mostly in high PA conditions. They represented approximately 17% and 18% of the top features for the raw and enhanced conditions, respectively. Coherence measures have been linked movement and visual-motion discrimination and are indicative of the additional mental resources involved during physical activity (Cheron et al., 2016; Händel et al., 2009). The important coherence features were mostly extracted from the pre-frontal regions, which have been linked to mental workload and attention (Mandrick et al., 2013), while a few were extracted from parietal regions, thus suggesting some contribution of balance control also involved (Hülsdünker et al., 2015).

Regarding brain hemispheres, features from the right regions were selected slightly more often than the left hemisphere, particularly in high PA conditions. This corroborates previous work (Perennou et al., 1999) that has shown the existence of a right hemispheric dominance for postural control. Inter-hemispheric signals, in turn, corresponded to roughly 33% of the top features for all PA conditions. Within the top features, inter-hemispheric parietal features typically appeared in low PA conditions, whereas inter-hemispheric pre-frontal features appeared during high PA conditions. This suggests a shift in visuo-motor (Iacoboni et al., 2004) and attention (Vossel et al., 2016) aspects during low PA, to more complex motor behaviours and sensorimotor integration aspects with high PA (Geschwind et al., 1999). Overall, in the enhancement scenario, the parietal regions were responsible for the majority of the top features, followed closely by the pre-frontal cortex, for both low and high PA conditions. These results are in line with the classical mental workload literature

with non-ambulant users (Al-Shargie, 2019; Aoki et al., 1999; Käthner et al., 2014; Borghini et al., 2012; Holm et al., 2009; Mandrick et al., 2013), thus further showing the promise of the proposed adaptive filtering scheme.

Lastly, regarding EEG subband frequencies, as expected, adaptive filtering combined with HAPPE reduced the importance of features extracted from theta and alpha bands, as these have the highest overlap with the accelerometry data. It did, on the other hand, boost the importance of features extracted from the beta and gamma bands. It is well known that gamma is highly sensitive to muscle activity (Muthukumaraswamy, 2013) and HAPPE is known to remove such artifacts. With the proposed enhancement scheme, gamma features (and $\gamma - m\delta$) remained consistent between low and high PA conditions and covered aspects related to sensory motor integration (Sauseng et al., 2015; Aoki et al., 1999), attention (Sammer et al., 2007; Wang et al., 2017), and balance control (Sipp et al., 2013; Gwin et al., 2011). The importance of the beta band, in turn, has been observed in other studies during intense physical exercises (Rahman et al., 2019), anticipation in a decision making game (Cohen et al., 2009) and increment of cognitive control and attention (Kakkos et al., 2019).

4.4 Conclusion

This chapter has proposed the use of an adaptive filtering scheme to remove movement artifacts from EEG signals, combined with proposed amplitude modulation features, for robust mental workload assessment for ambulant users. Experimental results have shown that the proposed adaptive filtering scheme is best combined with HAPPE and can result in 97% mental workload prediction accuracy for both low and high physical activity conditions. Moreover, an in-depth analysis of the top-selected features have shown the importance of modulation spectral features for the task at hand, as well as the potential of the proposed enhancement solution at maintaining important discriminant information from the EEG for mental workload measurement, in particular those captured by gamma frequency band-based features.

5 EEG ENHANCEMENT FOR CYBERSICKNESS CHARACTERIZATION AND THE IMPORTANCE OF AMPLITUDE MODULATION FEATURES

5.1 Preamble

This chapter is compiled from material extracted from the manuscript published in (Rosanne et al., 2024).

5.2 Introduction

Virtual Reality (VR) has experienced significant growth in recent years due to advances in hardware technology and its increasing availability to the general public. This technology enables the creation of highly realistic and versatile environments at relatively low costs. Today, it is a widely adopted solution in various fields beyond entertainment, including medicine, therapy, and professional training, just to name a few (Angelov et al., 2020; Stecuła, 2022; Cassani et al., 2020b; Cullen et al., 2021; Maples-Keller et al., 2017). However, the widespread adoption of VR has been hindered by a factor termed 'cybersickness', which is akin to motion sickness experienced by many in boats and moving cars.

Cybersickness is characterized by symptoms such as dizziness, nausea, headaches, disorientation, vertigo, visual disturbances, and increased salivation. The traditional method of assessing cybersickness involving subjective questionnaires, such as the Simulator Sickness Questionnaire (SSQ) and the Fast Motion Sickness Scale (FMS) (Keshavarz et al., 2011) disrupt quality of experience of users who must continuously report on their symptoms. In recent years, there has been a push for a more objective measure of the user's physiological state, enhancing our understanding and ability to quantify and compare the effectiveness of different VR systems and content designs to mitigate cybersickness. Characterizing cybersickness using biosignals has some disadvantages. For example, signals are often contaminated with artifacts. While automated enhancement algorithms exist (e.g., (Yildirim, 2020; Delorme, 2023)), it is not clear what impact they may have on signal patterns and, ultimately, on downstream cybersickness characterization tasks. Moreover, when it comes to electrical biosignals, physiological processes often serve as contaminants. With EEG, for example, signals may be contaminated by heart beats, as well as by eye and/or head movements. In this case, removal of eye/head movement artifacts may indeed be removing information that could help characterize cybersickness, as mentioned previously. Lastly, the latest trend in biosignal processing has involved the use of deep learning for both feature extraction and classification (Yildirim, 2020; Liao et al., 2020; Liu et al., 2024). In these scenarios, there is little interpretability and explainability (Jeong et al., 2019; Fan et al., 2021). As such, while

prediction/detection of cybersickness is possible with high accuracy, few insights on what occurs in the brain/body during cybersickness are available, thus limiting the development of tactics to reduce symptoms. Our contribution in this chapter can be summarized in the following: First, we explore the impact of different levels of artefact removal – from very basic techniques where head/body artifacts are kept, to more advanced pipelines leaving only neural signatures for evaluation – on cybersickness characterization. While the former effectively transforms the EEG into an embedded multimodal system, thus potentially improving detection accuracy, the latter can uncover the specific neurological patterns associated with cybersickness, thus leading to potential interventions to mitigate symptoms. Second, we extend our analysis beyond EEG conventional Power Spectral Density (PSD) features and propose the use of EEG Amplitude Modulation (AM) and connectivity features. Amplitude modulation is a fundamental mechanism in cognitive processes (Bondar' et al., 2000; Hidalgo et al., 2022; Hilla et al., 2020), thus may provide greater insights for cybersickness characterization. It has shown to be useful for mental and cognitive state characterization (Albuquerque et al., 2020; Clerico et al., 2015, 2018), as well as for health diagnostics (Fraga et al., 2013; Trambaiolli et al., 2011).

Three different ablation studies are conducted to investigate the impact of the Automatic artifact Removal (AAR) algorithm used, epoch size, and number of features. These ablation studies are used to find the optimal combination of such factors, which are then used to find the best cybersickness prediction model to be tested on an unseen test set. The goal of the first ablation study is to evaluate the efficacy of each AAR algorithm at removing head and eye movements. In the second ablation study, we investigate the predictive power of different combinations of AAR algorithms, feature types, and epoch sizes. Lastly, in the third ablation study, we explore the optimal number of features for cybersickness prediction.

5.3 Materials and Methods

5.3.1 Dataset

For this study, we relied on a cybersickness dataset described in (Li et al., 2021a), which followed an experimental protocol specifically designed to induce cybersickness. In particular, data is used from 20 participants that were immersed in two VR scenarios simulating realistic movement dynamics: a tunnel travel simulation and a roller coaster ride. The tunnel travel required navigation through an abstract tunnel, emphasizing the perception of moving in-depth to induce mild to moderate cybersickness. The roller coaster simulation, on the other hand, aimed to elicit a stronger cybersickness response through virtual linear and angular accelerations. The rationale behind these tasks was to cover a broad spectrum of motion stimuli, from mild to intense, to effectively trigger and measure cybersickness responses in a controlled manner.

Each session lasted up to 10 minutes, with the duration tailored to individual participant responses, as indicated by their cybersickness levels. Cybersickness severity was systematically measured using the 20-point FMS questionnaire, administered at the end of each minute, for as long as the participants could manage their symptoms until reaching an FMS score of 11. Some participants did not experience cybersickness and reported FMS values not exceeding 4 (out of 20). Specifically, there were 4 subjects in the Tunnel session and 14 in the Roller Coaster session who did not continue to the second part of the experiment due to severe discomfort after the first video; as such, data from these subjects are considered "incomplete".

The study recorded multi-channel EEG, 1-channel Electrooculography (EOG), and head movements via a 3-axis accelerometer. The seven EEG channel locations used in this study included Fz, Pz, P3, P4, Cz, CP5, and CP6, recording with a sampling rate of 500 Hz. The EOG channel, located on the left lower eyelid, was used to monitor eye movements and eye blinks. Both the ground and reference electrodes were connected together and attached to the right earlobe using an ear clip. The interested reader is referred to (Li et al., 2021a) for complete details about the data collection process and the dataset used.

5.3.2 Pre-Processing

Pre-processing is crucial in EEG research to remove unwanted physiological (e.g., heart beats, muscle/eye/head movements) and environmental (e.g., powerline, temperature, humidity) interferences (Tanner et al., 2016; Bigdely-Shamlo et al., 2020). With such pre-processing algorithms, a trade-off must always be achieved between the aggressiveness of the artifact removal step and the potential (unwanted) removal of useful discriminatory information from the collected signals (Robbins et al., 2020a; Delorme, 2023). For example, AAR algorithms based on Independent component analysis (ICA) are susceptible to causing phase distortion (Thatcher et al., 2020) and/or loss of useful information (Sadiya et al., 2021; Klug et al., 2021). Similarly, rejecting channels and segments of the signal contaminated by artifacts introduces information loss and discontinuities (Huberty et al., 2024; Sadiya et al., 2021).

With cybersickness prediction, however, artifact removal may play a crucial role, as the information that is often removed, such as head movements, eye movements, and heart beats, may indeed help in the prediction process. As such, here we explore three different levels of AAR, from light to aggressive, to gauge the effect this has on cybersickness characterization, as well as on the insights generated by the top features later used for the prediction task. This, in fact, has been recently emphasized in (Delorme, 2023) where a reduction in the amount of pre-processing was suggested to prevent the loss of relevant neural information of event related potentials. In addition, authors in (Thatcher et al., 2020) demonstrate that AAR based on ICA result in phase distortion that could compromise connectivity analysis. The three different pre-processing techniques explored herein are detailed next.

5.3.2.1 Minimal Pre-Processing

Inspired by the work in (Delorme, 2023), an extremely simple pre-processing pipeline – called 'Minimal' – was tested to minimize potential distortion of the EEG signals at the cost of limited noise reduction. The 'Minimal' pre-processing strategy comprised exclusively of a high-pass filtering using a zero-phase Butterworth filter set to a cutoff frequency of 0.25 Hz used to eliminate low-frequency drift. This method should preserve artifacts related to eye, muscle, and head movements, as well as powerline interference.

5.3.2.2 Artifact Subspace Reconstruction Pre-Processing

In this second approach, the widely-used Artifact Subspace Reconstruction (ASR) algorithm (Mullen et al., 2013) followed by an independent component rejection step using the ICLabel algorithm (Pion-Tonachini et al., 2019) was used. This configuration is known to remove many common EEG artifacts and to minimally interfere with relevant EEG information (Delorme, 2023). It is important to note that, while the efficiency of ICA may be reduced when applied to datasets with a small number of channels, empirical evidence suggests that ICA-based pre-processing has performed satisfactorily despite these limitations (Rejer et al., 2015). Following ASR pre-processing, any removed channels were replaced using default EEGLAB spherical interpolation (Delorme et al., 2004), ensuring a consistent dataset for subsequent analyses.

5.3.2.3 Data-driven Pre-processing

Automatic artifact detection algorithms, such as ASR, utilize threshold-based techniques or depend upon predefined templates and assumptions about the nature of EEG noise. In contrast to these conventional approaches, data-driven pre-processing pipelines make use of experiment-specific artifact data from both EOG and head movement measurements thereby offering more precise noise reduction of specific types of distortion.

Regression ICA (RegICA) is one such method which combines blind source separation and regression to more accurately remove e.g., ocular artifacts (Klados et al., 2011). Here, RegICA is used to dynamically attenuate EEG frequency components that originate from non-neuronal sources, such as ocular and head movements. Reference signals (i.e., EOG and head accelerometry) are used to characterize components of the EEG signal that have high correlations (here, characterized as a correlation greater than 0.25) with the non-neuronal signal.

Since EEG signals and reference signals have very different magnitudes, the data was scaled by subtracting the median of each channel and dividing by the median absolute deviation to avoid numerical instability. Subsequently, RegICA is applied twice: initially using the head accelerometer

signals as references, and then using EOG signals. Here, the following hyperparameters are used: a filter order of 3, sigma of 0.01, a forgetting factor of 0.999 and stable root mean square error as the optimization criterion. Using both EOG and accelerometer signals as reference with RegICA should remove eye and head movements in a data-driven manner.

5.3.3 Feature extraction

5.3.3.1 Power Spectral Density and Coupling

Traditional methods have relied on conventional power spectral density measures computed for different EEG frequency bands, namely: delta (1–4 Hz), theta (4–8 Hz), alpha (8–12 Hz), beta (12–30 Hz), and gamma (30–50 Hz) bands (Li et al., 2022; Ozkan et al., 2023). Here, band decomposition was achieved using a filter bank (FB) of zero-phase Finite impulse response (FIR) filter, which applied two successive filtering steps in opposite directions on a mirror-padded version of the input signal, thereby producing Band-filtered time-series (BFT). Band-filtered time-series were then epoched with window sizes corresponding to 2, 5, 8, 20 and 30 seconds and shifts of 2 seconds.

Power values were computed per sub-band by squaring the samples and then normalizing by the total EEG power. Three statistical functionals are then used to aggregate the per-epoch features: mean, standard deviation, and skewness. This approach resulted in 105 PSD candidate features per epoch duration (5 bands $\times$ 7 channels $\times$ 3 functionals) for each of the tested epoch sizes. For notation, henceforth, spectral power-based features are referred to as ⟨PSD⟩_{statistic} c=⟨channel⟩ b=⟨band⟩.

Moreover, to measure the coupling between brain regions (i.e., between different electrodes) and between EEG frequency bands, two coupling measures are computed using the Pearson correlation and mutual information to measure linear and non-linear properties, respectively, between different electrode pairs or frequency bands (Clerico et al., 2018; Akhand et al., 2024; Afshani et al., 2019; Lu et al., 2011). Here, Inter-channel coupling (CCPL) accounts for 630 candidate features (2 coupling types $\times$ 21 channel pairs $\times$ 5 bands $\times$ 3 functionals), while Inter-band coupling (BCPL) accounts for 420 features (2 coupling types $\times$ 7 channels $\times$ 10 band pairs $\times$ 3 functionals). For notation, Inter-band coupling (BCPL) are denoted as PSD_{feature subtype}_{statistic} c=⟨channel⟩ b=⟨band1⟩ $\times$ ⟨band2⟩, thus representing interactions between different frequency bands within the same EEG channel. Conversely, Inter-channel coupling (CCPL) features, referred to as PSD_{feature subtype}_{statistic} c=⟨channel1⟩ $\times$ ⟨channel2⟩ b=⟨band⟩, represent the interaction between channels within the same frequency band.

5.3.3.2 Amplitude Modulation Features and Coupling

AM time-series were extracted employing the implementation presented in section 2.3.4 of Chapter 2.

For these new AM features, the epoch duration is a critical parameter, as it directly influences the latency in feature extraction and resolution. Furthermore, identifying the optimal epoch duration is essential for gaining insights into the temporal dynamics at which cybersickness-related neuronal patterns become discernible. In the literature, epoch durations when using AM features have ranged from 5, 8, to 20 seconds (Cassani et al., 2019; Fraga et al., 2013; Trambaiolli et al., 2020) to effectively capture neuronal patterns needed for diagnostics.

As this is the first attempt at using these features for cybersickness detection, we leave epoch size as a hyper-parameter to be optimized in the experiments. To capture potential transient micro-state changes (Nam et al., 2022; Chang et al., 2023a; Aubonnet et al., 2023), shorter windows are also explored. For completeness, we explore epoch sizes of 2, 5, 8, 20, and 30 seconds. The power in each of the 14 ⟨modulated band⟩-m⟨modulant⟩ time series is computed per epoch and EEG channel, thus resulting in 294 candidate features. Here, the following notation is used for the features: ⟨AM⟩_{statistic} c=⟨channel⟩ b=⟨band⟩.

Moreover, as with spectral coupling measures, coupling between different AM times series was shown in (Clerico et al., 2018) to better characterize different mental states. As such, AM-CCPL is used to capture interactions between every possible pair of channels, while AM-BCPL to measure coupling across all possible cross-band combinations. Figures 2.4B and C presented in section 2.3.4 of Chapter 2 depict the processing steps to compute the coupling parameters for the two different scenarios, respectively. In both cases, the notation used for AM-CCPL and AM-BCPL are AM_{feature subtype}_{statistic} c=$< channel1 >\times< channel2 >$ b=$< band >$ and AM_{feature subtype}_{statistic} c=$< channel >$ b=$< band1 >\times< band2 >$, respectively.

5.3.4 Testing Setup

Figure 5.1 illustrates the general testing methodology employed in this experiment. With the dataset used, cybersickness FMS ratings were provided every minute. To augment the amount of data available for training of the classifiers, a bootstrapping method was applied where a random selection of epochs within a certain one-minute EEG segment under the same FMS rating were used. The statistical functionals, such as mean, standard deviation, and skewness were then computed from the resulting subset. This process can be repeated multiple times where after each iteration a distinct set is created. To avoid data leakage between training and test samples, a Stratified-group K-fold methodology was used to restrict groups of samples from the same minute segment to a unique data subset (i.e., train or test). This step corresponds to item (d) in Figure 5.1. Train and test

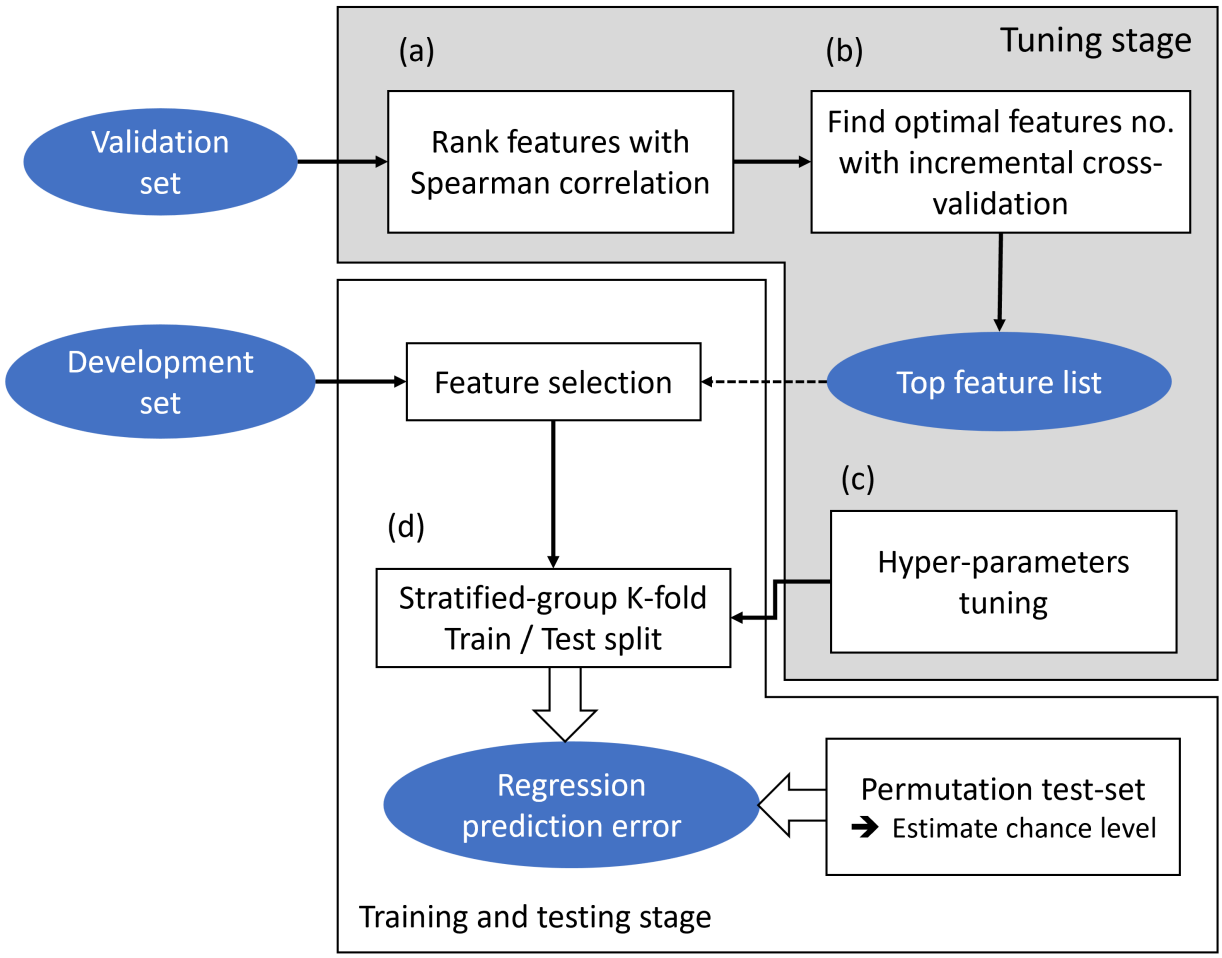

Figure 5.1 : Flowchart presenting the testing methodology which is divided into two main stages: Tuning stage (top light grey area) relies on the validation set (33% of the original dataset). Training and testing stage (bottom white area) relies on the development set (67% of the original dataset). (a) Features are ranked using their correlation with the FMS score. (b) Incremental cross-validation determines the optimal number of features, ensuring only the top features are retained in the development set. (c) The validation set is used to find the best hyperparameters for SVR. Once the tuning stage is completed, the optimal features and hyperparameters are used to train and validate the model (d).

set were generated from the development set which correspond to a portion of 67% of samples reserved exclusively for training and testing. The number of epochs taken per 1-minute segment and the number of times this bootstrap sampling was done was empirically set to 75% of total epoch number within the minute and 10 repetitions, respectively.

5.3.5 Post-Processing

After extracting features from each EEG recording session, outlier detection was conducted independently on each feature using a threshold of three times the median absolute deviation. Detected outliers, along with near infinite, near zero, and missing samples (Not-A-Number), were corrected via linear interpolation of time contiguous samples. Lastly, FMS ratings were normalized to a scale

ranging from 0 to 1 to facilitate the use of the Root-mean-square error (RMSE) as a figure-of-merit to gauge system accuracy.

5.3.6 Feature ranking and selection

Given that the used dataset has a low sample-to-feature ratio, feature selection is needed to reduce the number of features to a manageable number to prevent overfitting. Additionally, to mitigate the risk of data leakage, feature selection is performed on a validation subset (set as 33% samples of the dataset) of the data using the "StratifiedGroupKFold" module within scikit-learn (Pedregosa et al., 2011b) prior to the train/test split procedure. This approach ensures that the validation samples come from different time instances than those reserved for testing, keeping the test set completely unseen.

Here, a simple feature ranking method was utilized based on Spearman correlation. For each feature, the correlation was calculated between samples and their corresponding FMS rating. This process is represented by step (a) in Figure 5.1. The correlation score attributed to each feature is used in ablation study II presented in Section 5.4.2.

The rank ordering was based firstly by statistical significance (Holm-Bonferroni corrected with significance set at a threshold of 0.05), followed by absolute Spearman correlation coefficient values. After this ranking, the top 100 features were selected (empirically) for further analysis. To gauge the impact of including additional features on cybersickness measurement, top-features were added one by one and regression performance on the validation set was assessed via stratified 5-fold cross-validation. This step corresponds to item (b) of the Tuning stage presented in Figure 5.1; this step further described in the ablation study III in Section 5.4.3. The final number of features to be used is the one that leads to the smallest RMSE value obtained on the validation set after Gaussian smoothing.

5.3.7 Regression analysis

A Support Vector Regressor (SVR) was selected as the regression algorithm, motivated by its robustness to overfitting, a characteristic particularly advantageous for high dimensional datasets. Hyper-parameter optimization for the SVR model was carried out through an exhaustive 3-fold cross-validation grid search, exploring combinations of 3x4x20x20 for kernel types ('poly', 'rbf', and 'sigmoid'), polynomial degrees (2 through 5), and the parameters C and gamma. The search covered logarithmic scales from 10^{-4} to 1 for C, and from 10^{-4} to 10^{2} for gamma, with 'auto' and 'scale' additionally evaluated as specific gamma parameters. This step is represented by block (c) in Figure 5.1. Prior to training the SVR, data was normalized subtracting the mean and scaling to unit variance to address SVR sensitivity to scaling. Bootstrapping was done 100 times on the 5-fold

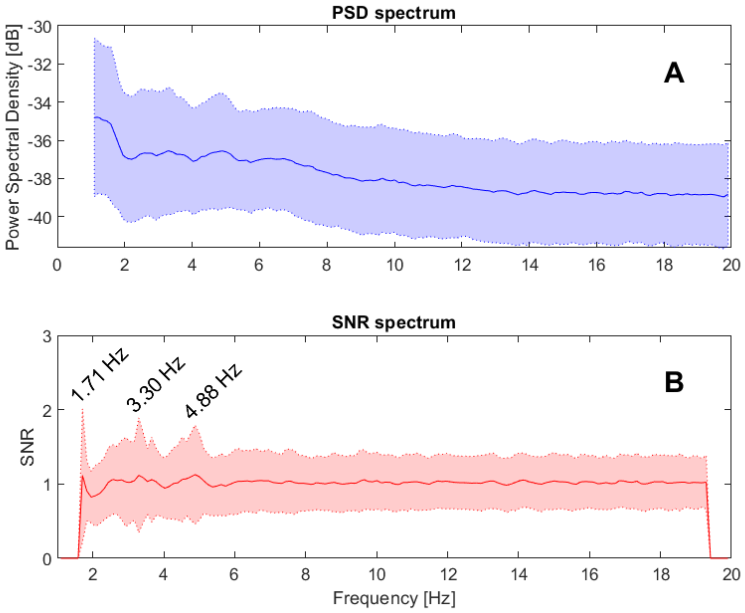

Figure 5.2 : A. Spectral analysis of accelerometer data: This graph presents the spectral representation of accelerometer data averaged across the x, y, and z axes for multiple subjects and sessions. On the y-axis, power is expressed in decibels (dB), while the x-axis displays frequency in Hertz (Hz), covering a spectrum from 1 Hz to 50 Hz. The blue curve illustrates the mean power spectrum, and the shaded area represents the standard deviation, reflecting variability across recordings. B. Signal-to-Noise Ratio (SNR): This part of the figure presents the SNR across the frequency spectrum, amplifying local activity in relation to adjacent background noise levels. The x-axis displays the frequency in Hertz (Hz), covering the same range as in Figure A.

cross-validation task to allow for significance calculation of the obtained RMSE values relative to chance.

5.4 Experimental Results

5.4.1 Ablation Study I: Artifacts and Artifact Removal

To better understand the impact of head movements and eye movements on certain EEG frequency bands, Figures 5.2 and 5.3 depict (top plots) the power spectral representation of the accelerometer signals (averaged across the x, y, and z axes) and the Signal-to-Noise Ratio (SNR) representation (bottom plot), for each of these two signal modalities, respectively. SNR is computed for each frequency bin as the ratio between the power of the bin's central frequency and the mean power of neighboring frequencies excluding immediately adjacent ones (Meigen et al., 1999).

As can be seen from Fig. 5.2, notable power peaks occur at 1.7 Hz, 3.3 Hz, and 4.9 Hz, likely harmonics of the head movements. These findings suggest that head movement information can likely be a confound for EEG features based on delta and theta bands. Similarly, from Fig. 5.3 ocular activity exhibits a 1/f spectral roll-off, suggesting that eye movements may also affect lower frequency bands, specifically the delta and theta bands.

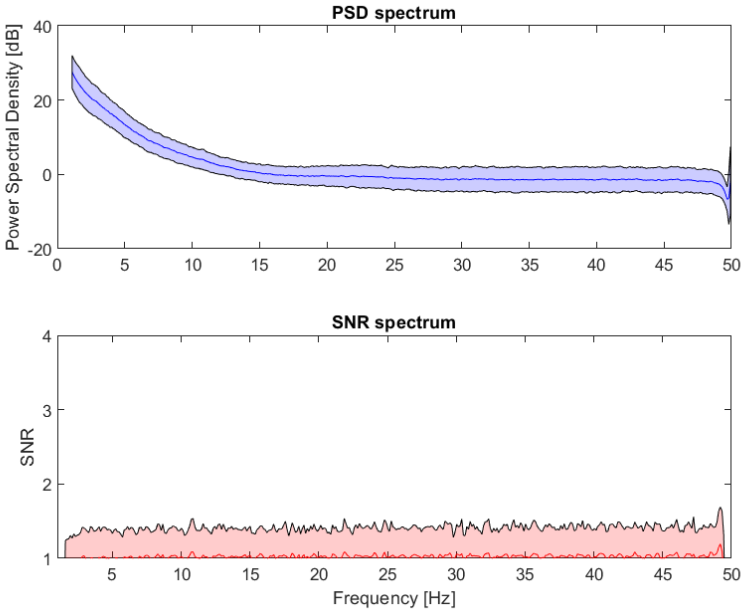

Figure 5.3 : A. Spectral representation of EOG signals: This graph presents the EOG signal averaged across various subjects and sessions, providing a spectral overview. The y-axis quantifies power in decibels (dB), and the x-axis represents frequency in Hertz (Hz), spanning from 1 Hz to 50 Hz. The blue curve indicates the average power spectrum, while the shaded area around this curve illustrates the standard deviation, reflecting variability among subjects and sessions. B. Signal-to-Noise Ratio (SNR) of the corresponding EOG spectrum.

Next, we wish to explore the potential of the three different AAR algorithms at removing these two artifact sources. To this end, we utilize the mutual information computed from the processed EEG signal and the temporal series of the EOG and the averaged tri-axes accelerometer signals. A higher mutual information will signal that the artifacts have not been removed and the EEG signal still contains substantial artifactual information embedded in the signal. In turn, lower mutual information values suggest that the artifacts were correctly removed. Figure 5.4 presents the computed mutual information (averaged over the head and eye movement signals) for each of the seven EEG channels. As can be seen, minimal processing showed the highest mutual information, as expected. The RegICA method removed some of the artifacts, while the more complex ASR + ICLabel combination resulted in the least amount of mutual information, suggesting the most aggressive removal of artifacts.

Lastly, Figure 5.5 depicts the EEG Power Spectral Density averaged across channels processed by the Minimal and the ASR+ICLabel pipelines. As can be seen, the 1.7 Hz, 2.5, and 3.2 Hz peaks, likely due to head movements, can be seen with the former, but not the latter. The spectral density above 6 Hz, in turn, closely matches in both scenarios.

Comparison of the spectra of the two pipelines, Minimal and ASR+ICLabel, suggests that the components identified as ocular and motion artifacts, in Figures 5.3 and 5.2 respectively, were eliminated by the ASR+ICLabel pipeline, but not by the Minimal pipeline. This observation in the spectral domain is consistent with the results obtained from the mutual information measurements.

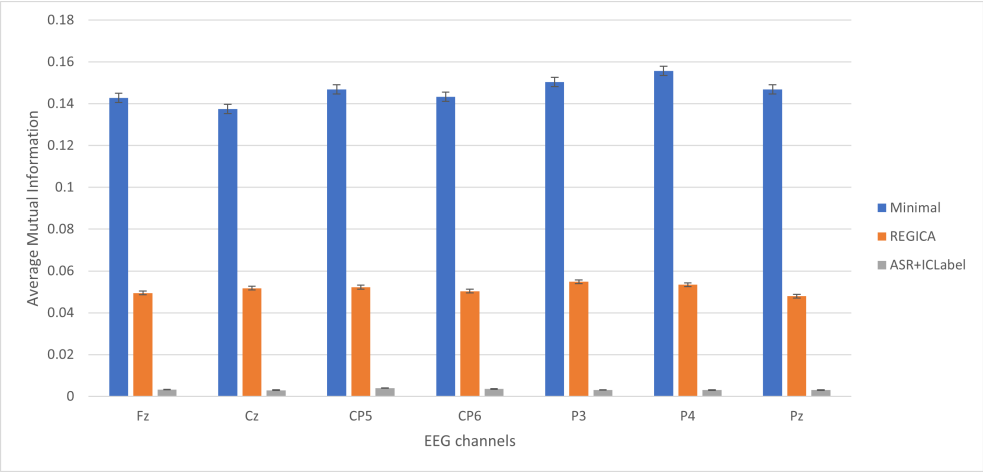

Figure 5.4 : Comparative analysis of pre-processing algorithms for EEG signals based on mutual information. The bar plots illustrate the average mutual information scores between EEG channels of pre-processed signals and recorded noise signals (EOG and accelerometer signals) for different pre-processing pipelines. The y-axis represents the mutual information score, quantifying the dependency between the EEG signals and noise, while the x-axis categorizes EEG electrodes. Error bars indicate standard error, reflecting variability among subjects and sessions.

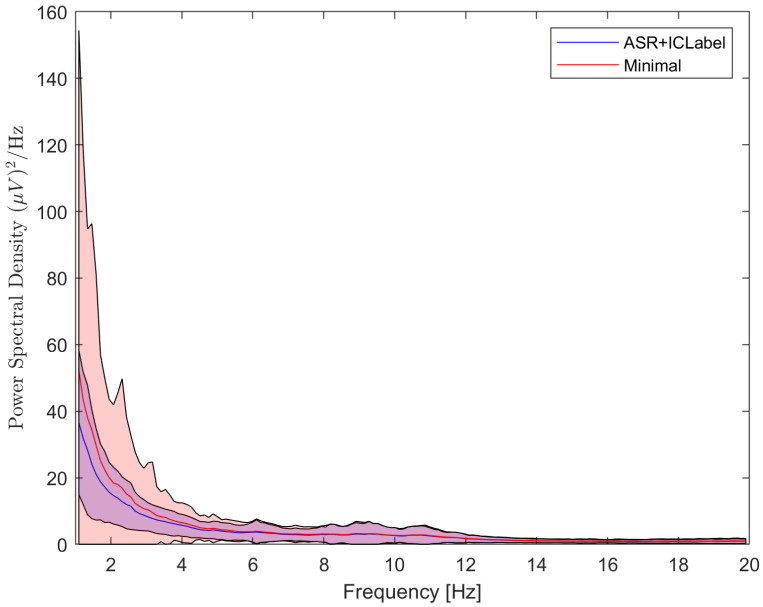

Figure 5.5 : Comparison of power spectral density between Minimal and ASR+ICLabel pre-processings methods. The y-axis quantifies power density in $(\mu V)^2$ /Hz, and the x-axis represents frequency in Hertz (Hz), spanning from 1 Hz to 20 Hz. The blue and red curve correspond to the average power spectrum of signal after ASR+ICLabel and Minimal pre-processings respectively, while the shaded area around each curves illustrates the standard deviation, reflecting variability among subjects, sessions and channels.

5.4.2 Ablation Study II: Combination of AARs, Epoch Size, and Feature Type

Despite the effective removal of artifacts, AARs can distort the signals. Therefore, we investigated their impact on the useful information related to cybersickness. We compared different combinations

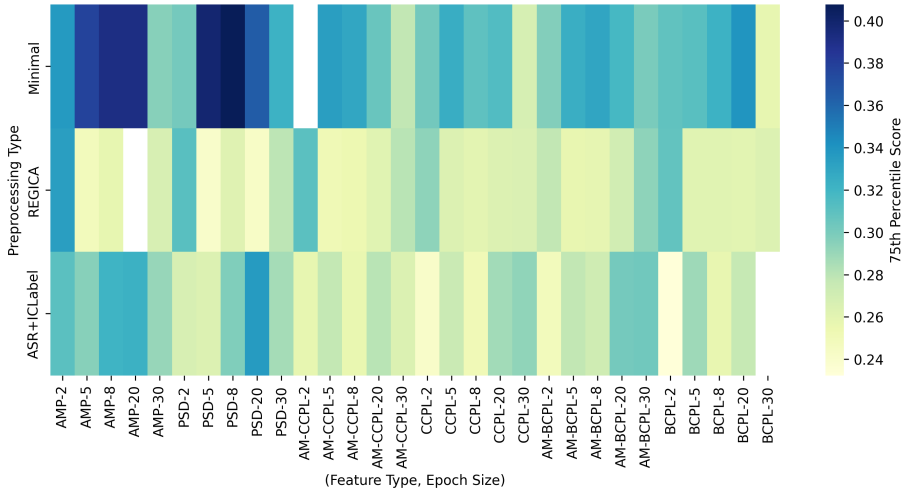

Figure 5.6 : Comparative analysis of feature type distribution across different pre-processing conditions and epoch sizes, encompassing six distinct feature types: AMP, PSD, AM-CCPL, CCPL, AM-BCPL, and BCPL. The color intensity within the heatmap denotes the magnitude of the average correlation between data of selected features and FMS ratings.

of epoch sizes and each AARs for the predictive power of each type of feature. As a figure-of-merit, we employed the correlation measures described in Section 5.3.6, which were calculated between the samples and the associated FMS rating independently for each feature.

Figure 5.6 presents the Spearman correlation between different features and the FMS scores in the training set. The correlation map shows results for the different AAR methods, feature types, and epoch sizes. As can be seen, PSD and AMP features showed the highest correlations with the Minimal processing pipeline with the 8 and 20 second epochs for AMP features and 8-second epochs for PSDs. Moreover, the band and channel coupling measures showed mild to moderate correlation with FMS across various pre-processing scenarios, suggesting their potential complementarity for cybersickness characterization.

Overall, the RegICA and ASR+ICLabel AAR methods showed lower correlation scores with FMS ratings across most epoch sizes and feature types, whereas the Minimal pre-processing showed the highest. These findings suggest that, indeed, retaining artifacts related to blinks, eye movements, and head movements can be useful to characterize the multimodal effects of cybersickness.

5.4.3 Ablation Study III: Feature Selection

Next, we explore the selection of the optimal number of features. Figure 5.7 shows the coefficient of determination (R^2) scores as a function of number of features for the case of ASR+ICLabel pre-processing and 5-second epochs. As can be seen, the R^2 score improves with the inclusion of more features until a plateau is reached, which starts with a R^2 score of 0.467 at around 71 selected features. The optimal feature number is selected for each pre-processing and epoch size

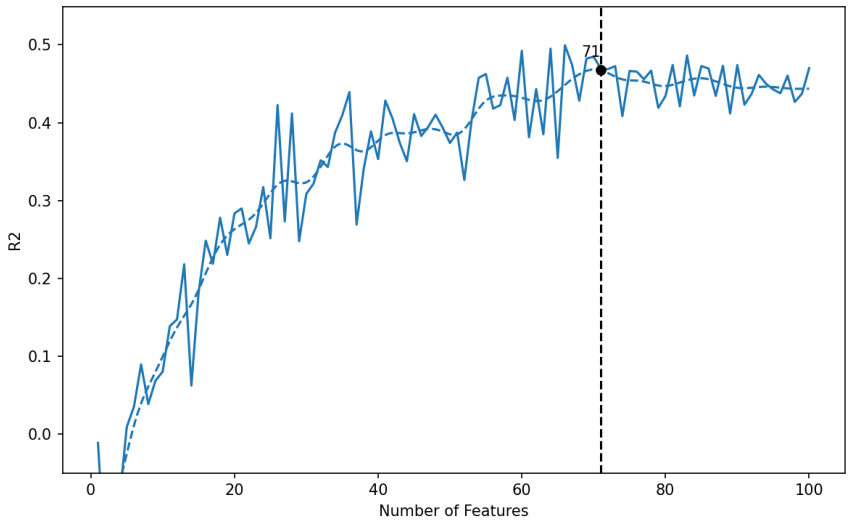

Figure 5.7 : Performance metrics for the ASR+ICLabel pre-processing method over a 5-second epoch, as a function of feature count. The graph illustrates the variation of coefficient of determination R^2 (blue) with increasing feature counts. Hashed lines correspond to the smoothed trends. The observed increase in R^2, indicates enhanced model efficacy with additional features. The vertical dashed line marks the automatically determined optimal feature count under these conditions.

Epoch Size	Minimal	REGICA	ASR+ICLabel
2	100	23	67
5	100	86	100
8	97	100	73
20	78	97	100
30	81	94	81

Tableau 5.1 : Optimal number of features selected for each combination of epoch sizes and pre-processing techniques. The maximum number of features is set (empirically) to 100 to prevent overfitting.

combination; the exact number of features selected for each of these combinations is shown in Table 5.1. These top features are discussed next.

5.4.4 Top-Features Analysis

To gain greater insight into cybersickness characterization, two analyses were performed based on the interpretation of the most relevant features. The first analysis explores the neural patterns indicative of cybersickness, while the second investigates the multi-modal potential of cybersickness detection with minimal EEG pre-processing.

We employed a strategy to summarize the multiple lists of top features generated for each combination of the AAR algorithm and epoch size. For each AAR, a unified list was created by gathering all features that appeared in at least one of the lists across various epoch sizes. A common list is then defined as the intersection of two unified lists, meaning that a feature must be

present in both lists to be included. Therefore, the analysis in the discussion section is based on common features between the two AARs, regardless of the epoch size.

5.4.4.1 Neurological patterns associated with cybersickness

For this analysis, the underlying assumption is that the common top-ranked features selected with and without pre-processing will most likely convey details about the neural underpinnings associated with cybersickness. Based on the ablation studies, we use the 'ASR+ICLabel' and the 'Minimal' pre-processing methods in this analysis. It was found that the common/overlapped top features list comprised 51 features with 22 accounting for AMP and PSD; 11 for inter-channel coupling features; and 18 for inter-band coupling features. More details about these top features are given next.

PSD and AM Power Features Figure 5.8 shows the average correlation with FMS ratings of the top-22 common features from the AMP and PSD categories. In the figure, the electrode locations and feature types are detailed in the x-axis labels, while the frequency bands are color-coded. Spatially, the neuronal patterns correlated with cybersickness form two distinct clusters: alpha-mtheta, alpha, and theta bands are prevalent in the parietal (P3, P4, Pz) and centro-parietal (CP5, CP6) areas, while alpha-mdelta, delta, and beta-mdelta bands are primarily observed in the central (Cz) and frontal (Fz) regions.

The average AM power (AMP_mean) primarily consists of alpha-mtheta frequencies, while the average band power (PSD_mean) is mainly characterized by theta and alpha frequencies. Notably, theta oscillations are more significant when their average power across an entire minute is taken, indicating their role as a persistent process.

Moreover, the variability in power, as indicated by the standard deviation features (AMP_std and PSD_std), is most closely associated with the alpha-mdelta and alpha bands, respectively. The observed increase in the variability of alpha-mdelta band power, taken over a 1-minute window indicate instability of the alpha band slow temporal dynamic as the perceived cybersickness symptoms increase. This feature may reflect neuronal mechanisms capable of flexible and adaptive responses to cybersickness.

Next, we take a more in-depth look at the two features with the highest correlation with FMS in Figure 5.8, namely mean alpha-mtheta at CP6 and the standard deviation of alpha-mdelta power at CP5. As can be seen in Figure 5.9, the average alpha-mtheta activity and the alpha-mdelta power standard deviation exhibits a significant positive correlation with FMS ratings. Notably, variability among participants is increased within the 0.5-1 normalized FMS score range, suggesting a more unstable/inconsistent pattern across this interval.

Figure 5.10, in turn, depicts the temporal changes of the two features over the 10-minute experiment which exhibited increased cybersickness levels over time. As can be seen, both

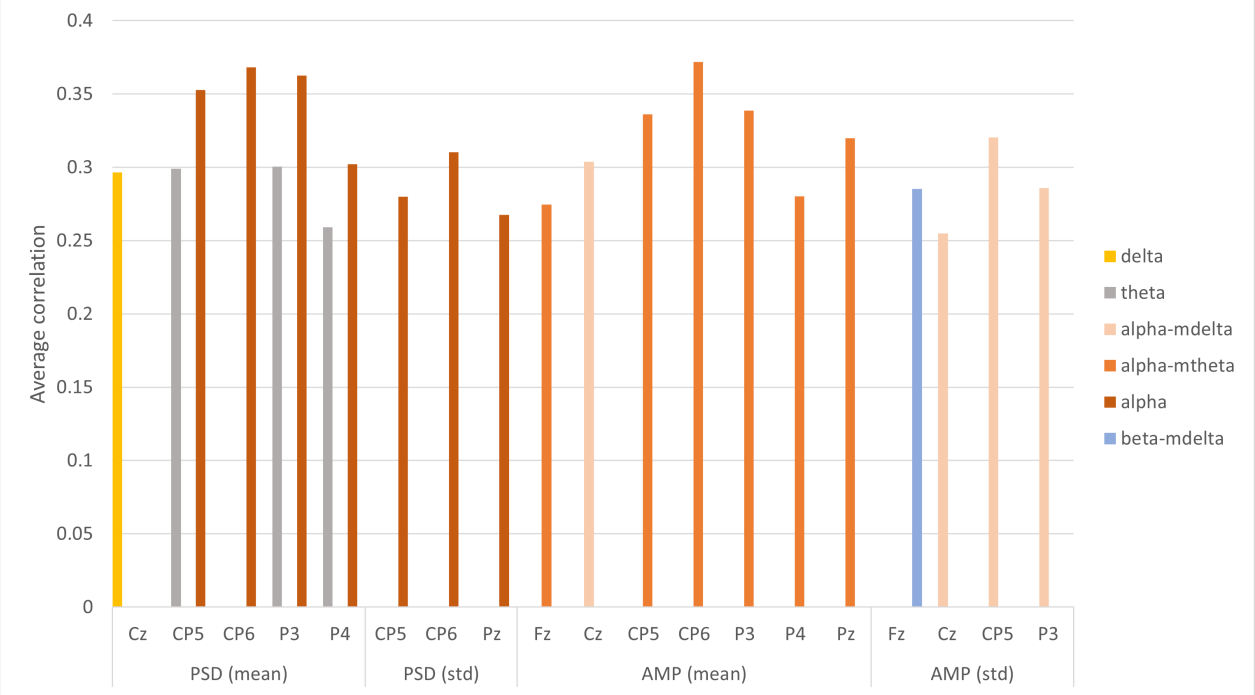

Figure 5.8 : Bar plot representing average correlation between overlapped AMP and PSD features and FMS ratings. The feature types and EEG electrodes are described on the x-axis, while the corresponding frequency bands are color-coded (see the figure legend).

features exhibited a significant increase over time, suggesting they may serve as a precursor to predict the onset of cybersickness, with symptomatic manifestation becoming consistently evident across participants only after they have been exposed to VR for an extended period. Moreover, it is important to highlight that the variability across subjects (represented by the shaded bands) increased towards the end of the experiment, likely attributed to the reduced amount of data available for accurate standard deviation estimation, as not all participants reached the end of the experiment due to nausea symptoms.

Inter-channel Coupling Features Figure 5.11 depicts the average correlation between data from CCPL based features and FMS ratings. As observed, the most relevant pattern appears to be associated with the beta band. Both average and standard deviation power exhibit similar correlations with cybersickness, specifically with beta-mtheta and beta for AM-CCPL and CCPL, respectively. Channel coupling seems to predominantly occur in centro-parietal (channels Cz, CP5, CP6) and parietal regions (channels P3, Pz, P4). The predominance of centro-parietal activity correlated with FMS ratings suggests involvement in proprioceptive processes, visual/sensorial stimulus processing, and the integration of contextual information (Albanese et al., 2023; Walter et al., 2008; Summerfield et al., 2005) during cybersickness.

Moreover, the figure reveals a significant pattern of coupling within the beta-mtheta band, evidenced by features such as AM_ccor_mean CP5$\times$CP6 and AM_ccor_std Pz$\times$Cz. This pattern

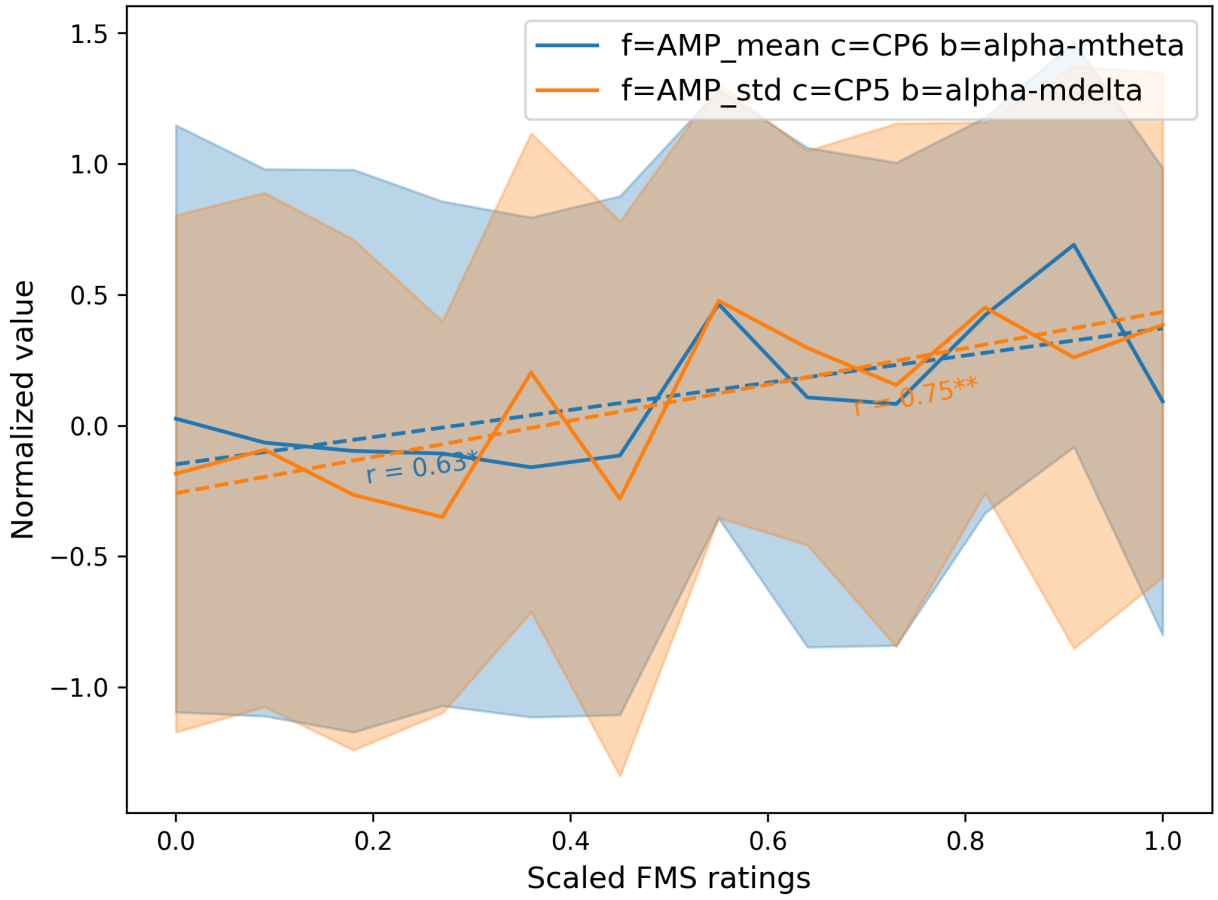

Figure 5.9 : Lateral Parietal Grand average feature values of AMP_mean_alpha-mtheta_CP6 and AMP_std_alpha-mdelta_CP5 versus FMS ratings using the ASR+ICLabel pre-processed dataset. The grand average was calculated by grouping individual subject ratings, averaging them within subjects, and then averaging these values across all subjects to obtain a unified measure for each feature. Both features show a significant positive correlation. The filled areas correspond to standard errors around each curve. Coefficients marked with * and ** represent the Pearson correlation between the grand average and FMS ratings with a p-value < 0.05 and < 0.01, respectively.

emphasizes the crucial role of the beta band in mediating interactions between various cortical areas.

Inter-band Coupling Features Figure 5.12 depicts the average correlations between data from inter-band coupling features and FMS ratings. Within BCPL features only two features appeared in the top: an average decoupling is observed between theta and gamma in left Parietal area (channel P3) whereas a strong coupling variability occurs between theta and beta band in left centro-parietal area (channel CP5).

AM-BCPL features are, in turn, predominant in the top feature list. As can be seen, activities correlated with cybersickness intensity are observed in multiples cortical regions with alpha and beta band couplings in the midline electrodes (Fz, Cz and Pz) represented by features alpha-mdelta$\times$beta-mdelta and alpha-mdelta$\times$beta-mbeta. In the centro-parietal region, increased coupling is observed

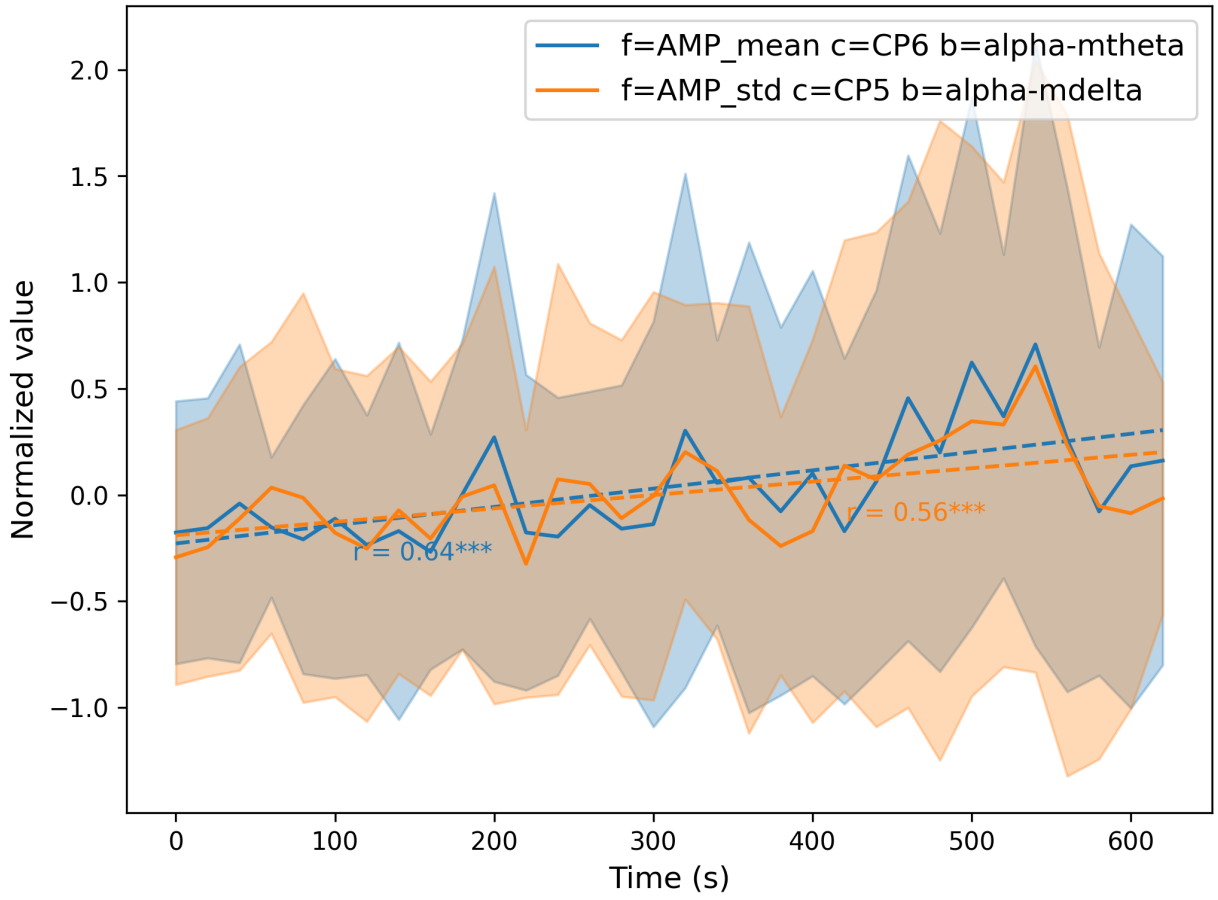

Figure 5.10 : Lateral Parietal Grand average feature value of AMP_mean_alpha-mtheta_CP6 (blue curve) and AMP_std_alpha-mdelta_CP5 (orange curve) as a function of time using ASR+ICLabel pre-processed dataset with 5s epoch size. Both features show an increase over time, suggesting potential tracking of cybersickness levels. The filled area corresponds to the standard error around each curves. Coefficients marked with * represent the Pearson correlation with a p-value < 0.001 between grand average and time stamps.**

in bilateral parietal area between gamma-mtheta and beta-mdelta (P4) and gamma-malpha (P3), accompanied by decoupling within the beta band: beta-mtheta×beta-malpha (Pz, P4).

The frontal lobe (channel Fz), like the centro-parietal area, seems to be particularly important in the coupling between frequency bands. A notable decoupling between gamma and alpha bands, represented by the feature alpha-mtheta×gamma-malpha, is concurrently observed with an increase in coupling within the temporal structure of both beta and gamma bands represented by the features gamma-mdelta×gamma-mtheta and beta-mdelta×beta-mtheta. Taking gamma as an example, gamma-mdelta and gamma-mtheta bands measure the slowest changes in the instantaneous amplitude of the band. The increased coupling between these two bands can be interpreted as the progressive homogenization of the long time scale structure of gamma oscillations.

Overall, the prevalent patterns involve the average coupling of the modulated beta band with alpha and gamma bands, suggesting that the beta band may act as a conduit between slow and rapid neuronal activities during cybersickness episodes. Furthermore, the coupling between beta-

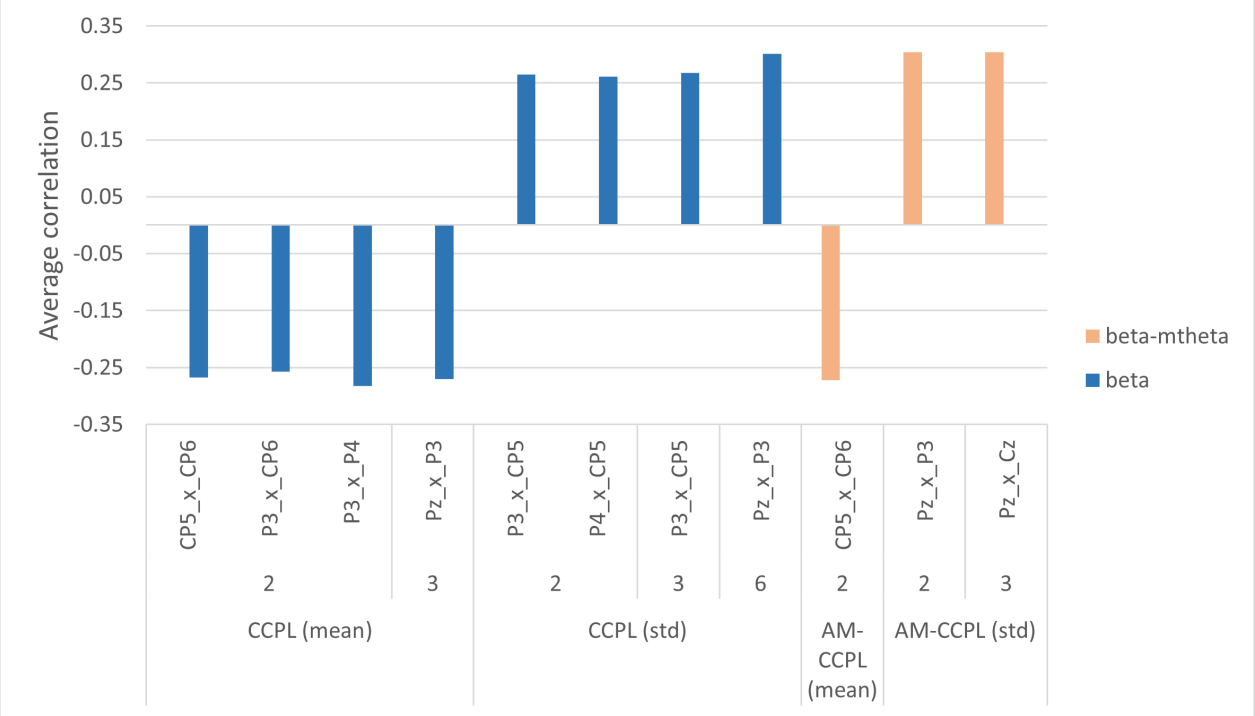

Figure 5.11 : Bar plot representing average correlation between overlapped CCPL features and FMS ratings. The feature subtype and coupled channel pairs are described in the x-axis, while the corresponding frequency bands are color coded (see figure legend).

mtheta and beta-malpha can be identified as a significant pattern associated with cybersickness. Theta and alpha bands appear to engage in a common neuronal mechanism that modulates the amplitude of fast oscillations, notably within the beta band. According to the top-down theory (Richter et al., 2017), this modulation could be attributed to changes in activity within local neuronal assemblies – represented by fast oscillations – under the remote control of deeper brain structures through slower waves.

The manifestation of coupling related to the beta band, both spatially across centro-parietal channels (Cz, CP5, CP6, Pz) and spectrally between the beta-mtheta and beta-malpha bands, highlights the beta band's central role in facilitating the dynamic formation and integration of cortical networks under cybersickness conditions.

The negative correlation between cybersickness severity and the coupling between beta-mtheta and beta-malpha indicates a diminishing interaction between their respective cortical processes as cybersickness intensifies, as depicted by Figures 5.13 and 5.14. It could be argued that increased presence of artifacts affecting the theta band with rising cybersickness levels, could lead to a decoupling. However, the temporal progression of both beta-mtheta and beta-malpha, shown in Figure 5.15, exhibits a significant increase over time. The increase is also observed in the P4 electrode, although not significant, as illustrated in Figure 5.16. Furthermore, the similar correlation values of -0.31 and -0.29 for the Minimal and ASR+ICLabel pipelines, respectively, suggest that the decoupling between beta-mtheta and beta-malpha bands is not primarily due to artifacts.

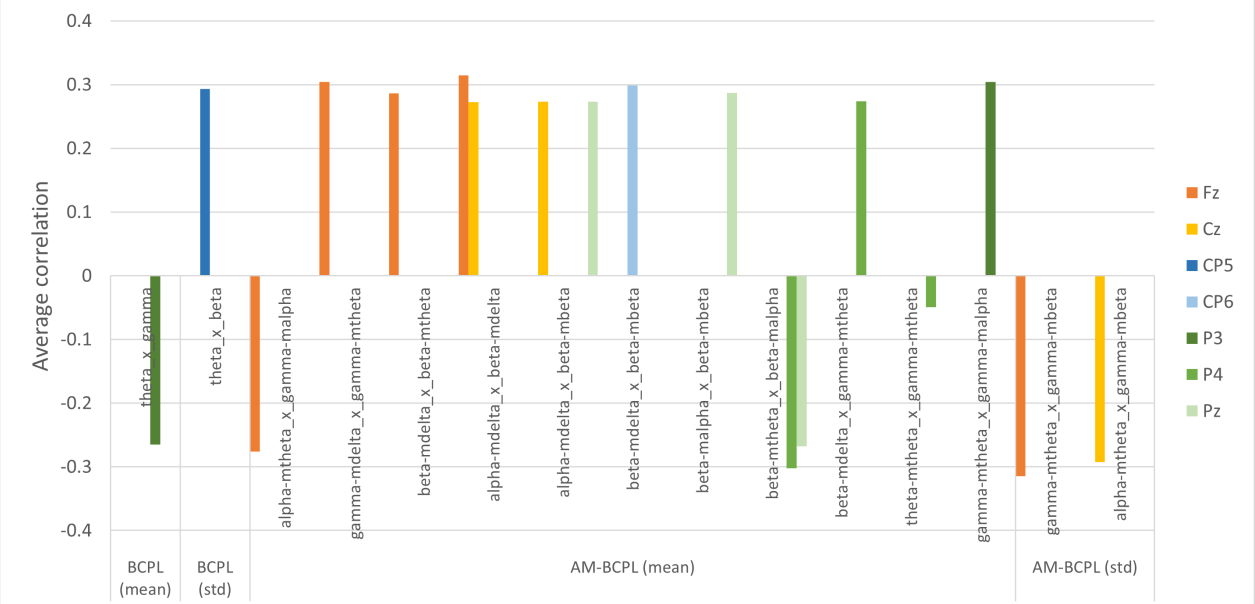

Figure 5.12 : Bar plot representing average correlation between overlapped BCPL features data and FMS ratings. The feature subtype and coupled band pairs are described in the x-axis, while the corresponding channels are color coded (see figure legend).

Additionally, both bands display a similarly weak, non-significant correlation with FMS ratings for both channels P4 and Pz, as illustrated in Figure 5.13 and Figure 5.14. Considering the absence of a significant correlation with FMS ratings, the observed decoupling between beta-mtheta and beta-malpha bands is unlikely to stem from direct changes in power within either band. Instead, this pattern underscores a more complex interaction, suggesting a dynamic rerouting or reorganization of the cortical network as an adaptive response to cybersickness. This observation support the robustness of AM-based features in extracting meaningful patterns regardless of the presence of artifacts.

5.4.4.2 EEG-Based Embedding of Multiple Modalities and their Role in Cybersickness Prediction

As mentioned previously, minimal pre-processing of the EEG signal leaves several artifacts within the EEG time series that may be useful for cybersickness prediction, such as eye and head movements. In this analysis, we take an in-depth look at the top-features selected with the Minimal pre-processing pipeline that did not overlap with those selected from the other two more complex pre-processing methods. The top-features were selected based on their prevalence within the top feature lists across at least three out of five epoch sizes tested within the Minimal pre-processing condition.

Figure 5.17 shows the top PSD and AM power-based features, which accounted to 23 of the 44 top features. As can be seen, the correlation values are higher than those reported from the previous analysis. Moreover, a marked increase in the occurrence of the delta and theta band features is shown, especially around the central and parietal regions (channels Cz, CP5, CP6, P3,

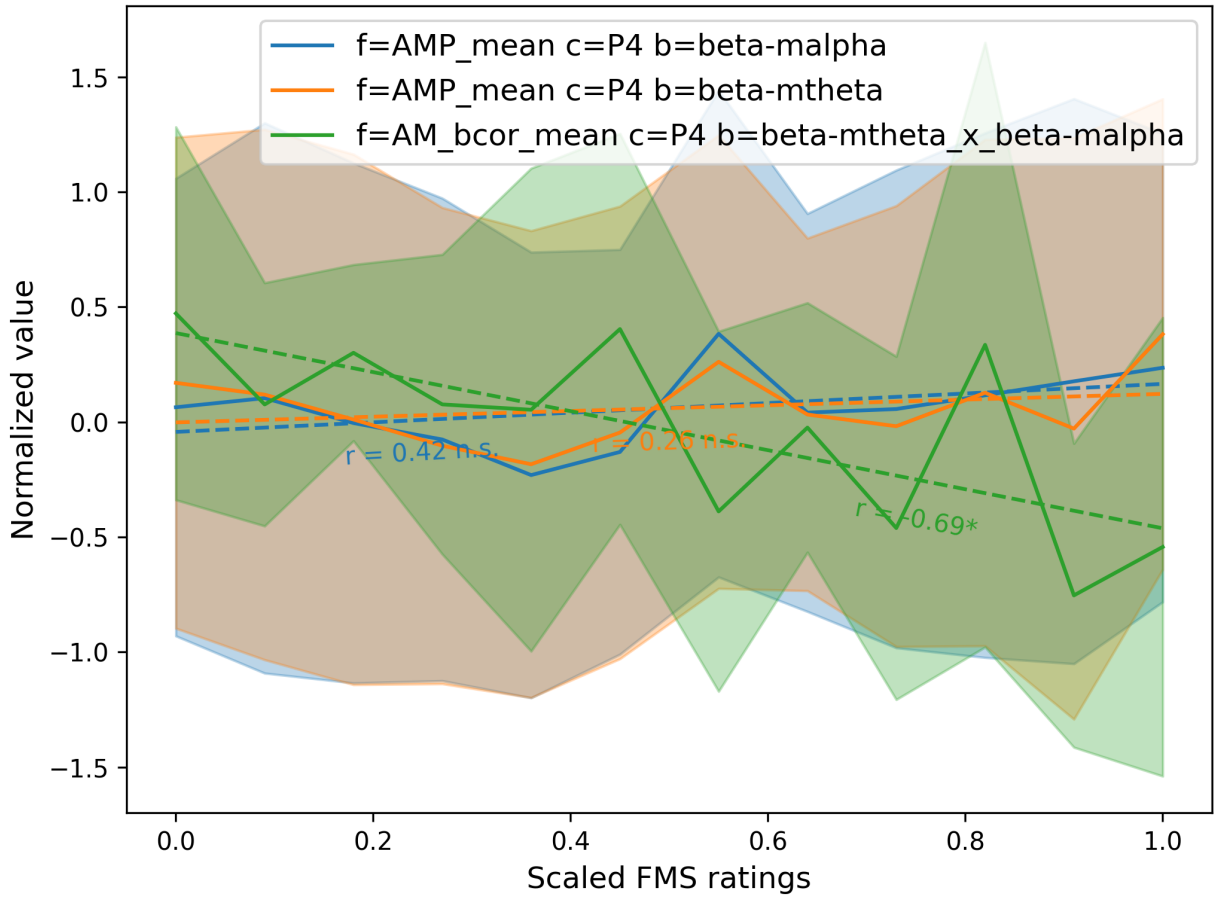

Figure 5.13 : Right Parietal Grand average feature value of AMP_mean_beta-malpha_P4 (blue), AMP_mean_beta-mtheta_P4 (orange) and AM_bcor_mean_P4_beta-mtheta_beta-malpha (green) across recordings as a function of normalized FMS ratings using ASR+ICLabel pre-processed dataset with 5s epoch size. A strong significant negative correlation is observed with AM_bcor_mean_P4_beta-mtheta_beta-malpha. Coefficients marked with * and n.s. represent the Pearson correlation between grand average and FMS ratings with a p-value < 0.05 and non-significance, respectively.

Pz, P4). As was discussed in Section 5.4.1, these bands tend to be more sensitive to head and eye movements artifacts, thus may be encoding such details.

Comparing Figure 5.17 with Figure 5.8, the presence of delta and theta bands in the latter remains limited. This is likely due to contamination by ocular and movement artifacts preserved by Minimal pipeline but removed by ASR+ICLabel. Notwithstanding, the previous analysis also showed the presence of theta band activity within the top features that overlapped the ASR+ICLabel and Minimal pre-processing approaches, thus suggesting that theta-band patterns may not be entirely attributed to artifacts, but may also convey some neurological origin related to cybersickness.

Table 5.2 shows the remaining top-21 features (out of total 44) from the CCPL and BCPL feature categories. As can be seen, the majority of the top features correspond to band coupling between amplitude modulated bands. The most recurring carrier band is gamma followed by beta, while the most recurring modulator band is theta.

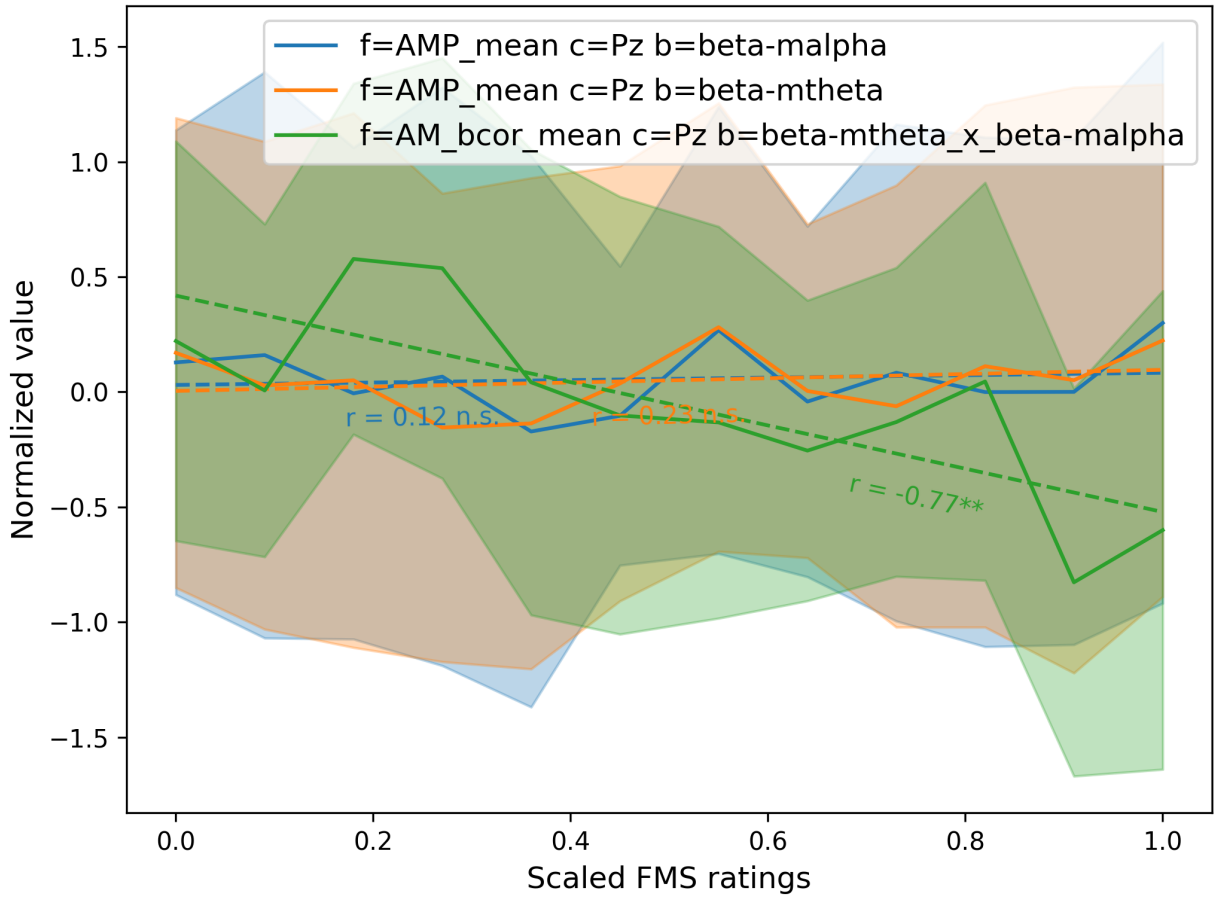

Figure 5.14 : Parietal Grand average feature value of AMP_mean_beta-malpha_Pz (blue), AMP_mean_beta-mtheta_Pz (orange) and AM_bcor_mean_Pz_beta-mtheta_beta-malpha (green) across subjects and sessions as a function of normalized FMS ratings using ASR+ICLabel pre-processed dataset. A strong significant negative correlation is observed with AM_bcor_mean_Pz_beta-mtheta_beta-malpha. Coefficients marked with ** and n.s. represent the Pearson correlation between grand average and FMS ratings with a p-value < 0.01 and non significance respectively.

5.4.5 Overall Cybersickness Characterization

Table 5.3 lists the final RMSE achieved between the real (normalized) FMS ratings and the predicted ones for each pre-processing strategy and epoch size. To gauge the significance of the results in the table over chance, a random classifier is also trained where the FMS ratings, which serve as regression labels, are randomized. As can be seen, across all tested configurations, performance significantly exceeded this chance level.

Overall, the 'Minimal' pre-processing approach achieved the lowest RMSE values with top features computed from 8-second epochs, achieving an RMSE of 0.234, significantly lower than chance-level (0.327), corroborating the importance of the multi-modal aspect achieved by leaving artifacts untouched. In contrast, the RegICA and ASR+ICLabel pre-processing approaches achieved their lowest RMSE values at higher epoch sizes. As these methods tend to remove artifacts, the

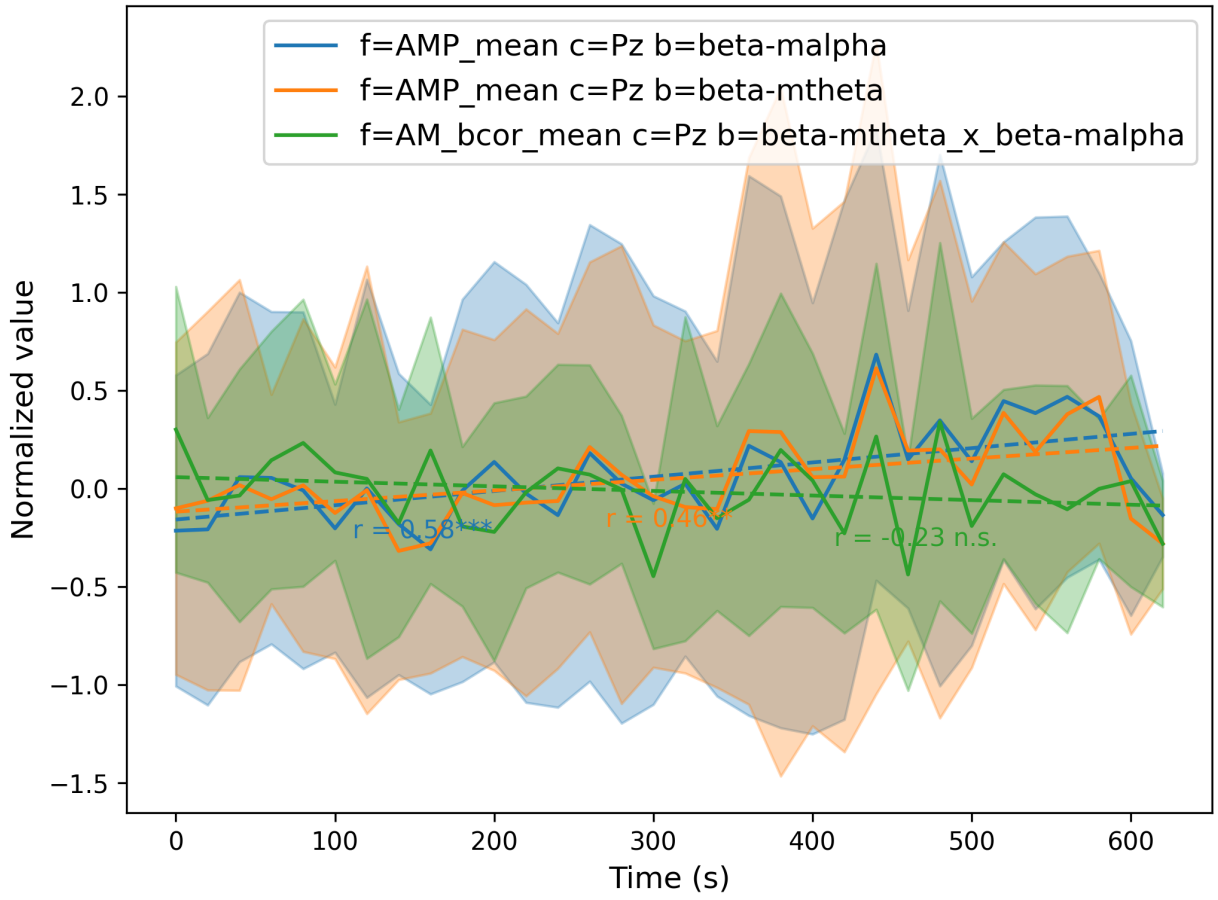

Figure 5.15 : Parietal Grand average feature value of AMP_mean_beta-malpha_Pz (blue), AMP_mean_beta-mtheta_Pz (orange) and AM_bcor_mean_Pz_beta-mtheta_beta-malpha (green) across subjects and sessions as a function of time using ASR+ICLabel pre-processed dataset. Both power beta-malpha and beta-mtheta features show a significant strong positive correlation with time. Coefficients marked with **, * and n.s. represent the Pearson correlation between grand average and FMS ratings with a p-value < 0.01, p-value < 0.05 and non significance, respectively.

regressors are relying solely on neural signatures for cybersickness prediction. In such cases, the longer duration epochs are needed to capture the neural underpinnings of cybersickness, which may be present in lower-frequency activity.

5.5 Discussion

In this study, we started with two main objectives: (1) to better understand the impact of artifact removal on EEG-based cybersickness prediction, and (2) to obtain more insights on the neural underpinnings of cybersickness via the use of new amplitude modulation features. Via a series of ablation studies, correlation analyses, and top-feature evaluations, our experiments have provided cues into these two objectives. In the subsequent sections, we discuss these findings in more detail.

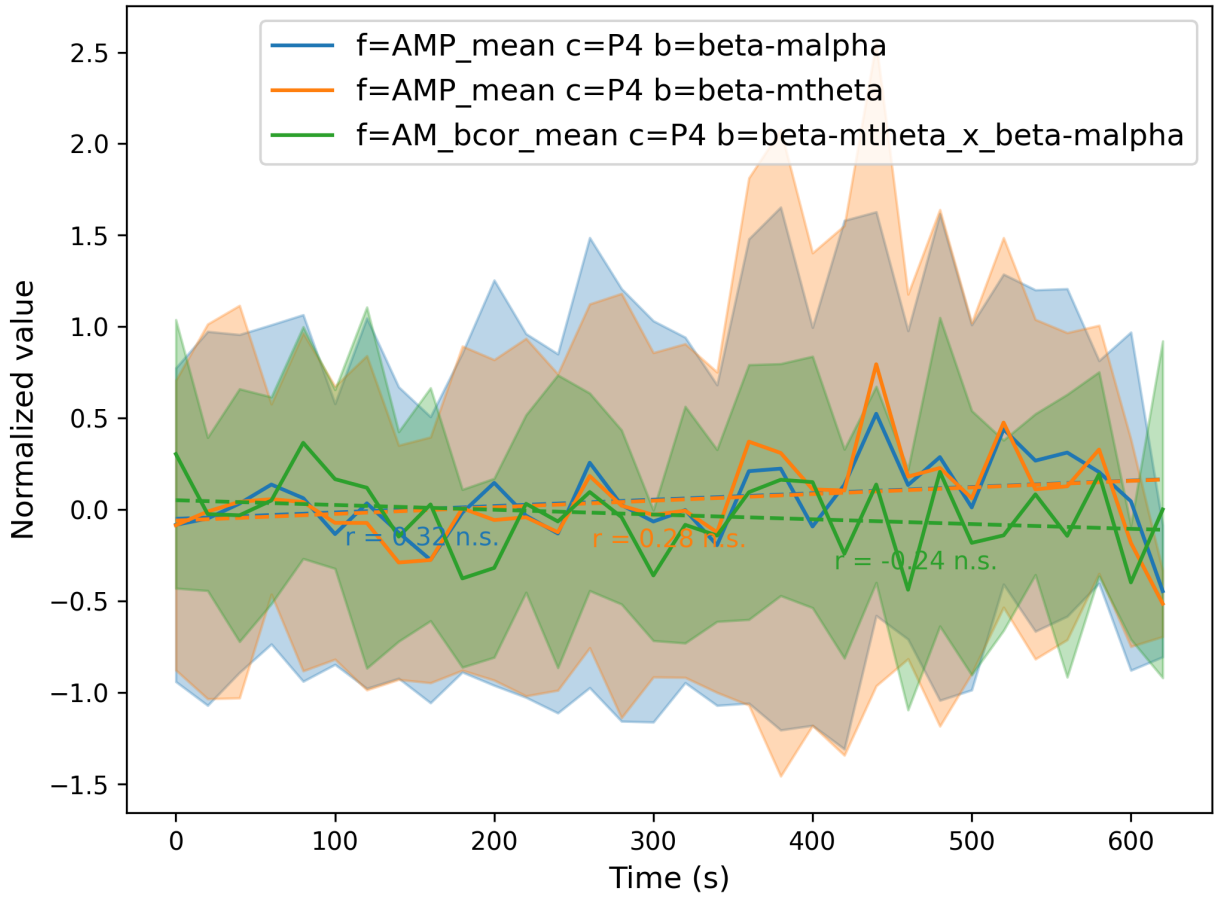

Figure 5.16 : Right Parietal Grand average feature value of AMP_mean_beta-malpha_P4 (blue), AMP_mean_beta-mtheta_P4 (orange) and AM_bcor_mean_P4_beta-mtheta_beta-malpha (green) across recordings as a function of time using ASR+ICLabel pre-processed dataset. Both power beta-malpha and beta-mtheta features show a weak positive correlation with time. Coefficients represent the Pearson correlation between grand average and FMS ratings. None of the correlations were significant as indicated by n.s.

5.5.1 To Pre-process or Not to Pre-process?

In EEG studies, the presence of artifacts can negatively influence the validity and interpretation of results (Zhou et al., 2023; Lopes et al., 2023; Bennett et al., 2021), as artifacts can take on various forms (Michel et al., 2019; Delorme, 2023; Jin et al., 2023) and overlap with neurological signals in spatial, temporal and spectral domains (Thompson et al., 2008; Chiarion et al., 2023). While this makes the use of pre-processing an essential step in EEG signal analysis, there is no universally accepted method. Algorithms are developed to target certain types of artifacts (e.g., (Robbins et al., 2020b; Yu et al., 2022b)) and each pre-processing method comes with its own set of advantages and limitations. As such, researchers must trade-off between effective artifact removal and minimal signal distortion (Bouazizi et al., 2024; Tajmirriahi et al., 2022; Bao et al., 2022).

Recently, the extensive use of AAR has been contested due to the excessive data distortions and destruction they might cause to the data (Chiarion et al., 2023; Delorme, 2023). For instance, ICA

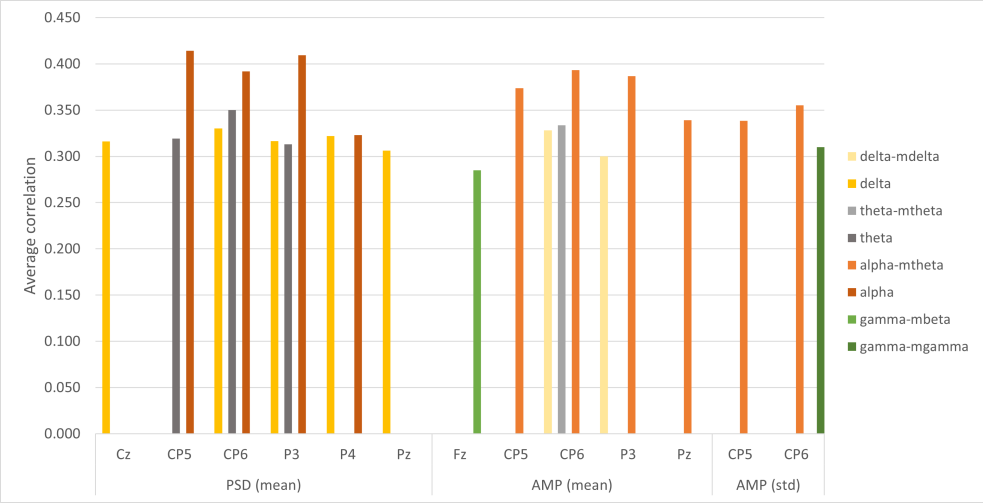

Figure 5.17 : Bar plot representing average correlation between feature data and FMS ratings from the top features list using Minimal pre-processing method that did not overlap with the other pre-processing pipelines. Only the AMP and PSD features are represented. The feature type and EEG electrodes are described in the x-axis, while the corresponding frequency bands are color coded (see figure legend).

Feature type	Band	Channel	Mean absolute correlation
beta	CCPL_std	Pz×P3	0.34
gamma-mtheta×gamma-malpha	AM_BCPL_mean	Fz	0.34
beta-malpha×beta-mbeta	AM_BCPL_mean	P4	0.33
alpha-mtheta×gamma-mbeta	AM_BCPL_mean	Fz	0.33
gamma-mtheta×gamma-malpha	AM_BCPL_mean	Pz	0.32
gamma-mbeta×gamma-mgamma	AM_BCPL_mean	P3	0.32
gamma-mdelta×gamma-malpha	AM_BCPL_mean	Pz	0.32
theta-mtheta×gamma-mbeta	AM_BCPL_mean	Cz	0.32
gamma-mtheta×gamma-malpha	AM_BCPL_mean	P3	0.32
theta-mtheta×gamma-mbeta	AM_BCPL_mean	P3	0.31
gamma-mdelta×gamma-mtheta	AM_BCPL_mean	CP6	0.31
beta-mdelta×beta-mtheta	AM_BCPL_mean	CP6	0.31
beta-mtheta×beta-malpha	AM_BCPL_mean	P4	0.31
beta-malpha×beta-mbeta	AM_BCPL_mean	P3	0.31
gamma-mtheta×gamma-mbeta	AM_BCPL_std	Fz	0.31
gamma-mtheta×gamma-malpha	AM_BCPL_mean	CP6	0.31
gamma-mdelta×gamma-malpha	AM_BCPL_mean	P3	0.30
gamma-mbeta×gamma-mgamma	AM_BCPL_std	CP5	0.30
gamma-mdelta×gamma-mtheta	AM_BCPL_mean	P3	0.30
beta-mdelta	AM_CCPL_std	Pz×P3	0.29
beta-mbeta×gamma-mgamma	AM_BCPL_mean	P4	0.29

Tableau 5.2 : Top-selected coupling features (BCPL, CCPL, AM-BCPL and AM-CCPL) identified using Minimal pre-processing across different epoch durations (2, 5, 8, 20, and 30 seconds).

	Minimal		REGICA		ASR+ICLabel	
Epoch size	Score	Random	Score	Random	Score	Random
2	0.253*	0.333	0.268*	0.337	0.254*	0.32
5	0.246*	0.331	0.249*	0.323	**0.247***	0.327
8	**0.234***	0.327	0.262*	0.326	0.254*	0.327
20	0.258*	0.327	0.248*	0.327	0.248*	0.309
30	0.25*	0.324	**0.245***	0.329	0.257*	0.332

Tableau 5.3 : RMSE values derived from a 5-fold cross-validation regression analysis, assessing the impact of various pre-processing techniques over different epoch durations on regression performance. The benchmark for random performance was established through successive permutation tests and random FMS ratings. Entries significantly surpassing this benchmark ($p < 0.05$) are denoted by an asterisk (*). Lower RMSE values, indicative of best model prediction across epoch sizes, are emphasized in bold for each pre-processing condition.

has been shown to produce distortions due to the non-stationary nature of EEG signals (Bouazizi et al., 2024; Chiarion et al., 2023). Additionally, it may mix neurological and non-neurological sources within the same components when the number of channels is much smaller than the number of sources (Thompson et al., 2008; Sun et al., 2023; Chaddad et al., 2023), which can often be the case in VR applications.

As with most EEG studies, our results also indicate that non-neurological activity is recorded along with neurological activity. More specifically, we show that ocular activity and head movements are observed in the lower frequencies of the EEG spectrum, such as delta and theta, and these were selected as top-features in the Minimal processing case. In turn, other features from these regions, but measuring temporal dynamics information, could be indicative of regulatory and coordinating roles in cognitive processes.

Unlike other studies, however, for cybersickness prediction, the presence of physiological artifacts can serve as useful sources of multimodal information to predict cybersickness levels (Chang et al., 2021; Dennison et al., 2016; Islam et al., 2021, 2022b; Shimada et al., 2023; Jeong et al., 2022). The obtained findings showed that Minimal processing, indeed, resulted in the lowest cybersickness level prediction error. Therefore, if one is interested in maximizing cybersickness prediction accuracy, performing minimal pre-processing may be the way to go. It is suggested, however, that careful scrutiny of the top-used features be evaluated, to ensure that indeed the developed models are also relying on relevant neural data, and not just physiological artifacts. Furthermore, the main sources of artifacts should be precisely identified when implementing an EEG-embedded multimodal system, as not all artifacts are useful for predictions and may negatively impact outcomes.

5.5.2 Cybersickness and Neural Insights

5.5.2.1 Beta Band Insights

We showed that the features measuring CCPL and AM-CCPL variability in the centro-parietal region (channels Cz, CP5, P3, Pz, P4) within the beta and beta-mtheta bands indicated an increase in coupling variability as the FMS score increased. With the increase in cybersickness symptoms reflected by the FMS score, not only did we observe a decrease in the interaction between distant regions of the parietal area, but their connections also become more unstable.

Although a decrease in beta power is the most recurrent pattern related to cybersickness in the literature (Chang et al., 2023b; Jang et al., 2022; Achanccaray et al., 2023), some studies showed that spectral activity above 11 Hz showed no significant difference (Nürnberger et al., 2021) (or inconsistent trend across subjects and electrodes (Ozkan et al., 2023)) between baseline and severe cybersickness conditions. In our analyses, features measuring beta power were not representative of the most correlated features with cybersickness. Thus, since most of the observed beta activity was related to coupling measures, our results better align with the theory that beta is linked to the temporary cohesion of distant cortical regions (Yang et al., 2022b; Li et al., 2021a), rather than due to a specific change in local activity.

Overall, cortical networks formed within the beta band have been associated with fundamental function of complex cognitive processes, such as active waiting and anticipation of a stimulus (Betti et al., 2021), temporary retention of sensory information (Liang et al., 2021; Silberstein, 2006a), and the dynamic allocation of cognitive resources (Betti et al., 2021). The dynamic nature of these networks explains the rapid changes in activity observed in the beta band, thereby leading to the disparity in observations across cybersickness studies. Moreover, power change observed during high levels of cybersickness might be attributed to cybersickness related physiological states such as arousal (Agić et al., 2019), cognitive effort (Arafat et al., 2018; Li et al., 2021a), as well as visual and mental fatigue (Foong et al., 2019; Yue et al., 2019).

Moreover, decreases in the correlation between the beta-mtheta and beta-malpha bands at the Pz and P4 electrodes were observed as the intensity of the cybersickness symptoms increased. As shown in Figures 5.14 and 5.13, the power of the two beta-malpha and beta-mtheta bands increases with the FMS score, and their correlation decreases. These findings corroborate the importance of the AM features in capturing the temporal dynamics of the beta band.

According to the literature, the theta band plays a role in the temporal organization of cognitive processes (Herweg et al., 2016; Popov et al., 2018). Therefore, we hypothesize that beta-mtheta may be linked to the process of integration of sensory information mentioned earlier. Moreover, since alpha is known to reflect selective inhibition of population of neurons (as per (Ahn et al., 2021) and (Sauseng et al., 2005)), and beta is associated with intense cognitive activity ((Borra

et al., 2023) and (Ghiani et al., 2021)), the beta-malpha feature may reflect a selective attention mechanism. Although alpha and beta are associated with opposite mechanisms, it is hypothesized that their interaction may serve a complementary role in the integration of extracted visual features into a coherent representation of the object (Di Dona et al., 2023). The proposed AM measures may be able to capturing and quantifying this interaction.

5.5.2.2 Alpha Band Insights

In addition to its interaction with beta, the alpha band power in the parietal cortex (channels P3, P4) was also highlighted in the analysis of the most correlated features. The increase in alpha activity in this area is indicative of sensory information processing inhibition in response to the sensory conflict induced by the VR experience. This activity appears to be a reliable marker of cybersickness, as this pattern is recurrent across EEG studies (Kim et al., 2019; Aboud, 2023; Ahn et al., 2021; Yang et al., 2022a).

Interestingly, the increase in alpha band identified by PSD features co-occurred with an increase in alpha-mtheta feature, suggesting that theta may play a regulatory role on inhibition similarly to what is observed with the beta band. While theta, alpha, and beta bands seem to have an intricate hierarchical role aligning with the top-down theory, the location of relevant activity in the cortex provides additional insights. In addition to revealing interactions between AM bands that suggest the coordination of distinct cognitive processes, AM features allow a better understanding of the nature of neurological processes, particularly those linked to top-down mechanisms.

5.5.2.3 Gamma Band Insights

The analysis the top-features obtained from the Minimal pre-processing method revealed the presence of activity in the gamma band potentially related to artifacts. Figure 5.17 showed that the average power in amplitude of gamma-mbeta was correlated with FMS scores, while Figure 5.12 showed the presence of average coupling of the gamma band with other AM bands present in Table 5.2. However, the presence of gamma modulated by theta and alpha in the top BCPL features presented in Figure 5.12 suggests rather an underlying neurological origin related to the symptom of cybersickness. Therefore, an increase in the coupling of the gamma-mtheta band would not be caused by the presence of artifacts but would serve as an additional marker of the brain's cognitive state during virtual reality sickness. Specifically, the fact that gamma activity is regulated by low-frequency oscillations suggests downward control mechanisms (Ahn et al., 2021).

The EEG high-frequency range, comprised of the gamma and beta bands, is thought to reflect intense local cognitive activity, as indicated by various studies (Freeman et al., 2016; Palva et al., 2012; Jerbi et al., 2010; Jensen et al., 2010). These bands are often observed in the occipito-parietal

region as correlated with increased cybersickness symptoms (Yang et al., 2022a). Given these findings, the gamma-band activity observed during the participants' exposure to the VR simulation can be, similarly to the beta band, attributed to sensory information processing. However, both bands have separate sources and serve different roles. Gamma rhythms often involve interactions between excitatory pyramidal cells and fast-spiking inter-neurons in the formation of cell assemblies (Neske et al., 2016; Nunez et al., 2010). In contrast, beta band rhythms mainly originating from gap junction–connected bursting pyramidal cells enable the binding of different neural assemblies thereby allowing a simultaneous manipulation of past and current input and the integration from different modalities (Alavash et al., 2017; Kopell et al., 2010).

5.5.2.4 Brain Regions and Lateralization Insights

The increase in coupling variability observed in Figure 5.11 for the beta (CCPL_std) and beta-mtheta (AM_CCPL_std) bands was predominant in the left hemisphere (i.e., the features most correlated with the FMS score in the beta-mtheta band concern the coupling between the Pz electrode and the P3 and Cz electrodes, and in the beta band between the CP5 electrode and the P3 and P4 electrodes, as well as the coupling between P3 and Pz). The mean coupling measurement (AM_CCPL_mean and CCPL_mean), in turn, was more correlated with the FMS ratings on the right hemisphere (i.e., with P4 and CP6 electrodes).

In addition, the left centro-parietal region (channels CP5, P3) exhibited highly variable power in the alpha-mdelta band, thus aligning with findings from (Angioletti et al., 2022). According to the study, increased delta band activity and decreased alpha band activity in the centro-temporal cortex were indicative of a shift in attention towards endogenous sensory information. This lateralization of activity has been recognized in the literature, with right-hemisphere parietal activity associated with visuospatial attention to the environment, whereas the left hemisphere has shown to be responsible for motor coordination and planning related to proprioception (Rushworth et al., 2001).

In contrast, when processing visuo-spatial information, the superior parietal lobe and the primary visual cortex are activated (Rolls, 2020; Li et al., 2018; Andersson et al., 2019), which have nearest electrodes Cz, Pz, P3, Pz, and P4. Consistent with these studies, we posit that the coupling variability is associated with active cognitive processes in this area, particularly those involving proprioceptive information rather than visual information. This implies that shifts of attention towards proprioceptive information may either instigate or respond to cybersickness. This hemispheric phenomenon during cybersickness was well captured by the new AM features.

In addition to the lateralized role, the study in (Limanowski et al., 2020) also revealed significant bilateral activity in the superior parietal lobe – covered by electrodes Pz and Cz – where its role would be to resolve inter-sensory conflict, enabling the maintenance of a unique body representation. Therefore, this region plays an important role in the management of the cognitive processes that process sensory information.

Interestingly, within Cz, an increasing alpha-mdelta power observed in Figure 5.8 was accompanied by an increase in its coupling with the beta-mdelta and beta-mbeta features over Cz and Fz observed in Figure 5.12. This coupling was shown with the mutual information measurement analysis, thus suggesting a nonlinear relationship between alpha and beta band activity.

Moreover, Figure 5.12 showed that the delta band frequently appears to modulate the amplitude of both the alpha and beta bands, thereby controlling their activity. This observation supports the top-down control theory, which suggests long-distance control from the brain's decision-making centers to local cortical activity.

5.5.3 Limitations and Future Work

This research presents some limitations. First, the use of a non-linear SVR kernel made it difficult to analyze feature ranking by inherent regularization, which is possible only with linear kernels. As a result, we relied on Spearman correlation for feature ranking, which does not consider the interaction between features. Future work may explore the use of more advanced feature selection methods that take such interactions into account, such as the Minimum redundancy maximum relevance (mRMR) (Ding et al., 2005).

Moreover, here we relied on the efficiency metrics for pre-processing algorithms based on the mutual information difference with head accelerometer and one EOG time serie. Other artifacts may contaminate the EEG signals, such as muscle movements, poor electrode-skin contact, and sweat, to name few. Continuous measurement of such signals are more challenging, but alternate modalities, such as galvanic skin response, facial electromyography (EMG), or impedance measurements may provide additional cues for future works. Emerging VR headsets are already including such modalities directly into the head-mounted display, thus facilitating this type of analyses in the future.

Lastly, the proposed work relied on publicly-available data, which was collected from a limited number of participants, of which not all of them completed the full task. As such, a large variability across subjects has been seen, especially at higher FMS rating levels. Future work could explore the use of different cross-subject generalization tools (Albuquerque et al., 2022).

5.6 Conclusion

In this study, we sought to answer two main research questions: (1) what role does EEG pre-processing play on overall cybersickness characterization?, and (2) what neural patterns can be indicative of cybersickness levels? To help answer these questions, we processed a publicly-available EEG-cybersickness dataset with three pre-processing methods, from minimal to more complex methods removing head and eye movements, as well as explored several benchmark power spectral and coupling features. To assist with question #2, we also explored new amplitude

modulation power and coupling measures to capture interactivity between frequency bands and channels. We showed that, indeed, minimal processing kept head and eye movement related cues that were important for cybersickness detection, but did not provide a full glimpse into the neural patterns associated with cybersickness. To this end, a more complex pre-processing method was used. Ultimately, several AM and coupling measures showed to be top-performing features, thus emphasizing their complementarity to PSD parameters and their importance for cybersickness prediction.

6 CONCLUSION

6.1 Summary of contributions

The contributions of this dissertation can be summarized in two major aspects.

6.1.1 Amplitude modulation as a better representation of cortical activity

In Chapter 3, we propose a new feature set for aBCI, based on the amplitude modulation dynamics of different EEG sub-bands. Through extensive experimentation, we demonstrated the benefits of the proposed features as well as their complementarity with conventional power spectral features. An in-depth discussion was provided to explore the complex cognitive mechanisms measured by the new features and to conjecture their roles in improving BCI accuracy for different mental tasks. Moreover, the results presented in Chapters 4 and 5 show the importance of the proposed measures for passive BCI applications used in mental workload and cybersickness prediction. Altogether, our results demonstrate the advantage of combining amplitude modulation, coupling, and PSD, as each of these features captures specific attributes of brain activity.

6.1.2 Impact of automated artifact removal algorithm in practical settings

Chapters 4 and 5 present a comparison of different AAR algorithms under two practical settings for BCI: highly ambulatory users and virtual reality simulations. In Chapter 4, experimental results showed that combining an adaptive filtering scheme with other traditional enhancement methods allowed for effective removal of movement artifacts in extreme recording settings. With this optimal pre-processing strategy, we were able to achieve the best mental workload prediction accuracy and find insightful information about the underlying cognitive activity of Mental workload and its interaction with Physical activity. Lastly, in Chapter 5, we processed a publicly available EEG-cybersickness dataset with three pre-processing methods, from minimal to more complex methods for removing head and eye movements. Our results highlight the importance of context-aware pre-processing strategies for both the interpretability of brain activity and improved accuracy of BCI.

6.2 Future research

6.2.1 Deep learning

Despite the major drawbacks of deep-learning techniques, the field is constantly improving, and recent innovations have progressively addressed many of the challenges highlighted here. For example, attention-based models (Cisotto et al., 2020; Toa et al., 2021) have context-aware capabilities that improve signal-to-noise ratio and accuracy. In addition, the attention layer provides straightforward information on the important aspects of the input data that justify model decisions. Moreover, recently, research has focused on AI explanability rather than performance, with the development of eXplainable AI (XAI) techniques (Islam et al., 2022a; Morabito et al., 2023). These proposed techniques may provide important insights for improved BCI usage and interpretability. In this context, incorporating neuroscience-supported features, such as the proposed AM ones, into deep learning models might provide a direct relationship between specific neuronal mechanisms supporting a prediction. Because AM is a fundamental mechanism in the human brain, AM features can be used in transfer learning models to further mitigate intra- and inter-subject variability (Bagheri et al., 2022).

6.2.2 Adaptive BCI

As discussed in Chapter 1, the user's psychological state significantly influences the performance of pattern detection in EEG-based active BCI. Since passive BCI are typically employed to monitor user mental state using biomarkers, combining them with active BCI can potentially improve explanability and adaptibility of BCI. Context-aware BCI can rely on passive BCI biomarkers working simultaneously with the active BCI to determine the best paradigms or change strategies to maximize accuracy depending on the situation.

6.2.3 Source localization

EEG sensors have an excellent temporal resolution; however, due to the physical properties of tissues and skull-only spectral activity below 100 Hz, they have sufficient signal-to-noise ratio to be useful. While spectrotemporal activity is important, spatial sources of activity and communication between distant local circuits also convey critical information (Shepherd, 2003). One workaround is to increase the spatial resolution of EEG by taking advantage of multiple EEG electrodes. The use of a source localization algorithms combined with a powerful spectrotemporal description, such as AM features, may further improve the accuracy and reduce the delay of modern BCI systems. Development of such tools should be explored as future work.

6.2.4 Optimal subject-specific band selection and calibration

Our study employs amplitude modulation features based on conventional frequency bands (i.e., delta, theta, alpha, beta, and gamma). However, numerous studies have highlighted the importance of personalizing the limits of such bands on a per user basis to reduce inter- and intra-subject variations. For instance, in the spectral domain, personalizing frequency bands, such as the individual alpha frequency (IAF), is an approach that adapts the analysis to an individual's own rhythm (Huster et al., 2014; Sciaraffa et al., 2022). Similarly, Empirical Mode Decomposition (EMD) allows the decomposition of the EEG signal into specific oscillatory components, enabling this method to adapt to signals from different individuals or different conditions. Extracting characteristics specific to a subject is also possible in the spatial domain (Guger et al., 2000). Therefore, it would be interesting in future projects to evaluate the impact of modulation features based on subject-specific frequency bands. These bands can be identified in the calibration phase before BCI is used. This was shown useful in the past for Alzheimer's disease diagnosis, for example (Lopes et al., 2021).

By extension, it would also be interesting to use, during the calibration phase, well-known paradigm-specific features within EEG data as calibration markers and to assess the likeliness of the BCI to work with a new subject. For example, the use of Steady-State Visual Evoked Potentials (SSVEP) in conjunction with source localization can help identify with greater accuracy the small structural differences in the cortex that are unique to each individual. Additionally, the spectral analysis of motor cortex signals during a motor imagery task can help estimate the quality of the brain-to-computer link and thus estimate the performance of the BCI for that user.

Ultimately, the study of patterns in extreme frequency bands is an important direction to explore. Neurotransmitters play a crucial role in modulating neuronal excitability. For example, changes in nor-epinephrine levels modulate the frequency of spike trains (spike frequency adaptation) in the order of minutes (Shepherd, 2003). Because this mechanism is directly linked to an individual's level of attention, the analysis of amplitude modulation of conventional frequency bands by ultralow frequencies (of the order of 10^{-3} Hz) might be a promising new marker for passive BCI.

6.3 Conclusion

BCI have recently undergone a transition from a technology designed for laboratory studies and specific medical treatment cases to a tool accessible to the general public and recognized for their usefulness in many industrial sectors. Innovations in deep learning, VR equipment, and electronic components have significantly influenced this development. However, BCI technologies still face several obstacles, such as reduced robustness, performance variability from one user to another, and a lack of interpretability of the measured brain activity. In this thesis, we hope to have contributed to the advancement of the field by proposing two innovations: a better representation of EEG signals through the use of Amplitude Modulation features, and their combined effect with optimized pre-

processing methods to enable reliable, generalizable, and interpretable results applicable to real-life situations and scenarios.

BIBLIOGRAPHY

Abbasi O, Gross J (2020) Beta-band oscillations play an essential role in motor–auditory interactions. *Human brain mapping*, 41(3):656–665.

Aboud A (2023) Identifying cybersickness features from eeg data using deep learning. Mémoire de maîtrise, A. Aboud.

Achanccaray D, Sumioka H (2023) A physiological approach of presence and vr sickness in simulated teleoperated social tasks. *2023 IEEE International Conference on Systems, Man, and Cybernetics (SMC)*, IEEE, pages 4562–4567.

Afshani F, Shalbaf A, Shalbaf R, Sleigh J (2019) Frontal–temporal functional connectivity of eeg signal by standardized permutation mutual information during anesthesia. *Cognitive neurodynamics*, 13:531–540.

Agarwal P, Kumar S (2023) Eeg-based imagined words classification using hilbert transform and deep networks. *Multimedia Tools and Applications*, pages 1–24.

Aggarwal S, Chugh N (2019) Signal processing techniques for motor imagery brain computer interface: A review. *Array*, 1:100003.

Aghajani H, Omurtag A (2016) Assessment of mental workload by eeg+ fnirs. *2016 38th Annual International Conference of the IEEE Engineering in Medicine and Biology Society (EMBC)*, IEEE, pages 3773–3776.

Agić A, Mandić L (2019) Evaluation of cybersickness in virtual reality in driving simulator. *Acta graphica: znanstveni časopis za tiskarstvo i grafičke komunikacije*, 30(2):11–16.

Ahn M, Lee M, Choi J, Jun SC (2014) A review of brain-computer interface games and an opinion survey from researchers, developers and users. *Sensors*, 14(8):14601–14633.

Ahn S, Gleghorn D, Doudican B, Fröhlich F, Cha YH (2021) Transcranial alternating current stimulation reduces network hypersynchrony and persistent vertigo. *Neuromodulation: Technology at the Neural Interface*, 24(5):960–968.

Akhand M, Maria MA, Kamal MAS, Shimamura T (2024) Emotion recognition from eeg signal enhancing feature map using partial mutual information. *Biomedical Signal Processing and Control*, 88:105691.

Al-Shargie F (2019) Multilevel assessment of mental stress using svm with ecoc: an eeg approach.

Alahmari A (2021) Neuroimaging role in mental illnesses j. *International Journal of Neural Plasticity*, 4(1).

Alavash M, Daube C, Wöstmann M, Brandmeyer A, Obleser J (2017) Large-scale network dynamics of beta-band oscillations underlie auditory perceptual decision-making. *Network Neuroscience*, 1(2):166–191.

Albanese GA, Marini F, Morasso P, Campus C, Zenzeri J (2023) μ-band desynchronization in the contralateral central and central-parietal areas predicts proprioceptive acuity. *Frontiers in Human Neuroscience*, 17:1000832.

Albuquerque I, Monteiro J, Rosanne O, Falk TH (2022) Estimating distribution shifts for predicting cross-subject generalization in electroencephalography-based mental workload assessment. *Frontiers in Artificial Intelligence*, 5:992732.

Albuquerque I, Monteiro J, Rosanne O, Tiwari A, Gagnon JF, Falk TH (2019a) Cross-subject statistical shift estimation for generalized electroencephalography-based mental workload assessment. *2019 IEEE International Conference on Systems, Man and Cybernetics (SMC)*, IEEE, pages 3647–3653.

Albuquerque I, Rosanne O, Gagnon JF, Tremblay S, Falk TH (2019b) Fusion of spectral and spectro-temporal eeg features for mental workload assessment under different levels of physical activity. *2019 9th International IEEE/EMBS Conference on Neural Engineering (NER)*, IEEE, pages 311–314.

Albuquerque I, Tiwari A, Gagnon JF, Lafond D, Parent M, Tremblay S, Falk T (2018) On the analysis of EEG features for mental workload assessment during physical activity. *2018 IEEE International Conference on Systems, Man, and Cybernetics (SMC)*, IEEE, pages 538–543.

Albuquerque I, Tiwari A, Parent M, Cassani R, Gagnon JF, Lafond D, Tremblay S, Falk TH (2020) Wauc: a multi-modal database for mental workload assessment under physical activity. *Frontiers in Neuroscience*, 14.

Andersson P, Ragni F, Lingnau A (2019) Visual imagery during real-time fmri neurofeedback from occipital and superior parietal cortex. *NeuroImage*, 200:332–343.

Angelov V, Petkov E, Shipkovenski G, Kalushkov T (2020) Modern virtual reality headsets. *2020 International congress on human-computer interaction, optimization and robotic applications (HORA)*, IEEE, pages 1–5.

Angioletti L, Balconi M (2022) Delta-alpha eeg pattern reflects the interoceptive focus effect on interpersonal motor synchronization. *Frontiers in Neuroergonomics*, 3:1012810.

Angsuwatanakul T, O'Reilly J, Ounjai K, Kaewkamnerdpong B, Iramina K (2020) Multiscale entropy as a new feature for eeg and fnirs analysis. *Entropy*, 22(2):189.

Anwar AR, Muthalib M, Perrey S, Galka A, Granert O, Wolff S, Heute U, Deuschl G, Raethjen J, Muthuraman M (2016) Effective connectivity of cortical sensorimotor networks during finger movement tasks: a simultaneous fnirs, fmri, eeg study. *Brain topography*, 29:645–660.

Aoki F, Fetz E, Shupe L, Lettich E, Ojemann G (1999) Increased gamma-range activity in human sensorimotor cortex during performance of visuomotor tasks. *Clinical Neurophysiology*, 110(3): 524–537.

Arafat IM, Ferdous SMS, Quarles J (2018) Cybersickness-provoking virtual reality alters brain signals of persons with multiple sclerosis. *2018 IEEE conference on virtual reality and 3D user interfaces (VR)*, IEEE, pages 1–120.

Aricò P, Borghini G, Di Flumeri G, Colosimo A, Bonelli S, Golfetti A, Pozzi S, Imbert JP, Granger G, Benhacene R et al. (2016) Adaptive automation triggered by eeg-based mental workload index: a passive brain-computer interface application in realistic air traffic control environment. *Frontiers in human neuroscience*, 10:539.

Aubonnet R, Hassan M, Mheich A, Di Lorenzo G, Petersen H, Gargiulo P (2023) Brain network dynamics in the alpha band during a complex postural control task. *Journal of Neural Engineering*, 20(2):026030.

Autthasan P, Du X, Arnin J, Lamyai S, Perera M, Itthipuripat S, Yagi T, Manoonpong P, Wilaiprasitporn T (2019) A single-channel consumer-grade eeg device for brain–computer interface: Enhancing detection of ssvep and its amplitude modulation. *IEEE Sensors Journal*, 20(6):3366–3378.

Aydore S, Pantazis D, Leahy RM (2013) A note on the phase locking value and its properties. *Neuroimage*, 74:231–244.

Azevedo FA, Carvalho LR, Grinberg LT, Farfel JM, Ferretti RE, Leite RE, Filho WJ, Lent R, Herculano-Houzel S (2009) Equal numbers of neuronal and nonneuronal cells make the human brain an isometrically scaled-up primate brain. *Journal of Comparative Neurology*, 513(5):532–541.

Bagheri M, Power SD (2022) Simultaneous classification of both mental workload and stress level suitable for an online passive brain–computer interface. *Sensors*, 22(2):535.

Banville H, Gupta R, Falk TH et al. (2017) Mental task evaluation for hybrid nirs-eeg brain-computer interfaces. *Computational intelligence and neuroscience*, 2017(1):3524208.

Bao C, Hao Z, Dou W (2022) Automatic removal of scalp eeg artifacts using an interpretable hybrid deep learning method. *2022 IEEE International Conference on Bioinformatics and Biomedicine (BIBM)*, IEEE, pages 1451–1456.

Barlow JS (1985) Methods of analysis of nonstationary eegs, with emphasis on segmentation techniques: a comparative review. *Journal of clinical neurophysiology*, 2(3):267–304.

Bascil MS, Tesneli AY, Temurtas F (2016) Spectral feature extraction of eeg signals and pattern recognition during mental tasks of 2-d cursor movements for bci using svm and ann. *Australasian physical & engineering sciences in medicine*, 39:665–676.

Basha D, Kalia SK, Hodaie M, Lopez Rios AL, Lozano AM, Hutchison WD (2023) Beta band oscillations in the motor thalamus are modulated by visuomotor coordination in essential tremor patients. *Frontiers in Human Neuroscience*, 17:1082196.

Bell MA, Cuevas K (2012) Using eeg to study cognitive development: Issues and practices. *Journal of cognition and development*, 13(3):281–294.

Bennett JD, John SE, Grayden DB, Burkitt AN (2021) Universal neurophysiological interpretation of eeg brain-computer interfaces. *2021 9th International Winter Conference on Brain-Computer Interface (BCI)*, IEEE, pages 1–6.

Bernal G, Hidalgo N, Russomanno C, Maes P (2022) Galea: A physiological sensing system for behavioral research in virtual environments. *2022 IEEE Conference on Virtual Reality and 3D User Interfaces (VR)*, IEEE, pages 66–76.

Betti V, Della Penna S, de Pasquale F, Corbetta M (2021) Spontaneous beta band rhythms in the predictive coding of natural stimuli. *The Neuroscientist*, 27(2):184–201.

Bhise PR, Kulkarni SB, Aldhaheri TA (2023) Statistical analysis of cognitive attention in students during learning using neurosky mindwave ii. *Grenze International Journal of Engineering & Technology (GIJET)*, 9(1).

Bigdely-Shamlo N, Touryan J, Ojeda A, Kothe C, Mullen T, Robbins K (2020) Automated eeg mega-analysis i: Spectral and amplitude characteristics across studies. *NeuroImage*, 207:116361.

Blum AL, Langley P (1997) Selection of relevant features and examples in machine learning. *Artificial intelligence*, 97(1-2):245–271.

Bonaci T, Calo R, Chizeck HJ (2014) App stores for the brain: Privacy & security in brain-computer interfaces. *2014 IEEE International Symposium on Ethics in Science, Technology and Engineering*, IEEE, pages 1–7.

Bondar' A, Fedotchev A (2000) Concerning the amplitude modulation of the human eeg. *Human Physiology*, 26:393–399.

Borg G (1998) *Borg's perceived exertion and pain scales.* Human kinetics.

Borghini G, Astolfi L, Vecchiato G, Mattia D, Babiloni F (2014) Measuring neurophysiological signals in aircraft pilots and car drivers for the assessment of mental workload, fatigue and drowsiness. *Neuroscience & Biobehavioral Reviews*, 44:58–75.

Borghini G, Vecchiato G, Toppi J, Astolfi L, Maglione A, Isabella R, Caltagirone C, Kong W, Wei D, Zhou Z et al. (2012) Assessment of mental fatigue during car driving by using high resolution eeg activity and neurophysiologic indices. *2012 Annual International Conference of the IEEE Engineering in Medicine and Biology Society*, IEEE, pages 6442–6445.

Borra D, Fantozzi S, Bisi MC, Magosso E (2023) Modulations of cortical power and connectivity in alpha and beta bands during the preparation of reaching movements. *Sensors*, 23(7):3530.

Bouazizi S, Ltifi H (2024) Enhancing accuracy and interpretability in eeg-based medical decision making using an explainable ensemble learning framework application for stroke prediction. *Decision Support Systems*, 178:114126.

Bourdillon P, Hermann B, Guénot M, Bastuji H, Isnard J, King JR, Sitt J, Naccache L (2020) Brain-scale cortico-cortical functional connectivity in the delta-theta band is a robust signature of conscious states: an intracranial and scalp eeg study. *Scientific Reports*, 10(1):14037.

Bouten CV, Koekkoek KT, Verduin M, Kodde R, Janssen JD (1997) A triaxial accelerometer and portable data processing unit for the assessment of daily physical activity. *IEEE transactions on biomedical engineering*, 44(3):136–147.

Brooks H, Goodman MS, Bowie CR, Zomorrodi R, Blumberger DM, Butters MA, Daskalakis ZJ, Fischer CE, Flint A, Herrmann N et al. (2020) Theta–gamma coupling and ordering information: a stable brain–behavior relationship across cognitive tasks and clinical conditions. *Neuropsychopharmacology*, 45(12):2038–2047.

Burbank DP, Webster JG (1978) Reducing skin potential motion artefact by skin abrasion. *Medical and Biological Engineering and Computing*, 16(1):31–38.

Burgess AP (2013) On the interpretation of synchronization in eeg hyperscanning studies: a cautionary note. *Frontiers in human neuroscience*, 7:881.

Buzsáki G, Anastassiou CA, Koch C (2012) The origin of extracellular fields and currents—eeg, ecog, lfp and spikes. *Nature reviews neuroscience*, 13(6):407–420.

Cassani R, Falk TH (2018) Spectrotemporal modeling of biomedical signals: Theoretical foundation and applications. *Reference Module in Biomedical Sciences*.

Cassani R, Falk TH (2019) Alzheimer's disease diagnosis and severity level detection based on electroencephalography modulation spectral "patch" features. *IEEE journal of biomedical and health informatics*, 24(7):1982–1993.

Cassani R, Falk TH, Fraga FJ, Kanda PA, Anghinah R (2014) The effects of automated artifact removal algorithms on electroencephalography-based alzheimer's disease diagnosis. *Frontiers in aging neuroscience*, 6:55.

Cassani R, Moinnereau MA, Ivanescu L, Rosanne O, Falk TH (2020a) Neural interface instrumented virtual reality headsets: Toward next-generation immersive applications. *IEEE Systems, Man, and Cybernetics Magazine*, 6(3):20–28.

Cassani R, Novak GS, Falk TH, Oliveira AA (2020b) Virtual reality and non-invasive brain stimulation for rehabilitation applications: a systematic review. *Journal of neuroengineering and rehabilitation*, 17:1–16.

Castellanos NP, Makarov VA (2006) Recovering eeg brain signals: artifact suppression with wavelet enhanced independent component analysis. *Journal of neuroscience methods*, 158(2):300–312.

Cattai T, Colonnese S, Corsi MC, Bassett DS, Scarano G, Fallani FDV (2021) Phase/amplitude synchronization of brain signals during motor imagery bci tasks. *IEEE Transactions on Neural Systems and Rehabilitation Engineering*, 29:1168–1177.

Cebolla AM, Palmero-Soler E, Leroy A, Cheron G (2017) Eeg spectral generators involved in motor imagery: a swloreta study. *Frontiers in psychology*, 8:2133.

Chaddad A, Wu Y, Kateb R, Bouridane A (2023) Electroencephalography signal processing: A comprehensive review and analysis of methods and techniques. *Sensors*, 23(14):6434.

Chakladar DD, Dey S, Roy PP, Dogra DP (2020) Eeg-based mental workload estimation using deep blstm-lstm network and evolutionary algorithm. *Biomedical Signal Processing and Control*, 60:101989.

Chang CY, Hsu SH, Pion-Tonachini L, Jung TP (2019) Evaluation of artifact subspace reconstruction for automatic artifact components removal in multi-channel eeg recordings. *IEEE Transactions on Biomedical Engineering*, 67(4):1114–1121.

Chang E, Billinghurst M, Yoo B (2023a) Brain activity during cybersickness: a scoping review. *Virtual reality*, 27(3):2073–2097.

Chang E, Billinghurst M, Yoo B (2023b) Brain activity during cybersickness: a scoping review. *Virtual reality*, 27(3):2073–2097.

Chang E, Kim HT, Yoo B (2021) Predicting cybersickness based on user's gaze behaviors in hmd-based virtual reality. *Journal of Computational Design and Engineering*, 8(2):728–739.

Cheron G, Petit G, Cheron J, Leroy A, Cebolla A, Cevallos C, Petieau M, Hoellinger T, Zarka D, Clarinval AM et al. (2016) Brain oscillations in sport: toward eeg biomarkers of performance. *Frontiers in psychology*, 7:246.

Chiarion G, Sparacino L, Antonacci Y, Faes L, Mesin L (2023) Connectivity analysis in eeg data: a tutorial review of the state of the art and emerging trends. *Bioengineering*, 10(3):372.

Cisotto G, Zanga A, Chlebus J, Zoppis I, Manzoni S, Markowska-Kaczmar U (2020) Comparison of attention-based deep learning models for eeg classification. *arXiv preprint arXiv:2012.01074*.

Clayton MS, Yeung N, Kadosh RC (2015) The roles of cortical oscillations in sustained attention. *Trends in Cognitive Sciences*, 19(4):188 – 195. DOI:https://doi.org/10.1016/j.tics.2015.02.004.

Clerico A, Gupta R, Falk TH (2015) Mutual information between inter-hemispheric eeg spectro-temporal patterns: A new feature for automated affect recognition. *2015 7th international IEEE/EMBS conference on neural engineering (NER)*, IEEE, pages 914–917.

Clerico A, Tiwari A, Gupta R, Jayaraman S, Falk TH (2018) Electroencephalography amplitude modulation analysis for automated affective tagging of music video clips. *Frontiers in Computational Neuroscience*, 11:115.

Cohen MX (2017) Where does eeg come from and what does it mean? *Trends in neurosciences*, 40(4):208–218.

Cohen MX, Elger CE, Fell J (2009) Oscillatory activity and phase–amplitude coupling in the human medial frontal cortex during decision making. *Journal of Cognitive Neuroscience*, 21(2):390–402.

Collins E, Robinson AK, Behrmann M (2018) Distinct neural processes for the perception of familiar versus unfamiliar faces along the visual hierarchy revealed by eeg. *NeuroImage*, 181:120–131.

Craik A, He Y, Contreras-Vidal JL (2019) Deep learning for electroencephalogram (eeg) classification tasks: a review. *Journal of neural engineering*, 16(3):031001.

Cullen AJ, Dowling NL, Segrave R, Carter A, Yücel M (2021) Exposure therapy in a virtual environment: Validation in obsessive compulsive disorder. *Journal of anxiety disorders*, 80: 102404.

Da Silva FL (2023) Eeg: origin and measurement. *EEG-fMRI: physiological basis, technique, and applications*, Springer, pages 23–48.

Daume J, Gruber T, Engel AK, Friese U (2017) Phase-amplitude coupling and long-range phase synchronization reveal frontotemporal interactions during visual working memory. *Journal of Neuroscience*, 37(2):313–322.

De Jesus Jr B, Lopes M, Moinnereau MA, Gougeh RA, Rosanne OM, Schubert W, Oliveira AA, Falk TH (2022) Quantifying multisensory immersive experiences using wearables: is (stimulating) more (senses) always merrier? *Proceedings of the 2nd Workshop on Multisensory Experiences-SensoryX'22*, SBC.

de Talhouet H, Webster JG (1996) The origin of skin-stretch-caused motion artifacts under electrodes. *Physiological Measurement*, 17(2):81.

Delorme A (2023) Eeg is better left alone. *Scientific reports*, 13(1):2372.

Delorme A, Makeig S (2004) Eeglab: an open source toolbox for analysis of single-trial eeg dynamics including independent component analysis. *Journal of neuroscience methods*, 134(1):9–21.

Dennison MS, Wisti AZ, D'Zmura M (2016) Use of physiological signals to predict cybersickness. *Displays*, 44:42–52.

Di Dona G, Ronconi L (2023) Beta oscillations in vision: a (preconscious) neural mechanism for the dorsal visual stream? *Frontiers in Psychology*, 14:1296483.

Dimitrakopoulos GN, Kakkos I, Dai Z, Lim J, deSouza JJ, Bezerianos A, Sun Y (2017) Task-independent mental workload classification based upon common multiband eeg cortical connectivity. *IEEE Transactions on Neural Systems and Rehabilitation Engineering*, 25(11):1940–1949. DOI:10.1109/TNSRE.2017.2701002.

Ding C, Peng H (2005) Minimum redundancy feature selection from microarray gene expression data. *Journal of bioinformatics and computational biology*, 3(02):185–205.

Diniz PS et al. (1997) *Adaptive filtering*. Springer.

Dzianok P, Kołodziej M, Kublik E (2021) Detecting attention in hilbert-transformed eeg brain signals from simple-reaction and choice-reaction cognitive tasks. *2021 IEEE 21st International Conference on Bioinformatics and Bioengineering (BIBE)*, IEEE, pages 1–4.

Edlinger G, Holzner C, Guger C (2011) A hybrid brain-computer interface for smart home control. *Human-Computer Interaction. Interaction Techniques and Environments: 14th International Conference, HCI International 2011, Orlando, FL, USA, July 9-14, 2011, Proceedings, Part II 14*, Springer, pages 417–426.

Eggermont JJ (2021) Chapter 3 - the alpha and delta rhythms and their interaction with other brain rhythms. *Brain Oscillations, Synchrony, and Plasticity*. Eggermont JJ, éditeur, Academic Press, pages 43–58.

Évain A, Argelaguet F, Strock A, Roussel N, Casiez G, Lécuyer A (2016). Influence of error rate on frustration of bci users. *Proceedings of the international working conference on advanced visual interfaces*, pages 248–251.

Fan FL, Xiong J, Li M, Wang G (2021). On interpretability of artificial neural networks: A survey. *IEEE Transactions on Radiation and Plasma Medical Sciences*, 5(6):741–760.

Fan J, Fan Y (2008). High dimensional classification using features annealed independence rules. *Annals of statistics*, 36(6):2605.

Ferguson KA, Cardin JA (2020). Mechanisms underlying gain modulation in the cortex. *Nature Reviews Neuroscience*, 21(2):80–92.

Fiałek S, Liarokapis F (2016). Comparing two commercial brain computer interfaces for serious games and virtual environments. *Emotion in Games: Theory and Praxis*, Springer, pages 103–117.

Foong R, Ang KK, Quek C, Guan C, Phua KS, Kuah CWK, Deshmukh VA, Yam LHL, Rajeswaran DK, Tang N et al. (2019). Assessment of the efficacy of eeg-based mi-bci with visual feedback and eeg correlates of mental fatigue for upper-limb stroke rehabilitation. *IEEE Transactions on Biomedical Engineering*, 67(3):786–795.

Fraga FJ, Falk TH, Kanda PA, Anghinah R (2013). Characterizing alzheimer's disease severity via resting-awake eeg amplitude modulation analysis. *PloS one*, 8(8):e72240.

Freeman WJ, Vitello G (2016). Matter and mind are entangled in eeg amplitude modulation and its double. *Society for Mind Matter Research*, 14(1):7–24.

French CC, Beaumont JG (1984). A critical review of eeg coherence studies of hemisphere function. *International Journal of Psychophysiology*, 1(3):241–254.

Fries P (2015). Rhythms for cognition: communication through coherence. *Neuron*, 88(1):220–235.

Fu R, Tian Y, Shi P, Bao T (2020). Automatic detection of epileptic seizures in eeg using sparse csp and fisher linear discrimination analysis algorithm. *Journal of medical systems*, 44:1–13.

Gabard-Durnam LJ, Mendez Leal AS, Wilkinson CL, Levin AR (2018). The harvard automated processing pipeline for electroencephalography (happe): standardized processing software for developmental and high-artifact data. *Frontiers in neuroscience*, 12:97.

Galiotta V, Quattrociocchi I, D'Ippolito M, Schettini F, Aricò P, Sdoia S, Formisano R, Cincotti F, Mattia D, Riccio A (2022). Eeg-based brain-computer interfaces for people with disorders of consciousness: features and applications. a systematic review. *Frontiers in Human Neuroscience*, 16:1040816.

Gao J, Zheng C, Wang P (2010). Online removal of muscle artifact from electroencephalogram signals based on canonical correlation analysis. *Clinical EEG and neuroscience*, 41(1):53–59.

George L, Lécuyer A (2010). An overview of research on" passive" brain-computer interfaces for implicit human-computer interaction. *International Conference on Applied Bionics and Biomechanics ICABB 2010-Workshop W1" Brain-Computer Interfacing and Virtual Reality"*.

Geschwind DH, Iacoboni M (1999). Structural and functional asymmetries of the human frontal lobes. *The human frontal lobes: Functions and disorders*, pages 45–70.

Getachew MN, Priyadarshini R, Mehra R (2021). Memristive biophysical neuron models forming an excitatory–inhibitory neural network for modeling ping rhythm generation. *Journal of Computational Electronics*, 20(1):681–708.

Ghiani A, Maniglia M, Battaglini L, Ronconi L (2021). Binding mechanisms in visual perception and their link with neural oscillations: a review of evidence from tacs. *Frontiers in Psychology*, 12:643677.

Gramfort A, Luessi M, Larson E, Engemann DA, Strohmeier D, Brodbeck C, Goj R, Jas M, Brooks T, Parkkonen L et al. (2013). Meg and eeg data analysis with mne-python. *Frontiers in neuroscience*, 267 pages.

Grass AM, Gibbs FA (1938). A fourier transform of the electroencephalogram. *Journal of neurophysiology*, 1(6):521–526.

Griffiths BJ, Martín-Buro MC, Staresina BP, Hanslmayr S (2021a). Disentangling neocortical alpha/beta and hippocampal theta/gamma oscillations in human episodic memory formation. *NeuroImage*, 242:118454.

Griffiths BJ, Martín-Buro MC, Staresina BP, Hanslmayr S, Staudigl T (2021b). Alpha/beta power decreases during episodic memory formation predict the magnitude of alpha/beta power decreases during subsequent retrieval. *Neuropsychologia*, 153:107755.

Guan A, Wang S, Huang A, Qiu C, Li Y, Li X, Wang J, Wang Q, Deng B (2022). The role of gamma oscillations in central nervous system diseases: Mechanism and treatment. *Frontiers in cellular neuroscience*, 16:962957.

Guger C, Ramoser H, Pfurtscheller G (2000). Real-time eeg analysis with subject-specific spatial patterns for a brain-computer interface (bci). *IEEE transactions on rehabilitation engineering*, 8(4):447–456.

Guyon I, Weston J, Barnhill S, Vapnik V (2002). Gene selection for cancer classification using support vector machines. *Machine learning*, 46:389–422.

Gwin JT, Gramann K, Makeig S, Ferris DP (2010). Removal of movement artifact from high-density eeg recorded during walking and running. *Journal of neurophysiology*, 103(6):3526–3534.

Gwin JT, Gramann K, Makeig S, Ferris DP (2011). Electrocortical activity is coupled to gait cycle phase during treadmill walking. *Neuroimage*, 54(2):1289–1296.

Han C, Shapley R, Xing D (2022a). Gamma rhythms in the visual cortex: functions and mechanisms. *Cognitive Neurodynamics*, 16(4):745–756.

Han Y, Wang B, Luo J, Li L, Li X (2022b). A classification method for eeg motor imagery signals based on parallel convolutional neural network. *Biomedical Signal Processing and Control*, 71:103190.

Händel B, Haarmeier T (2009). Cross-frequency coupling of brain oscillations indicates the success in visual motion discrimination. *Neuroimage*, 45(3):1040–1046.

Harmony T, Fernández T, Silva J, Bernal J, Díaz-Comas L, Reyes A, Marosi E, Rodríguez M, Rodríguez M (1996). Eeg delta activity: an indicator of attention to internal processing during performance of mental tasks. *International journal of psychophysiology*, 24(1-2):161–171.

Hart SG, Staveland LE (1988). Development of nasa-tlx (task load index): Results of empirical and theoretical research. *Advances in psychology*, Elsevier, volume 52, pages 139–183.

Haufe S, DeGuzman P, Henin S, Arcaro M, Honey CJ, Hasson U, Parra LC (2018). Elucidating relations between fmri, ecog, and eeg through a common natural stimulus. *NeuroImage*, 179:79–91.

He C, Chen YY, Phang CR, Stevenson C, Chen IP, Jung TP, Ko LW (2023). Diversity and suitability of the state-of-the-art wearable and wireless eeg systems review. *IEEE Journal of Biomedical and Health Informatics*, 27(8):3830–3843.

He C, Liu J, Zhu Y, Du W (2021). Data augmentation for deep neural networks model in eeg classification task: a review. *Frontiers in Human Neuroscience*, 15:765525.

Herrmann CS, Senkowski D, Röttger S (2004). Phase-locking and amplitude modulations of eeg alpha: Two measures reflect different cognitive processes in a working memory task. *Experimental psychology*, 51(4):311–318.

Herweg NA, Apitz T, Leicht G, Mulert C, Fuentemilla L, Bunzeck N (2016). Theta-alpha oscillations bind the hippocampus, prefrontal cortex, and striatum during recollection: evidence from simultaneous eeg–fmri. *Journal of Neuroscience*, 36(12):3579–3587.

Hidalgo VM, Díaz J, Mpodozis J, Letelier JC (2022). Envelope analysis of the human alpha rhythm reveals eeg gaussianity. *IEEE Transactions on Biomedical Engineering*, 70(4):1242–1251.

Hilla Y, Von Mankowski J, Föcker J, Sauseng P (2020). Faster visual information processing in video gamers is associated with eeg alpha amplitude modulation. *Frontiers in Psychology*, 11:599788.

Hinss MF, Somon B, Dehais F, Roy RN (2021). Open eeg datasets for passive brain-computer interface applications: Lacks and perspectives. *2021 10th International IEEE/EMBS Conference on Neural Engineering (NER)*, IEEE, pages 686–689.

Hogervorst MA, Brouwer AM, Van Erp JB (2014). Combining and comparing eeg, peripheral physiology and eye-related measures for the assessment of mental workload. *Frontiers in neuroscience*, 8:322.

Holm A, Lukander K, Korpela J, Sallinen M, Müller KM (2009). Estimating brain load from the eeg. *The Scientific World Journal*, 9:639–651.

Hougaard BI, Rossau IG, Czapla JJ, Miko MA, Skammelsen RB, Knoche H, Jochumsen M (2021). Who willed it? decreasing frustration by manipulating perceived control through fabricated input for stroke rehabilitation bci games. *Proceedings of the ACM on Human-Computer Interaction*, 5(CHI PLAY):1–19.

Huberty S, Desjardins J, Collins T, Elsabbagh M, O'Reilly C (2024). Pylossless: A non-destructive eeg processing pipeline. *bioRxiv*, pages 2024–01.

Hughes A, Jorda S (2021). Applications of biological and physiological signals in commercial video gaming and game research: a review. *Frontiers in Computer Science*, 3:557608.

Hülsdünker T, Mierau A, Neeb C, Kleinöder H, Strüder H (2015). Cortical processes associated with continuous balance control as revealed by eeg spectral power. *Neuroscience letters*, 592:1–5.

Huster RJ, Mokom ZN, Enriquez-Geppert S, Herrmann CS (2014). Brain–computer interfaces for eeg neurofeedback: Peculiarities and solutions. *International journal of psychophysiology*, 91(1):36–45.

Hwang HJ, Kwon K, Im CH (2009). Neurofeedback-based motor imagery training for brain–computer interface (bci). *Journal of neuroscience methods*, 179(1):150–156.

Hyvarinen A (1999). Fast and robust fixed-point algorithms for independent component analysis. *IEEE transactions on Neural Networks*, 10(3):626–634.

Iacoboni M, Zaidel E (2004). Interhemispheric visuo-motor integration in humans: the role of the superior parietal cortex. *Neuropsychologia*, 42(4):419–425.

IMARC Group (2023). *Brain Computer Interface Market Report by Product (Invasive BCI, Partially Invasive BCI, Non-invasive BCI), Application (Healthcare, Smart Home Control, Communication and Control, Entertainment and Gaming), and Region*. `https://www.imarcgroup.com/brain-computer-interface-market/`. Report ID: SR112024A4025, Last visited: July 2024.

Islam MS, Hussain I, Rahman MM, Park SJ, Hossain MA (2022a). Explainable artificial intelligence model for stroke prediction using eeg signal. *Sensors*, 22(24):9859.

Islam R, Desai K, Quarles J (2021). Cybersickness prediction from integrated hmd's sensors: A multimodal deep fusion approach using eye-tracking and head-tracking data. *2021 IEEE international symposium on mixed and augmented reality (ISMAR)*, IEEE, pages 31–40.

Islam R, Desai K, Quarles J (2022b). Towards forecasting the onset of cybersickness by fusing physiological, head-tracking and eye-tracking with multimodal deep fusion network. *2022 IEEE International Symposium on Mixed and Augmented Reality (ISMAR)*, IEEE, pages 121–130.

Iwama S, Ushiba J (2024). Rapid-iaf: Rapid identification of individual alpha frequency in eeg data using sequential bayesian estimation. *IEEE Transactions on Neural Systems and Rehabilitation Engineering*.

Jang KM, Kwon M, Nam SG, Kim D, Lim HK (2022). Estimating objective (eeg) and subjective (ssq) cybersickness in people with susceptibility to motion sickness. *Applied ergonomics*, 102:103731.

Jensen O, Mazaheri A (2010). Shaping functional architecture by oscillatory alpha activity: gating by inhibition. *Frontiers in human neuroscience*, 4:186.

Jeong D, Jeong M, Yang U, Han K (2022). Eyes on me: Investigating the role and influence of eye-tracking data on user modeling in virtual reality. *PLoS One*, 17(12):e0278970.

Jeong D, Yoo S, Yun J (2019). Cybersickness analysis with eeg using deep learning algorithms. *2019 IEEE conference on virtual reality and 3D user interfaces (VR)*, IEEE, pages 827–835.

Jerbi K, Vidal JR, Ossandon T, Dalal SS, Jung J, Hoffmann D, Minotti L, Bertrand O, Kahane P, Lachaux JP (2010). Exploring the electrophysiological correlates of the default-mode network with intracerebral eeg. *Frontiers in systems neuroscience*, 4:1442.

Jesus Jr B, Cassani R, McGeown WJ, Cecchi M, Fadem K, Falk TH (2021). Multimodal prediction of alzheimer's disease severity level based on resting-state eeg and structural mri. *Frontiers in Human Neuroscience*, 15:700627.

Jeunet C, N'Kaoua B, Lotte F (2016). Advances in user-training for mental-imagery-based bci control: Psychological and cognitive factors and their neural correlates. *Progress in brain research*, 228:3–35.

Jiang X, Zhang X, Wu D (2019). Active learning for black-box adversarial attacks in eeg-based brain-computer interfaces. *2019 IEEE Symposium Series on Computational Intelligence (SSCI)*, IEEE, pages 361–368.

Jin X, Wang J, Liu L, Lin Y (2023). Uncertainty-aware denoising network for artifact removal in eeg signals. *IEEE Transactions on Neural Systems and Rehabilitation Engineering*, 31:4470–4480.

John SE, Opie NL, Wong YT, Rind GS, Ronayne SM, Gerboni G, Bauquier SH, O'Brien TJ, May CN, Grayden DB et al. (2018). Signal quality of simultaneously recorded endovascular, subdural and epidural signals are comparable. *Scientific reports*, 8(1):8427.

Johnson MK, Blanco JA, Gentili RJ, Jaquess KJ, Oh H, Hatfield BD (2015). Probe-independent eeg assessment of mental workload in pilots. *2015 7th International IEEE/EMBS Conference on Neural Engineering (NER)*, IEEE, pages 581–584.

Joucla C, Gabriel D, Ortega JP, Haffen E (2022). Three simple steps to improve the interpretability of eeg-svm studies. *Journal of Neurophysiology*, 128(6):1375–1382.

Kakkos I, Dimitrakopoulos GN, Gao L, Zhang Y, Qi P, Matsopoulos GK, Thakor N, Bezerianos A, Sun Y (2019). Mental workload drives different reorganizations of functional cortical connectivity between 2d and 3d simulated flight experiments. *IEEE Transactions on Neural Systems and Rehabilitation Engineering*, 27(9):1704–1713.

Kamiński J, Brzezicka A, Gola M, Wróbel A (2012). Beta band oscillations engagement in human alertness process. *International Journal of Psychophysiology*, 85(1):125–128.

Käthner I, Wriessnegger SC, Müller-Putz GR, Kübler A, Halder S (2014). Effects of mental workload and fatigue on the p300, alpha and theta band power during operation of an erp (p300) brain–computer interface. *Biological psychology*, 102:118–129.

Kearney K, Thomas C, McAdams E (2007). Quantification of motion artifact in ecg electrode design. *2007 29th Annual International Conference of the IEEE Engineering in Medicine and Biology Society*, IEEE, pages 1533–1536.

Keener JP (1993). The perron–frobenius theorem and the ranking of football teams. *SIAM review*, 35(1):80–93.

Keshavarz B, Hecht H (2011). Validating an efficient method to quantify motion sickness. *Human factors*, 53(4):415–426.

Khademi Z, Ebrahimi F, Kordy HM (2022). A transfer learning-based cnn and lstm hybrid deep learning model to classify motor imagery eeg signals. *Computers in biology and medicine*, 143:105288.

Khalaf A, Sejdic E, Akcakaya M (2019). A novel motor imagery hybrid brain computer interface using eeg and functional transcranial doppler ultrasound. *Journal of neuroscience methods*, 313:44–53.

Kim JY, Son JB, Leem HS, Lee SH (2019). Psychophysiological alteration after virtual reality experiences using smartphone-assisted head mount displays: an eeg-based source localization study. *Applied Sciences*, 9(12):2501.

Klados MA, Papadelis C, Braun C, Bamidis PD (2011). Reg-ica: a hybrid methodology combining blind source separation and regression techniques for the rejection of ocular artifacts. *Biomedical Signal Processing and Control*, 6(3):291–300.

Kleih SC, Kübler A (2015). Psychological factors influencing brain-computer interface (bci) performance. *2015 IEEE International Conference on Systems, Man, and Cybernetics*, IEEE, pages 3192–3196.

Klimesch W (1999). Eeg alpha and theta oscillations reflect cognitive and memory performance: a review and analysis. *Brain research reviews*, 29(2-3):169–195.

Klug M, Gramann K (2021). Identifying key factors for improving ica-based decomposition of eeg data in mobile and stationary experiments. *European Journal of Neuroscience*, 54(12):8406–8420.

Ko W, Jeon E, Jeong S, Suk HI (2021). Multi-scale neural network for eeg representation learning in bci. *IEEE Computational Intelligence Magazine*, 16(2):31–45.

Kopell N, Kramer MA, Malerba P, Whittington MA (2010). Are different rhythms good for different functions? *Frontiers in human neuroscience*, 4:187.

Kumar S, Sahin F (2015). A framework for a real time intelligent and interactive brain computer interface. *Computers & Electrical Engineering*, 43:193–214.

Lean Y, Shan F (2012). Brief review on physiological and biochemical evaluations of human mental workload. *Human Factors and Ergonomics in Manufacturing & Service Industries*, 22(3):177–187.

Lee YE, Kwak NS, Lee SW (2020). A real-time movement artifact removal method for ambulatory brain-computer interfaces. *IEEE Transactions on Neural Systems and Rehabilitation Engineering*, 28(12):2660–2670.

Lewis C, Ni J, Wunderle T, Jendritza P, Lazar A, Diester I, Fries P (2021). *Cortical gamma-band resonance preferentially transmits coherent input. Cell Rep. 35, 109083*.

Li G, McGill M, Brewster S, Chen CP, Anguera JA, Gazzaley A, Pollick F (2021a). Multimodal biosensing for vestibular network-based cybersickness detection. *IEEE Journal of Biomedical and Health Informatics*, 26(6):2469–2480.

Li M, Pan J, Gao Y, Shen Y, Luo F, Dai J, Hao A, Qin H (2022). Neurophysiological and subjective analysis of vr emotion induction paradigm. *IEEE Transactions on Visualization and Computer Graphics*, 28(11):3832–3842.

Li P, Yin C, Li M, Li H, Yang B (2021b). A dry electroencephalogram electrode for applications in steady-state visual evoked potential-based brain–computer interface systems. *Biosensors and Bioelectronics*, 187:113326.

Li X, Yang X, Sun Z (2020). Alpha rhythm slowing in a modified thalamo-cortico-thalamic model related with alzheimer's disease. *PLoS One*, 15(3):e0229950.

Li Y, Hu X, Yu Y, Zhao K, Saalmann YB, Wang L (2018). Feedback from human posterior parietal cortex enables visuospatial category representations as early as primary visual cortex. *Brain and Behavior*, 8(1):e00886.

Li Z, Zhang S, Pan J et al. (2019). Advances in hybrid brain-computer interfaces: Principles, design, and applications. *Computational Intelligence and Neuroscience*, 2019.

Liang WK, Tseng P, Yeh JR, Huang NE, Juan CH (2021). Frontoparietal beta amplitude modulation and its interareal cross-frequency coupling in visual working memory. *Neuroscience*, 460:69–87.

Liao CY, Tai SK, Chen RC, Hendry H (2020). Using eeg and deep learning to predict motion sickness under wearing a virtual reality device. *Ieee Access*, 8:126784–126796.

Limanowski J, Friston K (2020). Attentional modulation of vision versus proprioception during action. *Cerebral Cortex*, 30(3):1637–1648.

Liu M, Yang B, Xu M, Zan P, Chen L, Xia X (2024). Exploring quantitative assessment of cybersickness in virtual reality using eeg signals and a cnn-eca-lstm network. *Displays*, 81:102602.

Liu Y, Ayaz H, Shewokis PA (2017). Mental workload classification with concurrent electroencephalography and functional near-infrared spectroscopy. *Brain-Computer Interfaces*, 4(3):175–185.

Liu Z, de Zwart JA, Yao B, van Gelderen P, Kuo LW, Duyn JH (2012). Finding thalamic bold correlates to posterior alpha eeg. *Neuroimage*, 63(3):1060–1069.

Liu Z, Han F, Wang Q (2022). A review of computational models for gamma oscillation dynamics: from spiking neurons to neural masses. *Nonlinear Dynamics*, 108(3):1849–1866.

Liu Z, Shore J, Wang M, Yuan F, Buss A, Zhao X (2021). A systematic review on hybrid eeg/fnirs in brain-computer interface. *Biomedical Signal Processing and Control*, 68:102595.

Liv N, Greenbaum D (2023). Cyberneurosecurity. *Policy, Identity, and Neurotechnology: The Neuroethics of Brain-Computer Interfaces*, Springer, pages 233–251.

Llinás RR, Steriade M (2006). Bursting of thalamic neurons and states of vigilance. *Journal of neurophysiology*, 95(6):3297–3308.

Lopes F, Leal A, Pinto MF, Dourado A, Schulze-Bonhage A, Dümpelmann M, Teixeira C (2023). Removing artefacts and periodically retraining improve performance of neural network-based seizure prediction models. *Scientific Reports*, 13(1):5918.

Lopes MK, de Jesus BJ, Moinnereau MA, Gougeh RA, Rosanne OM, Schubert W, de Oliveira AA, Falk TH (2022). Nat (ur) e: Quantifying the relaxation potential of ultra-reality multisensory nature walk experiences. *2022 IEEE International Conference on Metrology for Extended Reality, Artificial Intelligence and Neural Engineering (MetroXRAINE)*, IEEE, pages 459–464.

Lopes MK, Falk TH (2024). Audio-visual-olfactory immersive digital nature exposure for stress and anxiety reduction: a systematic review on systems, outcomes, and challenges. *Frontiers in Virtual Reality*, 5:1252539.

Lopes MKS, Cassani R, Falk TH (2021). On the use of saliency maps and convolutional neural networks for improved alzheimer's disease assessment. *Alzheimer's & Dementia*, 17:e054710.

Lotte F, Bougrain L, Clerc M (2015). Electroencephalography (eeg)-based brain-computer interfaces. *Wiley encyclopedia of electrical and electronics engineering*, 44 pages.

Lotte F, Roy RN (2019). Brain–computer interface contributions to neuroergonomics. *Neuroergonomics*, Elsevier, pages 43–48.

Lu CF, Teng S, Hung CI, Tseng PJ, Lin LT, Lee PL, Wu YT (2011). Reorganization of functional connectivity during the motor task using eeg time–frequency cross mutual information analysis. *Clinical Neurophysiology*, 122(8):1569–1579.

Lupu RG, Irimia DC, Ungureanu F, Poboroniuc MS, Moldoveanu A (2018). Bci and fes based therapy for stroke rehabilitation using vr facilities. *Wireless Communications and Mobile Computing*, 2018(1):4798359.

Mai ND, Long NMH, Chung WY (2021). 1d-cnn-based bci system for detecting emotional states using a wireless and wearable 8-channel custom-designed eeg headset. *2021 IEEE International Conference on Flexible and Printable Sensors and Systems (FLEPS)*, IEEE, pages 1–4.

Mak JN, Chan RH, Wong SW (2013). Evaluation of mental workload in visual-motor task: Spectral analysis of single-channel frontal eeg. *IECON 2013-39th Annual Conference of the IEEE Industrial Electronics Society*, IEEE, pages 8426–8430.

Mandrick K, Derosiere G, Dray G, Coulon D, Micallef JP, Perrey S (2013). Prefrontal cortex activity during motor tasks with additional mental load requiring attentional demand: a near-infrared spectroscopy study. *Neuroscience research*, 76(3):156–162.

Maples-Keller JL, Yasinski C, Manjin N, Rothbaum BO (2017). Virtual reality-enhanced extinction of phobias and post-traumatic stress. *Neurotherapeutics*, 14:554–563.

Marcos-Martínez D, Santamaría-Vázquez E, Martínez-Cagigal V, Pérez-Velasco S, Rodríguez-González V, Martín-Fernández A, Moreno-Calderón S, Hornero R (2023). Itaca: An open-source framework for neurofeedback based on brain–computer interfaces. *Computers in Biology and Medicine*, 160:107011.

Market.us (2024). *Global Brain Computer Interface Market By Component (Hardware and Software), By Product (Invasive Brain Computer Interface, Partially Invasive Brain Computer Interface, and Non-Invasive Brain Computer Interface), By Application, By End-User, By Region and Companies - Industry Segment Outlook, Market Assessment, Competition Scenario, Trends, and Forecast*. `https://market.us/report/brain-computer-interface-market/`. Report ID: 47864, Page total: 347, Last visited: July 2024.

Markiewicz CJ, Gorgolewski KJ, Feingold F, Blair R, Halchenko YO, Miller E, Hardcastle N, Wexler J, Esteban O, Goncavles M et al. (2021). The openneuro resource for sharing of neuroscience data. *Elife*, 10:e71774.

McDonnell AS, Crabtree KW, Cooper JM, Strayer DL (2024). This is your brain on autopilot 2.0: The influence of practice on driver workload and engagement during on-road, partially automated driving. *Human factors*, 66(8):2025–2040.

McMenamin BW, Shackman AJ, Greischar LL, Davidson RJ (2011). Electromyogenic artifacts and electroencephalographic inferences revisited. *Neuroimage*, 54(1):4–9.

McSweeney M, Morales S, Valadez EA, Buzzell GA, Yoder L, Fifer WP, Pini N, Shuffrey LC, Elliott AJ, Isler JR et al. (2023). Age-related trends in aperiodic eeg activity and alpha oscillations during early-to middle-childhood. *Neuroimage*, 269:119925.

Meigen T, Bach M (1999). On the statistical significance of electrophysiological steady-state responses. *Documenta Ophthalmologica*, 98:207–232.

Meng L, Jiang X, Wu D (2023). Adversarial robustness benchmark for eeg-based brain–computer interfaces. *Future Generation Computer Systems*, 143:231–247.

Michel CM, Brunet D (2019). Eeg source imaging: a practical review of the analysis steps. *Frontiers in neurology*, 10:446653.

Mihajlović V, Patki S, Grundlehner B (2014). The impact of head movements on eeg and contact impedance: An adaptive filtering solution for motion artifact reduction. *2014 36th Annual International Conference of the IEEE Engineering in Medicine and Biology Society*, IEEE, pages 5064–5067.

Milani G, Antonioni A, Baroni A, Malerba P, Straudi S (2022). Relation between eeg measures and upper limb motor recovery in stroke patients: A scoping review. *Brain Topography*, 35(5-6):651–666.

Mizuhara H, Wang LQ, Kobayashi K, Yamaguchi Y (2004). A long-range cortical network emerging with theta oscillation in a mental task. *Neuroreport*, 15(8):1233–1238.

Mizuhara H, Wang LQ, Kobayashi K, Yamaguchi Y (2005). Long-range eeg phase synchronization during an arithmetic task indexes a coherent cortical network simultaneously measured by fmri. *Neuroimage*, 27(3):553–563.

Mizuhara H, Yamaguchi Y (2007). Human cortical circuits for central executive function emerge by theta phase synchronization. *Neuroimage*, 36(1):232–244.

Mognon A, Jovicich J, Bruzzone L, Buiatti M (2011). Adjust: An automatic eeg artifact detector based on the joint use of spatial and temporal features. *Psychophysiology*, 48(2):229–240.

Molla MKI, Al Shiam A, Islam MR, Tanaka T (2020). Discriminative feature selection-based motor imagery classification using eeg signal. *IEEE Access*, 8:98255–98265.

Morabito FC, Ieracitano C, Mammone N (2023). An explainable artificial intelligence approach to study mci to ad conversion via hd-eeg processing. *Clinical EEG and Neuroscience*, 54(1):51–60.

Mousavi M, de Sa VR (2019). Spatio-temporal analysis of error-related brain activity in active and passive brain–computer interfaces. *Brain-computer interfaces*, 6(4):118–127.

Mucarquer JA, Prado P, Escobar MJ, El-Deredy W, Zañartu M (2019). Improving eeg muscle artifact removal with an emg array. *IEEE transactions on instrumentation and measurement*, 69(3):815–824.

Mukundan C, Sumit S, Chetan S (2017). Brain electrical oscillations signature profiling (beos) for measuring the process of remembrance. *EC Neurology*, 8(6):217–230.

Mullen T, Kothe C, Chi YM, Ojeda A, Kerth T, Makeig S, Cauwenberghs G, Jung TP (2013). Real-time modeling and 3d visualization of source dynamics and connectivity using wearable eeg. *2013 35th annual international conference of the IEEE engineering in medicine and biology society (EMBC)*, IEEE, pages 2184–2187.

Mullen TR, Kothe CAE, Chi YM, Ojeda A, Kerth T, Makeig S, Jung TP, Cauwenberghs G (2015). Real-time neuroimaging and cognitive monitoring using wearable dry eeg. *IEEE Transactions on Biomedical Engineering*, 62(11):2553–2567. DOI:10.1109/tbme.2015.2481482.

Müller KR, Tangermann M, Dornhege G, Krauledat M, Curio G, Blankertz B (2008). Machine learning for real-time single-trial eeg-analysis: from brain–computer interfacing to mental state monitoring. *Journal of neuroscience methods*, 167(1):82–90.

Murias M, Webb SJ, Greenson J, Dawson G (2007). Resting state cortical connectivity reflected in eeg coherence in individuals with autism. *Biological psychiatry*, 62(3):270–273.

Muthukumaraswamy S (2013). High-frequency brain activity and muscle artifacts in meg/eeg: a review and recommendations. *Frontiers in human neuroscience*, 7:138.

Myrden A, Chau T (2015). Effects of user mental state on eeg-bci performance. *Frontiers in human neuroscience*, 9:308.

Nam S, Jang KM, Kwon M, Lim HK, Jeong J (2022). Electroencephalogram microstates and functional connectivity of cybersickness. *Frontiers in Human Neuroscience*, 16:857768.

Naser MY, Bhattacharya S (2023). Towards practical bci-driven wheelchairs: A systematic review study. *IEEE Transactions on Neural Systems and Rehabilitation Engineering*.

Nathan K, Contreras-Vidal JL (2016). Negligible motion artifacts in scalp electroencephalography (eeg) during treadmill walking. *Frontiers in Human Neuroscience*, 9:708. DOI:10.3389/fnhum.2015.00708.

Neske GT, Connors BW (2016). Synchronized gamma-frequency inhibition in neocortex depends on excitatory-inhibitory interactions but not electrical synapses. *Journal of neurophysiology*, 116(2):351–368.

Newson JJ, Thiagarajan TC (2019). Eeg frequency bands in psychiatric disorders: a review of resting state studies. *Frontiers in human neuroscience*, 12:521.

Nijboer F, Birbaumer N, Kübler A (2010). The influence of psychological state and motivation on brain–computer interface performance in patients with amyotrophic lateral sclerosis–a longitudinal study. *Frontiers in Neuropharmacology*, 4:55.

Nisar H, Boon KW, Ho YK, Khang TS (2022). Brain-computer interface: Feature extraction and classification of motor imagery-based cognitive tasks. *2022 IEEE International Conference on Automatic Control and Intelligent Systems (I2CACIS)*, IEEE, pages 42–47.

Norman KA, O'Reilly RC (2003). Modeling hippocampal and neocortical contributions to recognition memory: a complementary-learning-systems approach. *Psychological review*, 110(4):611.

Nunez PL, Srinivasan R (2010). Scale and frequency chauvinism in brain dynamics: too much emphasis on gamma band oscillations. *Brain Structure and Function*, 215(2):67–71.

Nürnberger M, Klingner C, Witte OW, Brodoehl S (2021). Mismatch of visual-vestibular information in virtual reality: is motion sickness part of the brains attempt to reduce the prediction error? *Frontiers in Human Neuroscience*, 15:757735.

Obeid I, Picone J (2016). The temple university hospital eeg data corpus. *Frontiers in neuroscience*, 10:195498.

Onikura K, Iramina K (2015). Evaluation of a head movement artifact removal method for eeg considering real-time prosessing. *2015 8th Biomedical Engineering International Conference (BMEiCON)*, IEEE, pages 1–4.

Oostenveld R, Praamstra P (2001). The five percent electrode system for high-resolution eeg and erp measurements. *Clinical neurophysiology*, 112(4):713–719.

Oosugi N, Kitajo K, Hasegawa N, Nagasaka Y, Okanoya K, Fujii N (2017). A new method for quantifying the performance of eeg blind source separation algorithms by referencing a simultaneously recorded ecog signal. *Neural Networks*, 93:1–6.

Oshiro TM, Perez PS, Baranauskas JA (2012). How many trees in a random forest? *Machine Learning and Data Mining in Pattern Recognition*. Perner P, éditeur, Springer Berlin Heidelberg, pages 154–168, Berlin, Heidelberg.

Ozkan A, Uyan U, Celikcan U (2023). Effects of speed, complexity and stereoscopic vr cues on cybersickness examined via eeg and self-reported measures. *Displays*, 78:102415.

Padfield N, Zabalza J, Zhao H, Masero V, Ren J (2019). Eeg-based brain-computer interfaces using motor-imagery: Techniques and challenges. *Sensors*, 19(6):1423.

Palumbo A (2022). Microsoft hololens 2 in medical and healthcare context: state of the art and future prospects. *Sensors*, 22(20):7709.

Palva JM, Palva S (2018). Functional integration across oscillation frequencies by cross-frequency phase synchronization. *European Journal of Neuroscience*, 48(7):2399–2406.

Palva S, Palva JM (2012). Discovering oscillatory interaction networks with m/eeg: challenges and breakthroughs. *Trends in cognitive sciences*, 16(4):219–230.

Park S, Han CH, Im CH (2020). Design of wearable eeg devices specialized for passive brain–computer interface applications. *Sensors*, 20(16):4572.

Pedregosa F, Varoquaux G, Gramfort A, Michel V, Thirion B, Grisel O, Blondel M, Prettenhofer P, Weiss R, Dubourg V, Vanderplas J, Passos A, Cournapeau D, Brucher M, Perrot M, Duchesnay E (2011a). Scikit-learn: Machine learning in Python. *Journal of Machine Learning Research*, 12:2825–2830.

Pedregosa F, Varoquaux G, Gramfort A, Michel V, Thirion B, Grisel O, Blondel M, Prettenhofer P, Weiss R, Dubourg V, Vanderplas J, Passos A, Cournapeau D, Brucher M, Perrot M, Duchesnay E (2011b). Scikit-learn: Machine learning in Python. *Journal of Machine Learning Research*, 12:2825–2830.

Peng H, Long F, Ding C (2005). Feature selection based on mutual information: criteria of max-dependency, max-relevance, and min-redundancy. *IEEE Transactions on Pattern Analysis & Machine Intelligence*, (8):1226–1238.

Perennou D, Benaim C, Rouget E, Rousseaux M, Blard J, Pelissier J (1999). Postural balance following stroke: towards a disadvantage of the right brain-damaged hemisphere. *Revue Neurologique*, 155(4):281–290.

Peron S, Pancholi R, Voelcker B, Wittenbach JD, Ólafsdóttir HF, Freeman J, Svoboda K (2020). Recurrent interactions in local cortical circuits. *Nature*, 579(7798):256–259.

Pignatelli M, Beyeler A, Leinekugel X (2012). Neural circuits underlying the generation of theta oscillations. *Journal of Physiology-Paris*, 106(3-4):81–92.

Pion-Tonachini L, Kreutz-Delgado K, Makeig S (2019). Iclabel: An automated electroencephalographic independent component classifier, dataset, and website. *NeuroImage*, 198:181–197.

Plank M, Müller HJ, Onton J, Makeig S, Gramann K (2010). Human eeg correlates of spatial navigation within egocentric and allocentric reference frames. *Spatial Cognition VII: International Conference, Spatial Cognition 2010, Mt. Hood/Portland, OR, USA, August 15-19, 2010. Proceedings 7*, Springer, pages 191–206.

Plass-Oude Bos D, Reuderink B, van de Laar B, Gürkök H, Mühl C, Poel M, Nijholt A, Heylen D (2010). Brain-computer interfacing and games. *Brain-computer interfaces: applying our minds to human-computer interaction*, pages 149–178.

Popov T, Popova P, Harkotte M, Awiszus B, Rockstroh B, Miller GA (2018). Cross-frequency interactions between frontal theta and posterior alpha control mechanisms foster working memory. *NeuroImage*, 181:728–733.

Prada L, Barcelo F, Herrmann CS, Escera C (2014). Eeg delta oscillations index inhibitory control of contextual novelty to both irrelevant distracters and relevant task-switch cues. *Psychophysiology*, 51(7):658–672.

Prinsen J, Pruss E, Vrins A, Ceccato C, Alimardani M (2022). A passive brain-computer interface for monitoring engagement during robot-assisted language learning. *2022 IEEE International Conference on Systems, Man, and Cybernetics (SMC)*, IEEE, pages 1967–1972.

Qi Y (2012). Random forest for bioinformatics. *Ensemble machine learning*, Springer, pages 307–323.

Rahman M, Karwowski W, Fafrowicz M, Hancock PA (2019). Neuroergonomics applications of electroencephalography in physical activities: A systematic review. *Frontiers in Human Neuroscience*, 13:182. DOI:10.3389/fnhum.2019.00182.

Raya MAD, Sison LG (2002). Adaptive noise cancelling of motion artifact in stress ecg signals using accelerometer. *Proceedings of the Second Joint 24th Annual Conference and the Annual Fall Meeting of the Biomedical Engineering Society][Engineering in Medicine and Biology*, IEEE, volume 2, pages 1756–1757.

Rejer I, Górski P (2015). Benefits of ica in the case of a few channel eeg. *2015 37th Annual International Conference of the IEEE Engineering in Medicine and Biology Society (EMBC)*, IEEE, pages 7434–7437.

Remeseiro B, Bolon-Canedo V (2019). A review of feature selection methods in medical applications. *Computers in biology and medicine*, 112:103375.

Richter CG, Thompson WH, Bosman CA, Fries P (2017). Top-down beta enhances bottom-up gamma. *Journal of Neuroscience*, 37(28):6698–6711.

Riès SK, Dronkers NF, Knight RT (2016). Choosing words: Left hemisphere, right hemisphere, or both? perspective on the lateralization of word retrieval. *Annals of the New York Academy of Sciences*, 1369(1):111–131.

Robbins KA, Touryan J, Mullen T, Kothe C, Bigdely-Shamlo N (2020a). How sensitive are eeg results to preprocessing methods: a benchmarking study. *IEEE transactions on neural systems and rehabilitation engineering*, 28(5):1081–1090.

Robbins KA, Touryan J, Mullen T, Kothe C, Bigdely-Shamlo N (2020b). How sensitive are eeg results to preprocessing methods: a benchmarking study. *IEEE transactions on neural systems and rehabilitation engineering*, 28(5):1081–1090.

Rolls E (2020). The parietal cortex, spatial functions, and navigation. *Brain Computations*, pages 363–378.

Rosanne O, Albuquerque I, Cassani R, Gagnon JF, Tremblay S, Falk TH (2021). Adaptive filtering for improved eeg-based mental workload assessment of ambulant users. *Frontiers in Neuroscience*, 15:611962.

Rosanne O, Albuquerque I, Gagnon JF, Tremblay S, Falk TH (2019a). Performance comparison of automated eeg enhancement algorithms for mental workload assessment of ambulant users. *2019 9th International IEEE/EMBS Conference on Neural Engineering (NER)*, IEEE, pages 61–64.

Rosanne O, Albuquerque I, Gagnon JF, Tremblay S, Falk TH (2019b). Performance comparison of automated eeg enhancement algorithms for mental workload assessment of ambulant users. *2019 9th International IEEE/EMBS Conference on Neural Engineering (NER)*, IEEE, pages 61–64.

Rosanne O, Alves de Oliveira A, Falk TH (2023). Eeg amplitude modulation analysis across mental tasks: Towards improved active bcis. *Sensors*, 23(23):9352.

Rosanne O, Benesch D, Kratzig G, Paré S, Bolt N, Falk TH (2024). To pre-process or not to pre-process? on the role of eeg enhancement for cybersickness characterization and the importance of amplitude modulation features. *Frontiers in Virtual Reality*.

Roux F, Wibral M, Singer W, Aru J, Uhlhaas PJ (2013). The phase of thalamic alpha activity modulates cortical gamma-band activity: evidence from resting-state meg recordings. *Journal of Neuroscience*, 33(45):17827–17835.

Roy RN, Hinss MF, Darmet L, Ladouce S, Jahanpour ES, Somon B, Xu X, Drougard N, Dehais F, Lotte F (2022). Retrospective on the first passive brain-computer interface competition on cross-session workload estimation. *Frontiers in Neuroergonomics*, 3:838342.

Roy Y, Banville H, Albuquerque I, Gramfort A, Falk TH, Faubert J (2019). Deep learning-based electroencephalography analysis: a systematic review. *Journal of neural engineering*, 16(5): 051001.

Ruiz S, Buyukturkoglu K, Rana M, Birbaumer N, Sitaram R (2014). Real-time fmri brain computer interfaces: self-regulation of single brain regions to networks. *Biological psychology*, 95:4–20.

Rushworth MF, Krams M, Passingham RE (2001). The attentional role of the left parietal cortex: the distinct lateralization and localization of motor attention in the human brain. *Journal of cognitive neuroscience*, 13(5):698–710.

Sadiya S, Alhanai T, Ghassemi MM (2021). Artifact detection and correction in eeg data: A review. *2021 10th International IEEE/EMBS Conference on Neural Engineering (NER)*, IEEE, pages 495–498.

Said RR, Heyat MBB, Song K, Tian C, Wu Z (2022). A systematic review of virtual reality and robot therapy as recent rehabilitation technologies using eeg-brain–computer interface based on movement-related cortical potentials. *Biosensors*, 12(12):1134.

Sammer G, Blecker C, Gebhardt H, Bischoff M, Stark R, Morgen K, Vaitl D (2007). Relationship between regional hemodynamic activity and simultaneously recorded eeg-theta associated with mental arithmetic-induced workload. *Human brain mapping*, 28(8):793–803.

Santiago-Espada Y, Myer R, Latorella K, Comstock J (2011). The multi-attribute task battery ii (matb-ii) software for human performance and workload research: A user's guide (nasa/tm-2011–217164). *Hampton, Virginia: NASA Langley Research Center*.

Sauseng P, Conci M, Wild B, Geyer T (2015). Predictive coding in visual search as revealed by cross-frequency eeg phase synchronization. *Frontiers in psychology*, 6:1655.

Sauseng P, Klimesch W, Stadler W, Schabus M, Doppelmayr M, Hanslmayr S, Gruber WR, Birbaumer N (2005). A shift of visual spatial attention is selectively associated with human eeg alpha activity. *European journal of neuroscience*, 22(11):2917–2926.

Schmidt RM (2019). Recurrent neural networks (rnns): A gentle introduction and overview. *arXiv preprint arXiv:1912.05911*.

Sciaraffa N, Di Flumeri G, Germano D, Giorgi A, Di Florio A, Borghini G, Vozzi A, Ronca V, Babiloni F, Aricò P (2022). Evaluation of a new lightweight eeg technology for translational applications of passive brain-computer interfaces. *Frontiers in Human Neuroscience*, 16:901387.

Seeber M, Scherer R, Wagner J, Solis-Escalante T, Müller-Putz GR (2014). Eeg beta suppression and low gamma modulation are different elements of human upright walking. *Frontiers in human neuroscience*, 8:485.

Shepherd GM (2003). *The synaptic organization of the brain*. Oxford university press.

Shi N, Miao Y, Huang C, Li X, Song Y, Chen X, Wang Y, Gao X (2024). Estimating and approaching the maximum information rate of noninvasive visual brain-computer interface. *Neuroimage*, 289:120548.

Shimada S, Pannattee P, Ikei Y, Nishiuchi N, Yem V (2023). High-frequency cybersickness prediction using deep learning techniques with eye-related indices. *IEEE Access*.

Shin J, Kwon J, Im CH (2018). A ternary hybrid eeg-nirs brain-computer interface for the classification of brain activation patterns during mental arithmetic, motor imagery, and idle state. *Frontiers in neuroinformatics*, 12:5.

Shindo K, Kawashima K, Ushiba J, Ota N, Ito M, Ota T, Kimura A, Liu M (2011). Effects of neurofeedback training with an electroencephalogram-based brain-computer interface for hand paralysis in patients with chronic stroke: a preliminary case series study. *Journal of rehabilitation medicine*, 43(10):951–957.

Shishkin SL (2022). Active brain-computer interfacing for healthy users. *Frontiers in Neuroscience*, 16:859887.

Sikarwar R, Shakya HK, Singh SS (2021). A review on social network analysis methods and algorithms. *2021 13th International Conference on Computational Intelligence and Communication Networks (CICN)*, IEEE, pages 1–5.

Silberstein R (2006a). *Dynamic sculpting of brain functional connectivity and mental rotation aptitude In Neuper C., & Klimesch W.(Eds.), Event-related dynamics of brain oscillations (pp. 63–78)*.

Silberstein RB (2006b). Dynamic sculpting of brain functional connectivity and mental rotation aptitude. *Progress in brain research*, 159:63–76.

Simpson SL, Bowman FD, Laurienti PJ (2013). Analyzing complex functional brain networks: Fusing statistics and network science to understand the brain. *Statistics Surveys*, 7:1–36. DOI:10.1214/13-SS103.

Sipp AR, Gwin JT, Makeig S, Ferris DP (2013). Loss of balance during balance beam walking elicits a multifocal theta band electrocortical response. *Journal of neurophysiology*, 110(9):2050–2060.

So WK, Wong SW, Mak JN, Chan RH (2017). An evaluation of mental workload with frontal eeg. *PloS one*, 12(4):e0174949.

Soltanlou M, Artemenko C, Dresler T, Haeussinger FB, Fallgatter AJ, Ehlis AC, Nuerk HC (2017). Increased arithmetic complexity is associated with domain-general but not domain-specific magnitude processing in children: a simultaneous fnirs-eeg study. *Cognitive, Affective, & Behavioral Neuroscience*, 17:724–736.

Spüler M, Walter C, Rosenstiel W, Gerjets P, Moeller K, Klein E (2016). Eeg-based prediction of cognitive workload induced by arithmetic: a step towards online adaptation in numerical learning. *Zdm*, 48:267–278.

Steculа K (2022). Virtual reality applications market analysis—on the example of steam digital platform. *Informatics*, MDPI, volume 9, 100 pages.

Steriade M, Dossi RC, Nuñez A (1993). Intracellular studies of thalamic neurons generating sleep delta waves and fast (40-hz) oscillations during arousal. *Basic Mechanisms of the EEG*, Springer, pages 129–144.

Südhof TC (2021). The cell biology of synapse formation. *Journal of Cell Biology*, 220(7): e202103052.

Summerfield C, Mangels JA (2005). Coherent theta-band eeg activity predicts item-context binding during encoding. *Neuroimage*, 24(3):692–703.

Sun C, Mou C (2023). Survey on the research direction of eeg-based signal processing. *Frontiers in Neuroscience*, 17:1203059.

Tajmirriahi M, Amini Z, Rabbani H, Kafieh R (2022). An interpretable convolutional neural network for p300 detection: Analysis of time frequency features for limited data. *IEEE Sensors Journal*, 22(9):8685–8692.

Tanner D, Norton JJ, Morgan-Short K, Luck SJ (2016). On high-pass filter artifacts (they're real) and baseline correction (it'sa good idea) in erp/ermf analysis. *Journal of neuroscience methods*, 266:166–170.

Tao X, Yi W, Wang K, He F, Qi H (2021). Inter-stimulus phase coherence in steady-state somatosensory evoked potentials and its application in improving the performance of single-channel mi-bci. *Journal of Neural Engineering*, 18(4):046088.

Thatcher R, Soler E, North D, Otte G (2020). Independent components analysis "artifact correction" distorts eeg phase in artifact free segments. *J Neurol Neurobiol*, 6(4):5–7.

Thatcher RW (2012). Coherence, phase differences, phase shift, and phase lock in eeg/erp analyses. *Developmental neuropsychology*, 37(6):476–496.

Thompson T, Steffert T, Ros T, Leach J, Gruzelier J (2008). Eeg applications for sport and performance. *Methods*, 45(4):279–288.

Tiwari A, Albuquerque I, Gagnon JF, Lafond D, Parent M, Tremblay S, Falk TH (2019). Mental workload assessment during physical activity using non-linear movement artefact robust electroencephalography features. *2019 IEEE International Conference on Systems, Man and Cybernetics (SMC)*, IEEE, pages 4149–4154.

Tiwari S, Goel S, Bhardwaj A (2022). Midnn-a classification approach for the eeg based motor imagery tasks using deep neural network. *Applied Intelligence*, pages 1–20.

Toa CK, Sim KS, Tan SC (2021). Electroencephalogram-based attention level classification using convolution attention memory neural network. *IEEE Access*, 9:58870–58881.

Torres JMM, Medina-DeVilliers S, Clarkson T, Lerner MD, Riccardi G (2023). Evaluation of interpretability for deep learning algorithms in eeg emotion recognition: A case study in autism. *Artificial intelligence in medicine*, 143:102545.

Tort AB, Komorowski R, Eichenbaum H, Kopell N (2010). Measuring phase-amplitude coupling between neuronal oscillations of different frequencies. *Journal of neurophysiology*, 104(2):1195–1210.

Trajin B, Chabert M, Régnier J, Faucher J (2008). Space vector analysis for the diagnosis of high frequency amplitude and phase modulations in induction motor stator current. *5th International Conference on Condition Monitoring and Machinery Failure Prevention Technologies-CM/MFPT 200810*, pages 1–8.

Trambaiolli L, Cassani R, Biazoli C, Cravo A, Sato J, Falk T (2018). Resting-awake eeg amplitude modulation can predict performance of an fnirs-based neurofeedback task. *2018 IEEE International Conference on Systems, Man, and Cybernetics (SMC)*, IEEE, pages 1128–1132.

Trambaiolli LR, Cassani R, Falk TH (2020). Eeg spectro-temporal amplitude modulation as a measurement of cortical hemodynamics: An eeg-fnirs study. *2020 42nd Annual International Conference of the IEEE Engineering in Medicine & Biology Society (EMBC)*, IEEE, pages 3481–3484.

Trambaiolli LR, Falk TH, Fraga FJ, Anghinah R, Lorena AC (2011). Eeg spectro-temporal modulation energy: a new feature for automated diagnosis of alzheimer's disease. *2011 Annual International Conference of the IEEE Engineering in Medicine and Biology Society*, IEEE, pages 3828–3831.

Tröndle M, Popov T, Pedroni A, Pfeiffer C, Barańczuk-Turska Z, Langer N (2023). Decomposing age effects in eeg alpha power. *Cortex*, 161:116–144.

Tsimenidis S (2020). Limitations of deep neural networks: a discussion of g. marcus' critical appraisal of deep learning. *arXiv preprint arXiv:2012.15754*.

Tzouvadaki I, Gkoupidenis P, Vassanelli S, Wang S, Prodromakis T (2023). Interfacing biology and electronics with memristive materials. *Advanced Materials*, 35(32):2210035.

Urigüen JA, Garcia-Zapirain B (2015). Eeg artifact removal—state-of-the-art and guidelines. *Journal of neural engineering*, 12(3):031001.

Värbu K, Muhammad N, Muhammad Y (2022). Past, present, and future of eeg-based bci applications. *Sensors*, 22(9):3331.

Varshney A, Ghosh SK, Padhy S, Tripathy RK, Acharya UR (2021). Automated classification of mental arithmetic tasks using recurrent neural network and entropy features obtained from multi-channel eeg signals. *Electronics*, 10(9):1079.

Vatinno AA, Simpson A, Ramakrishnan V, Bonilha HS, Bonilha L, Seo NJ (2022). The prognostic utility of electroencephalography in stroke recovery: a systematic review and meta-analysis. *Neurorehabilitation and neural repair*, 36(4-5):255–268.

Vossel S, Weidner R, Moos K, Fink GR (2016). Individual attentional selection capacities are reflected in interhemispheric connectivity of the parietal cortex. *Neuroimage*, 129:148–158.

Vourvopoulos A, Pardo OM, Lefebvre S, Neureither M, Saldana D, Jahng E, Liew SL (2019). Effects of a brain-computer interface with virtual reality (vr) neurofeedback: A pilot study in chronic stroke patients. *Frontiers in human neuroscience*, 13:460405.

Voytek B, Canolty RT, Shestyuk A, Crone N, Parvizi J, Knight RT (2010). Shifts in gamma phase–amplitude coupling frequency from theta to alpha over posterior cortex during visual tasks. *Frontiers in human neuroscience*, 4:191.

Vukovic N, Feurra M, Shpektor A, Myachykov A, Shtyrov Y (2017). Primary motor cortex functionally contributes to language comprehension: An online rtms study. *Neuropsychologia*, 96:222–229.

Waisberg E, Ong J, Lee AG (2024). Ethical considerations of neuralink and brain-computer interfaces. *Annals of Biomedical Engineering*, pages 1–3.

Walter E, Dassonville P (2008). Visuospatial contextual processing in the parietal cortex: an fmri investigation of the induced roelofs effect. *Neuroimage*, 42(4):1686–1697.

Wang D, Chen J, Zhao D, Dai F, Zheng C, Wu X (2017). Monitoring workers' attention and vigilance in construction activities through a wireless and wearable electroencephalography system. *Automation in Construction*, 82:122–137.

Wang L, Huang W, Yang Z, Zhang C (2020). Temporal-spatial-frequency depth extraction of brain-computer interface based on mental tasks. *Biomedical Signal Processing and Control*, 58:101845.

WANG X, LI S, LI R, NING H (2023). Advances in the application of a brain–computer interface to the metaverse. *Chinese Journal of Engineering*, 45(9):1528–1538.

Weiss S, Mueller HM (2012). "too many betas do not spoil the broth": the role of beta brain oscillations in language processing. *Frontiers in psychology*, 3:201.

Winkler I, Haufe S, Tangermann M (2011). Automatic classification of artifactual ica-components for artifact removal in eeg signals. *Behavioral and brain functions*, 7:1–15.

Won K, Kwon M, Ahn M, Jun SC (2022). Eeg dataset for rsvp and p300 speller brain-computer interfaces. *Scientific data*, 9(1):388.

Wood G, Kober SE, Witte M, Neuper C (2014). On the need to better specify the concept of "control" in brain-computer-interfaces/neurofeedback research. *Frontiers in systems neuroscience*, 8:171.

Wriessnegger SC, Müller-Putz GR, Brunner C, Sburlea AI (2020). Inter-and intra-individual variability in brain oscillations during sports motor imagery. *Frontiers in human neuroscience*, 14:576241.

Wu J (2017). Introduction to convolutional neural networks. *National Key Lab for Novel Software Technology. Nanjing University. China*, 5(23):495.

Xu K, Huang YY, Duann JR (2019). The sensitivity of single-trial mu-suppression detection for motor imagery performance as compared to motor execution and motor observation performance. *Frontiers in human neuroscience*, 13:302.

Xu M, Han J, Wang Y, Jung TP, Ming D (2020). Implementing over 100 command codes for a high-speed hybrid brain-computer interface using concurrent p300 and ssvep features. *IEEE Transactions on Biomedical Engineering*, 67(11):3073–3082.

Xu M, He F, Jung TP, Gu X, Ming D (2021). Current challenges for the practical application of electroencephalography-based brain–computer interfaces. *Engineering*, 7(12):1710–1712.

Xu R, Jiang N, Mrachacz-Kersting N, Lin C, Prieto GA, Moreno JC, Pons JL, Dremstrup K, Farina D (2014). A closed-loop brain–computer interface triggering an active ankle–foot orthosis for inducing cortical neural plasticity. *IEEE Transactions on Biomedical Engineering*, 61(7):2092–2101.

Yang AHX, Kasabov N, Cakmak YO (2022a). Machine learning methods for the study of cybersickness: a systematic review. *Brain Informatics*, 9(1):24.

Yang S, Hwang HS, Zhu BH, Chen J, Enkhzaya G, Wang ZJ, Kim ES, Kim NY (2022b). Evaluating the alterations induced by virtual reality in cerebral small-world networks using graph theory analysis with electroencephalography. *Brain Sciences*, 12(12):1630.

Yildirim C (2020). A review of deep learning approaches to eeg-based classification of cybersickness in virtual reality. *2020 IEEE international conference on artificial intelligence and virtual reality (AIVR)*, IEEE, pages 351–357.

Yu H, Ba S, Guo Y, Guo L, Xu G (2022a). Effects of motor imagery tasks on brain functional networks based on eeg mu/beta rhythm. *Brain Sciences*, 12(2):194.

Yu J, Li C, Lou K, Wei C, Liu Q (2022b). Embedding decomposition for artifacts removal in eeg signals. *Journal of Neural Engineering*, 19(2):026052.

Yu W, Zhang J, Tang J (2017). Effects of dynamic synapses, neuronal coupling, and time delay on firing of neuron. *Wuli Xuebao/Acta Physica Sinica*, 66. DOI:10.7498/aps.66.200201.

Yue K, Wang D (2019). Eeg-based 3d visual fatigue evaluation using cnn. *Electronics*, 8(11):1208.

Zander TO, Andreessen LM, Berg A, Bleuel M, Pawlitzki J, Zawallich L, Krol LR, Gramann K (2017). Evaluation of a dry eeg system for application of passive brain-computer interfaces in autonomous driving. *Frontiers in human neuroscience*, 11:78.

Zander TO, Jatzev S (2009). Detecting affective covert user states with passive brain-computer interfaces. *2009 3rd International Conference on Affective Computing and Intelligent Interaction and Workshops*, IEEE, pages 1–9.

Zander TO, Kothe C (2011). Towards passive brain–computer interfaces: applying brain–computer interface technology to human–machine systems in general. *Journal of neural engineering*, 8(2):025005.

Zanto TP, Rubens MT, Thangavel A, Gazzaley A (2011). Causal role of the prefrontal cortex in top-down modulation of visual processing and working memory. *Nature neuroscience*, 14(5):656.

Zarjam P, Epps J, Lovell NH (2015). Beyond subjective self-rating: Eeg signal classification of cognitive workload. *IEEE Transactions on Autonomous Mental Development*, 7(4):301–310.

Zarjam P, Epps J, Lovell NH, Chen F (2012). Characterization of memory load in an arithmetic task using non-linear analysis of eeg signals. *2012 annual international conference of the IEEE engineering in medicine and biology society*, IEEE, pages 3519–3522.

Zhang C, Yu X, Yang Y, Xu L (2014a). Phase synchronization and spectral coherence analysis of eeg activity during mental fatigue. *Clinical EEG and neuroscience*, 45(4):249–256.

Zhang P, Wang X, Chen J, You W, Zhang W (2019). Spectral and temporal feature learning with two-stream neural networks for mental workload assessment. *IEEE Transactions on Neural Systems and Rehabilitation Engineering*, 27(6):1149–1159.

Zhang X, Wu D, Ding L, Luo H, Lin CT, Jung TP, Chavarriaga R (2021). Tiny noise, big mistakes: adversarial perturbations induce errors in brain–computer interface spellers. *National Science Review*, 8(4):nwaa233.

Zhang Y, Xu P, Cheng K, Yao D (2014b). Multivariate synchronization index for frequency recognition of ssvep-based brain–computer interface. *Journal of neuroscience methods*, 221:32–40.

Zhang Y, Zhou G, Jin J, Wang X, Cichocki A (2015). Ssvep recognition using common feature analysis in brain–computer interface. *Journal of neuroscience methods*, 244:8–15.

Zhang Z, Silva I, Wu D, Zheng J, Wu H, Wang W (2014c). Adaptive motion artefact reduction in respiration and ecg signals for wearable healthcare monitoring systems. *Medical & biological engineering & computing*, 52(12):1019–1030.

Zhao X, Chu Y, Han J, Zhang Z (2016). Ssvep-based brain–computer interface controlled functional electrical stimulation system for upper extremity rehabilitation. *IEEE Transactions on Systems, Man, and Cybernetics: Systems*, 46(7):947–956.

Zhou Q, Cheng R, Yao L, Ye X, Xu K (2022). Neurofeedback training of alpha relative power improves the performance of motor imagery brain-computer interface. *Frontiers in Human Neuroscience*, 16:831995.

Zhou X, Liu C, Zhai L, Jia Z, Guan C, Liu Y (2023). Interpretable and robust ai in eeg systems: A survey. *arXiv preprint arXiv:2304.10755*.

Zhou Y, He S, Huang Q, Li Y (2020). A hybrid asynchronous brain-computer interface combining ssvep and eog signals. *IEEE Transactions on Biomedical Engineering*, 67(10):2881–2892.

Zhu HY, Hieu NQ, Hoang DT, Nguyen DN, Lin CT (2024). A human-centric metaverse enabled by brain-computer interface: A survey. *IEEE Communications Surveys & Tutorials*.

Zou L, Chen X, Dang G, Guo Y, Wang ZJ (2019). Removing muscle artifacts from eeg data via underdetermined joint blind source separation: A simulation study. *IEEE Transactions on Circuits and Systems II: Express Briefs*, 67(1):187–191.